

Table of contents

Table of contents	i
1 Introduction	1
1.1 BNCT research activities in Pavia	3
1.2 BNCT of Osteosarcoma	5
1.3 Summary of the Thesis	7
2 Boron Measurements	9
2.1 Introduction to Neutron Autoradiography	11
2.1.1 The action of the etching	15
The action of the etching	15
2.1.2 Geometry of track development for constant V_t	16
Geometry of track development for constant V_t	16
Bulk etch rate and track etch rate	17
2.1.3 Neutron autoradiography and BNCT	18
Neutron autoradiography and BNCT	18
2.2 Material and Methods	20
2.2.1 Bulk etch rate measurement.	20
2.2.2 Calibration samples preparation and irradiation	21
2.2.3 Track density analysis	22
2.2.4 Boron distribution analysis	23
2.3 Results	24
2.3.1 Bulk etch rate	24
2.3.2 Calibration for the liquid sample	24
2.3.3 Calibration for the tissue sample	26
2.3.4 Boron concentration map	26
2.4 Discussion and conclusions	27
3 Study of BNCT mixed field energy deposition	29
3.1 $^{10}\text{B}(\text{n},\alpha)^7\text{Li}$ energy deposit in a cell	31
3.2 Cell geometry	33
3.2.1 Oligodendrocytes	33

3.2.2	Hepatocyte	34
3.2.3	Basal Keratinocyte	34
3.2.4	Tissue like geometry	35
3.3	Nucleus hit probability	35
3.3.1	Single cell nucleus hit probability	36
3.3.2	Surrounding cells nucleus hit probability	37
3.4	Energy deposition distribution inside the nucleus	38
3.4.1	Single cell nucleus energy deposit	38
3.4.2	Surrounding cell nuclei energy deposit	38
3.5	Discussion	45
4	Design of an epithermal neutron beam for limb osteosarcoma	47
4.1	Accelerator neutron sources	49
4.1.1	MUNES-BNCT project	52
4.2	Neutron source from 5 MeV protons on beryllium	55
4.3	Epithermal Beam Shaping Assembly (BSA) characteristics	59
4.3.1	Materials	64
4.4	Simulation work flow	68
4.4.1	Phase 1 - <i>in air</i> figure of merit optimization	68
4.4.2	Phase 2 - Optimal epithermal neutron beam selection	69
4.5	Epithermal neutron beam tailoring	71
4.5.1	Slowing down of the neutron spectra	73
4.5.2	Extraction angle selection.	75
4.5.3	optimization of neutron reflection	81
4.5.4	Lateral Neutron Beam profile	85
4.6	Final Epithermal Beam	89
4.7	Beam efficiency clinical cases comparison	94
4.7.1	Osteosarcoma TPS	95
4.7.2	Treatment Planning	98
4.8	INFN RFQ epithermal beam V.S. ideal 1 keV beam	105
5	Conclusions and future perspectives	111
	Appendices	115
A	A - MCNP: Monte Carlo Code	115
A.1	MCNP $^9\text{Be}(p,n)^9\text{B}$ neutron source	116
A.2	MCNP neutron source at beam port	118
A.3	MIRD Analitical phantom	127
B	B - GEANT4 and geometrical cell implementation	141
B.1	Basal keratinocytes	142
B.2	Oligodendrocytes	143
B.3	Hepatocytes	145

TABLE OF CONTENTS

C	C - Cross Section Table and MCNP Material compositions	149
C.1	Cross Sections	149
C.1.1	Hydrogen	149
C.1.2	Lithium	150
C.1.3	Beryllium	150
C.1.4	Carbon	151
C.1.5	Oxygen	152
C.1.6	Fluorine	153
C.1.7	Magnesium	154
C.1.8	Aluminium	155
C.1.9	Titanium	156
C.1.10	Nickel	157
C.1.11	Lead	158
C.1.12	Bismuth	159
C.2	MCNP Material composition	159
C.2.1	Aluminium Alloys	159
C.2.2	Lithium fluoride	160
C.2.3	Lithium loaded polyethilene	160
C.2.4	Lithium carbonate	160
C.2.5	Titanium	161
D	List of publications	163
	Bibliography	167

dedica

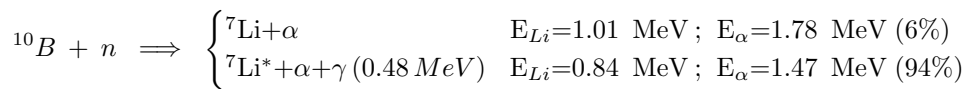
Chapter 1

Introduction

Boron Neutron Capture Therapy (BNCT) is a form of radiation therapy that exploits the high capture¹ cross section of thermal neutrons² in the non-radioactive ^{10}B nuclide. This reaction releases two high LET (Linear Energy Transfer) particles, an α particle with a LET of about $150 \text{ keV}\mu\text{m}^{-1}$ and a ^7Li ion with a LET of $175 \text{ keV}\mu\text{m}^{-1}$. The range of these particles in tissue is similar to the cell diameter, approximately $10 \mu\text{m}$ and $4.5 \mu\text{m}$ respectively for the α particle and ^7Li ion. BNCT effectiveness depends on the possibility to convey ^{10}B in neoplastic cells more than in healthy ones. Hence, thermal neutron irradiation causes a higher number of boron neutron capture reactions within the neoplastic tissue. Moreover, the short range of the generated particles, ensures that all the energy is deposited inside the cells where the reactions took place. Knowing the boron concentration in tumour and in normal tissues it is thus possible to deliver a potentially therapeutic dose to the tumour while sparing the normal tissue, by dosing the neutron fluence.

BNCT research is multidisciplinary, joining the efforts of: medical doctors, chemists, engineers, biologists and physicists. The major focus point of this collaboration is improving selective tumour targeting to increase therapeutic effectiveness. To achieve this goal recent developments are focused on various aspects, one of these is the formulation of a new ^{10}B delivery system[2, 3, 4, 5, 6, 7, 8, 9, 10], with higher selectivity for the tumour compared to clinically used sodium borocaptate (BSH) and boronophenylalanine (BPA). Another field of research is the technological development to obtain suitable neutron beams employing proton accelerators [11, 12, 13, 14]. This would be a major boost to clinical BNCT due to the fact that an accelerator can be easily installed and maintained inside an health care facility, if compared to the traditional

¹ Boron neutron capture reaction is a prompt nuclear reaction:



² Neutrons with energies $< 25 \text{ meV}$

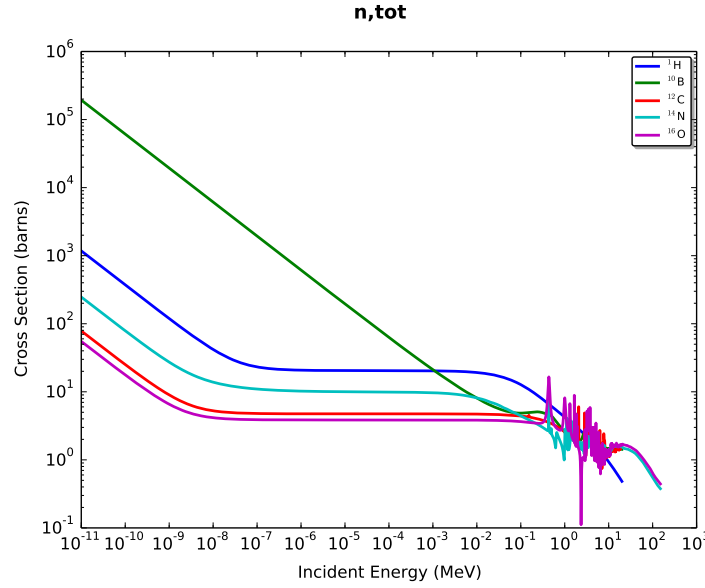


Figure 1.1: Total neutron cross section data [1]. The figure shows that at thermal neutron energies, the cross section on ^{10}B atoms is at least ≈ 100 times higher than the cross section with elements commonly found in biological tissue.

neutron source available for BNCT: the research nuclear reactors. Along with the development of new ^{10}B carriers and more efficient neutron beams another area of research is devoted to improve and uniformate the description of clinical outcome as a function of the dose delivered to patients. Dosimetry in BNCT is a fundamental yet complex issue due to the fact that the radiation field is mixed, being made up of charged particles produced by neutron capture in ^{10}B and in ^{14}N , protons due to neutron scattering in H and gamma rays from the primary beam and from radiative neutron capture in H . Therefore, many groups are working on new models to express BNCT dose in a way that it can be compared coherently with radiation dose delivered in photon-therapy [15, 16]. Together with on-line boron concentration measuring techniques a more refined BNCT dosimetry can improve the outcome of the clinical treatments [17, 18].

The most clinically used boronated formulation is boronophenylalanine (BPA) [19, 20], in Figure (1.2) the BPA molecular structure is represented. The uptake of BPA in the tumor is promoted by the increase of amino acid transport through the membrane of the tumoral cell. Therefore, it is absorbed by cells through an active process and selectively internalized in tumoral cells [21]. The selectivity of BPA permits to perform effective BNCT with substantial sparing of the normal tissues. BPA major disadvantage is the low solubility in water, which is due to hydrogen bonds that tend to aggregate BPA into a crystalline structure [22], which hinders a greater boron uptake in cancer tissue. As higher concentration ratios between tumor and healthy tissue would allow shorter and more effective neutron irradiations, for this reasons,

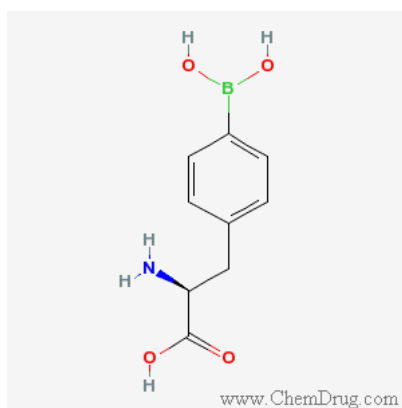


Figure 1.2: Molecular structure of boronphenylalanine. It's structure is formed by a boron atom bound with an amino acid called phenylalanine.

new boron delivery agents more effective than BPA in conveying boron to the tumor tissue are being studied. The characteristics of an ideal boronated drug for BNCT should be:

- Low toxicity for healthy cells;
- High selectivity for tumour cells;
- Capacity of accumulate in tumour a sufficient boron concentration and with a uniform distribution inside nodules;
- Rapid clearance from blood and normal tissues and persistence in tumour;
- Capacity to cross the mebrane and penetrate inside cells (i.e. being not too hydrophobic nor too lipo-phobic).

1.1 BNCT research activities in Pavia

The BNCT group in Pavia is presently active in various frontiers of BNCT research; one of these aspects deals with the assessment of new boron carriers to explore the potentiality of BNCT for osteosarcoma[23], mesothelioma and diffused thoracic tumors[24]. The feasibility of BNCT mediated by one of these new formulations is studied by *in-vitro* and *in-vivo* studies. Boron uptake measurements for different boronated substances are performed by different techniques such as: Alpha Spectroscopy (AS) and Quantitative Neutron Capture Radiography (QNCR).

The tumours that have been studied as potential target for BNCT are hepatic metastates from colon adenocarcinoma, disseminated lung petastases, malignant pleural mesotelioma and limb osteosarcoma. In particular, cell cultures of murine osteosarcoma have been used to prove the effectiveness of new

formulations to concentrate boron inside cells. New carriers developed at the Universities of Florence, Novara, Potenza, Padua are being tested: preliminary measurements demonstrate that new systems based on liposomes and gold nanoparticles functionalized with ^{10}B show a higher uptake in osteosarcoma cell cultures[23] with respect to BPA. The next step is the assessment of the pharmacokinetics of the most performing formulations, that is the behaviour of boron concentration in normal tissues and in osteosarcoma as a function of the time. The information obtained from the pharmacokinetics is then used to set the optimal time that must elapse between the administration of the boron carrier and the neutron irradiation.

A second field of research addressed in Pavia is the tailoring of neutron beams, suited for clinical BNCT. The optimal neutron energy spectrum for BNCT depends on the depth of the tumor. For shallow tumors the appropriate energy is the thermal energy range³, while for deep seated cancers the correct energy is epithermal⁴. In both cases the final neutron beam should have low contamination of fast neutron and gamma rays: these components in fact deliver a non-selective background dose to the patients that must be lowered as much as possible. Up to date, the only adequate neutron source for BNCT have been research nuclear reactors, capable of ensuring a sufficiently high flux of neutrons even after moderation and collimation. Today, the technology is ready to obtain high neutron fluxes employing proton or deuteron accelerators coupled with beryllium or lithium targets, through the (p/d,n) reactions [16].

To design a proper BSA able to tailor an effective beam, particle transport Monte Carlo codes are used, in particular MCNP[25]. Traditionally, the criteria to evaluate the performance of a beam for clinical application were based on physical parameters concerning the neutron flux in the energy range of interest for the treatment, and the dose due to the unwanted components of fast neutrons and gamma radiation ???. However, more recently, the evaluation of the performance of a beam, has been faced from another point of view, that is based on the capacity to achieve a uniform and sufficient dose distribution inside a tumour when the surrounding normal tissues receive a dose below their tolerance levels. This means that the physical characterization of a neutron beam is not sufficient per se to ensure a good results in a treatment: on the contrary, it is necessary to simulate a treatment planning with a realistic clinical situation and evaluate the Dose Volume Histograms for the organs at risk and for the target. In this work, the computational tool employed to perform BNCT treatment planning is NCTPlan [26] a code developed by MIT/CNEA (USA and Argentina), able to transform a CT scan into a voxelized model to be used as an input for MCNP. Furthermore, it is able to process the output of the dosimetry and to superimpose the dose to the CT geometry. Finally, another tool developed by CNEA (Argentina) has been used to calculate DVH: DVHTool.

³ $< 0.5 \text{ eV}$

⁴ $0.5 \text{ eV} < E < 10 \text{ keV}$

1.2 BNCT of Osteosarcoma

This dissertation develops in the framework of a project aiming to treat Osteosarcoma with BNCT. Osteosarcoma is a tumor that still represents a challenge due to its high malignancy associated to the fact that it is most frequent in children and young population. It is the most common kind of primary bone tumor, developing in the connective tissue where it produces osteoid cells[27]. It is a malignant tumor of connective tissue within which the tumor cells produce osteoid cells. The statistical distribution of this tumor with age is roughly parallel to skeletal growth. Therefore it is most frequent in late childhood or early adolescence, reaching a peak of incidence of 25 cases per million persons at the age of 15 years[27]. On average, malignant bone tumors account for 3-5% of cancers diagnosed in children under 15 years of age[28] and 7-8% of those in adolescents aged 15-19 years in western populations[29]. Taking into account a 5-year survival rate, adolescents have a lower survival rate than children. Moreover, bones having the fastest rates of growth, such as the limbs bones, have the highest probability to be hit. When osteosarcoma appears much earlier than the second decade, or after the cessation of the skeletal growth, it is often associated with other osseous abnormalities, that can be due to genetic predisposition or can be correlated to ionizing radiation exposure[30]. Osteosarcoma is characterized by an infiltrative growth and lack of cleavage planes between healthy and neoplastic tissue. Both features act as important risk factors for local recurrence because they introduce a difficulty in the total removal of the malignancy during the surgery[31].

A common feature of osteosarcoma is the predisposition to produce variable amounts of cartilage matrix and fibrous tissue. Sometimes, the growth of the cartilage matrix and the fibrous tissue dominates the expansion of the tumor tissue. In these cases it can be a challenge to make the right diagnosis. Symptoms can vary from patient to patient, although the most frequent is pain, which can persist for weeks or months. On the other hand, the most common visible manifestation is a solid inflamed mass, that can cause the loss of function of the associated limb. Any of these symptoms should be cause of further clinical investigation. In most instances the diagnosis can be made from conventional radiographies, as shown in Figure 1.3.

Osteosarcoma can give rise to lung metastases, usually about 2 years after the first diagnosis, and this fact lowers sensibly the 5-years survival rate. A bad prognosis is very probable also in case of local reoccurrence of the tumor. Prior to 1970, amputation was the only surgical treatment available for osteosarcoma, and 80 % of patients died of metastatic disease mainly of the lungs [32]. These historical cases led to the conclusion that more than 80% of patients without radiologic evidence of metastases at diagnosis had subclinical micro-metastases. This assumption was the basis for the adoption of chemotherapy protocols over the past four decades, which have led to a significant increase in the overall survival rate [33].

With the introduction of *adjuvant chemotherapy* the 5-years survival rate

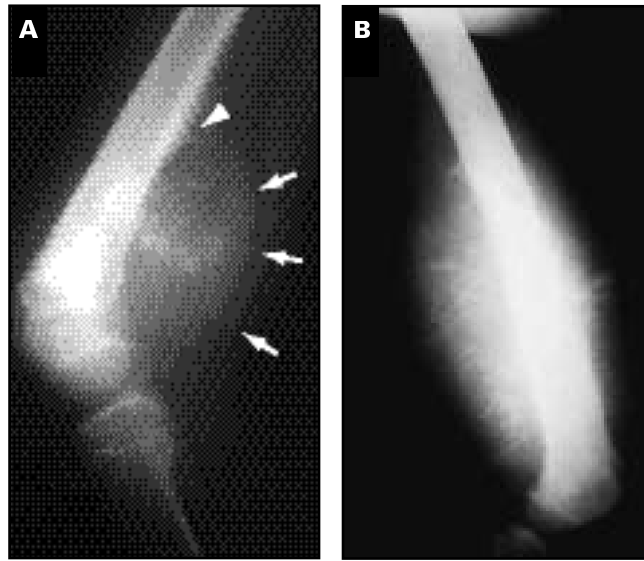


Figure 1.3: A, Lateral radiograph of the distal femur demonstrates typical radiographic features of osteosarcoma. Radiodense, cloudy bone lies within an ill-defined radiolucency of the femoral metadiaphysis. The arrows delimit a very large soft tissue mass containing bone matrix. B, Lateral radiograph in a different case demonstrating a very large extraosseous, radiodense mass that contains extensively interrupted periosteal “streamers,” forming a “sunburst” periosteal reaction[30].

was increased to 60%, although the cure rate is about 30%[34, 35, 36]. Adjuvant chemotherapy allows the neutralization of microscopic tumor masses not visible during surgery, thus decreasing the probability of local recurrence or metastasis. Moreover, osteosarcoma is a radioresistant tumor and the conventional radiotherapy is used only for palliative purposes, although local irradiation with high doses in one fraction have been administered in some clinical trials [37, 38]. The result of the treatment, with chemotherapy and surgery, of non-metastatic osteosarcoma has reached a plateau. The 5 year disease free survival of $\approx 65\%$ can be expected. There is a need of new active drugs, but at the same time, different approaches have to be planned [39].

For all these reasons, there is place for a research dedicated to find and validate a new therapeutical approach to improve the clinical outcome of osteosarcoma. The selective targeting of tumor cells achievable by BNCT could be a valid option. Anyway BNCT would not be necessarily an alternative to surgery and chemotherapy, but an adjuvant treatment able to inactivate the tumor cells surviving the standard treatments and potential cause of recurrence and metastasis. Thanks to this possibility, the surgery itself may be less aggressive, with a substantial improvement of quality of life.

The employ of BNCT as an integrative technique to treat osteosarcoma can be achieved with some adjustments in the administration ways of the boron carrier or by the use of new boronated compounds, in a way to meet the

therapeutic requirements and hence offer a new curative option to a highly malignant disease.

1.3 Summary of the Thesis

In this work different aspects of BNCT research will be covered starting, in Chapter 2, from the development and set-up of a nuclear track detector for boron concentration measurements. Here it is shown that it is possible to reduce the overall time to obtain boron concentration measurements from biological samples with respect to the set-up previously adopted. The new system was then adapted to evaluate the spatial boron concentration in a tissue sample. This was achieved by automating the image acquisition process through a software that manages the motorized table connected to the microscope. This technique is very useful to visualize the selective uptake in tumour especially when the tissue section comprises both healthy areas and tumour nodules. With this technique the boron concentration map can be overlapped with an histological image. Hence it is easy to view if boron actually concentrates in the neoplastic tissue and it helps in separating the concentration measurements in healthy areas and tumoral regions. Finally another important parameter that can be retrieved is the uniformity of boron concentration in the neoplastic tissue, which is fundamental for the outcome of clinical BNCT. The uniformity of boron distribution in the tumoral volume and the boron concentration pattern at cellular level are as important as the mean boron concentration in the tumour. Moreover the same boron concentration gives different outcome on different tissues. This may be due to interplay of the boron distribution at cellular level and the cell morphology of the affected tissue. This subject is covered in Chapter 3, where simulations with Geant4 are performed to study the energy deposition distribution of alpha particles and lithium ions when varying the boron distribution and cellular morphology. Together with the energy pattern in the nucleus from boron neutron capture reactions also the nucleus hit probability is evaluated. These two pieces of information are related to the cell survival subject to the BNCT mixed radiation field. The work exposed in Chapter 3 wants to study if there are some patterns, in the energy deposit and nucleus hit, that might justify a difference in response to BNCT in distinct tissues and boron distribution at cellular level.

Boron is not the only actor in BNCT, neutron are as important. In particular, a uniform thermal neutron field in the target volume is needed. In the past years many neutron beams were developed from nuclear reactors. From the experience of the various groups treating especially brain tumours, the optimal neutron energy was set around 10 keV. However, more recent studies based on treatment planning simulations using CT scans of real patients affected by lung tumours demonstrated that for such deep-seated cancers the ideal energy is peaked towards 1 keV [40]. The same holds for knee osteosarcoma. Such a beam can now be obtained from an accelerator neutron source.

In Chapter 4 the tailoring of an epithermal Accelerator Based BNCT neutron source is shown. Based on the RFQ accelerator designed and manufactured by INFN in Italy, able to deliver a proton current of 30 mA, thus producing a very high neutron flux at the Be target. Here an initial introduction to accelerator based neutron sources is presented, followed by the design of the Beam Shaping Assembly to produce an epithermal beam. The different configurations have been analysed both from the point of view of their physical parameters (compared to the suggested IAEA values) and from the point of view of their performance in the treatment of a real osteosarcoma. A final summary of the obtained results is shown in the conclusive Chapter 5.

Chapter 2

Boron Measurements

The development of new ^{10}B delivery systems, with higher selectivity for the tumor with respect to clinically used sodium borocaptate (BSH) and boronophenylalanine (BPA), will trigger future improvements in clinical outcomes of Boron Neutron Capture Therapy[41]. A ^{10}B concentration measuring technique for biological samples is needed in order to evaluate the performance of new boronated formulations. The most common one is Prompt Gamma Neutron Activation Analysis (PGNAA)[42, 43], a radio-analytic technique which exploits the 0.478 MeV γ ray that is emitted from the excited ^7Li in 93.9% of the capture reactions. With a facility dedicated to BNCT, it is usually possible to measure few ppms of ^{10}B in relatively large samples (0.5 cm^3) with irradiation times of some minutes. Anyhow, to measure low boron concentrations in small samples it is necessary to increase the measurement time. This technique is limited by the relatively high dimensions and the heterogeneity of the analyzed samples. In this case, the concentration that is obtained from the measurement procedure is an average value that cannot represent the uptake of the various cell fractions of the sample, such as viable tumor cells, healthy cells, necrosis, fibrosis and so on. The same problem is shared by other measurement methods such as ICP-AES (Inductively-Coupled Plasma-Atomic Emission Spectrometry), which allows measuring concentrations in the range 0.2–70 ng/g [44].

We developed two boron concentration measuring techniques at the Triga Mark II nuclear reactor in Pavia : Alpha Spectrometry¹ (AS)[45, 46] and Quantitative Neutron Capture Radiography (QNCR) [47]. The latter was recently improved, to ensure higher accuracy and optimized efficiency when a high number of samples is analyzed.

The QNCR technique exploits Solid State Nuclear Track Detectors (SS-

¹The Alpha Spectroscopy is a macroscopic boron measuring technique, where thin slices of tissue samples are irradiated in front of a Silicon detector that collects the charged particles produced by neutron interaction in the tissue. The spectrum is then analyzed and the boron content calculated.

NTD)², the one used in this work is CR-39 [49] which is based on polyallyldiglycol carbonate. The science of SSNTD was born in 1958 when D.A. Young discovered the first tracks in a crystal of LiF [50], produced by the fission fragments of uranium that had damaged the crystal. The damaged regions are more active than the surrounding undamaged areas if exposed to a chemical attack. Therefore, by opportunely etching the SSNTD, the track dimensions in the etched material are increased and become visible. The map of the tracks is acquired by a microscope connected to a computer and the tracks are then counted using specific software; for more details on this technique see Section 2.1.

In our first QNCR set-up [47] a suitable calibration curve and a sufficient resolution were achieved; however, there was still potential for improvements. Firstly it was necessary to reduce the time of the overall procedure, determined by an etching time longer than 2 hours. This would increase the efficiency of the set-up and possibly opening the road to quasi-online blood boron concentration measurements. Secondly, in order to reduce the background signal, a better selection of the tracks left on the SSNTD by ^7Li and α particles had to be achieved. The latter condition would simplify the data acquisition, avoiding the implementation of a complex morphological track selection algorithm that was previously necessary to reject the tracks due to protons³. Furthermore, this would improve the resolution of the measurement. These goals were reached employing PEW40⁴ as a chemically etching solution at 70 °C, instead of the NaOH solution previously used. This set-up decreased the etching time from 2 hours to 10 minutes. Moreover only tracks from ^7Li and α ions are thus detected, decreasing by consequence, the relative error of the calibration from 7% at 1σ of C.L to 5% at 1σ of C.L.

To further exploit the features of autoradiography, another QNCR technique was set-up to perform a quantitative imaging of the ^{10}B distribution in a biological tissue sample[51]. These images can then be compared to histological preparation of contiguous tissue sections in order to demonstrate that ^{10}B concentrates in the tumor with respect to the normal tissue. This quantitative imaging was attained by merging adjacent pictures throughout a scan of the area where the sample was fixed on the SSNTD. The tracks of each image were then analyzed with the QNCR set-up reported in Section 2.2.4. Consequently it was possible to reassemble the image of the whole sample outlining the ^{10}B concentration distribution.

The QNCR set-up was then validated by comparing the outcome of boron concentration measurements, of the same sample, with alpha-spectrometry (AS) results[46]. Moreover, through a collaboration with a group working at Comisión Nacional de Energía Atómica (CNEA, Argentina), tissue and cell

²These kind of detectors were recently used to display boron at cellular level [48]

³In biological tissues protons with an energy of 590keV are produced by the neutron capture reaction on Nitrogen: $^{14}\text{N}(\text{n,p})^{14}\text{C}$

⁴ PEW40 is a solution composed by: KOH, C₂H₅OH and H₂O. With a mass percentage of respectively: 0.15%, 0.4% and 0.45% .

samples treated with BPA (following a routine administration protocol.) are being measured by QNCR and AS in Pavia and by ICP-AES, ICP-MS and QNCR with different films in Buenos Aires. Results show that all the cited techniques are consistent for ^{10}B concentration measurements.

This improved neutron autoradiography method was then applied to ^{10}B concentration measurements in tissues from small animals and cell cultures treated with new carriers, in the frame of the BNCT feasibility study for osteosarcoma [23]. The experiments were carried out testing three categories of carriers: gold nano-particles, liposomes, polymeric nano-particles and BPA⁵. In particular, ^{10}B loaded liposomes and BPA were administered to Sprague-Dawley rats bearing osteosarcoma. After treatment, healthy muscle and tumor mass were explanted and prepared for QNCR and AS. The results concerning boron biodistribution obtained in these tissues are presented and discussed here. Boron biodistribution obtained *in vivo* will be used in the following part of the experiment, consisting in *in vivo* irradiation of rats with osteosarcoma to test BNCT efficacy in tumor remission and BNCT toxicity for healthy tissues.

This chapters begins with a brief description of the principles of Autoradiography, also introducing the past work done in Pavia, followed by the description of the present QNRC set-up.

2.1 Introduction to Neutron Autoradiography

The neutron autoradiography is a non destructive technique that allows verifying the presence of nuclei like Li, B, N, O in samples deposited on the detector. It is also used to point out defects in materials. Our goal was to measure the concentration of ^{10}B inside samples of biological materials that can be solid (tissues or cells) or liquid (urine, blood, culture medium). The neutron capture on ^{10}B produces directly ionizing particles, which are detectable by a sensitive film where the sample is directly deposited. This method is known as neutron induced autoradiography. During the irradiation, ionizing particles are produced like: photons, e^- , e^+ , p , α and heavy charged ions. Hence, the film used as detector should be sensitive only to the radiation of interest.

The limit of this technique is the thickness of the sample that can be studied, which is less than the range of the particle in the sample material that is studied. An advantage of the technique is that there is no need to develop a collimated neutron beam. The only requirement is that the thermal neutron field is uniform on the entire sample. The thermal column of the Triga Mark II reactor is a suitable facility for the autoradiography of biological samples, in fact they can be irradiated in an uniform thermal neutron field. The common neutron capture reactions and their characteristics are summarized in Table 2.1.

⁵BPA was taken as a reference, since it is the standard boronated formulation used in clinical BNCT.

Nuclear reactions	Cross section (barn) $E_n=25\text{ meV}$	Type	Emitted particles Proportion (%)	Energy (MeV)	Q Value (MeV)
${}^6\text{Li} (n, \alpha) {}^3\text{H}$	954	${}^3\text{H}$ α	100 100	2.73 2.05	4.8
${}^{10}\text{B} (n, \alpha) {}^7\text{Li}$	3842	${}^7\text{Li}$ α ${}^7\text{Li}$ α	6 6 94 94	1.78 1.01 0.84 1.47	2.8
${}^{14}\text{N} (n, p) {}^{14}\text{C}$	1.75	${}^{14}\text{C}$ p	100 100	0.042 0.584	0.63
${}^{17}\text{O} (n, \alpha) {}^{14}\text{C}$	0.23	${}^{14}\text{C}$ α	100 100	0.404 1.410	1.8

Table 2.1: Possible reactions that can be seen by the neutron capture radiography (NCR).

2.1. Introduction to Neutron Autoradiography

After the irradiation, the films must be etched in order to visualize the tracks produced by the ionizing particles in the detector. The etching parameters determine if different particles can be recognized on the basis of the dimensions of the tracks as explained below.

The autoradiography was used to analyze the concentration of ^{10}B inside the cell samples, treated with different boron carriers. As the charged particles involved are protons, alpha and lithium ions, it was necessary to study how the tracks are formed inside the sensitive film, depending on the type of particles and on their energy as a function of the etching time. The track formation inside a SSNTD is based on the fact that heavy charged particles produce an high spatial density of ionization when they pass through a material ⁶.

The primary ionizing process triggers a series of new chemical processes that result in the creation of free radicals and other chemical species. These species are grouped along the path of the charged particle, and this damaged zone is called a *latent track*.

If a piece of material containing latent tracks is exposed to some chemically aggressive solution, chemical reactions are more intense along the latent tracks. Aqueous solutions of NaOH or KOH are the most frequently used chemical solutions employed for this purpose. The overall effect is that the chemical solution etches the whole surface of the detector, but with a faster rate in the damaged region. In this way, a hole in correspondence of the track is formed, and it can be seen under an optical microscope. This procedure is called “detector etching” or track visualization, and the effect itself is called the “track effect”. Only the dielectric materials show the track effect, since in conductors and semiconductors materials the recombination dominates and the tracks are unstable, thus preventing their clear visualization.[53].

The track effect inside a SSNTD is relatively straightforward. Even if there are many theories explaining the track formation mechanism, the damaging of the material can be basically reconstructed by describing the different stages of the particle interaction with the material. The first stage is known as “physical” phase, which lasts a few picoseconds. At this time, while slowing down, the primary ionizing particle creates ionizations and excitations close to its path. The secondary particles produced also deposit their energy and generate a series of other excitation and ionization. Some of these may go further away from the initial particle path creating the so-called delta rays. Excluding the delta rays, most ionizations and damaged molecules are created close to the particle track.

The second stage is the “chemical” phase, which lasts few microseconds. During this period of time the damaged area, where the particle has crossed the SSNTD, gets back to chemical equilibrium. The excited molecules interact to produce new chemical species, producing an inhomogeneity in the material,

⁶For example: an alpha particle with 1.5 MeV creates about 40.000 ion pairs in tissue equivalent material. Since the range of those alpha particle is about $10\text{ }\mu\text{m}$ it means that 4 ion pairs on average are created per nanometer..

where the etching solution interacts in a stronger way compared to the undamaged detector areas. However, it is difficult to say which chemical species are produced and the nature of the damage is not entirely known, although some theories have been developed in order to understand these processes[54].

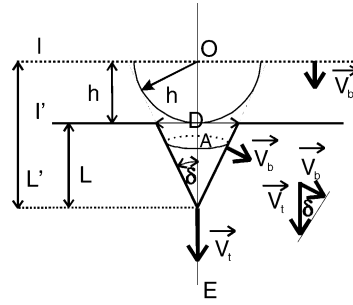
The track structure inside the material depends on the type of the particle and on its energy. The only particles that can produce a track in the SSNTD are heavy charged particles, that interact mostly through the Coulomb force with the electrons of the material. The collisions with the atomic nuclei and the loss of energy through bremsstrahlung or Cherenkov radiation can be neglected. Taking into account only the interactions with the atomic electrons, it is known that for every excitation the primary particle loses on average ≈ 30 eV [55], that is 10^{-5} to 10^{-6} times the particle energy (assuming that the particle is in the MeV region). Thereafter, the slowing down of the particle can be considered as continuous, and it can be described by the stopping power $\frac{dE}{dx}$, where dE is the energy lost in the distance dx . The first expression of the stopping power was given by Bohr [56] and was a classical treatment of the particle interaction with a free electron, taking into account an impact parameter and the classical radius of the atom. Later on, the stopping power expression was modified, firstly by Bethe [57], who introduced the quantum effects, and in a second moment by Bloch, who added the relativistic effects [58]. Hence, the final well-known Bethe-Bloch expression for the stopping power was given as:

$$-\frac{dE}{dx} = \frac{Z^2 e^4}{4\pi\epsilon_0^2 m_0 v^2} N \left[\ln \frac{2m_0 v^2 W_{max}}{\bar{I}^2 (1 - \beta^2)} - 2\beta^2 - \delta - U \right] \quad (2.1)$$

Where Z is the charge of the incident particle, v its velocity, $\beta = v/c$, m_0 the rest mass of the electron, N the number of electrons per volume, \bar{I} the average excitation potential of electrons in the stopping material, W_{max} the maximal value of transferred energy of electron, δ the correction for polarization of the material and U takes into account the shell structure of the atom. The stopping power given in the above equation takes into account only the collisions with the electrons, neglecting the ones with the nuclei.

Although Bethe-Bloch stopping power formula is widely used, there is a strong limitation to its applicability since further corrections have to be taken into account. One of the most important corrections must be made at low energies, where the ion can capture electrons from the material, therefore changing the amount of energy deposited per path. This event can be considered in the Bethe-Bloch equation by introducing an effective charge Z_{eff} .

Nowadays, softwares are available for the calculation of the stopping power and the range of charged particles in different media. One of the most widely used is SRIM (Stopping and Range of Ions in Matter), a collection of software packages which calculate many features of the transport of ions in matter developed by Ziegler et al. [59, 60].



The etching of the SSNTD can be described considering that the damage occurs along a straight line. To date, there are many theories that describe the physical aspect of the track formation. However, none of them manages to explain exhaustively the track formation in a way to classify different particles with parameters connected to the damage of the SSNTD. The problem of the track development during the etching will be thus treated in its geometrical aspects.

Starting the geometrical description from the easiest case, the incident particle is assumed to enter under normal incidence with respect to the detector surface, as shown in Figure (2.1). In this figure, I is the initial detector surface, I' is the surface after the etching, V_t is the etch rate along the particle trajectory (track etch rate), V_b is the etch rate of the undamaged regions of the detector (bulk etch rate), O is the entrance point and E is the end point of a particle in the detector material, and $OE = R$ is the particle range in the detector material. The distance between I and I' is equal to h , i.e., the thickness of the layer removed by etching, L' is the total distance traveled by the etching solution along the particle track, and L is the track depth.

The track development is characterized by two parameters: the bulk etch rate V_b and the track etch rate V_t . These quantities describe the development of the etching during a period of time t . It can be assumed that tracks development is analogous to wave propagation. Just as Huygen's principle, stating that each point in the wave front is the source of a new spherical wave, each point on the surface of the detector can be assumed to generate an "etching" front with radius $h = V_b \cdot t$. This happens all over the surface, except in the direction of the particle path, where the etching progresses with the rate V_t . Moreover, the track develops only when the ratio $V = V_t/V_b$ is higher than 1. This follows from the fact that the etch rate of the undamaged material should be less than the etch rate along the track of the particle. As shown in Figure 2.1 the local development angle δ can be defined as:

$$\sin \delta = \frac{1}{V} \quad (2.2)$$

where the track develops forming a cone. The wall of the cone will expand with the same etching rate of the bulk, in the direction parallel to the wall surface.

2.1.2 Geometry of track development for constant V_t

Recalling Figure (2.1) and the analogy between track development and wave propagation, according to the Huygen's principle, the track development for normal incidence can be considered in two dimensions, where the track depth L is given by:

$$L = (V_t - V_b) t \quad (2.3)$$

where t is the etching time. Moreover, it can be seen that:

$$\tan \delta = \frac{D}{2L} = \frac{h}{\sqrt{L^2 - h^2}} \quad (2.4)$$

by combining the previous equations, the diameter of the track opening is given:

$$D = 2h \sqrt{\frac{V - 1}{V + 1}} \quad (2.5)$$

If $V \gg 1$, from the previous equations :

$$D \cong 2h \quad (2.6)$$

Based on EQ. (2.6), an indirect method for bulk etch rate measurements was developed. If the track etch rate is very large, which is the case when heavy ions or fission products are used for the irradiation, the removed layer is directly related to the track-opening diameter which is easily measurable. Since $h = V_b t$, it is easy to calculate V_b .

Once the etchant has reached the end of the track, point E in Figure (2.1), the etching progresses in all directions with the same rate V_b , and the corresponding track becomes "over-etched". A sphere is now formed around the point E, and the shape of the track becomes a cone jointed with a sphere. With prolonged etching, the spherical part is enlarged and the conical part becomes smaller and smaller. Finally, if the etching lasts sufficiently long, the whole track will become spherical. The contrast of a spherical track is lost and the track might be seen with difficulties or might even become invisible.

In the cases studied in this thesis, normal incidence is not a real condition, the particles generated during the neutron irradiation of the sample are uniformly distributed on the entire solid angle. In these conditions the track opening becomes elliptical. The ellipse is characterized by its major axis D

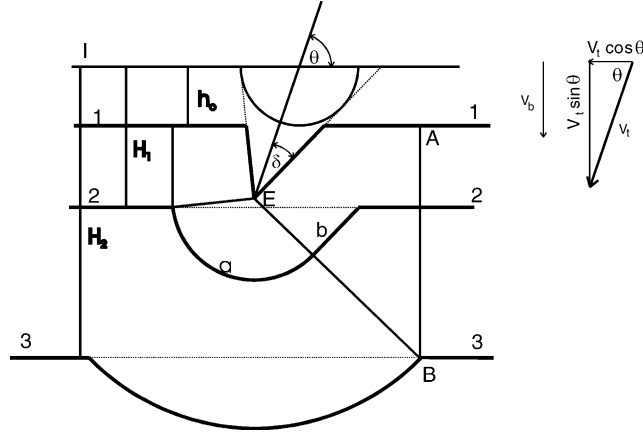


Figure 2.2: Phases of track development for oblique incidence.

and its minor axis d . These two parameters are important characteristics of a track opening for oblique incidence. If the track is over-etched, the post-etching surface might cut both the elliptical and spherical parts of the track wall. In this case, the track-opening contour is a complex curve that consists of an ellipse and a circle jointed at some points. With prolonged etching, the spherical part of the track wall, and thus the circular part of the track opening, are enlarged. Finally, the track becomes totally spherical and the opening becomes completely circular.

Geometry of track development for variable V_t

In the previous section the theoretical approach of track growth for a constant V_t was considered. In the real case V_t is variable in most cases, thus the track wall cannot be described as a regular cone anymore, and the track is now a semi-conical surface as shown in Figure (2.3). The cross-section between the post-etching detector surface and the track is now more complex than a simple ellipse, depending on the removed layer, the range of the particles and V_t . The description of this situation is beyond the purpose of this thesis, a deepening of these concepts can be found in the article by Nikezic et al. [55].

Bulk etch rate and track etch rate

The bulk etch rate V_b is the rate at which the undamaged surface of the detector is removed by the etching. Due to the chemical reaction between the etching solution (etchant) and the detector material, some molecules of the detectors are removed even if there is no track. The final effect is the removal of a layer of material from the detector surface.

For the CR-39 films used in this work, the V_b measurement, was done by

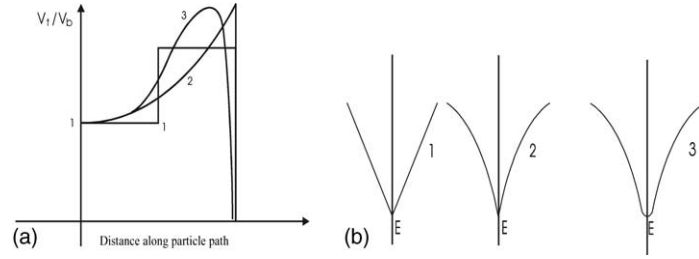


Figure 2.3: (a) Variation of the V_t function along the particle path: (1) $V_t = \text{constant}$; (2) V_t is variable with maximum at the end of the particle path; (3) V_t is variable with the maximum before the end of particle path (this is the realistic situation). (b) Track profiles for the cases (1), (2) and (3), respectively.

irradiation with a $^{252}\text{Cf}^7$ source and etched for the following times: 30, 45, 60, 70 and 80 min, in a 6.25 N NaOH solution at 70 °C⁸. The etching solution was prepared mixing 99.0 % purity NaOH with pure water. After etching, CR-39 films were washed out with cold water in order to remove the etchant solution from the detector surface. Finally the tracks were analyzed and V_b were determined by Eq. (2.6). The complete analysis and results have been published in the article by Gadan et al. [47]. The results showed that, the track diameter increased with the etching time for the whole considered time range, and a linear response with a constant bulk etch rate of $V_b = (1.64 \pm 0.02) \mu\text{m}/h$ was obtained.

The track etch rate V_t is the rate of detector etching along the particle track. For normal incidence a track is formed when $V_t > V_b$ although for an oblique incidence of the particle, a track is formed when $\cos \theta > V_b/V_t$, where θ is the angle between the track and the normal to the detector surface. For this thesis V_t was not calculated, since there are different particles interacting with the SSNTD, having their own V_t depending on their linear energy deposition in the CR-39. For our purposes it is sufficient to know that the V_t depends on the energy deposition of the ionizing particle, therefore from Eq. (2.5) the diameter of the tracks depends from the energy deposition of the ionizing particle.

2.1.3 Neutron autoradiography and BNCT

The autoradiography can be very useful in BNCT, since it allows visualizing the distribution of the boron concentration inside the samples. Although the process of image development and data acquisition can be time consuming,

⁷ ^{252}Cf can decay through spontaneous fission, these fission fragments are the ones that induce the damage to the SSNTD.

⁸This characterization was performed by Ing. M.A. Gadan (CNEA, Argentina) during his research period in Pavia.

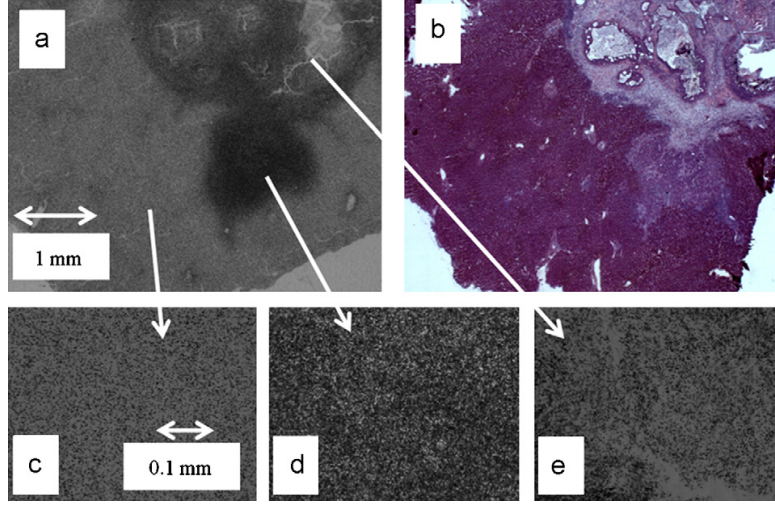


Figure 2.4: Comparison between two images of a sample coming from a tumor nodule of first patient treated by the TAOOrMINA method: (a) neutron radiography and (b) histological image. In the neutron radiography the boron distribution seems to be rather uniform in the healthy tissue (c), and quite irregular in the tumor area. (d), (e). In (d) darker zones correspond to an almost 100% presence of tumor cells, and in (e) lighter areas are filled with necrotic cells or with the tumor disseminated through healthy hepatocytes.

there is the advantage of measuring concentrations of the order of a few $\frac{\mu g}{g}$. Another benefit is the low cost of the process compared to other techniques like prompt gamma neutron activation analysis or ICP. This is due to the low cost of the CR-39 sensitive film and the possibility of irradiating simultaneously a number of samples in short irradiation times.

In Pavia, this technique was exploited as a method for qualitative imaging of the boron biodistribution in tissues [61, 62]. The irradiation and the etching parameters were set as to obtain darker areas due to higher track density in correspondence of higher boron concentration zones. The obtained images were compared with histological preparations of tissue sections contiguous to the ones used for autoradiographies. In this way it was possible to verify if the tumor nodules visible in the histological glass matched with the darkest zone in the autoradiography images. It was a way to visualize the selective uptake of boron in tissues.

Recently, this technique was exploited to set-up and calibrate a quantitative measurement of boron concentration, irradiating and etching the detectors in a way that the tracks remain separated and countable. The first part of this thesis work was dedicated to find the best parameters for the irradiation and the etching in order to reach the best working conditions for both in liquid and solid samples. An example of neutron autoradiography for boron quantification is shown in Figure 2.5.

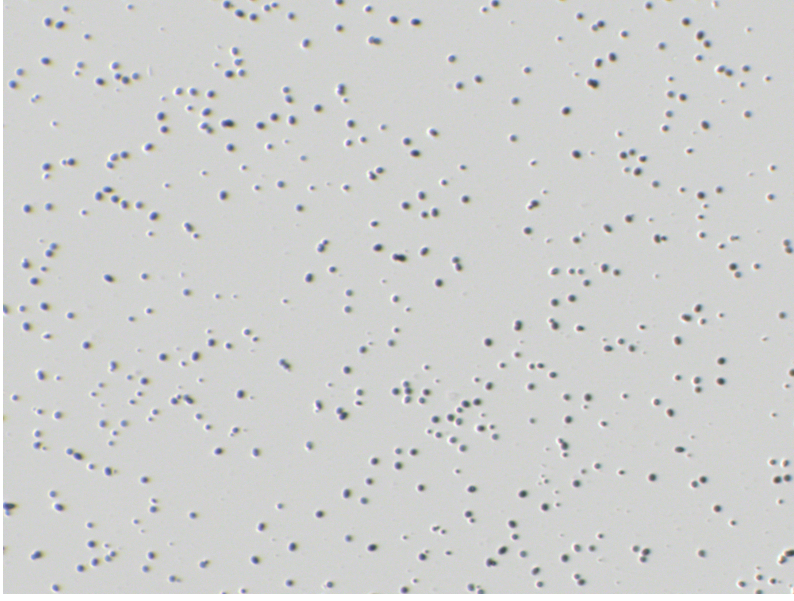


Figure 2.5: This image is an example of the tracks that form from the irradiation with 30 ppm of ^{10}B a CR-39 SSNTD. The picture represents an area of 0.2961 mm^2 .

2.2 Material and Methods

CR-39⁹ was used as SSNTD, as described in Gadan et al. [47], thus, before proceeding with boron concentration measurements, the bulk etch rate associated with the new etching method was characterized as a comparison to the previous set-up. Subsequently the most favorable irradiation conditions were chosen. Calibration curves were built both for liquids and tissue samples. These results were then used for boron concentration measurements of tissue samples from animals administered with different boronated substances. The same samples were then analyzed with the AS method [46, 23], therefore validating this new QNCR set-up.

Subsequently, a c++ code in the ROOT framework[63] was written in order to employ the calibration curves in the assessment of boron concentration of measured samples. The microscopic images obtained from a scan of the whole tissue section were analyzed and recombined in a map of boron concentrations.

2.2.1 Bulk etch rate measurement.

The bulk etch rate V_b was measured and compared to the one obtained by Gadan et al. [47], highlighting therefore the differences of the etching conditions in the two set-ups. For V_b measurement, the CR-39 films were etched for the following times: 0, 2, 4, 8, 10, 20, 30 and 60 minutes, in a PEW40 solution

⁹Rectangular polyallyldiglycol carbonate (PADC), from Intercast Europe manufacturer, with 75x25 mm² area and 1 mm width.

2.2. Material and Methods

at 70°C, which was obtained by mixing: 15% of KOH, 40% of C₂H₆O and 45% of pure water; where % represents the mass per cent. After each etching time the thickness of the SSNTD was measured employing a Mitutoyo device (LITEMATIC VL-50AS, with a sensitivity of 0.1 μm) in 20 randomly chosen points. The mean values of thickness and the standard deviation were then calculated, plotted and analyzed by means of a routine in ROOT framework.

2.2.2 Calibration samples preparation and irradiation

For boron measurement by neutron autoradiography a calibration curve expressing the track density as a function of boron concentration must be assessed. The first step was to perform measurements using tissue and liquid standards with known boron concentration in order to obtain two calibration curves, expressed as density of tracks [$\text{tracks}/\text{mm}^2$] versus boron concentration in ppm. Standard liquid and tissue samples with known boron concentration are used as reference.

The liquid standards consisted of water solutions of ¹⁰B at 5, 10, 25, 50 and 100 ppm. About 1 ml of each solution was poured on CR-39 films, using the device constructed on purpose for the irradiation of liquid samples, that allows irradiating 4 films a time with 4 samples each[47]. This device was irradiated at the end of the thermal column of the TRIGA Mark II reactor, operating at 20 kW for 30 min, receiving a neutron fluence of $(10.4 \pm 0.4) \cdot 10^{10} \text{n}/\text{cm}^2$. After irradiation, CR-39 films were chemically etched for 10 min with the same etching parameters used for the bulk etch rate calculations.

The tissue standards were obtained from a mixture of liver cells and a solution of BPA fructose in different fixed proportions[47], obtaining reference concentrations of 10, 19, 43, 57 and 75 $\mu\text{g}/\text{g}$. These samples were frozen in small cylindrical rods at -80°C. Afterwards, 60 μm thick sections were obtained using a Leica cryostat and were deposited on CR-39 films, that were then irradiated at the end of the thermal column with the reactor operating at 2 kW for 30 min, receiving a neutron fluence of $(1.97 \pm 0.01) \cdot 10^{10} \text{n}/\text{cm}^2$. After irradiation, films were chemically etched with described etching conditions for 10 min.

and before neutron irradiation; la quantità di acqua presente nel campione influenza il trasporto delle alfa nel campione stesso e quindi il numero di tracce sul rivelatore

Another parameter that must be taken into account for tissue calibration is the amount of water loss occurring after the preparation of the tissue sections. This is necessary since distinct tissues may loose water in different percentages before neutron irradiation. The amount of water in the sample influences the transport of the α particle and lithium ion, which affects the number of latent tracks on the detector. Therefore, the dry to fresh mass ratio is needed to renormalize the result with respect to the calibration curve. To measure the mass loss due to evaporation, the same set-up as in [47] was used.

2.2.3 Track density analysis

After the irradiation and etching (see result in Figure 2.6), the procedure consisted of 3 further steps: image acquisition, image analysis and data analysis. The experimental set up for the Image acquisition is composed by a microscope¹⁰ connected to a lamp¹¹ and a joystick¹². The microscope has an integrated camera connected to a PC and images are acquired and analyzed with Image Pro Plus 7.0[64]. Once the acquisition process is concluded, Image Pro Plus allows performing some operations in the picture. The first one is the background subtraction to eliminate the inhomogeneities light field. Subsequently, the contrast of the picture is enhanced, in a way to increase the visibility of the tracks left by the particles. The contrast enhancement is performed keeping the same parameters for all the analyzed pictures, since the acquisition conditions are the same.

The last phase of image analysis consists in selecting and counting¹³ the tracks, according to the gray scale¹⁴. For the purpose of the analysis, only dark objects are selected, the range of the selected gray scale is fixed for all the analyzed pictures. Finally, before counting the tracks, the interesting morphological parameters of the dark objects are selected: the ratio of the radii¹⁵ of the tracks and their area. The first one is important since it is an estimator of track roundness; if the value is near to 1 then the track has a circular shape, at increasing ratios the track becomes less circular. The latter parameter depends on the ionizing particle energy[55]. From each analyzed picture a file is created reporting these parameters for each analyzed track.

These files are then analyzed with a ROOT program. The data analysis starts by imposing a threshold to reject objects with radius less than 2 pixels and radius ratio greater than 1.6, to remove artifacts or film defects from the counting mechanism. Non perpendicular tracks and overlapping tracks can be neglected since the etching time and neutron irradiation were accurately selected. Moreover, Figure 2.7 shows that tracks, from boron neutron capture reaction, have circular shape and well defined area. Therefore, it is easy to separate physical tracks from artifacts or superimposed tracks. Subsequently the remaining tracks are counted yielding the density of tracks in one picture. The identical method is applied to each analyzed random microscopic picture of the same sample. These data are then converted in an histogram plotting the distribution of the track density per picture. The histogram follows a normal distribution, that is then fitted with a Gaussian, giving the mean track density and the associated standard deviation. Finally the track density is divided by

¹⁰LEICA MZ16A

¹¹LEICA CLS150X

¹²PRIOR OPTISCAN II

¹³*Count/Size* function of Image Pro

¹⁴The light set-up is repeatable, the lamp is fixed at a certain luminosity output and the effect of surrounding light is negligible.

¹⁵The radii ratio is the ratio between the maximum and minimum distance from the border to the center of the track.



Figure 2.6: Microscopic image of an irradiated and etched SSNTD of a tissue standard with 10ppm of boron.

the area of a picture¹⁶ in mm².

2.2.4 Boron distribution analysis

Once the calibration curves were obtained, it was possible to use them to measure boron concentration in samples treated with boronated substances. Instead of randomly taking picture through the sample area, a uniform scan in a predetermined area¹⁷ ($\approx 1 \text{ cm}^2$) was implemented. This picture sampling was possible because Image Pro Plus can manage the movable table that is installed in the Leica microscope. Again, as in Section 2.3, the software outputs files recording the track morphological characteristics.

These files were analyzed with an home made c++ software that makes use of ROOT functionalities. Accordingly, threshold values were imposed, then for each picture the track density was calculated. Thus, by comparison with the tissue calibration curve, for each picture the boron concentration was evaluated by taking into account water evaporation. Finally, these values were plotted in a 3D histogram where each color represents a ^{10}B concentration value, resulting

¹⁶The picture has an area of 0.2961 mm^2 , each picture has 5Mp resolution corresponding to 2739×1826 pixels.

¹⁷The selection of the area depends on the dimensions of the analyzed sample.

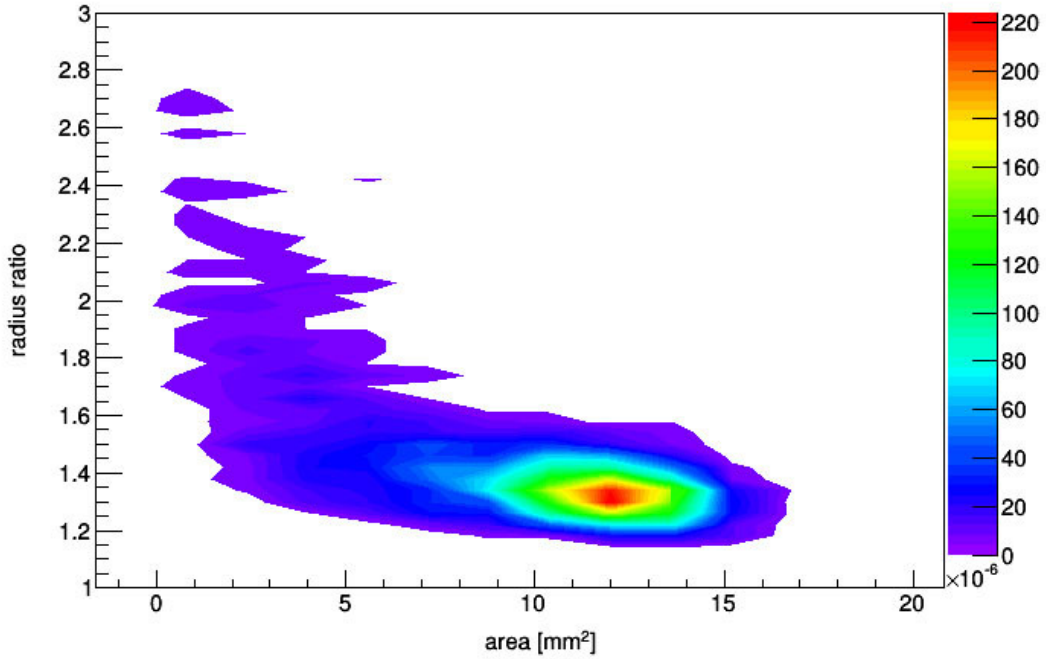


Figure 2.7: Scatter plot showing the relation between the track area and the radius ratio.

in a map of the boron concentration.

For this analysis two sections of the same sample were taken. The first $60\ \mu\text{m}$ thick slice was deposited on the SSNTD for the quantitative analysis. While the second adjacent slice of $10\ \mu\text{m}$ was deposited on a microscope slide which was then stained with hematoxylin and eosin. This enabled the comparison of the boron distribution map with an histological image, allowing an immediate evaluation of the selectivity in boron absorption by the tumor nodules.

2.3 Results

2.3.1 Bulk etch rate

The thickness of the removed layer as function of the etching time, measured as described in Section 2.2.1, is shown in Figure 2.8.

Etching increases linearly in time with a bulk etch rate of $V_b = (25.1 \pm 0.6)\ \mu\text{m}/\text{h}$. This is ≈ 15 times faster than the previous etching conditions [47].

2.3.2 Calibration for the liquid sample

The calibration curve for the liquid sample is shown in Figure 2.9, the fit results linear with a slope of $0.112 \pm 0.006\ \text{ppm} \cdot \text{mm}^2/\text{tracks}$.

2.3. Results

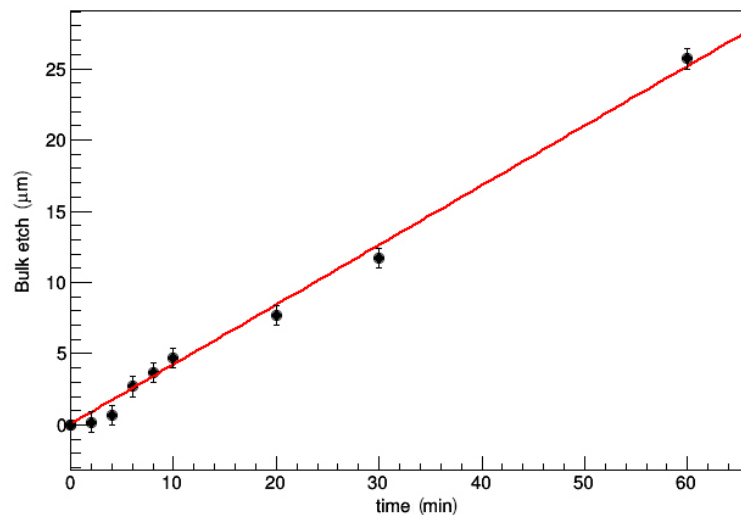


Figure 2.8: Amount of material removed (bulk etched) as a function of time. The fit was performed with a linear equation .

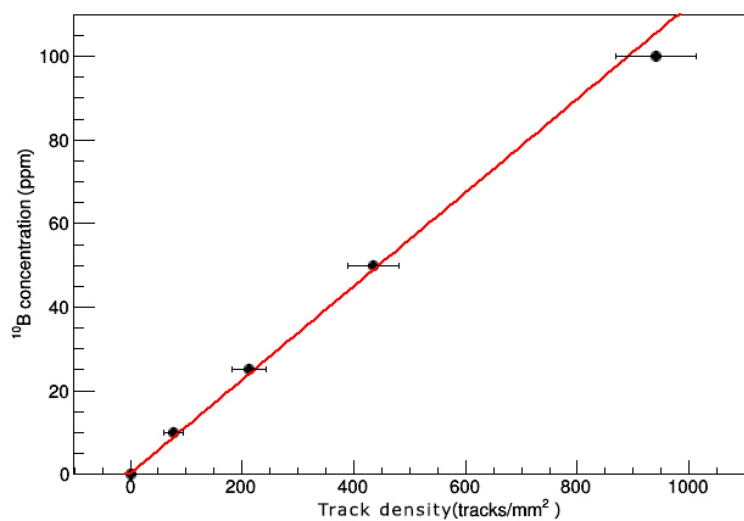


Figure 2.9: Calibration curve for liquid samples; boron concentration as a function of track density. The fit has been performed with a linear equation.

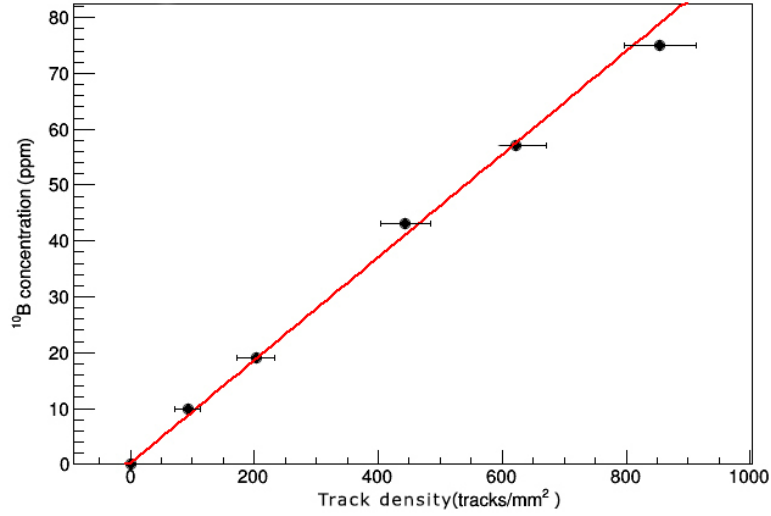


Figure 2.10: Tissue calibration curve; boron concentration as a function of track density. The fit has been performed with a linear equation.

There is no visible saturation effect, in the studied range, and values are expressed with 1σ confidence level. The limit of boron detection (LOD) is ≈ 0.5 ppm while the limit of quantification (LOQ) is ≈ 1.5 ppm. Therefore, this set-up can be reliably used to measure boron concentrations from 1.5 to 100 ppm, which is the usual range found in clinical BNCT.

2.3.3 Calibration for the tissue sample

The calibration curve for the tissue sample is shown in Figure 2.10, again the fit results linear with a slope of $0.092 \pm 0.004 \text{ ppm} \cdot \text{mm}^2/\text{tracks}$.

As stated in Section 2.2.2 the dry to fresh mass ratio was measured, for the reference tissue sample this value corresponds to 0.17 ± 0.01 . There is no visible saturation effect and values are expressed with 1σ confidence level. The LOD is ≈ 0.5 ppm while the LOQ is ≈ 1.5 ppm. Therefore, this set-up can be reliably used to measure boron concentrations from 1.5 to 100 ppm, which is the usual range found in clinical BNCT.

2.3.4 Boron concentration map

This technique was applied on tissue samples of Sprague-Dawley rats bearing osteosarcoma and administered with BPA. The result of the analysis is shown in Figure 2.11a. From the comparison with the histological image (Figure 2.11b) of the same sample, it is evident that boron concentrates more in the cancerous mass with respect to the healthy tissue. Moreover, the ratio between boron concentration in the tumor with respect to the normal tissue (≈ 3.5)

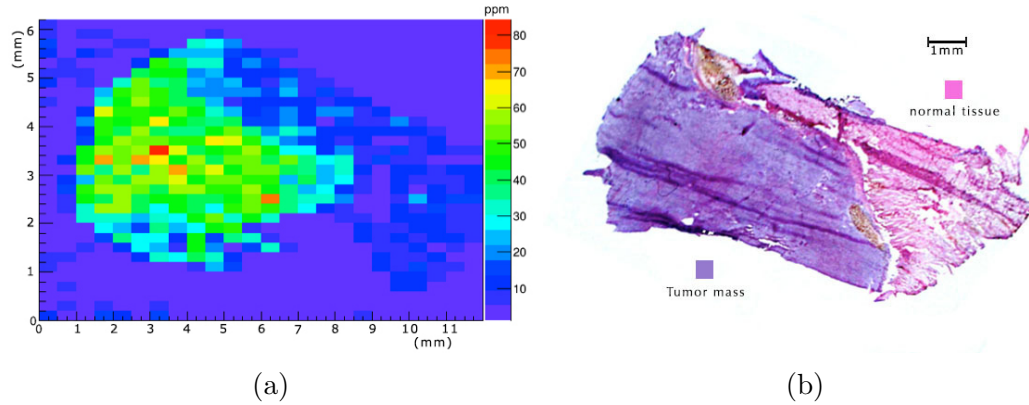


Figure 2.11: Comparison of (Figure 2.11a) ^{10}B distribution in a tissue sample of a Sprague-Dawley rat bearing osteosarcoma with the corresponding (Figure 2.11b) histological image of a subsequent slice of the tissue sample.

resulted very similar to the value found in literature, in other tumours treated with BPA[19].

2.4 Discussion and conclusions

The calibration curves obtained for both liquid and solid samples have an error of less than 5% and the linearity in the whole range of concentrations tested is good, thus they can be employed for boron concentration measurements in BNCT studies. More precisely this set-up was, and will be, adopted for the research of new boronated compounds such as : ^{10}B loaded liposomes, gold nano particles and polymeric nano particles. Results obtained in these works are described in [10] and [23].

Comparing the new set-up with [47] some improvements were achieved. At first, the etching time was reduced from ≈ 2 hours to 10 minutes: this dramatically increases the efficiency of the method because it speeds up the sample preparation before the microscopic analysis. Moreover, there is no evidence of proton contamination, from neutron capture reaction in nitrogen. Since the track density in tissue samples without boron is almost 0 and the tracks detected in such samples come only from protons generated by neutron capture in nitrogen. Therefore, the results with control samples demonstrate that this method is not sensitive to protons. This simplifies the image analysis, since there is no need to morphological separate the tracks generated by protons from the tracks generated by α particles or lithium ions. The only selection is the constraint on radius and radius ratio to remove signals originated by artifacts or film defects. In fact, the calibration accuracy, that is determined by the relative error of the calibration slopes, was reduced from 6% to 4%. Another aspect that has changed with respect to the former protocol is the

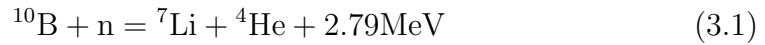
fact that the track density is now lower. As a consequence it was possible to calibrate the system for a wider range of ^{10}B concentrations.

Finally, as shown in Section 2.3.4, it was possible to employ the tissue calibration curve for quantitative boron distribution measurements. This increases the possible applications of neutron autoradiography in BNCT, in fact it is a useful method to have deeper insights into boron biodistribution in tumour and different healthy tissues. As demonstrated by dedicated studies performed by Argentinean BNCT group, in order to obtain a more effective BNCT treatment, it is essential that boron is taken up uniformly by tumour [65]. Thus it is important to quantify boron concentration in terms of tumour to normal tissue ratio, but also to investigate carefully the homogeneity of boron distribution inside tumour. Neutron autoradiography allows this kind of analysis with high precision at a tissutal level. Therefore autoradiography might be an actor in increasing knowledge on the correlation between boron distribution and BNCT outcome, thanks to its ability to quantify the micro distribution of boron in tumor and healthy tissues.

Chapter 3

Study of BNCT mixed field energy deposition

During BNCT treatment the patient is exposed to a mixed field radiation. Along with α particles and Lithium ions from the neutron capture on Boron 3.1 this radiation field is composed by γ photons and protons. These photons arise both from the neutron beam and induced by the neutron capture reaction on hydrogen in tissue 3.2. Protons complete the array of particle acting in the BNCT mixed field irradiation, these particles are the result of neutron elastic scattering on hydrogen and neutron capture reaction on Nitrogen in tissue 3.3. All those particles have a distinct interaction with biological matter, as a consequence the dose evaluation depends on the reactions:



To estimate the absorbed dose given by BNCT all the particles that are quoted above have to be considered. In Patient treatment planning, these various absorbed dose components are usually assumed to act independently of each other. Accordingly the total photon equivalent dose (D_w) is give by equation 3.4.

$$D_w = (d_\gamma \times \text{DRF}) + (d_n \times \text{RBE}_n) + (d_N \times \text{RBE}_N) + (^{10}\text{B} \times \text{CBE}) \quad (3.4)$$

where the dose by γ rays (d_γ) is multiplied by a Dose Reduction Factor (DRF), which depends on the dose-rate; the dose given by the recoiling protons (d_n) from fast neutrons¹ interaction is multiplied by the Radio Biological

¹Neutron with energy > 10 keV.

effectiveness (RBE_n) which depends on the neutron energy; the dose deposited by protons nitrogen d_N is multiplied by (RBE_N) which represents the radio biological effectiveness of 0.58 MeV protons. Finally the dose from the neutron capture reaction on Boron is multiplied by the Compound Biological effectiveness (CBE); which is depends from two factors: the RBE of α particles and ^7Li ions and the micro-distribution of ^{10}B in a particular tissue.

It is established that clinical outcome of BNCT is related to the ^{10}B concentration and its spatial distribution at cellular and sub-cellular level[66]. This is due to complex interactions between the mixed field radiation of BNCT and the involved tissue cellular structure. In 1987 D. Gabel published an article where a Monte Carlo (MC) method was used to study the biological effect of $^{10}\text{B}(n,\alpha)^7\text{Li}$ reaction [67]. There it was observed that not every hit to the cell nucleus coincided with cell death, and it stated that the average dose is of limited use to predict the biological effect of Boron Neutron Capture Therapy (BNCT). Moreover, the cell killing effectiveness of boron distributed selectively in cytoplasm, nucleus or surface was studied in a simple tissue morphology. It was established that, the most efficient way to achieve cell death, is by accumulating boron inside the nucleus. Followed by boron concentrated in cytoplasm and as least effective boron distributed on the cell surface.

While the calculating capacity of computers increased, many more MC studies were carried on the energy deposited by the mixed radiation field (protons, α and ^7Li ions) of BNCT in cells, particularly in the nucleus. One example is the study by D.E Charlton and B.J. Allen (1993)[68, 69, 70], where they treated ion tracks as lines and used simple mathematical cell models to evaluate energy deposit and hits in the cell nucleus. They concluded that there was an evidence that, the Radio Biological Effectiveness (RBE) of the $^{10}\text{B}(n,\alpha)^7\text{Li}$ reaction depends upon the distribution of boron in the tissue. Other studies on boron in blood and contiguous cell contribution to dose inside the nucleus where carried out. By 1997 a first review about BNCT microdosimetry by R.G. Zamenhof [71] was published, where (as stated by the author) the missing block was the understanding of the basic mechanism of radiation effects by secondary particles produced though the neutron capture on ^{10}B . Which could be found, throughout the correlation of analytical and experimental BNCT microdosimetry with experimental radiobiology.

In recent years, T.L. Nichols et al. [72, 73, 74] investigated (by MC studies) the efficacy of BNCT as a function of tumor cell dimensions and growth pattern (from compact tumor mass or more disperse and infiltrative cells), and compared the results with different boron distributions inside and outside the cells. It was shown that densely packed cells will receive a larger dose to the nucleus compared to cells that are more sparsely packed, this difference can possibly lead to different clinical outcomes. By these means there are tumors which can be more efficiently treated by BNCT than others.

Even though the extensive literature, the topic is still not conclusively covered. Much can be done with the calculating capacity of modern computers and

3.1. $^{10}\text{B}(\text{n},\alpha)^7\text{Li}$ energy deposit in a cell

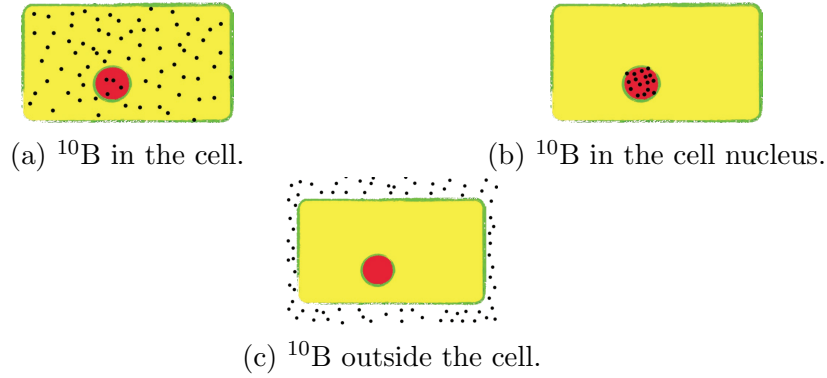


Figure 3.1: Figures 3.1a, 3.1b and 3.1c represent three possible ^{10}B distributions at cellular level, respectively boron uniformly distributed: in the cell, in the cell nucleus and outside the cell.

improved particle MC simulation codes like: MCNP6 [75], Fluka [76], PHITS [77] and Geant4 [78]. Until now tissue structures were approximated by regular geometries, that do not accurately reproduce the actual tissue structure. Therefore real tissue structure has to be reproduced to improve the knowledge of BNCT dosimetry in: healthy cells, neoplastic cells and interface between tumour and healthy tissue. Not only these studies can improve the understanding of clinical trials, but they are relevant for the characterization of new drugs according to the the tumour morphology.

3.1 $^{10}\text{B}(\text{n},\alpha)^7\text{Li}$ energy deposit in a cell

As stated in the previous paragraph, in BNCT the boron distribution at cellular level is pivotal for the outcome of the therapy. Taking Figure 3.1 as a reference and given the same macroscopic boron concentration, the single cell killing efficiency is greater if boron concentrates within the nucleus whereas if boron stays outside the cell.

Therefore, depending on its distribution at cellular level, every boronated compound will have its own Compound Biological Effectiveness (CBE). This parameter can be measured from *in-vivo* experiments [79, 80, 81] and, as the Radio Biological Effectiveness (RBE), it depends on the chosen cellular endpoint. An important aspect of CBE is that, for the same compound, it varies according to the tissue type [82]. This difference may also be due to the cell morphology.

The study presented in this chapter wants to deepen the dependence between: cell morphology and ^{10}B microscopic distribution. Anyhow, with the present work there is no attempt to determine the CBE through simulations. The aim is to study certain physical parameters, like the energy deposit, while varying ^{10}B distribution and cell morphology. The work is done by Geant4 simulations and the observed physical parameters are studied both for single

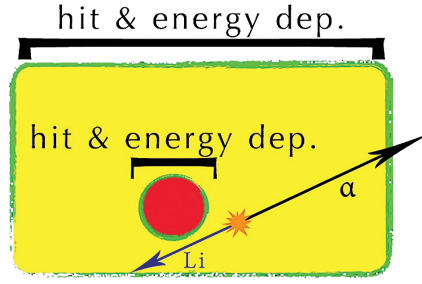


Figure 3.2: A schematic representation of the stored physical parameters: cell hit, nucleus hit, hits by particles originating from inside the cell, hits from particles arising in neighbouring cells and finally energy deposit distribution in the nucleus and whole cell

cell and tissue like structure.

As shown in Figure 3.5, the studied parameters where: cell hit², nucleus hit, hits by particles originating from inside the cell, hits from particles arising in neighbouring cells and finally energy deposit distribution in the nucleus and whole cell. The study of those parameters was performed in a new geometrical approach where real tissue structures such as : glia, skin and hepatic tissue are reproduced with the highest possible accuracy. Boron distributions are set as uniform in different parts of the geometry: in the whole cell, only in the nucleus, only in the cytoplasm, concentrated on the cell surface or nucleus surface.

Simulations were performed with the Geant4 toolkit starting from the microbeam application [83, 84]. This Geant4 application uses realistic human keratinocyte voxelized cell as an input geometry, taking into account realistic nucleus and cytoplasm chemical composition³. The simulation implemented in this chapter was performed on different cell geometries (more details in Section 3.2). The physics list activated for the simulations takes into account low energy electromagnetic interaction with matter (for lithium ions, alpha particles, electrons and photons) and hadronic elastic and inelastic scattering for alpha particle and lithium ions. The neutron capture reactions on boron were simulated by a back to back simultaneous emission of an alpha particle and a lithium ion. The initial energy of those particles follows the distribution given by the Branching Ratio (BR) of the neutron capture reaction on ^{10}B . More details about the Geant4 code used in this chapters are in Appendix B.

²Hit is defined as: every time the product of a ^{10}B neutron capture reaction (α particle or lithium ion) deposits energy in a predefined area of the cell.

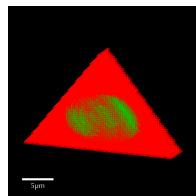
³The material compositions are defined by the International Commission on Radiation Units and Measurements (ICRU), in this simulation the ICRU soft tissue composition was used.

3.2 Cell geometry

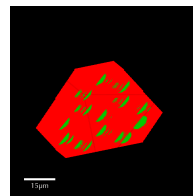
As for conventional radiotherapy and hadrontherapy also in BNCT it is important to deepen the understanding of the radiation induced damage to normal tissue. A consequence of a deeper knowledge of healthy tissue response to BNCT irradiation may be the improvement of the Treatment Planning System (TPS). Furthermore, such an insight would increase the understanding over the clinical outcome and consequently refine the tools to predict the tumor control probability. In this light, the simulations were performed by trying to reproduce three healthy cell structure in the best possible way. The chosen tissues are related to past BNCT clinical trials like: Glia cells in Section 3.2.1 are related to the first BNCT treatment [85, 86]; Hepatocytes of Section 3.2.2 are related to the liver treatment with multiple metastases from colorectal cancer [87, 88], and basal keratinocyte cells (Section 3.2.3) are related to skin acute reaction after the BNCT treatment of melanoma [89, 90]. Even though common three dimensional geometries are used to reproduce these kind of cells, the voxelization is maintained. This might seem a complication in the investigation, anyhow this implementation was kept to simplify the reuse of the code when more detailed cell structures can be reproduced.

3.2.1 Oligodendrocytes

Oligodendrocytes are approximately 76% of the cerebral cortex Glia cells, which are all those non-neuronal cells that maintain homeostasis, form myelin, and provide support and protection for neurons in the central nervous system [91]. The role of oligodendrocytes is that to support neurons and insulate the axons. To perform this role those cells can extend to 50 μm in diameter but are usually 10 μm thick, while the tissue structure results very compact and irregular [92]. There is no simple geometrical shape that can be associated to those cells. Anyhow, since Oligodendrocytes have few branches they are compactly bound one to another. In a first approximation a flat triangular structure can represent well a single cell and can help to reproduce somehow a chaotic tissue structure. More on the voxelized implementation of this geometry in Appendix B.



(a) Cell geometry

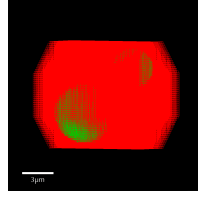


(b) Tissue like geometry.

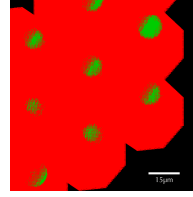
Figure 3.3: Geometrical structure of an oligodendrocyte cell (a) and tissue like geometry (b).

3.2.2 Hepatocyte

The liver is assembled by approximately 80% of Hepatocytes playing a fundamental role in the function of the liver, like: protein synthesis and storage, conversion of carbohydrates and so on [92]. The hepatocytes are arranged in irregular, interconnected plates. These cells have a simple cubical structure with sides approximately $25\mu\text{m}$ thick. As a consequence, the geometrical implementation of hepatocytes is straight forward and the voxelization is shown in Appendix B.



(a) Cell geometry

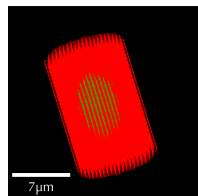


(b) Tissue like geometry.

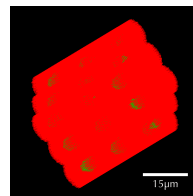
Figure 3.4: Geometrical structure of an hepatocyte cell (a) and tissue like geometry (b).

3.2.3 Basal Keratinocyte

The deepest layer of the epidermis is the stratum basale which is primarily made up of basal keratinocyte cells, which can be considered the stem cells of the epidermis. If this row of cell is severely damaged by radiation an acute reaction can occur. Even though there is no evidence that the grade 1 RTOG/EORTC⁴ acute skin reaction after BNCT [90] is related to this cells, it is interesting to study the cellular energy deposition of α particles and lithium ions from boron neutron capture reactions. The stratum basale of human skin is composed by a single row of columnar Basal Keratinocytes [92]. A good geometrical approximation of these cells would be a stretched cylindrical shape of $14\mu\text{m}$ high and $5\mu\text{m}$ in radius. The voxelized implementation of this geometry is described in Appendix B.



(a) Cell geometry



(b) Tissue like geometry.

Figure 3.5: Geometrical structure of an hepatocyte cell (a) and tissue like geometry (b).

⁴Radiation Oncology Toxicity Grading and the European Organization for Research and Treatment of Cancer.

3.2.4 Tissue like geometry

The implementation of a single cell geometry gives the ability to probe the effect of boron distribution on that cell. Anyhow, all the cells that were described in the previous sections are closely bound one to the other. Knowing that the range of ionizing radiation from boron neutron capture reactions is approximately $15\text{ }\mu\text{m}$ ⁵ in biological tissue, the ^{10}B distribution will affect both the cell containing boron and the surrounding first neighboring cells. Therefore, it is attractive to probe the effect of boron distribution inside a biological tissue. Accordingly the reproduced tissue is a lattice cube with three cells for each side, the voxelized implementation of this geometry is described in Appendix B. This structure has a central cell surrounded by first neighboring cells. The simulated microscopic boron distribution was performed around this central cell, while physical parameters (such as energy deposit) were evaluated in the surrounding tissue.

3.3 Nucleus hit probability

The nucleus of a cell is the most sensitive region to ionizing radiation. Different boronated compounds, with distinct boron distribution at cellular level, have all their own effectiveness to kill cells. This difference could be associated to the probability of hitting the nucleus which is related to the ability to deposit energy in this sensitive region of the cell. Therefore, it is important to study the probability of hitting the cell nucleus. This also depends on the cell morphology, so here we'll show the results of nucleus hit probability by varying both the cell morphology and the boron micro distribution. The cell geometries adopted here are the ones shown in Section 3.2. These cells were also used as base unit for the tissue like geometry as described in Section 3.2.4. During the simulations different boron distributions were considered: uniform in cell, uniform on cell surface, uniform inside the cell nucleus and uniform on the nucleus surface.

⁵The range of an α particle from the neutron capture on boron is approximately $10\text{ }\mu$, while the range of a lithium ion is approximately $5\text{ }\mu$.

3.3.1 Single cell nucleus hit probability

Table 3.1: Oligodendrocytes nucleus hit probability for a single cell.

Boron distribution	% Nucleus Hit	% α Hit	% Li Hit
Uniform in Cell	45.6	52	48
Uniform on Cell Surface	21.5	62.4	37.6
Uniform in Nucleus	100	50	50
Uniform on Nucleus Surface	96.9	50	50

Table 3.2: Hepatocyte nucleus hit probability for a single cell.

Boron distribution	% Nucleus Hit	% α Hit	% Li Hit
Uniform in Cell	35.7	54.7	45.3
Uniform on Cell Surface	10.5	70.3	29.7
Uniform in Nucleus	100	50	50
Uniform on Nucleus Surface	98.6	50	50

Table 3.3: Basal Keratinocyte nucleus hit probability for a single cell.

Boron distribution	% Nucleus Hit	% α Hit	% Li Hit
Uniform in Cell	31	53.3	46.7
Uniform on Cell Surface	8	82.4	17.6
Uniform in Nucleus	100	50	50
Uniform on Nucleus Surface	96.8	50	50

Table 3.1 shows the nucleus hit probability of different boron distributions in an Oligodendrocyte. It is evident that the most effective way of damaging the nucleus is by concentrating boron in this region. Whereas if ^{10}B goes on the cell surface the nucleus hit probability decreases drastically. These results are similar to Hepatocytes as shown in Table 3.2 and to Basal Keratinocytes shown in Table 3.3. An other interesting fact that can be depicted from these outcomes is that by increasing the distance of boron from the nucleus, the probability of hitting it is mainly due to α particles. This is a consequence of the range in tissue of α particles and lithium ions.

3.3.2 Surrounding cells nucleus hit probability

As the most clinically used boronated compounds are BPA and BSH it is attractive to study the nucleus hit probability in a tissue like geometry simulating their boron distribution at sub-cellular level. There are evidences showing that BSH concentrates outside the cell membrane [93], while BPA concentrates ^{10}B uniformly inside the cell [94]. In Section 3.2.4 it was shown that boron was extracted around the central cell in a cubical lattice of three cells for each side. The results from such an analysis gives an idea of how the boron around a cell affects the surrounding tissue, which, together with the previous analysis on a single cell, completes the information of the nucleus hit probability.

Table 3.4 represents the scenario of boron uniformly distributed on the central cell surface. Around this cell there are other 26 cells and the probability of hitting one of the nuclei of these cells ranges from 10% to 20% depending on the cell morphology. The higher probability of hitting the nuclei of Oligodendrocyte is due to their big nuclei and to the thickness which is usually less than $10\text{ }\mu\text{m}$. An other general consideration is that α particles are the dominant ionizing radiation hitting surrounding nuclei. Table 3.5 shows the results when boron is uniformly distributed inside the central cell. For Basal Keratinocytes and Oligodendrocytes there is no big difference compared to situation where boron is found on the cell surface. On the other hand for hepatocytes there is a significant difference, the nuclei hit probability in this latter case is approximately 3 times lower. This is mainly due to the dimensions of hepatocytes with respect to other cells.

Table 3.4: Nucleus Hit when ^{10}B is uniform on central Cell Surface, in a tissue like geometry.

Tissue	% Nucleus Hit	% α Hit	% Li Hit
Basal Keratinocyte	12	82.4	17.6
Oligodendrocytes	22.3	64.2	35.8
Hepatocyte	11.7	71.3	28.7

Table 3.5: Nucleus Hit when ^{10}B is uniform in central Cell, in a tissue like geometry.

Tissue	% Nucleus Hit	% α Hit	% Li Hit
Basal Keratinocyte	10	95.4	4.6
Oligodendrocytes	19.5	84.3	15.7
Hepatocyte	3.5	88.8	11.2

3.4 Energy deposition distribution inside the nucleus

The mere nucleus hit probability doesn't take into account the quality and quantity of the cell damage. Therefore an interesting parameter to study is the energy deposition inside the nucleus while varying both cell morphology and initial boron distribution. A natural development of this study would be the evaluation of the probability of hitting the DNA, which is the most sensitive biological target of the cell. In this section the energy deposit distributions will be shown for both single cells and tissue like geometries. These quantities were calculated starting from different initial boron configurations: uniform in cell, uniform on cell surface, uniform inside the cell nucleus and uniform on the nucleus surface.

3.4.1 Single cell nucleus energy deposit

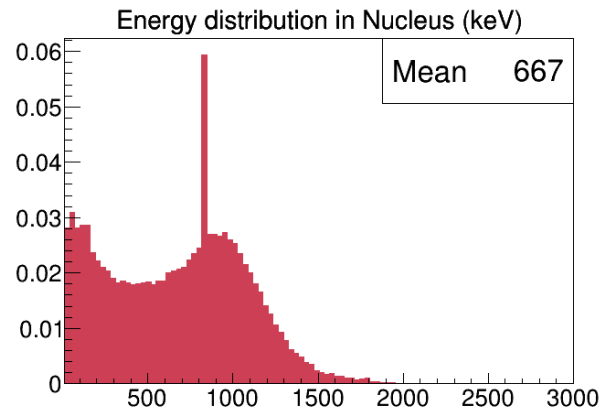
Figures 3.6, 3.7, 3.8 and 3.9 show the energy deposit distribution of respectively boron uniformly distributed in the cell, uniformly distributed on the cell surface, uniformly distributed inside the cell nucleus and uniformly distributed on the nucleus surface. The quasi mono energetic peaks that can be recognized in those graphs correspond to the total energy of: ${}^7\text{Li}$ ion alone, α particle alone and ${}^7\text{Li}$ ion + α particle together. There are also minor peaks given by the boron neutron capture reaction without the emission of the prompt γ photon at 480 keV, which is 6% of the branching ratio.

A general trend can be deduced, which is that the deposited energy distribution shape has a correlation with the cell morphology when boron is absorbed by the cell. This is also highlighted by the differences in the average energy deposition within the sensitive volume of the cell. Though when boron stays outside the cell surface (Figure 3.8), the nuclear deposited energy distribution shape and mean energy deposition doesn't have a strong correlation with the morphology of the cell. Therefore, these results show that the quality of the nuclear damage to a cell depends both on the morphology and the boron distribution at sub-cellular level.

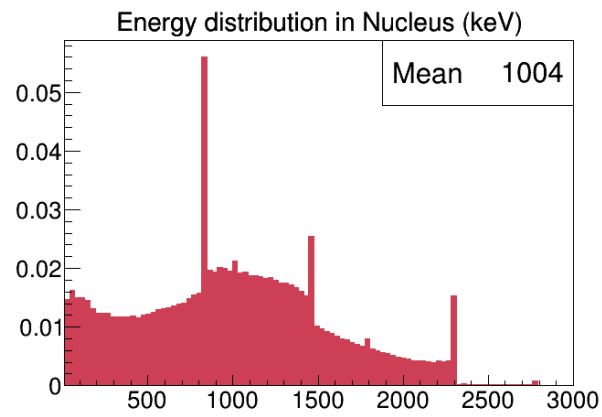
3.4.2 Surrounding cell nuclei energy deposit

In Figure 3.10 and 3.11 the energy deposition in the nuclei of a tissue like geometry is shown. The boron neutron capture events are generated on the central cell following respectively BPA and BSH like ${}^{10}\text{B}$ sub-cellular distributions, the energy deposition is then accumulated in the surrounding cell nuclei. As a general remark, the energy deposition distribution to external cell nuclei does not have a strong correlation with the microscopic ${}^{10}\text{B}$ distribution or cell morphology of the central cell.

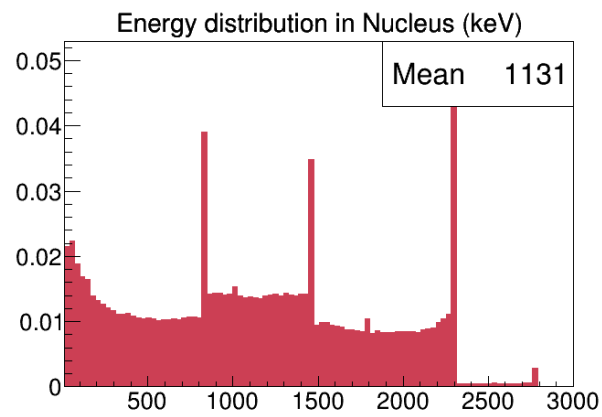
3.4. Energy deposition distribution inside the nucleus



(a) Basal Keratinocyte

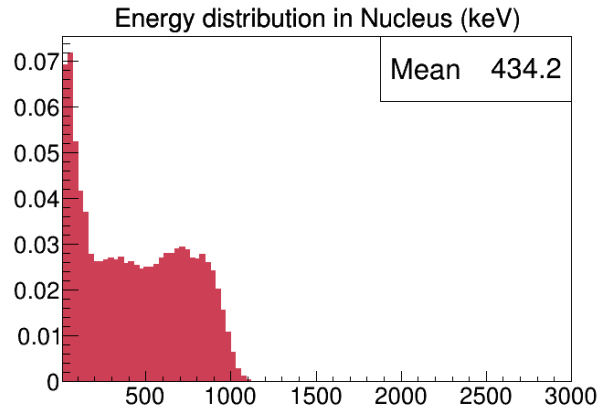


(b) Oligodendrocytes

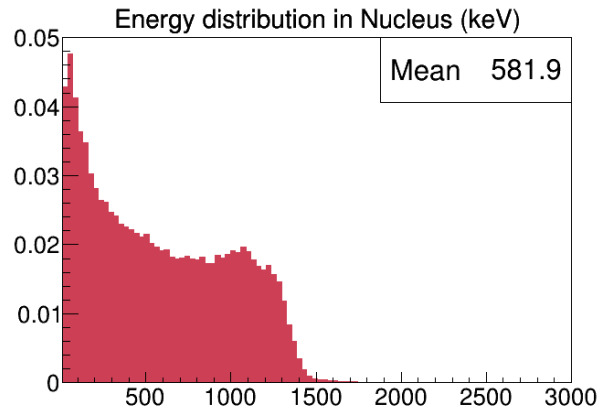


(c) Hepatocyte

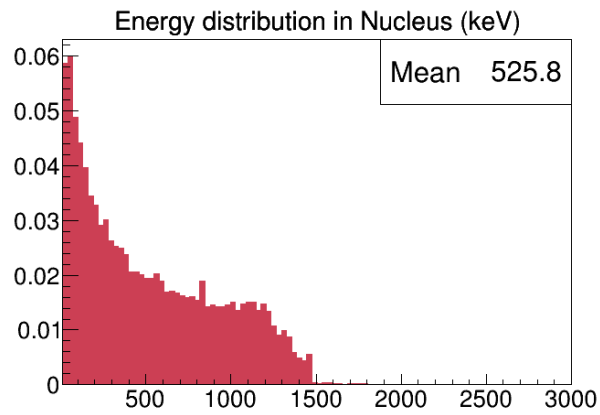
Figure 3.6: Comparison ^{10}B uniform in Cell. Figures (a), (b) and (c) show respectively the energy spectrum and mean energy deposited in nuclei of Basal Keratinocyte, Oligodendrocytes and Hepatocyte



(a) Basal Keratinocyte



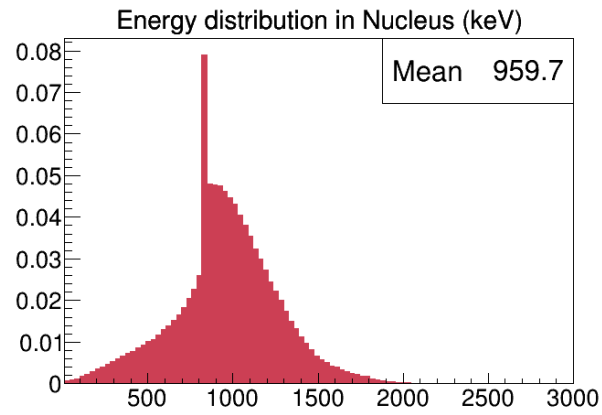
(b) Oligodendrocytes



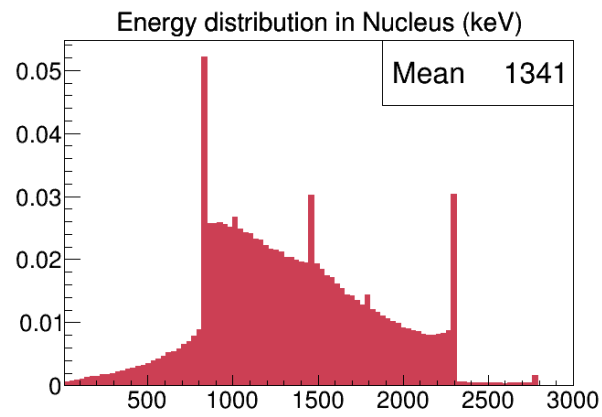
(c) Hepatocyte

Figure 3.7: Comparison ^{10}B uniform on cell surface. Figures (a), (b) and (c) show respectively the energy spectrum and mean energy deposited in nuclei of Basal Keratinocyte, Oligodendrocytes and Hepatocyte

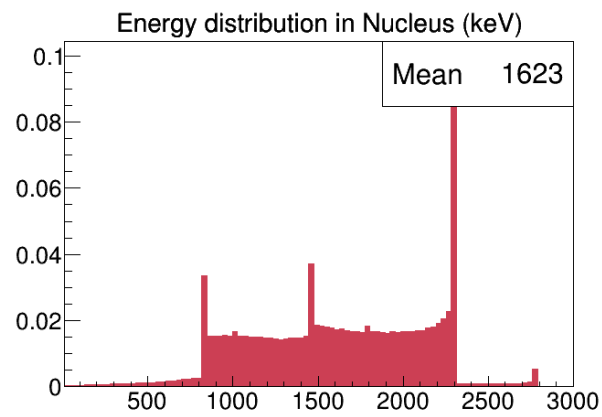
3.4. Energy deposition distribution inside the nucleus



(a) Basal Keratinocyte

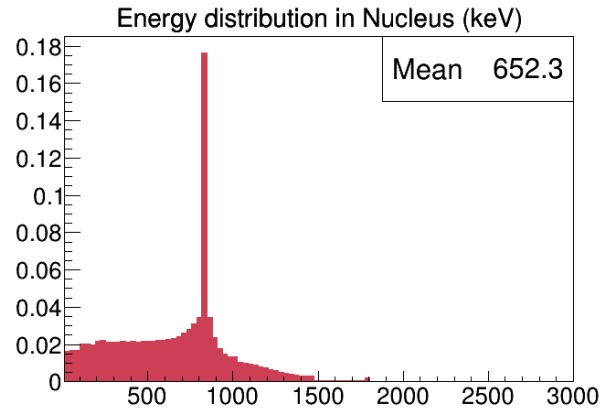


(b) Oligodendrocytes

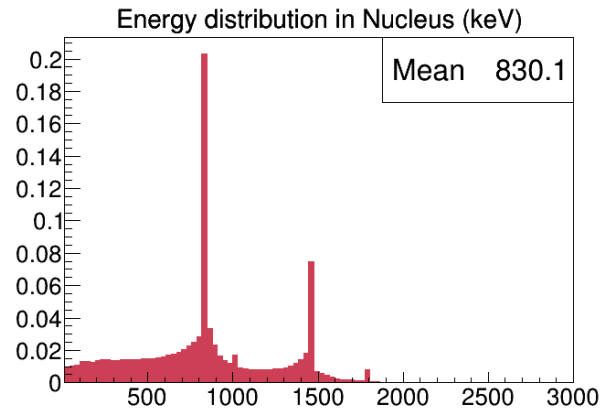


(c) Hepatocyte

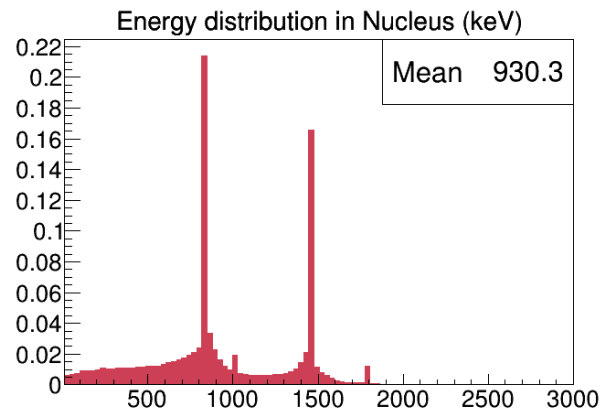
Figure 3.8: Comparison ^{10}B uniform in nucleus. Figures (a), (b) and (c) show respectively the energy spectrum and mean energy deposited in nuclei of Basal Keratinocyte, Oligodendrocytes and Hepatocyte



(a) Basal Keratinocyte



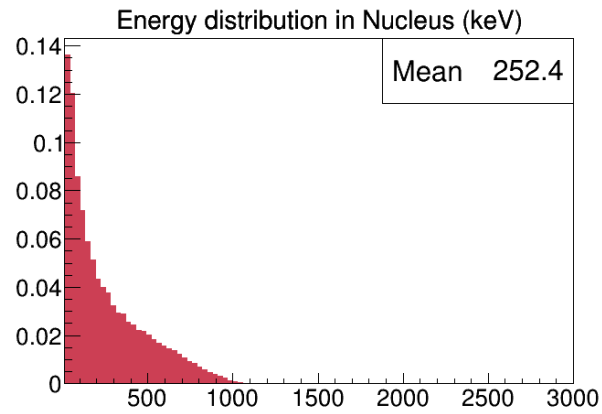
(b) Oligodendrocytes



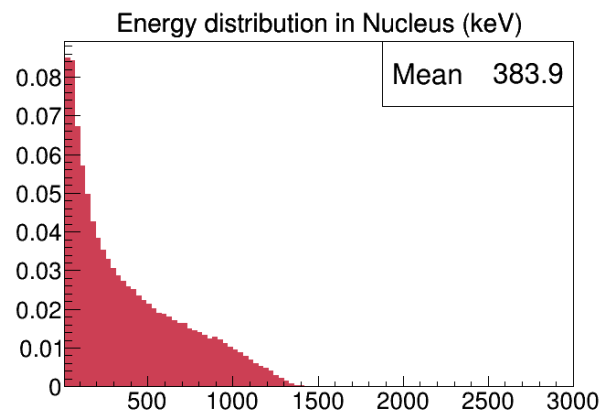
(c) Hepatocyte

Figure 3.9: Comparison ^{10}B uniform on nucleus surface. Figures (a), (b) and (c) show respectively the energy spectrum and mean energy deposited in nuclei of Basal Keratinocyte, Oligodendrocytes and Hepatocyte

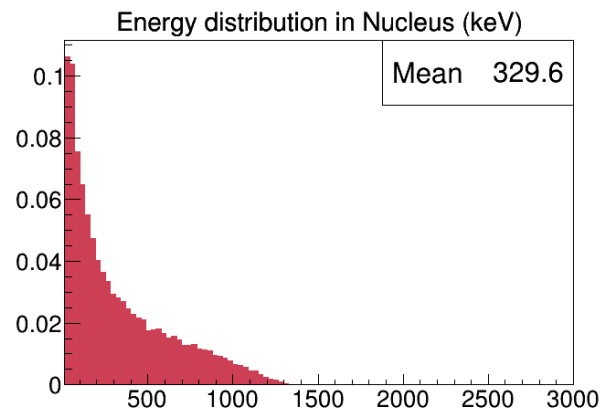
3.4. Energy deposition distribution inside the nucleus



(a) Basal Keratinocyte

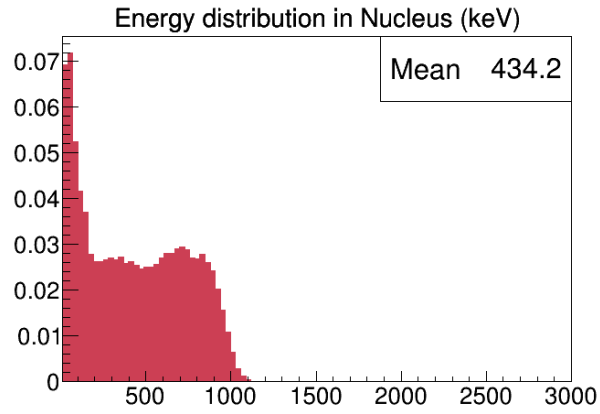


(b) Oligodendrocytes

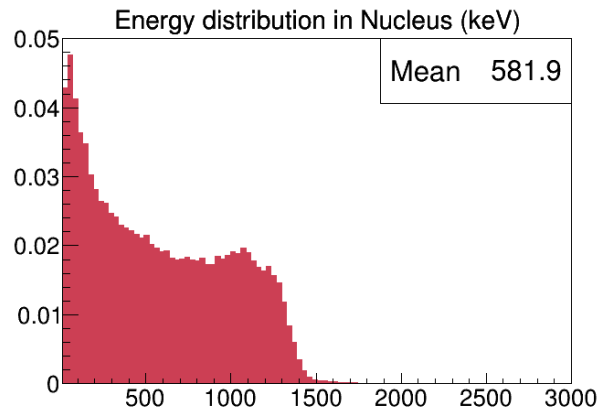


(c) Hepatocyte

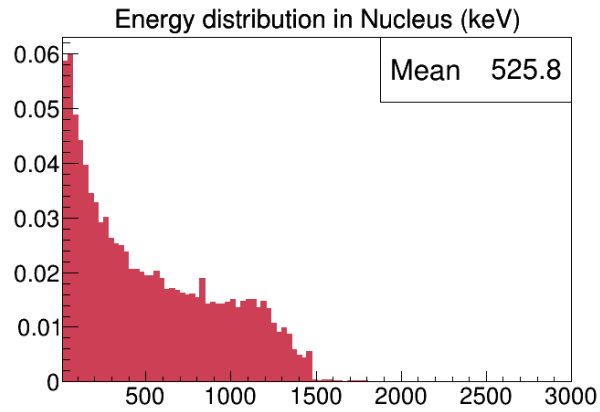
Figure 3.10: Comparison ^{10}B uniform in central cell. Figures (a), (b) and (c) show respectively the energy spectrum and mean energy deposited in nuclei of Basal Keratinocyte, Oligodendrocytes and Hepatocyte



(a) Basal Keratinocyte



(b) Oligodendrocytes



(c) Hepatocyte

Figure 3.11: Comparison ^{10}B uniform on central cell Surface. Figures (a), (b) and (c) show respectively the energy spectrum and mean energy deposited in nuclei of Basal Keratinocyte, Oligodendrocytes and Hepatocyte

3.5 Discussion

From these simulation studies with approximated real cell like structure, some interesting patterns of boron neutron capture reaction radiation field are computed. Even though the tissue and cell like structure are still geometrical approximations, this study highlights how the quality of the BNCT treatment can depend on cell morphology and ^{10}B distribution at cellular level. From the geometrical point of view at fixed boron distribution the most important differences are in the cross-fire, which is the contribution to nucleus hit from boron neutron capture reactions generated in surrounding cells. As an example the cross fire hit probability of Oligodendrocyte cells is approximately 7 times higher than cross fire nucleus hits in hepatocytes. This huge difference can have important consequences in the outcome of BNCT.

Another observed characteristic is the quality of the nucleus hit, which can be deduced from the energy distribution histograms. Here the highest energy deposition is given for boron uniformly distributed in the cell nucleus and it increases with cell and nucleus size. A downfall is that at increasing cell size the nucleus hit probability decreases. Therefore, some morphological conclusions of this work can be made. At decreasing cell size the mean energy deposition in the nucleus decreases but the hit probability on the single cell and the hit probability given by cross-fire events increases. Concurrently at decreasing cell size both Hit probability by α particles and Lithium ions increases. On the other hand, at increasing cell size the mean energy deposited in the sensitive volume of the cell increases although the nucleus hit probability decreases. In this case α particles deposit the majority of the energy in the nucleus.

Other conclusion can be taken by considering different boron distributions at sub-cellular level. When ^{10}B uniformly distributes within the cell the mean nucleus hit probability is $\approx 40\%$ for internal events and $\approx 10\%$ from cross fire events. The mean deposited energy in the cell nucleus is $\approx 800\text{keV}$ internal events and $\approx 300\text{keV}$ from cross-fire events as shown in Table 3.6 and Table 3.7. Li ions and α particles have the same nucleus hit probability when neutron capture reactions happen within the cell, while for cross-fire events α particles have the dominant role in generating possible cell damaging events. Finally if we consider the instance where boron is uniformly distributed on the cell surface, which mimics the action of BSH, the nucleus hit probability is $\approx 13\%$ on the central cell and $\approx 15\%$ for the surrounding nuclei. The energy deposition is $\approx 500\text{keV}$ on the central cell and $\approx 300\text{keV}$ for the surrounding nuclei and α particles play the major role in depositing this energy.

The study presented in this chapter is still in an early stage, a missing brick is a way to verify experimentally the simulation results. This may be done by trying to evaluate the Compound Biological Effectiveness and comparing the results with values calculated in clinical trials. A deeper insight of these future prospect will be covered in Chapter 5.

Table 3.6: Mean energy deposited in basal keratinocytes, oligodendrocytes and hepatocytes for boron distributed in a single cell: uniformly in the cell, uniformly on the cell surface, uniformly on the nucleus and uniformly on the nucleus surface.

cell type	uniform on nucleus surface (keV)	uniform on cell surface (keV)	uniform in nucleus (keV)	uniform in cell (keV)
Basal Keratinocyte	652	434	956	667
Oligodendrocytes	830	582	1314	1004
Hepatocyte	930	526	1623	1131

Table 3.7: Mean energy deposited in basal keratinocytes, oligodendrocytes and hepatocytes for boron distributed in a tissue like geometry: uniformly in the cell, uniformly on the cell surface, uniformly on the nucleus and uniformly on the nucleus surface.

cell type	uniform in central cell (keV)	uniform on central cell surface (keV)
Basal Keratinocyte	252	434
Oligodendrocytes	384	582
Hepatocyte	330	526

Chapter 4

Design of an epithermal neutron beam for limb osteosarcoma

The characteristics of a neutron beam for BNCT must ensure a uniform distribution of thermal neutrons in the neoplastic tissue and regions around the gross disease with suspected infiltrating neoplastic cells. As mentioned in Chapter 1 the appropriate energy spectrum of neutron beams for BNCT depends on the depth of the tumour and on the organ in which it is located. The rationale of irradiation with epithermal neutrons is that they are slowed down while passing through biological tissue by elastic scattering interactions mainly with hydrogen. This generates a neutron radiation field where the maximum flux of thermal energy is within the irradiated tissue. Consequently the highest probability for neutron capture reactions is at a certain depth within the treated volume. When the tumour is superficial like skin melanoma, a tissue-equivalent material is placed between the target and the beam in order to shift the peak of the thermal neutron flux in the desired position [95]. As an alternative, hypertheramal beams have been designed to ensure a thermal uniform irradiation of melanoma patients without the need of such moderators [90].

As the selectivity of BNCT depends mainly on the boron distribution in the cancer tissue, there is no need for complex tailoring of the beam spatial profile or to follow the organs movement during the irradiation. This is the difference from conventional radio and hadron therapy, where the selectivity of the treatment is determined by the high precision targeting of the tumour by the beam. The clinical application of BNCT is optimized within the constraints of normal tissue dose limits. This dose is given by neutrons interacting with normal tissue constituents, boron retained in this tissue and by photons generated in the moderation of neutrons. Neutrons have to be sufficiently collimated to avoid the irradiation of sensible organs during the treatment, and fast neutrons and gamma contamination must be lowered as much as possible. Parametric guidelines to evaluate neutron beam quality were studied in the past [96, 97, 98] and summarized in the IAEA tech-doc dedicated to BNCT. Such parameters are the neutron flux, the ratio between dose rate by fast neu-

4. Design of an epithermal neutron beam for limb osteosarcoma

Table 4.1: Some examples of measured in-air parameters from epithermal BNCT facilities.

Neutron source	ϕ_{epi} ($^9 \text{ cm}^{-2} \text{ s}^{-1}$)	$\frac{\dot{D}_f}{\phi_{epi}}$ (10^{-13} Gy cm^2)	$\frac{\dot{D}_\gamma}{\phi_{epi}}$ (10^{-13} Gy cm^2)
FCB [103]	4.3	1.4	3.6
JRR-4 [82]	2.2	3.1	1.5
THOR [104]	1.1	3.4	1.3
FiR-1 [105]	1.1	2.1	0.5
KURR [106]	0.46	6.2	2.8
HFR [107]	0.33	12.1	3.8
Li ABNS 30 mA [95]	0.95	5.2	4.9

trons and the neutron flux and the ratio between gamma dose rate and the neutron flux. The neutron flux defines the duration of a BNCT treatment; for beams with more than $10^9 \text{ cm}^{-2} \text{ s}^{-1}$ the treatment may last less than one hour. The relation between gamma or fast neutron dose rate and the neutron flux defines the contamination by gamma or fast neutrons respectively; it was assumed that a good neutron beam should have both contamination of less than $2.0 \cdot 10^{-13} \text{ Gy cm}^2$.

Neutron sources capable to deliver a flux of more than $10^9 \text{ cm}^{-2} \text{ s}^{-1}$ are nuclear reactors. Many research nuclear research reactors were adapted for BNCT clinical purposes since its early stages in 1951 [99, 100, 101, 102], where epithermal or hyperthermal neutron beams have been employed. Some of those beams are shown in Table 4.1, where their quality is compared though the parameters described in the previous paragraph.

Although the encouraging clinical outcome reported in literature, BNCT struggles to become widely used therapy. The reason is that nuclear reactors are facilities that are not completely dedicated to medical treatment, are difficult to install and maintain, depend on political and social support and require security issues that prevent their employ in hospitals. Therefore, a new boost for BNCT clinical application will come from the development of alternative neutron sources such as Accelerator Based Neutron Sources (ABNS).

In this chapter the design of a neutron field from an accelerator neutron source is described. Neutrons from nuclear reactions in the target of the accelerator have an harder spectrum than the epithermal one necessary for BNCT, thus it is mandatory to design a Beam Shaping Assembly (BSA) aimed at moderating, shaping and collimating the neutron beam. A brief overview of neutron sources based on accelerators will be shown together with the description of INFN project, that consists in the production of a high neutron flux

4.1. Accelerator neutron sources

Table 4.2: Characteristics of charged particle nuclear reactions considered for accelerator-based BNCT [108].

Reaction	Projectile energy (MeV)	Average n energy (MeV)	Max n energy (MeV)	n production rate (mA ⁻¹ s ⁻¹)
⁷ Li(p, n) ⁷ Be	2.5	0.55	0.8	9.1 · 10 ¹¹
⁹ Be(p, n) ⁹ B	4.0	1.06	2.1	1.0 · 10 ¹²
⁹ Be(p, n) ⁹ B	30.0		28.0	1.9 · 10 ¹⁴
⁹ Be(d, n) ¹⁰ B	1.5	2.01	5.8	3.3 · 10 ¹¹
¹³ C(d, n) ¹⁴ N	1.5	1.08	6.8	1.9 · 10 ¹¹
² H(d, n) ³ He	0.15	2.50	2.5	4.7 · 10 ⁸
³ H(d, n) ⁴ He	0.15	14.10	14.1	5.0 · 10 ¹⁰

exploiting the (p,n) reaction in Be. From such a neutron source various BSA configurations are presented, to compare the quality of those beams through the parameters shown in Table 4.1. To evaluate their performance on a clinical scenario the chosen beams are then used in a Treatment Planning System (TPS) to asses which is the most performing one.

4.1 Accelerator neutron sources

Neutrons are produced through nuclear reactions like the spontaneous fission of ²⁴⁹Cf or fission reactions such as the ones that happen in nuclear reactors. Another neutron source can be obtained by nuclear reactions induced by charged particles, some of which are reported in Table 4.2.

For accelerator based BNCT, endothermic reactions such as ⁷Li(p,n)⁷Be and ⁹Be(p,n)⁹B are attractive because of their high neutron yield near threshold and because the spectra of the obtained neutrons are relatively soft. The neutron energy range from those reaction is closely related to the proton energy interacting with the target. Thus, depending on the chosen reaction and of the charged particle beam, a specific BSA has to be developed. As the research in this field is still active there are no standard primary beam, target or BSA. Therefore different groups all over the world are optimizing their beam energy, target and BSA [109, 11, 110, 111, 112, 113, 114, 115, 116, 117]. A summary of the considered nuclear reaction for neutron production is shown in Table 4.2, Both lithium and berillyum reactions have advantages and disadvantages; lithium has a good neutron yield near threshold which means that it

produces spectra more similar to the ones needed in BNCT, but on the other hand it is more difficult to handle because it activates¹, it reacts with air oxygen and it has a very low melting point, thus it melts with the high intensity proton beam. Some groups are studying the possibility to employ liquid lithium targets [118, 119]. To obtain a intense neutron source from a beryllium target, the energy of the proton beam should be at least two times the threshold energy of the ${}^9\text{Be}(p,n){}^9\text{B}$ reaction². This implies that the neutron spectra of beryllium is harder than the one of lithium. Moreover, another disadvantage is the low permeability to hydrogen in beryllium, that accumulates once the proton ends its slowing down in the target. This has consequences since a high proton current can cause the blistering of the target. The advantages of the beryllium target are its high melting point and the fact that it does not activate.

The endothermic reactions in Accelerator Based BNCT have a cross section that is less than 1 b. The measured cross section for lithium and beryllium is shown in Figure 4.1 and Figure 4.2 respectively. For this reason the accelerators should achieve an high current beam with tens of mA to obtain more than 10^{12} neutrons per second on the entire solid angle. Accelerators with such characteristics are presently available and they can be distinguished in two categories: electrostatic [120, 121, 122, 123] and electrodynamic [124, 125, 126]. The main difficulty to accelerate such intense beams is to provide sufficiently strong transverse focusing to counteract space charge effects of the beam, this confinement can be obtained with quadrupoles. Another technological challenge concerns the stopping of the projectile within the target. All the power provided to accelerate the projectile is released on the target that must be efficiently cooled down in order to avoid melting.

¹The (p,n) reaction produces ${}^7\text{Be}$ which emits 477 keV photons.

²to generate a sufficiently intense neutron source the projectile energy should be more than 4 MeV. This shifts the neutron spectra up till 3 MeV and this maximum energy increases with the projectile energy

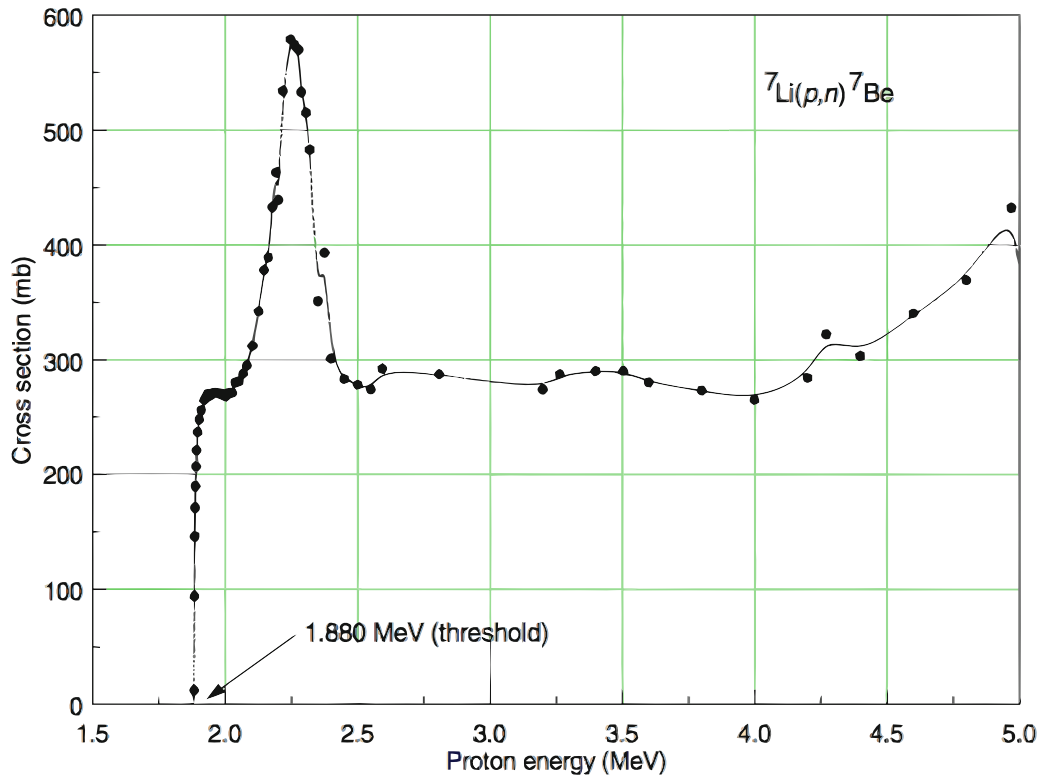


Figure 4.1: Reaction cross section for ${}^7\text{Li}(p,n)$ for different proton bombarding energies. The pronounced resonance is at ≈ 2.25 MeV [127].

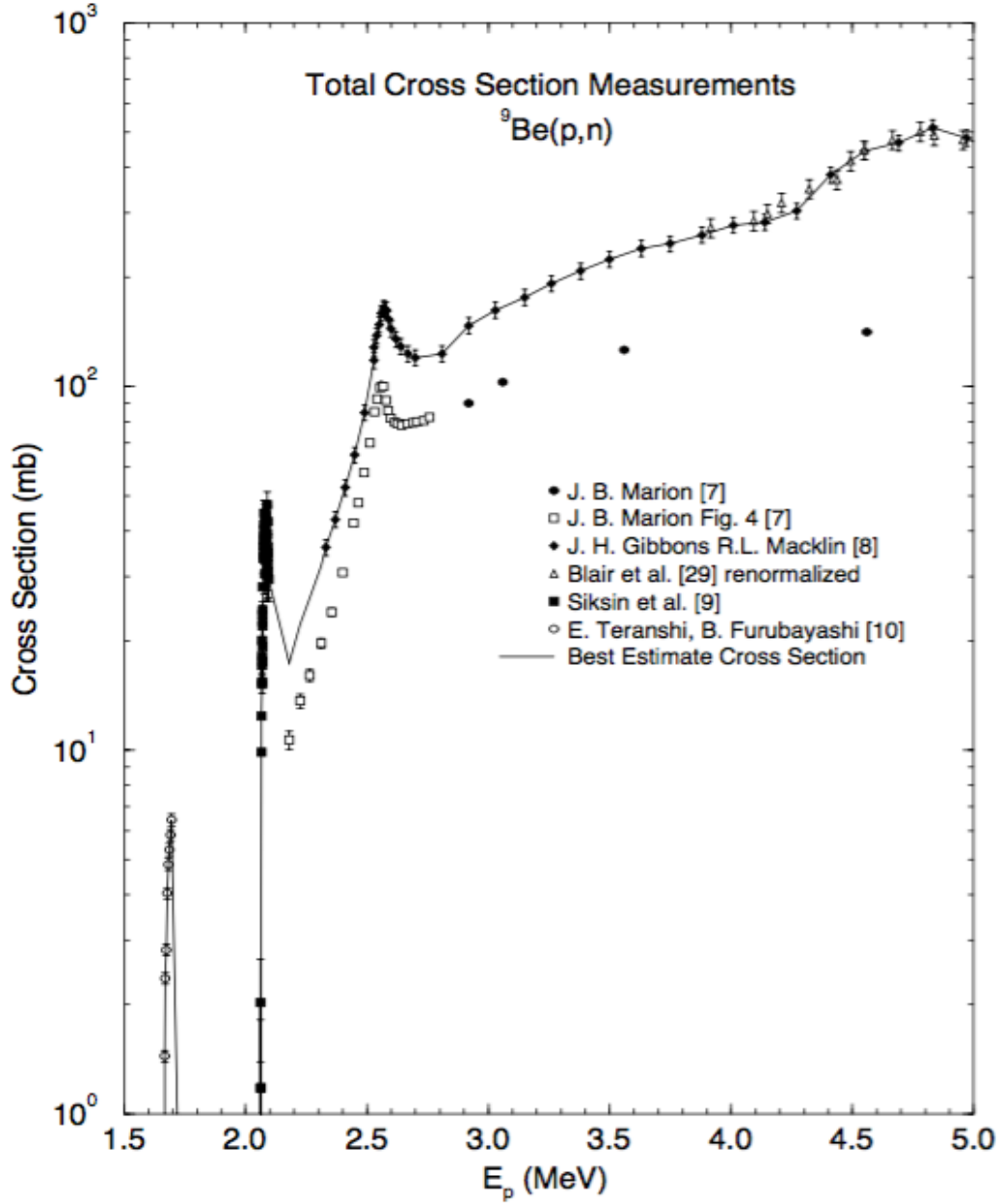


Figure 4.2: Reaction cross section for ${}^9\text{Be}(p,n)$ for different proton bombarding energies [116].

4.1.1 MUNES-BNCT project

The Italian National Institute of Nuclear Physics (INFN) in the framework of the project Multidisciplinary Neutron Source (MUNES), developed and realized a Radio Frequency Quadrupole (RFQ) [128] proton accelerator. This research program in nuclear and interdisciplinary physics, concerns BNCT with a neutron source based on accelerators technology for clinical applications. The

Table 4.3: TRASCO CW RFQ specifications [129]

Particle	p	
Input Energy	0.08	MeV
Output Energy	5	MeV
Frequency	352.2	MHz
Current	30	mA
RF power consumption	<800	kW
Duty factor	100	%

main RFQ characteristics are shown in Table 4.3. It consists of six brazed segments of 1.2 m each, the structure is shown in Figure 4.3. This accelerator is of interest to BNCT for the delivery of 5 MeV protons with 30 mA current in a Continuous Wave (CW) mode. It was shown that through the (p,n) reaction on a beryllium target and an appropriate BSA the machine can develop a thermal neutron flux of $4.29 \pm 0.01 \times 10^9 \cdot \text{cm}^{-2} \text{s}^{-1}$ [117]. This energy range is suitable to treat shallow cancers like skin melanoma.

Beryllium was chosen as the beam target material, due to the neutron yield $\approx 10^9 \text{s}^{-1}$ and maximum neutron energy $< 3.2 \text{ MeV}^3$ expected at the fixed RFQ output power. Two target prototypes were developed with similar geometries (as shown in Figure 4.4), one with the structural components based on zirconium alloy and beryllium while the other one was based on bulk beryllium. These targets were tested in the past years and results showed that the target geometry was well optimized for heat removal. Anyhow research is ongoing to further improve the target resistance to radiation and to fix the drawback of blistering [114].

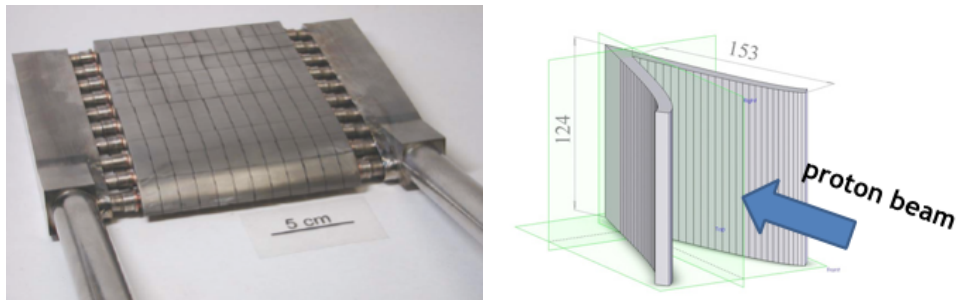


Figure 4.4: Beryllium target layout [125].

As stated before, to treat deeper seated tumours an epithermal neutron en-

³The maximum neutron energy depend on the proton energy, which for this accelerator is 5 MeV

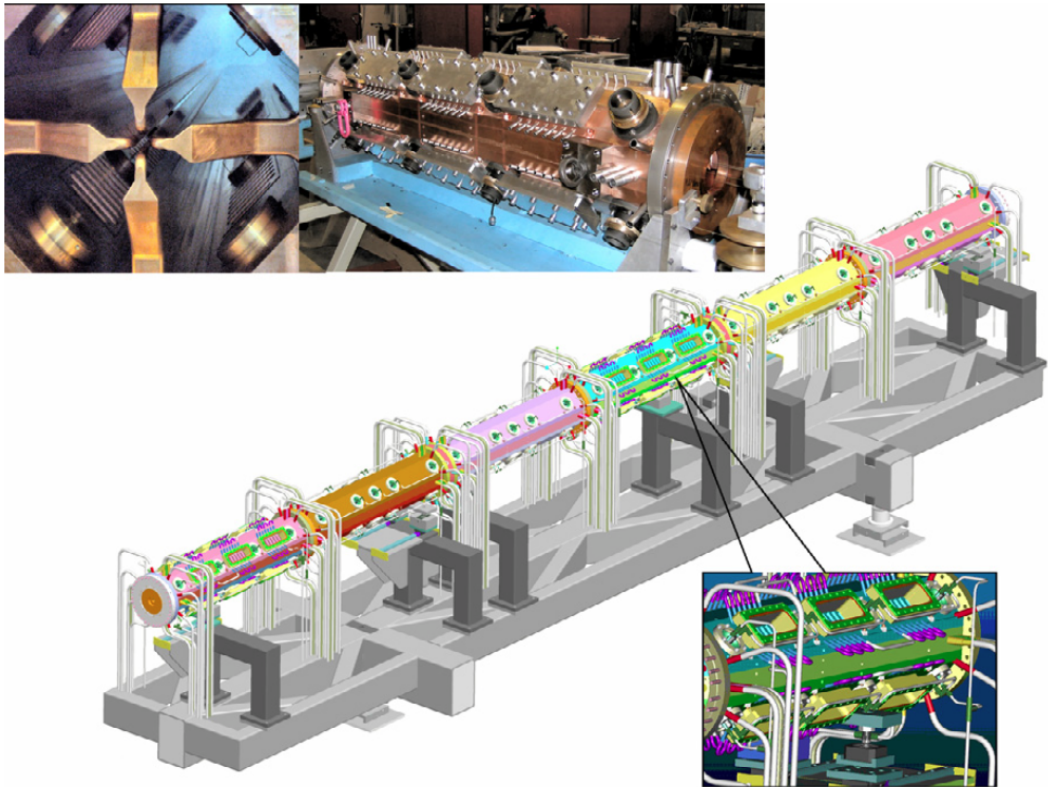


Figure 4.3: The TRASCO RFQ (5 MeV, 30 mA). Layout of the 7.13 m long accelerating structure on the support system, the main cooling pipes connections, quadrupole cross section and view of the first module constructed [125].

ergy beam is needed. In the following section the results of the simulation work performed for the development of the optimal BSA to obtain an epithermal energy beam is presented.

4.2 Neutron source from 5 MeV protons on beryllium

This work started with the optimization of the design process for a simpler target configuration. At the National Laboratories of Legnaro a proton beam of 5 MeV and 3 μA is available (CN facility) and it is coupled with a thick beryllium target. This set-up allows the production of 10^{10} neutrons per second in the target, which makes it an optimal playground for experimental activities such as dosimetry and microdosimetry. Neutron spectra have been measured at many laboratory angles and in the whole energy range by Agosteo et al. [130], leading to the definition of the double-differential spectra for the (p,n) reaction in Be at 5 MeV.

Measurements were performed with a detection system consisting of a monolithic silicon telescope coupled to polyethylene converter. This detection system is capable of discriminating selectively recoil protons from secondary electrons generated by background photons. The energy distribution of the neutron yield was measured at 0° , 20° , 40° , 60° , 80° , 90° , 100° and 120° angles, Figure 4.5. The distance between the beryllium target and the detector surface was $5 \pm 0.1 \text{ cm}$, while the sensible area was 1 mm^2 , corresponding to an angular aperture of about 0.6° . From the kinematics of the ${}^9\text{Be}(\text{p},\text{n}){}^9\text{B}$ reaction, it turns out that the maximum neutron energies are about 3.2, 3.1, 3.0, 2.7, 2.5, 2.3, 2.2 and 2.1 MeV for each angle respectively, as shown in Figure 4.6b. The neutron yields distribution versus the laboratory angle shows a maximum close to 0° and then it drops sharply with increasing angle up to about 60° where it reaches a minimum value, as shown in Figure 4.6a. The total neutron yield per unit charge of the reaction is determined by integrating the neutron spectra over the energy range and solid angle and it turns to be $(3.50 \pm 0.3) \cdot 10^{12} \text{ mC}^{-1}$.

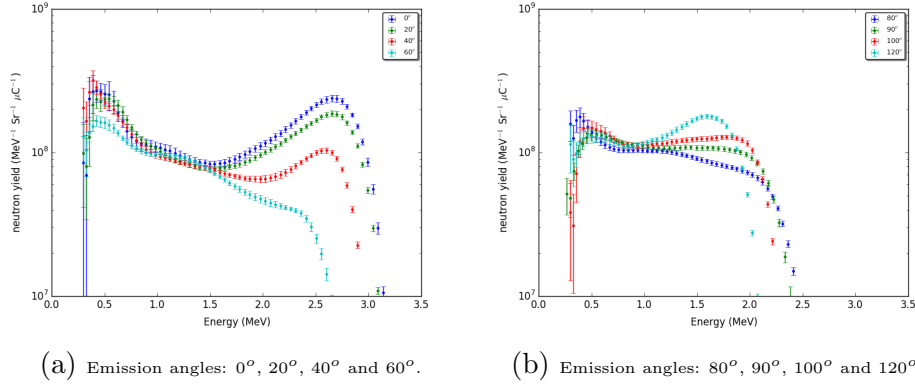


Figure 4.5: Distribution of neutron yield measured at different emission angles [130].

The first step consisted in reproducing the experimental data with MCNP. Thanks to the capabilities of MCNP6, the double differential spectra may be obtained by simulating the proton beam and by tallying the neutron flux in the same positions as the measurements were performed. The transport of charged particles is achieved down to few keV with good accuracy, however it is necessary to prove that the nuclear data in the libraries are correct and that the models implemented for the physical processes reproduce the experiments. For this reason tests were performed to prove the accuracy of neutron yielding by simulating 5 MeV protons interacting with a thick beryllium target, with the same configuration as in the experiment by Agosteo et al. [130]. This assessment was performed for MCNP6, MCNPX and PHITS, that are commonly used MC transport codes in the field of BNCT [131, 132, 133]. In Figure 4.7 the results of the simulations compared with the experimental data is shown. All tested MC codes fail in reproducing the neutron spectra yielded by the ${}^9\text{Be}(p,n){}^9\text{B}$ reaction for both nuclear reaction models and cross section. For this reason, a second approach was adopted: reconstructing the neutron source starting from the double differential experimental spectra directly in the target. This method has the advantage to be more efficient in terms of calculation time.

4.2. Neutron source from 5 MeV protons on beryllium

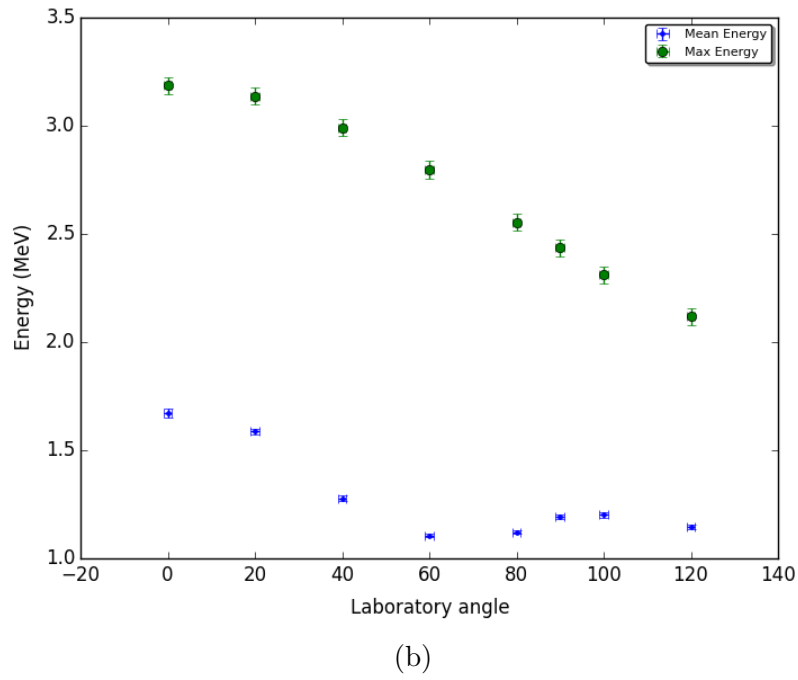
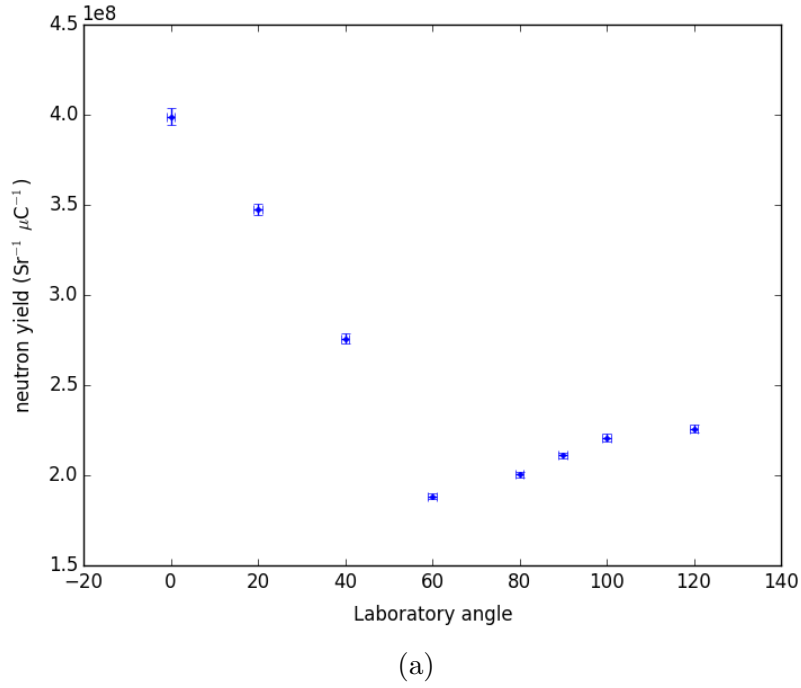


Figure 4.6: Characteristics of the neutron production from the (p,n) reaction on Be. 4.6a represents the Neutron yield at different laboratory angles. 4.6b shows the Mean and Maximum energy at different laboratory angles [130].

The MCNP6 neutron source from ${}^9\text{Be}(\text{p},\text{n}){}^9\text{B}$ reaction with 5 MeV protons was designed by extracting neutrons on the surface of the thick beryllium

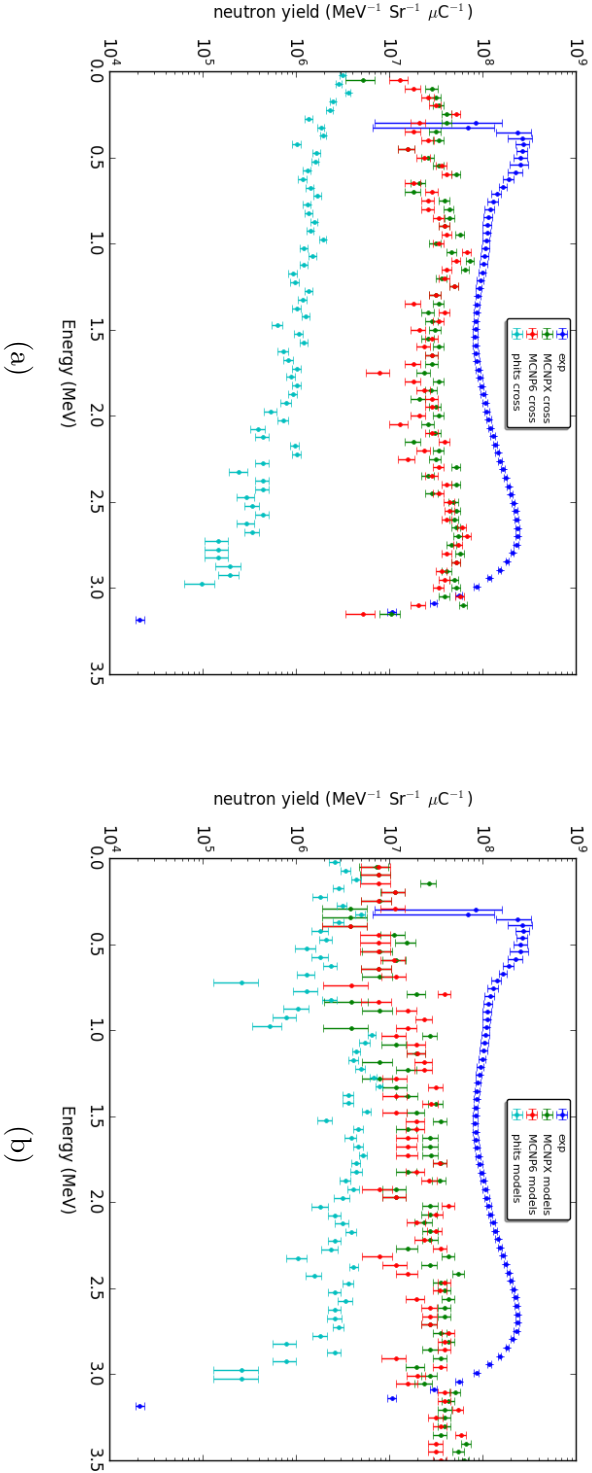


Figure 4.7: neutron energy spectra from the simulating a 5 MeV proton interacting with a thick beryllium target. The spectra was collected on a 1 mm² surface 5 cm from the interaction point. Figure a) shows the results of MCNPX, MCNP6 and PHITS respectively in green, red and light blue when using cross section tables compared to the experimental data. Figure b) shows the results of MCNPX, MCNP6 and PHITS respectively in green, red and light blue when using reaction models compared to the experimental data.

4.3. Epithermal Beam Shaping Assembly (BSA) characteristics

Table 4.4: In-air parameters from the CN ABNS epithermal beam.

Neutron source	ϕ_{epi} ($^9 \text{ cm}^{-2} \text{ s}^{-1}$)	$\frac{\dot{D}_f}{\phi_{epi}}$ (10^{-13} Gy cm^2)	$\frac{\dot{D}_\gamma}{\phi_{epi}}$ (10^{-13} Gy cm^2)
Be ABNS 30 mA	2.2	8.7	2.4

target. To check the correctness of the simulated neutron source, the neutron fluence was then tallied at 5 cm from the target and at different laboratory angles to be compared with the experimental values. While more details on the code for the neutron source generation with MCNP are in Appendix A, Figure 4.8 and Figure 4.9 show the validation of the simulated neutron source spectra at various laboratory angles. The same check was performed on the neutron yield, mean and maximum energy; respectively shown in Figure 4.10a and Figure 4.10b, demonstrating a very good agreement between simulation and experiments. Furthermore, in the implementation of the neutron source the angles 140° , 160° and 180° were added to complete the neutron extraction for the entire solid angle. The neutron yield and energy distributions were extrapolated from the experimental data, results of those extrapolations are shown in Figure 4.10.

4.3 Epithermal Beam Shaping Assembly (BSA) characteristics

Having validated the neutron source, the next step was to design a BSA to obtain two neutron beams of different spectral characteristics at the CN facility [134]. This work demonstrated that it is possible to obtain a thermal and an epithermal neutron beam for experimental measurements and it represented a good starting point for the design of the BSA for the RFQ accelerator. In fact, many geometries and materials were tested, leading to an optimal configuration in terms of beam parameters. The final configuration of the channel is shown in Figure 4.11 and the corresponding spectrum is shown in Figure 4.12. The parametric output at the beam port of this configuration is shown in Table 4.4 Demonstrating the feasibility to develop a clinical beam for BNCT with a 5 MeV proton beam and a Be target.

The BSA development was performed taking as a reference the beam characteristics advised by the IAEA's recommendations on beam quality [135], that are shown in Table 4.5. Moreover, the epithermal neutron flux in the range of 1-10 keV was maximized. Care was taken to decrease the fast neutron component and to absorb or avoid the creation of γ photons. At start a simple beam geometry was implemented to perform some studies to establish the optimal moderating material to use. Once this step was concluded, the beam geometry and shape was refined to further improve the in air beam parameters at the

4. Design of an epithermal neutron beam for limb osteosarcoma

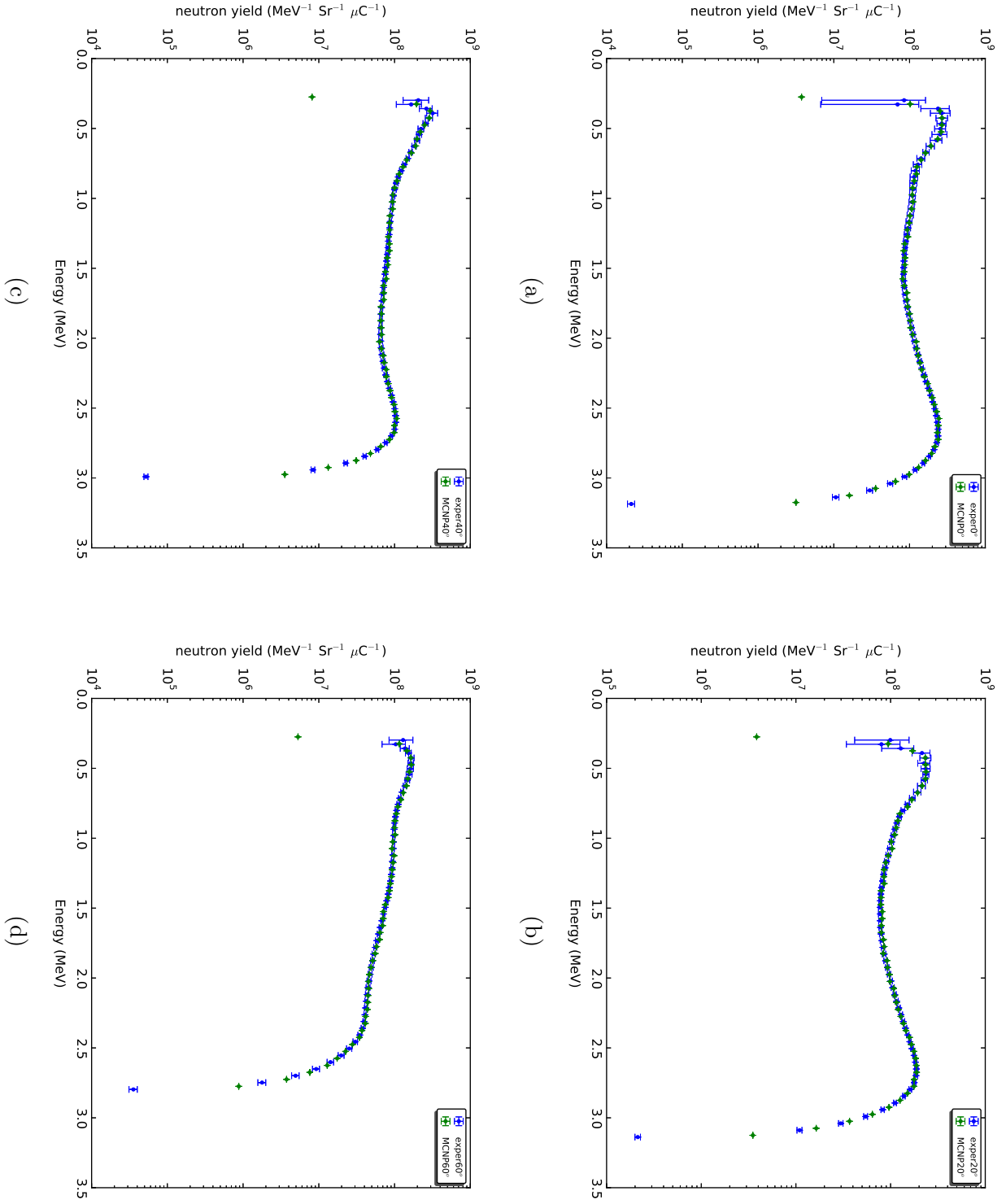


Figure 4.8: (a), (b), (c) and (d) show respectively the comparison between simulated (green) and measured (blue) data from 0 till 60 degrees in laboratory angles.

4.3. Epithermal Beam Shaping Assembly (BSA) characteristics

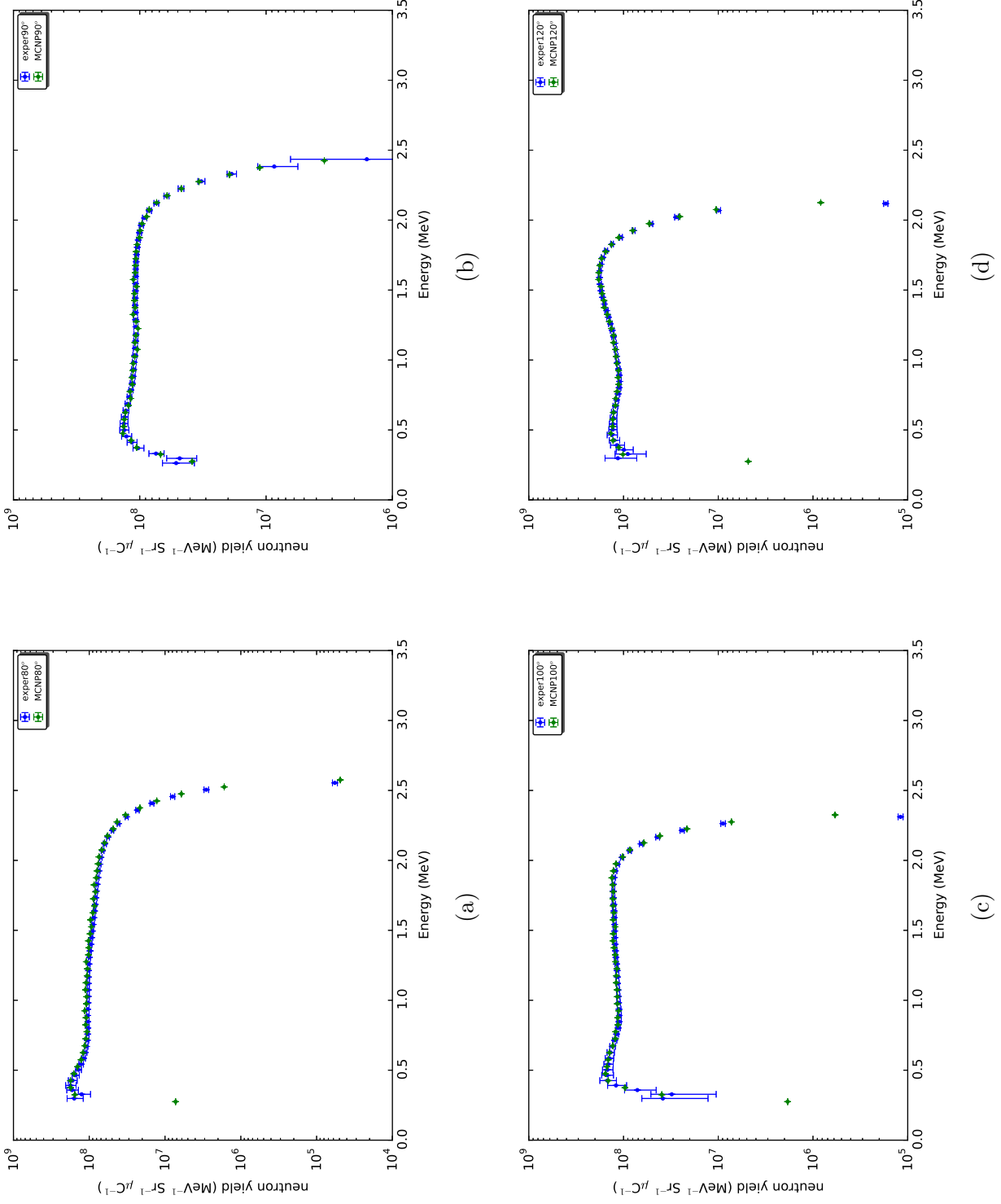


Figure 4.9: (a), (b), (c) and (d) show respectively the comparison between simulated (green) and measured (blue) data from 80 till 120 degrees in laboratory angles.

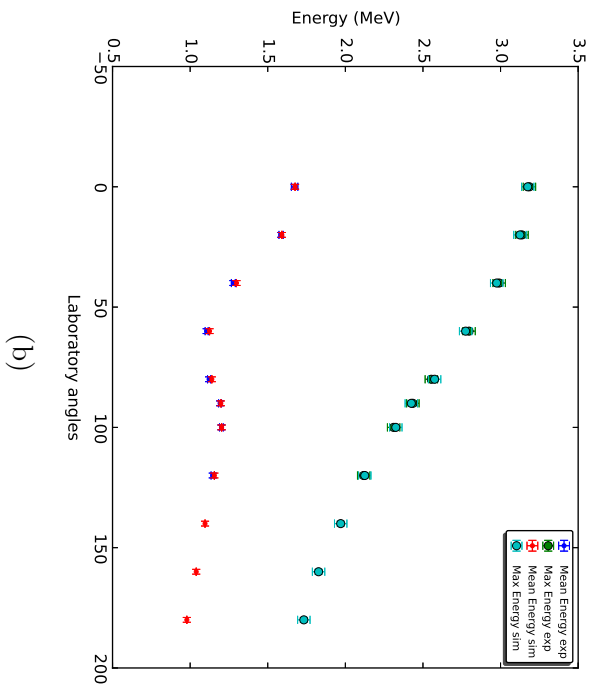
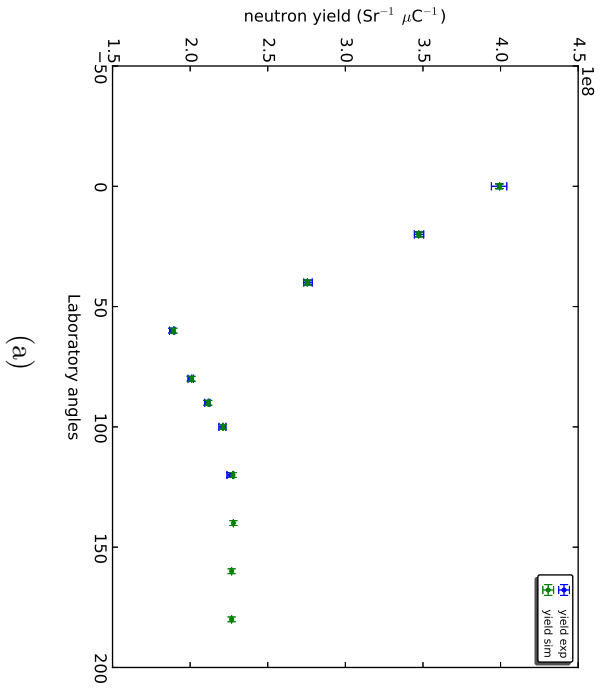


Figure 4.10: MCNP neutron source validation, (a) shows the neutron yield at various laboratory angles and the yield extrapolations for angles greater than 120°. Simulated mean and maximum neutron energies are shown in figure (b), for angles greater than 120° an extrapolation was performed.

4.3. Epithermal Beam Shaping Assembly (BSA) characteristics

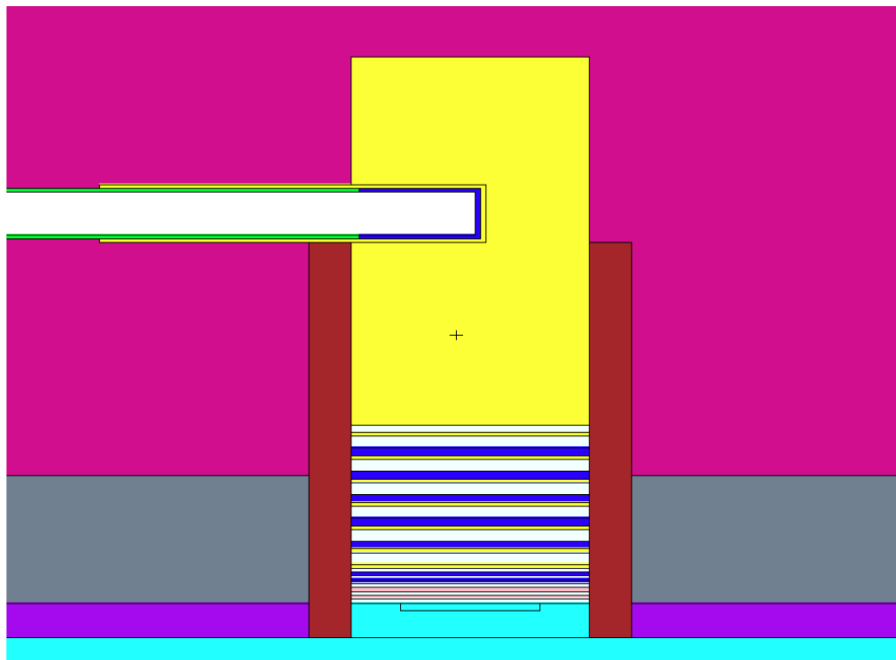


Figure 4.11: The final epithermal beam set-up at the CN accelerator facility, composed of (starting from the neutron source): 200mm teflon, 10mm magnesium alloy, 5mm teflon, 10mm magnesium alloy, 5x (10 mm aluminium / 5 mm teflon / 15 mm magnesium alloy), 5mm teflon, 2x(5 mm magnesium alloy / 5 mm aluminium), 2x(5 mm magnesium alloy / 5 mm titanium) and 5 mm magnesium alloy.

Table 4.5: IAEA’s recommendations on beam quality.

Beam parameter	Recommended value
Epithermal Flux (ϕ_{epi})	$10^9 \text{ cm}^{-2} \text{ s}^{-1}$
$\frac{\dot{D}_{fast}}{\phi_{epi}}$	$2,5 \cdot 10^{-13} \text{ cm}^{-2} \text{ Gy}$
$\frac{\dot{D}_{\gamma}}{\phi_{epi}}$	$2,0 \cdot 10^{-13} \text{ cm}^{-2} \text{ Gy}$

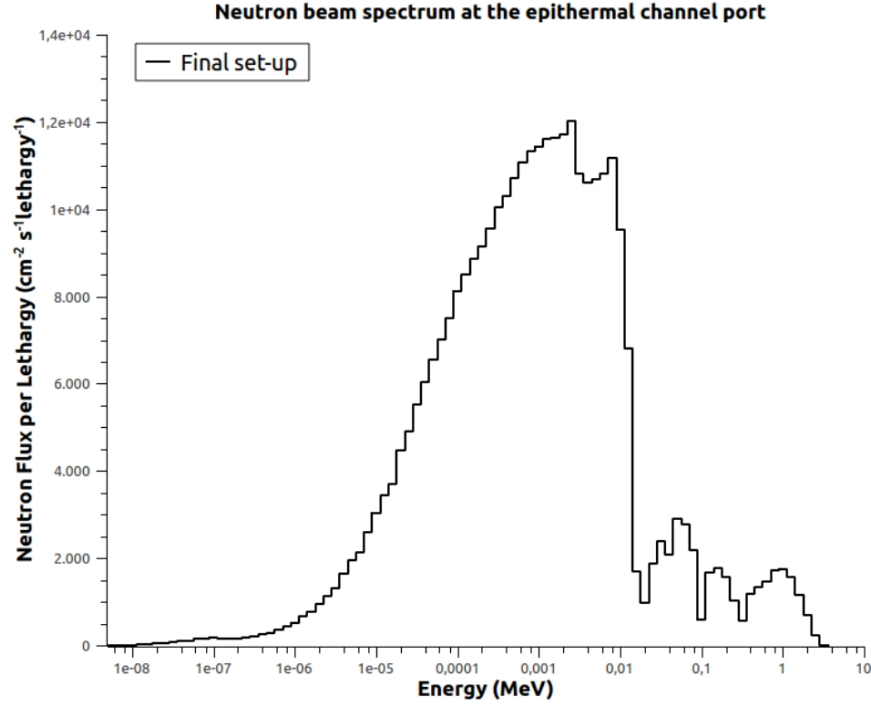


Figure 4.12: Neutron spectrum obtained with the final designed for the epithermal beam, shown in Figure 4.11

beam port.

4.3.1 Materials

To obtain an epithermal neutron beam from the accelerator neutron source spectra of Section 4.2, appropriate neutron moderating materials have to be used, with a high scattering cross section for neutrons with energies greater than 10 keV. Obviously to obtain a neutron peak at the desired epithermal energy the cross section between 0.5 eV and 10 keV should be low. At the same time thermal neutrons have to be absorbed and material producing γ rays by neutron interaction should be avoided. In fact it is very rare to find a material with such a neutron cross section. The most abundant atom with an interesting cross section behaviour is ^{60}Ni , Figure 4.13. Natural nickel is composed by ^{58}Ni , ^{60}Ni , ^{61}Ni , ^{62}Ni and ^{64}Ni where their abundance is respectively 68,077%, 26,233%, 1,14%, 3,634%, 0,926%. The cross section of the other isotopes on Ni is not as useful to this end as the one of ^{60}Ni . Anyhow it would be too expensive to effectively produce a pure ^{60}Ni BSA. A solution to avoid the use of overly expensive materials is to combine atoms with different cross sections to obtain an adequate moderating material for epithermal neutron beam design. Effective shaping materials for epithermal neutron beams, capable of reducing the fast component without removing neutrons in the energy range of interest are described in Table 4.6. ^{19}F , ^{24}Mg , ^{27}Al and ^{28}Si are the most common

4.3. Epithermal Beam Shaping Assembly (BSA) characteristics

materials used in the shaping of an epithermal neutron beam. All of these have low cross section at epithermal energies compared to their fast neutron cross section, shown in Figure 4.14. ^6Li and ^{48}Ti [1] are two nuclei with interesting neutron cross section characteristics, shown in Figure 4.15. Lithium has an high cross section for thermal neutrons, therefore it is a good thermal neutron and it does not produce gamma rays. Titanium has an interesting peak in the scattering cross section around 10 keV, helpful to refine the epithermal spectrum.

The study briefly introduced above, leading to an epithermal beam with good characteristics, was used as a starting point for the simulations performed for the RFQ dedicated to clinical BNCT, especially regarding the materials that were chosen.

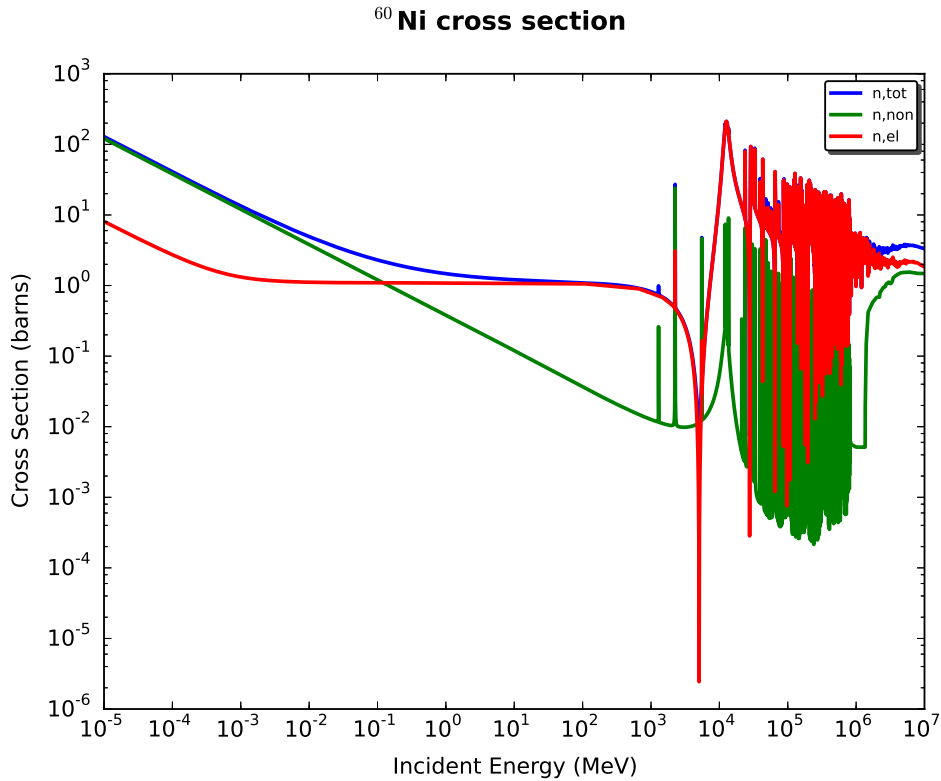


Figure 4.13: Neutron cross section for Ni [1], red line is the neutron elastic cross section, green represents non elastic scattering while the blue line is the total cross section.

Table 4.6: Brief description of commonly used material for epithermal neutron beam design.

Material	description
Fluental TM	Al 30%, AlF ₃ 69%, LiF 1%. It is a patented neutron moderating material and it turns out to be an excellent fast neutron filter
Al, F, Mg Si compounds	They are all interesting materials due to their resonances in the scattering cross section above 10 keV. Al and AlF ₃ are the most common materials in epithermal beam development.
Ti	It has a pronounced resonance in the scattering cross section at 10 keV and a $1/v$ behaviour in the absorption cross section. It has been suggested as a good chopper for the upper epithermal energy ranges.
Li and compounds	⁶ Li is the best thermal neutron absorber because no γ rays are released in the absorption process. The only drawback is that the natural abundance of ⁶ Li is only 7.5%

4.3. Epithermal Beam Shaping Assembly (BSA) characteristics

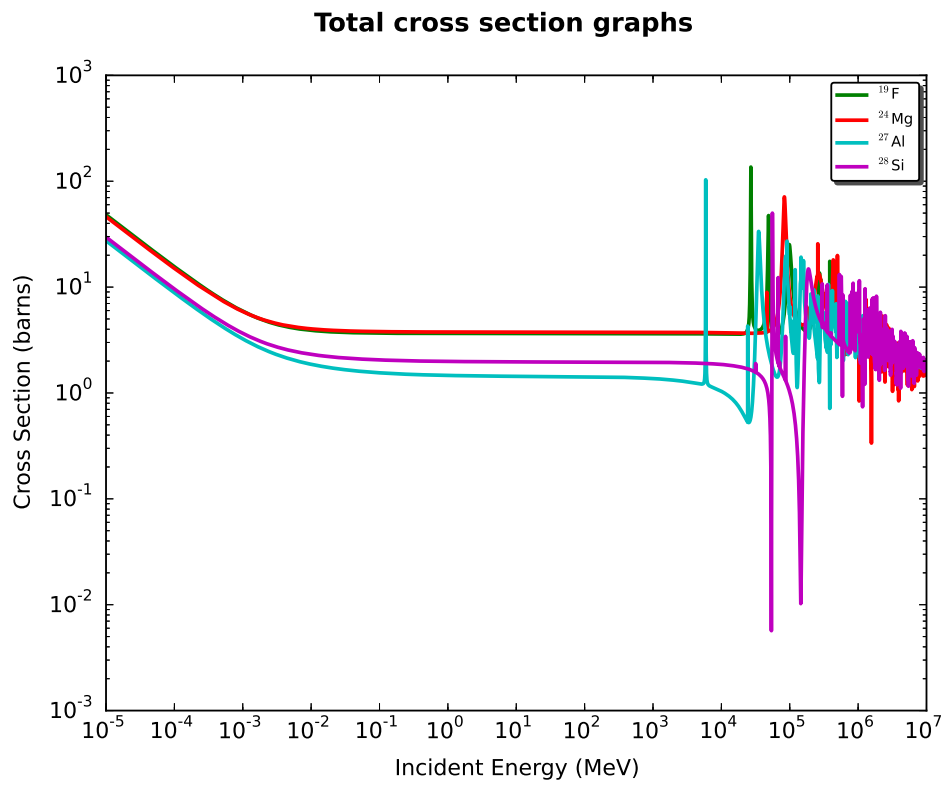


Figure 4.14: Neutron cross section for ^{19}F , ^{24}Mg , ^{27}Al and ^{28}Si [1].

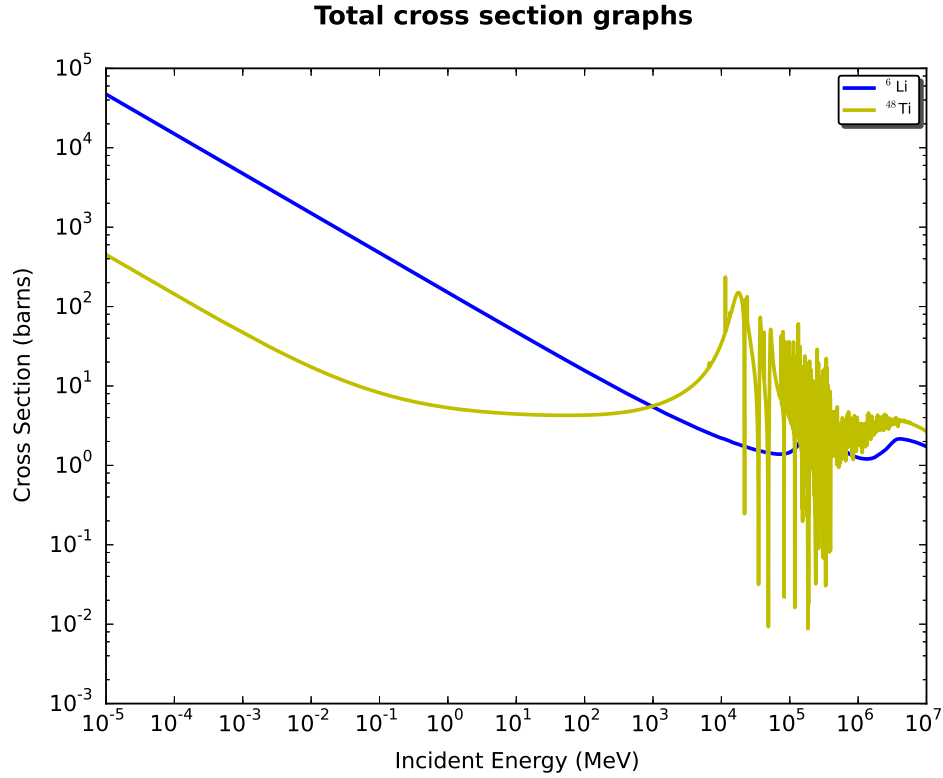


Figure 4.15: Neutron cross section for ${}^6\text{Li}$ and ${}^{48}\text{Ti}$ [1].

4.4 Simulation work flow

The exposition of the work flow performed in this dissertation can help the interpretation of the following sections. The neutron transport simulations were performed by the Monte Carlo (MC) code MCNP6, the inputs are further described in Appendix A. With this MC code the first simulations were performed to define and optimise the neutron source produced by 5 MeV protons interacting on a beryllium target, as described in Section 4.2. This is the starting point for the tailoring of the epithermal neutron beam as shown in Figure 4.16, which is divided in two phases.

4.4.1 Phase 1 - *in air* figure of merit optimization

This phase consisted in optimizing IAEA parameters for the simulated beams. The simulations results were used as feedback to redefine and optimize the BSA materials and structure. Physical parameters as flux, current and dose were calculated along the beam axis and at the beam port. Along the beam axis the parameters were evaluated on a 6 cm radius circle perpendicular to the beam axis located every centimeter. These quantities are:

$\phi_n(E)$ Neutron flux as function of the neutron energy, measured through MCNP6's

4.4. Simulation work flow

F2:n flux tally, see Appendix for the meaning of "tally" in MCNP language.

$\dot{D}_n(E)$ Dose rate as a function of the neutron energy. The dose rate was evaluated by an F2 tally multiplied by the appropriate kerma factors⁴.

At beam port different evaluations were performed on two geometrical configurations. One composed by 40 annular rings each 1 cm thick. The other evaluations were performed on a circle of 6 cm radius and on the ring enclosing this central circle with an external radius of 12 cm.

$J_n(E, \theta)$ Neutron current as a function of the neutron energy and angle with respect to the beam axis, measured through MCNP6's F1:n flux tally.

$\phi_n(E)$ Neutron flux as function of the neutron energy, measured through MCNP6's F2:n flux tally.

$\dot{D}_n(E)$ Dose rate as a function of the neutron energy. The dose rate was evaluated through an F2 tally multiplied by the appropriate kerma factors.

4.4.2 Phase 2 - Optimal epithermal neutron beam selection

At the end of the first phase some beams were selected on the basis of their performance with respect to IAEA guidelines for epithermal neutron beams. The beams were then tested in a clinical scenario, of a true Osteosarcoma patient. This phase is divided in two parts: the first being the treatment planning evaluation through NTCPlan and DVHTool from which the computed parameters are:

DVH Dose to Volume Histogram, expressed in equivalent photon dose. This histograms shows the percent of volume that has absorbed a given dose. For Osteosarcoma the DVH is evaluated for the: cancerous tissue, skin and soft tissue.

T(min) The treatment time, which evaluated by imposing the maximum tolerable dose to the skin that was considered as the organ at risk being the tissue with the lowest tolerance to radiation in this clinical case.

The second part uses the treatment time to evaluate the dose deposition to peripheral organs employing the geometrical MIRD phantom [25].

⁴Neutron Kerma Factors for A-150 Tissue Equivalent Plastic Calculated from Kerma data in ICRU Report 63 and JENDL-3.2 cross sections and Q-values. These kerma factors are reported in J.T. Goorley, W.S. Kiger, III, R.G. Zamenhof, "Reference Dosimetry Calculations for Neutron Capture Therapy with Comparison of Analytical and Voxel Models," Medical Physics, February 2002.

4. Design of an epithermal neutron beam for limb osteosarcoma

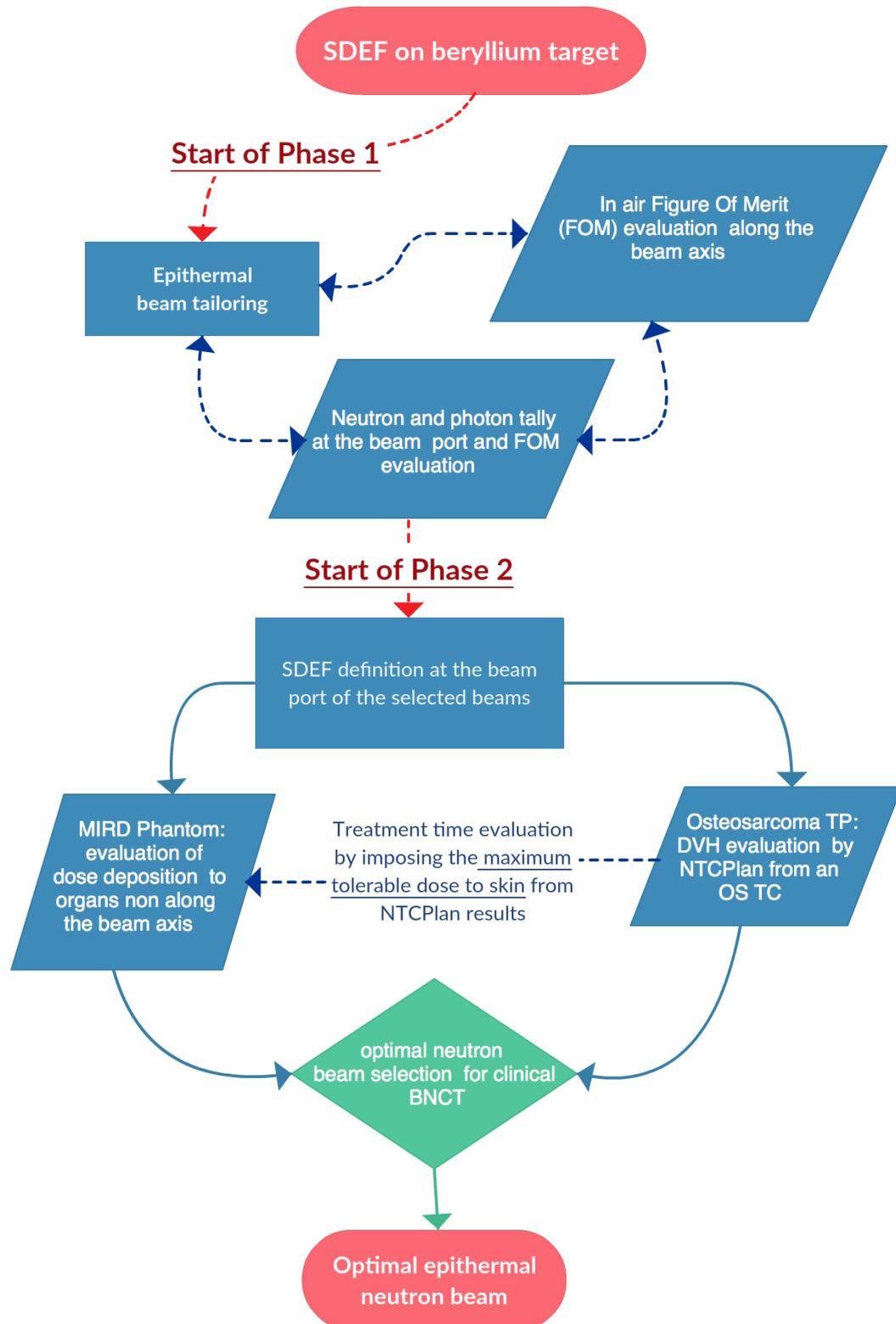


Figure 4.16: Simulation work flow chart, graphical representation of the performed work for the tailoring of the epithermal neutron beam.

4.5. Epithermal neutron beam tailoring

Table 4.7: In-air parameters concerning the BSA configuration of Figure 4.17.

Neutron source	ϕ_{epi} ($10^9 \text{ cm}^{-2} \text{ s}^{-1}$)	$\frac{\dot{D}_f}{\phi_{epi}}$ (10^{-13} Gy cm^2)	$\frac{\dot{D}_\gamma}{\phi_{epi}}$ (10^{-13} Gy cm^2)
Figure 4.17a	4.0	15	28
Figure 4.17b	4.2	15	23
Figure 4.17c	3.2	9.9	25
Figure 4.17d	3.7	32	2.8

4.5 Epithermal neutron beam tailoring

For the accelerator described in Section 4.2 four initial BSA configurations were tested, shown in Figure 4.17. Materials used are lead as external shielding and different combinations of Teflon and of a material mixture of aluminium/Teflon/magnesium alloy and a mixture of titanium/Teflon/magnesium alloy, starting from the neutron source the composition of the tested set-ups are:

Figure 4.17a 200 mm of Teflon, 6 sandwiches of (10 mm Al / 10 mm Teflon / 10 mm MgAl) and 3 sandwiches of (10 mm Ti / 10 mm Teflon / 10 mm MgAl) cut by a titanium cylinder along the beam axis or 6 cm radius.

Figure 4.17b 250 mm of Teflon, 6 sandwiches of (10 mm Al / 10 mm Teflon / 10 mm MgAl) and 3 sandwiches of (10 mm Ti / 10 mm Teflon / 10 mm MgAl) cut by a titanium con along the beam axis with final radius of 6 cm.

Figure 4.17c 200 mm of Teflon, 6 sandwiches of (10 mm Al / 10 mm Teflon / 10 mm MgAl) and 3 sandwiches of (10 mm Ti / 10 mm Teflon / 10 mm MgAl) cut by a titanium con along the beam axis with final radius of 6 cm.

Figure 4.17d 20 sandwiches of (10 mm Al / 10 mm Teflon / 10 mm MgAl) and 3 sandwiches of (10 mm Ti / 10 mm Teflon / 10 mm MgAl) cut by a titanium con along the beam axis with final radius of 6 cm.

The parametric results of these set up are summarized in Table 4.7, while the neutron spectra at the beam port are shown in Figure 4.18. None of those configurations is able to suppress the fast neutron component originated from the beryllium target; the configuration represented by Figure 4.17d suppresses photons satisfactory, while the configuration of Figure 4.17c has the lowest fast neutron contamination. Therefore, cladding materials together helps to reduce the beam photon component, while increasing the amount of Teflon improves the absorption of fast neutron without decreasing too much the epithermal neutron flux.

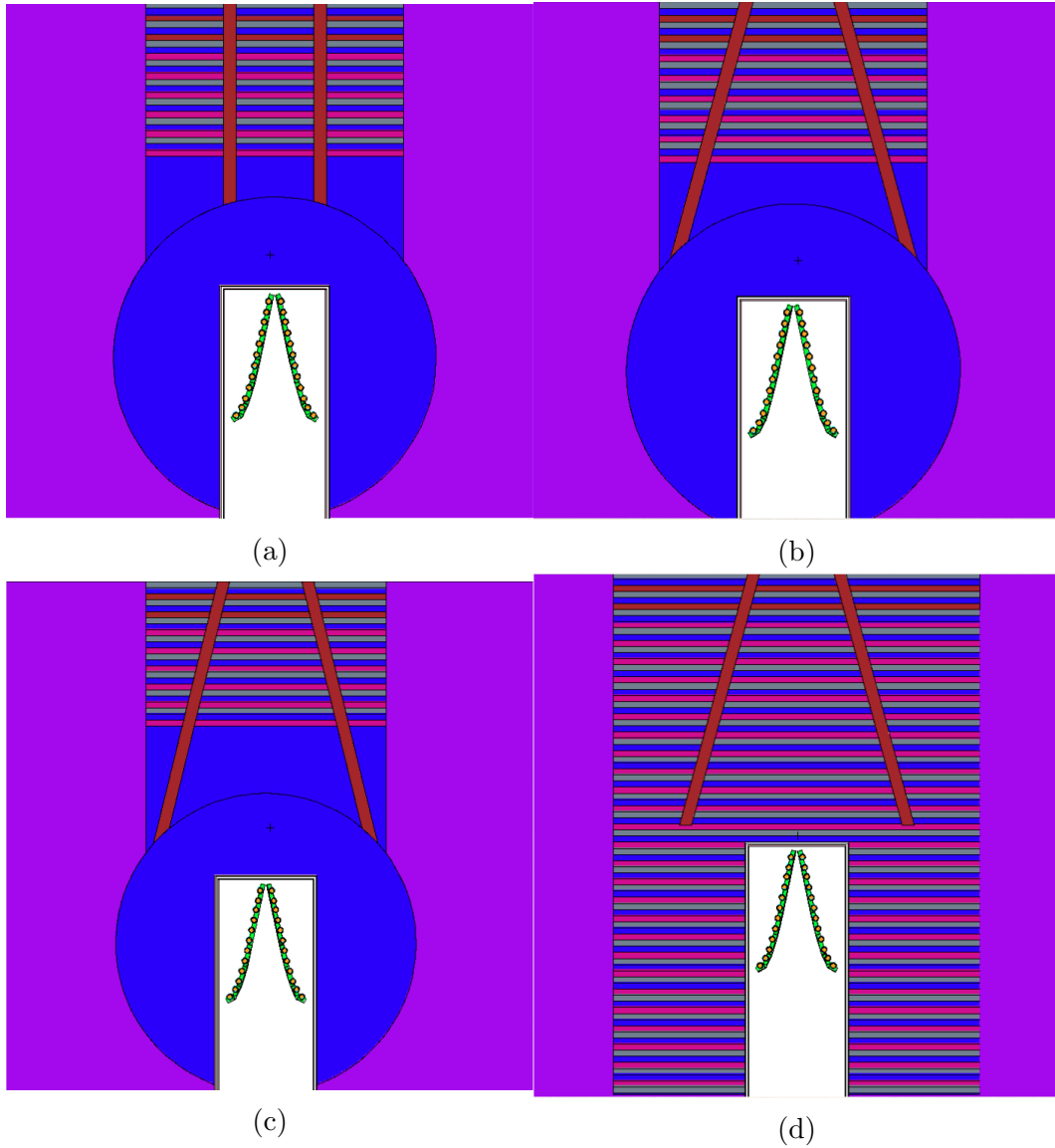


Figure 4.17: Different BSA configurations with the same base materials. The outer material is lead. In (a) and (b) 200 mm of teflon was chosen as reflector, while in (c) 250 mm of teflon was used. in (d), a different approach was chosen, the neutron source is surrounded by a sandwich material made up of (10 mm Al / 10 mm Teflon / 10 mm MgAl). The same sandwich is found 6 times in (a), (b) and (c). Finally for all the configurations the beam port is made by two sandwiches of (10 mm Ti / 10 mm Teflon / 10 mm MgAl). A titanium cone (a) or cylinder (b)/(c)/(d) crosses the BSA to drift epithermal neutrons towards the beam port.

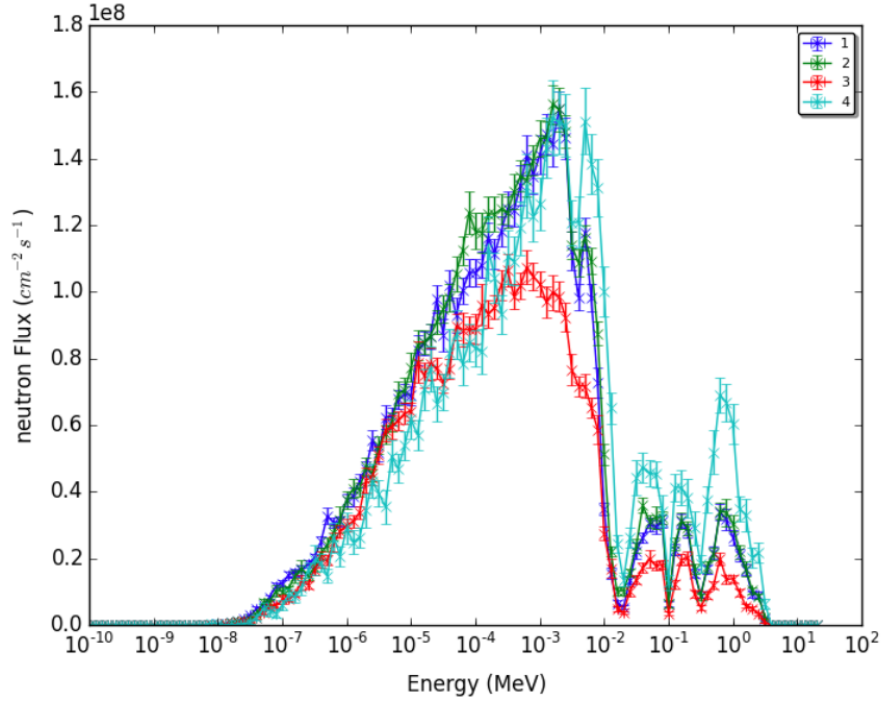


Figure 4.18: Neutron spectra concerning the BSA configuration of Figure 4.17. Line 1,2,3 and 4 represent respectively the configuration of Figure 4.17a, Figure 4.17b, Figure 4.17c, and Figure 4.17d

4.5.1 Slowing down of the neutron spectra

The results obtained from the BSA of Figure 4.17 are not satisfactory yet, the fast neutron contamination is still too high and photons are not sufficiently suppressed. This section shows the study of the neutron moderation performance of: aluminium, aluminium fluoride, lithium fluoride, magnesium alloy, ⁶⁰Ni⁵, silicon, Teflon and titanium; material composition and cross sections are summarized in Appendix C. The test of these materials was performed on the structure represented in Figure 4.19, composed by: lead shield, Teflon reflector, lithium loaded polyethylene and the central axis housing one of the materials listed before. Evaluated physical parameters are:

- 1 - Along the Beam axis. Starting at the top interface of the vacuum tube till the beam port, every 1 cm the: neutron flux intensity and dose rate for thermal, epithermal and fast neutron components are tallied.
- 2 - At the Beam Port, neutron energy spectra is tallied.

Apart from the neutron spectra all the other parameters are evaluated as a function of the distance within the BSA, starting at the top interface of the vacuum tube .

⁵ ⁶⁰Ni was examined to show the interesting cross section characteristic of this element.

4. Design of an epithermal neutron beam for limb osteosarcoma

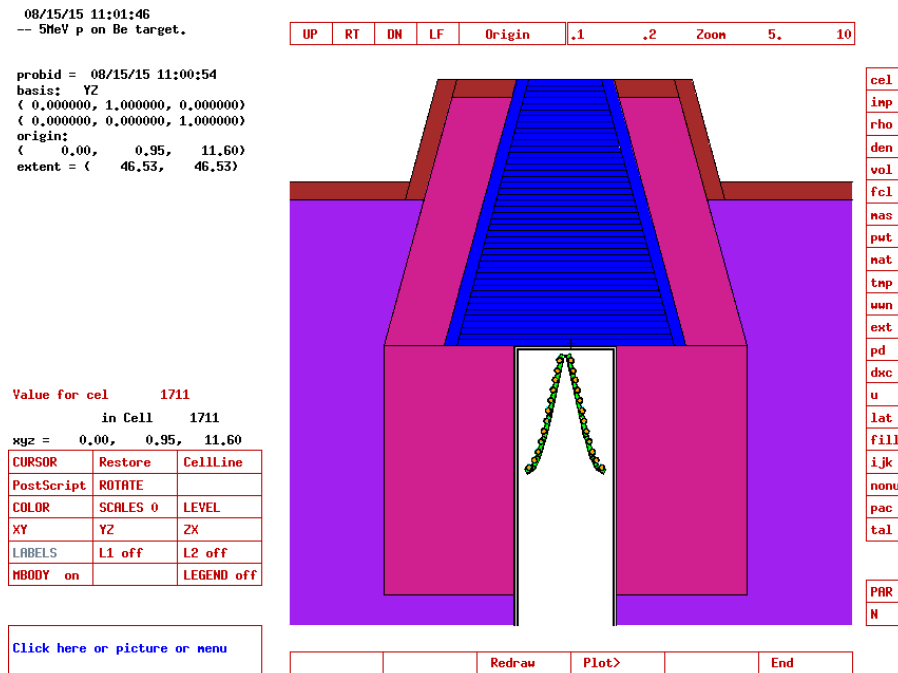


Figure 4.19: Geometrical structure to perform neutron moderation studies to lower fast neutron and photons contamination. The shielding material is lead, the reflector was chosen to be graphite and the external structure is covered by a layer of lithium loaded polyethylene. The central structure, represented in blue, was filled with the materials to be tested.

4.5. Epithermal neutron beam tailoring

Results are shown in Figure 4.20 for thermal, epithermal and fast neutron flux component. Figure 4.20a shows that Ti, ^{60}Ni and LiF are good thermal neutron absorbers. While the rest of the considered materials interact nearly in the same way with this neutron component. As shown in Figure 4.20b, apart from LiF, all the considered materials produce an epithermal neutron component greater than $10^9 \text{ cm}^{-2} \text{ s}^{-1}$ after 45 cm of moderation. Finally Figure 4.20c shows that LiF, Teflon and AlF_3 are good fast neutron absorbers while all the other materials fail in filtering this neutron component. Dose rate as a function of the distance within the beam is shown Figure 4.21 where the prevalent dose component (also after 45 cm of moderation) is the one due to the fast neutrons.

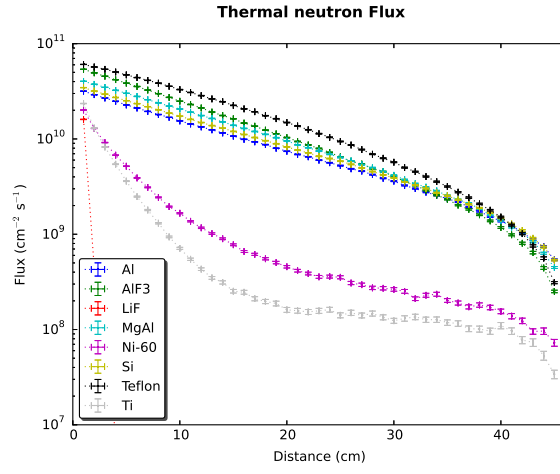
Figure 4.22 displays the ratio between dose rate and the epithermal neutron flux component as a function of the distance for the previously listed materials. It is interesting to see how aluminium fluoride produces a contamination lower than $^{-12} \text{ Gy cm}^2$ after 30 cm of moderation. Apart from Teflon and lithium fluoride, AlF_3 is the only material obtaining such a low fast neutron contamination with epithermal fluxes well above $10^9 \text{ cm}^{-2} \text{ s}^{-1}$. Figure 4.23 exhibits the neutron energy spectra after 45 cm of moderation on a circle surface with a radius of 6 cm. As expected, the fast neutron component obtained using Teflon, lithium fluoride and aluminium fluoride is consistently lower than the one obtained with other materials. As mentioned before, Ni^{60} is interesting because it produces a neutron spectrum with a sharp peak between 1 and 10 keV, that is exactly the goal of the work. However it would be impossible to purchase such quantity of enriched nickel, thus other solutions must be studied.

To conclude, this investigation helped in the selection of the optimal moderating material. From this point on, the bulk moderating material will be aluminium fluoride, while other elements will be used to shape the final neutron energy distribution and to reduce the photon contamination.

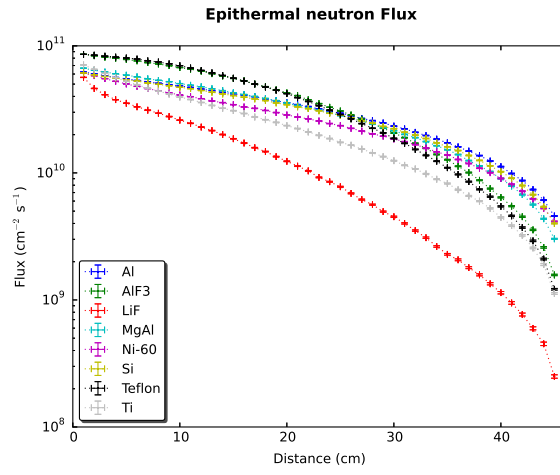
4.5.2 Extraction angle selection.

As shown in the previous paragraph, aluminium fluoride is an adequate material to reduce the fast neutron component for an epithermal neutron beam development. Anyhow a better beam would be characterized by a smaller fast neutron component. This can be achieved taking advantage of the angular dependence of the source neutron spectra emitted by the reaction $^9\text{Be}(p,n)^9\text{B}$ shown in Figure 4.5: at increasing laboratory angles the mean and maximum neutron energy decreases. Therefore, the performance of the BSA was studied in the forward direction and at 90° with respect to the proton beam direction. The geometry and material composition of the neutron tailoring is shown in Figure 4.24. The moderating region is composed by 36 cm of aluminium fluoride, 1 cm of lithium fluoride, 1 cm of titanium and a final 2 cm layer of bismuth. Lithium fluoride helps the reduction of the thermal neutron component while titanium removes neutrons in the 40 keV region. The final bismuth layer was chosen as a gamma absorber.

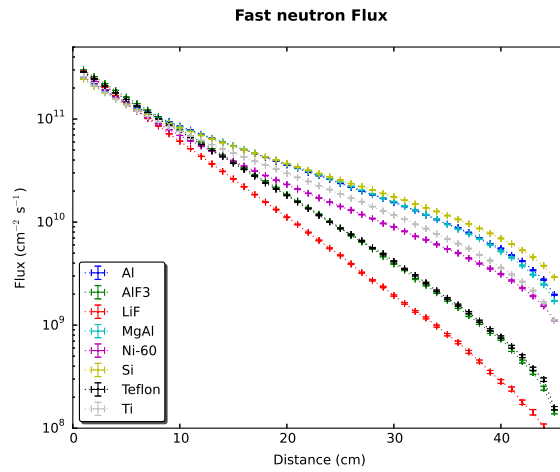
4. Design of an epithermal neutron beam for limb osteosarcoma



(a)



(b)



(c)

Figure 4.20: (a) Thermal, (b) Epithermal and (c) Fast flux comparison as a function of the distance inside the BSA.

4.5. Epithermal neutron beam tailoring

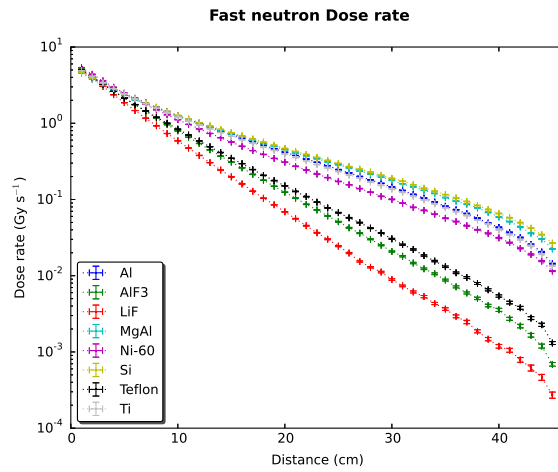
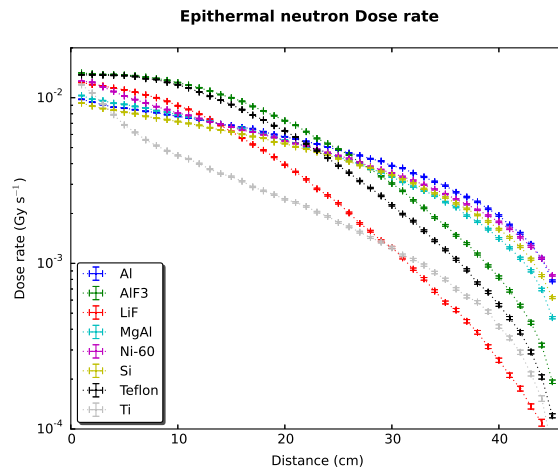
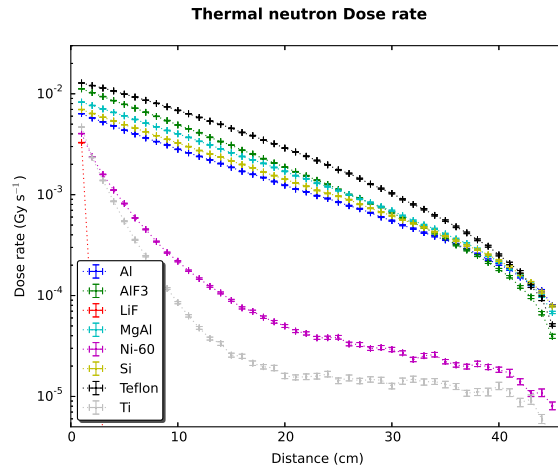


Figure 4.21: (a) Thermal, (b) Epithermal and (c) Fast dose rate comparison as a function of the distance inside the BSA.

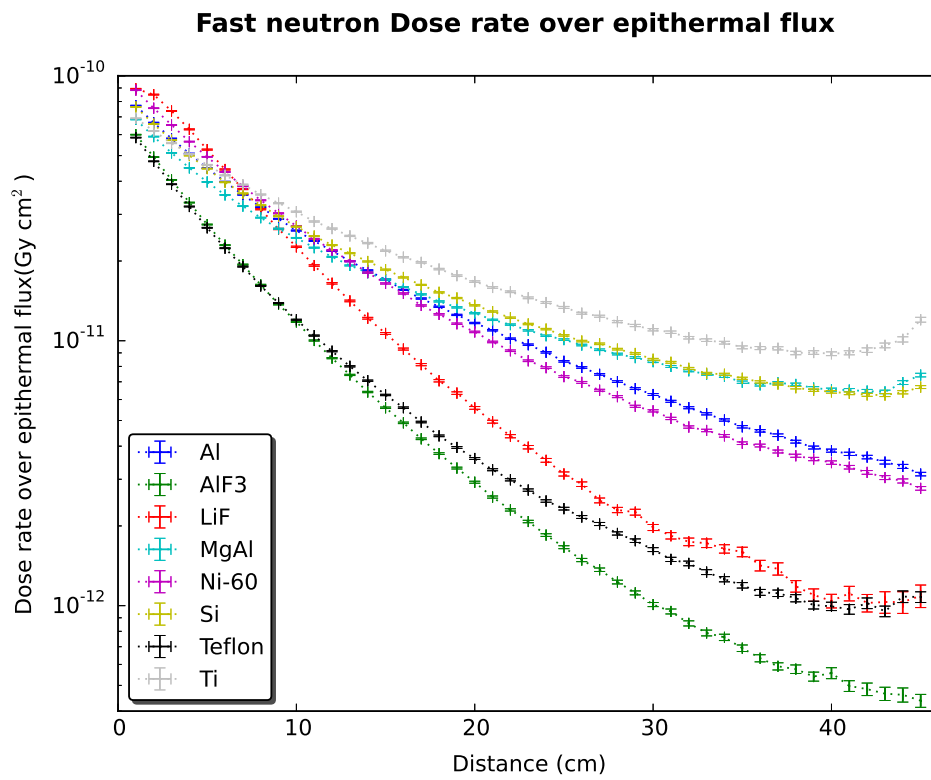


Figure 4.22: Dose rate over epithermal neutron flux comparison as a function of the distance within the BSA.

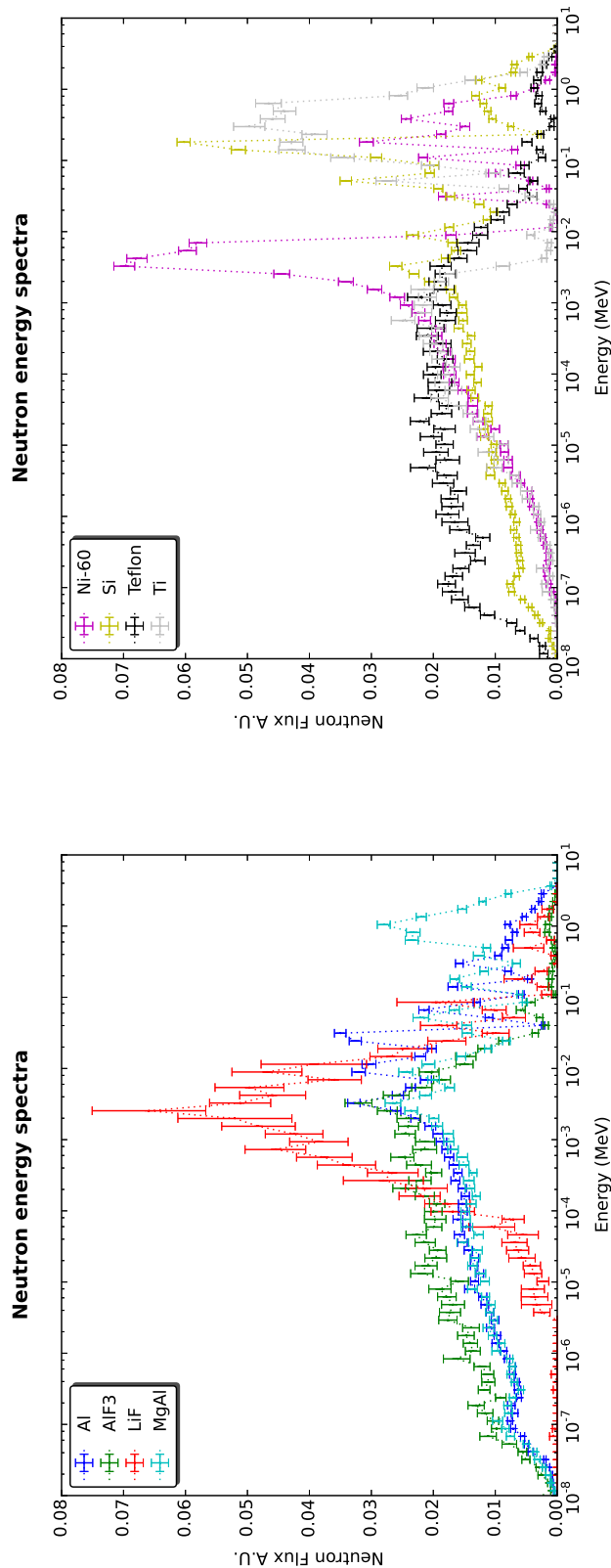


Figure 4.23: Neutron energy spectra comparison at the beam port. The area of each spectra is normalized to 1.

4. Design of an epithermal neutron beam for limb osteosarcoma

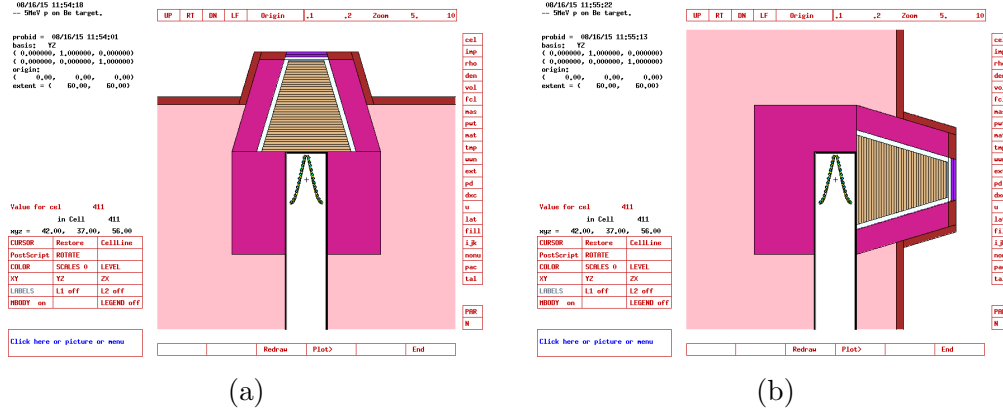


Figure 4.24: Figure (a) and (b) show respectively the geometrical set up at 0° and 90° with respect to the proton direction. The moderating region is composed by 36 cm of aluminium fluoride, 1 cm of lithium fluoride, 1 cm of titanium and a final 2 cm layer of bismuth. The shield is lead, the reflector is graphite and the external structure is covered by a layer of lithium loaded polyethylene. The moderating cone is covered by a 1cm layer of titanium.

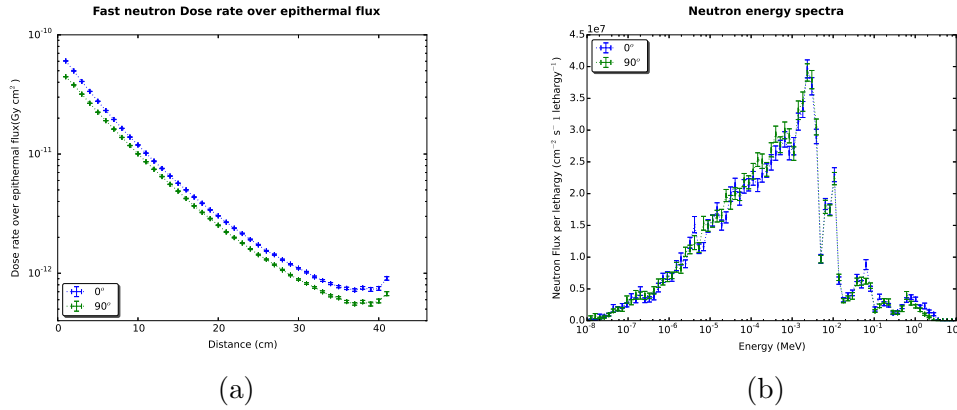


Figure 4.25: Figure (a) shows the comparison of the dose rate over epithermal neutron flux ratio as a function of the distance within the moderating region for 0° and 90° with respect to the interaction direction of the proton beam on the beryllium target. Figure (b) compares the 0° and 90° neutron energy spectra at the beam port

Some of the parameters considered in Section 4.5.1 were used here to perform the comparison between the 0° and 90° configurations. Figure 4.25a shows the ratio between fast neutron dose rate and the epithermal neutron flux as a function of the distance within the moderating region of the BSA. The results are clear, the 90° configuration gives the advantage of reducing the fast neutron component compared to the 0° . Even though this difference is not appreciable in Figure 4.25b, the dose rate related to the fast neutron component is reduced by a factor of 20% as shown in Table 4.8.

4.5. Epithermal neutron beam tailoring

Table 4.8: In-air parameters concerning the BSA configuration of Figure 4.24.

Neutron source	ϕ_{epi} ($10^9 \text{ cm}^{-2} \text{ s}^{-1}$)	$\frac{\dot{D}_f}{\phi_{epi}}$ (10^{-13} Gy cm^2)	$\frac{\dot{D}_\gamma}{\phi_{epi}}$ (10^{-13} Gy cm^2)
Figure 4.24a	1.8	8.9	16
Figure 4.24b	1.8	6.9	16

From now on the chosen direction for the epithermal neutron beam development is 90° with respect to the proton beam direction.

4.5.3 optimization of neutron reflection

In this section the tested configurations to increase the epithermal neutron flux and to decrease the photon contamination, while keeping a low fast neutron contamination are described. To maximise the neutron peak in the range 1-10 keV, also the material surrounding the neutron source has to moderate neutrons and by scattering send them back into the beam with an appropriate energy; such a material will be called from now on *reflecting material* and it must maximize the epithermal neutron flux, while keeping low fast neutron and γ photons contamination.

Possible good reflecting materials have low neutron capture cross section and high scattering cross section in the unwanted energy ranges. These materials are summarized in Table 4.6. Figure 4.26 shows the configurations that were tested to select the optimal reflecting material. Beam material composition and the reflector material for each figure are shown in Table 4.9. The main difference between those four trials is that in the one represented in Figure 4.26a, lithium fluoride is employed only in the first layer of the beam, while in Figure 4.26b, 4.26c and 4.26d lithium fluoride was placed as first layer and after the 35.5 cm bulk of aluminium fluoride.

4. Design of an epithermal neutron beam for limb osteosarcoma

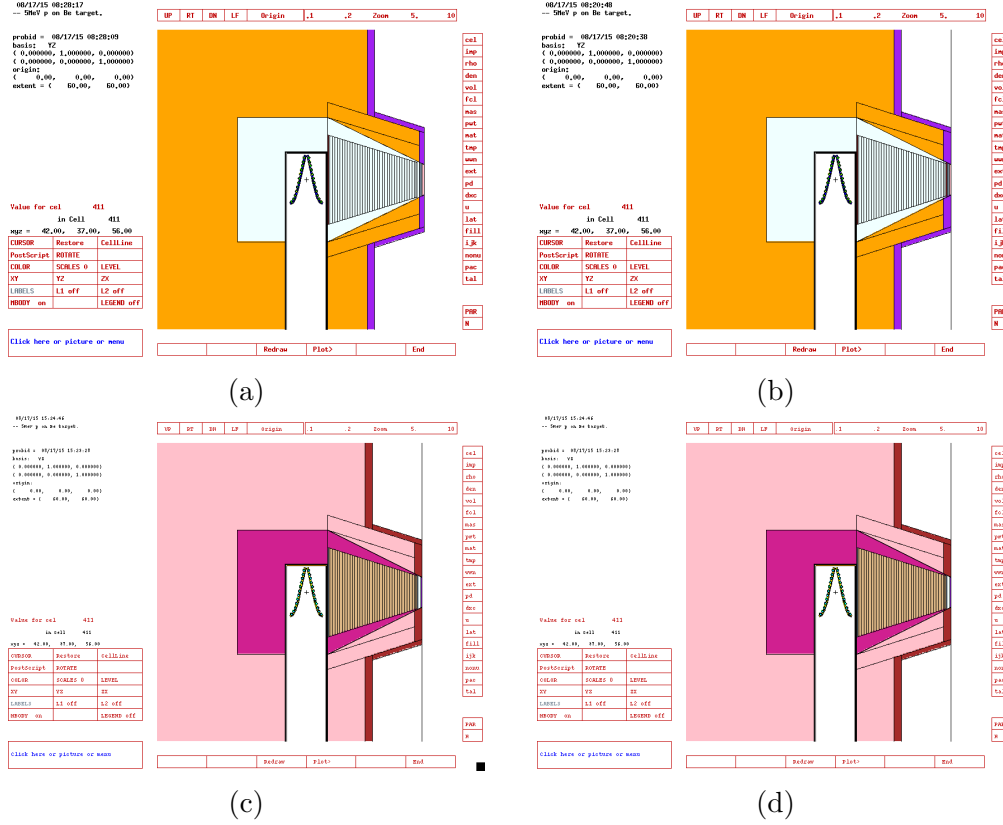


Figure 4.26: Schematic representation of the BSA where the reflecting material was tested. Material composition of the beam and reflector are summarized in Table 4.9. The shield is made of lead while the BSA is covered with a layer of lithium loaded polyethylene.

The obtained neutron energy spectra are shown in Figure 4.27. In the fast energy range, Figure 4.27c, there is no difference in the response in this energy range. There are differences in the epithermal energy range, Figure 4.27b. Here the reflecting material that maximises the neutron flux is aluminium fluoride, then Teflon and finally graphite. Figure 4.27a shows the thermal energy range. It is clear that without the lithium fluoride layer after 35.5 cm of aluminium fluoride, configuration shown in Figure 4.26a, thermal neutrons are not absorbed: this final lithium fluoride slab helps in reducing thermal neutrons without affecting the spectrum in the energy range between 1 keV and 10 keV.

Considering the in-air parameters summarized in Table 4.10 and the results of Figure 4.27, the best material acting as a reflector is aluminium fluoride. Furthermore, a lithium fluoride slab before and after the bulk layer of AlF_3 helps in reducing thermal neutrons. Consequently, the most interesting configuration is the one of Figure 4.26b. In the next section, starting from this final configuration, different materials will be tested to increase the neutron flux peak in the epithermal energy range.

4.5. Epithermal neutron beam tailoring

Table 4.9: Material composition of geometries represented in Figure 4.26

Figure	Reflector Material	Beam Material
Figure 4.26a	AlF_3	0.5 cm LiF
		36.5 cm AlF_3
		1 cm Ti
		1 cm Bi
Figure 4.26b	AlF_3	0.5 cm LiF
		36.5 cm AlF_3
		0.5 cm LiF
		1 cm Ti
Figure 4.26c	graphite	0.5 cm Bi
		0.5 cm LiF
		36.5 cm AlF_3
		1 cm Ti
Figure 4.26d	Teflon	0.5 cm Bi
		0.5 cm LiF
		36.5 cm AlF_3
		1 cm Ti

Table 4.10: In-air parameters concerning the BSA configuration of Figure 4.26.

Neutron source	ϕ_{epi} ($10^9 \text{ cm}^{-2} \text{ s}^{-1}$)	$\frac{\dot{D}_f}{\phi_{epi}}$ (10^{-13} Gy cm^2)	$\frac{\dot{D}_\gamma}{\phi_{epi}}$ (10^{-13} Gy cm^2)
Figure 4.26a	3.0	6.7	7.2
Figure 4.26b	2.7	6.8	6.2
Figure 4.26c	2.0	9.2	9.2
Figure 4.26d	2.4	8.3	6.6

4. Design of an epithermal neutron beam for limb osteosarcoma

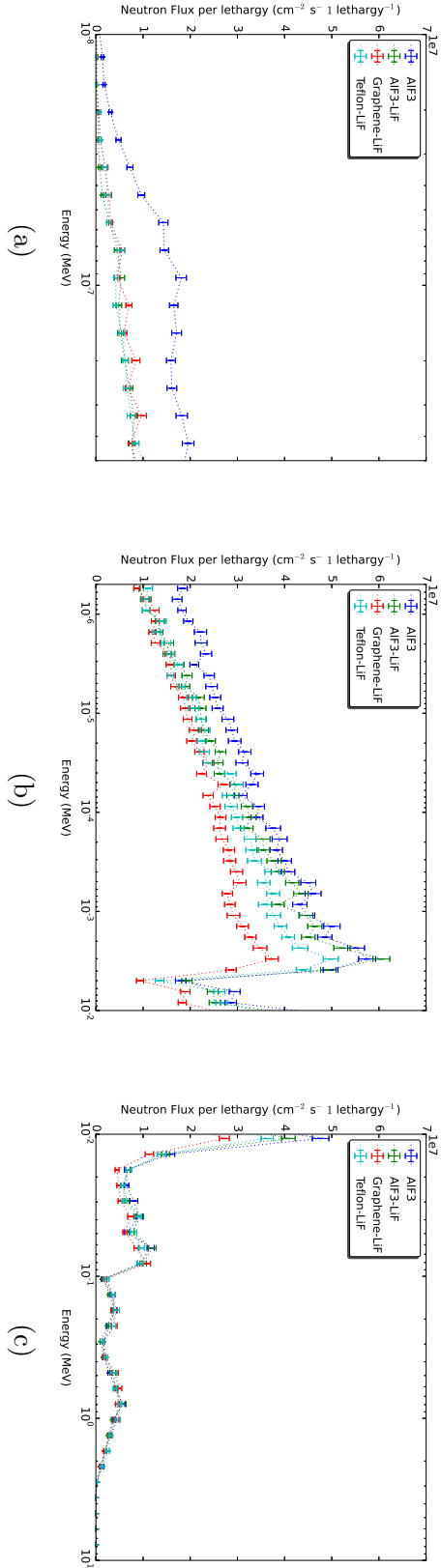


Figure 4.27: Neutron energy spectra comparison at the beam port separated in thermal, epithermal and fast neutron energy ranges respectively in Figure (a), (b) and (c).

4.5.4 Lateral Neutron Beam profile

The achieved in-air beam parameters, obtained with the configuration shown in Figure 4.26b, compared with the epithermal neutron beams found in literature of Table 4.1, are quite satisfactory. However some care should be given to the lateral beam profile. The goal of developing a beam for clinical BNCT is to confine most of the neutrons within the beam opening. In this work, the radius at the beam port was chosen to be 6 cm, thus the highest neutron flux should be found in this region. Taking the geometry shown in Figure 4.26b as the reference beam, its lateral flux distribution is shown in Figure 4.28. Clearly, the neutron flux is centred on the beam axis and mainly composed by epithermal energy neutrons. Anyhow, the lateral dose distribution is not negligible since it is higher than on the beam itself as shown in Figure 4.29. This dose is mainly given by the fast neutron component along the entire plane transverse to the beam axis.

Effort were dedicated to lower the lateral dose distribution due to fast neutrons, introducing materials with low mass that do not emit γ rays while slowing down neutrons. For this reason graphite was chosen, Figure 4.30 shows three configurations. One is the previous geometrical assembly, another has graphite to moderate neutrons only externally to the beam and the last one contains graphite externally and along the beam axis. The lateral dose rate profile comparison, Figure 4.31, shows that the configuration of Figure 4.30c has the same dose rate on the center of the beam and laterally. Figure 4.32 and Figure 4.33 show in more detail the radial flux components and dose rate components of this last configuration. The IAEA in air parameters are shown in Table 4.11, marking that the differences at the beam port are negligible apart from the greater photon contamination of the configuration shown in Figure 4.30b.

These tests demonstrate that improving the neutron shield, without modifying the BSA material, does not influence the beam performance. It is clear from Table 4.11 that this is the case, since the in air figure of merit are very similar for the configurations of Figure 4.30a and Figure 4.30c, also allowing for an easier configuration of the treatment room shielding.

4. Design of an epithermal neutron beam for limb osteosarcoma

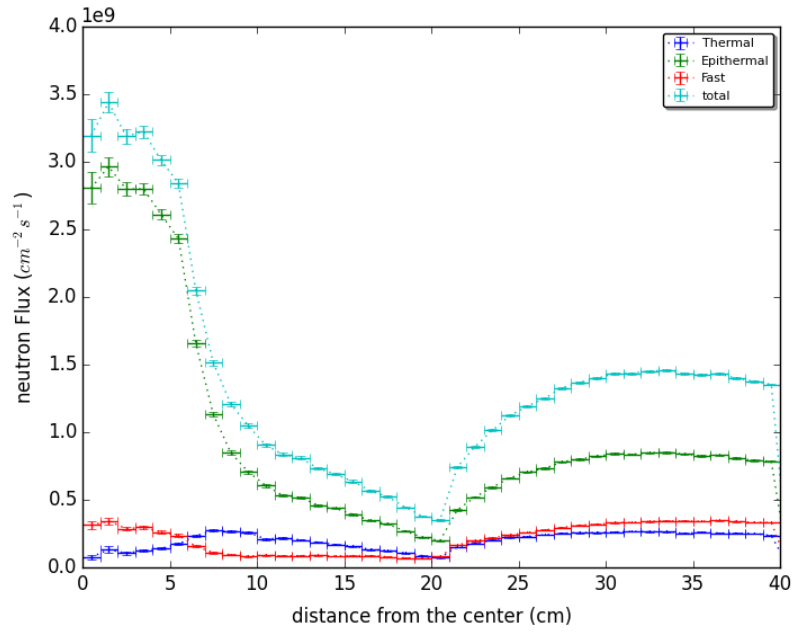


Figure 4.28: Neutron Flux at the beam port as a function of the distance from the axis of the beam.

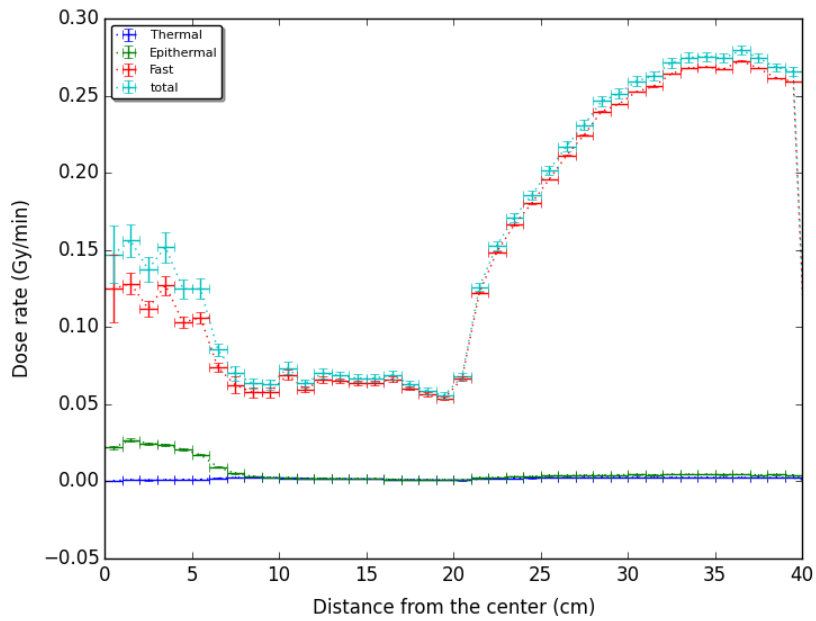


Figure 4.29: Neutron dose rate at the beam port as a function of the distance from the axis of the beam.

4.5. Epithermal neutron beam tailoring

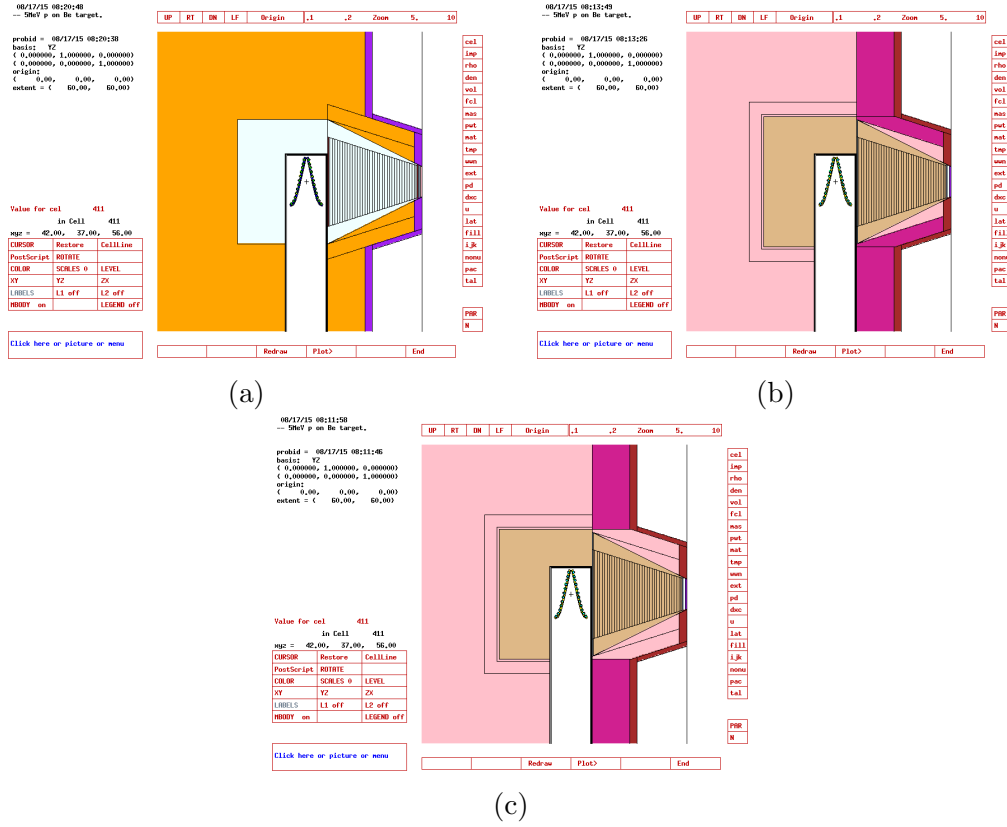


Figure 4.30: Schematic representation of the lateral shielding. The beam is composed by: 0.5 cm of Li, 36.5 cm of AlF_3 , 0.5 cm of Li, 1 cm Ti and 0.5 cm Bi. The main shield is lead and the entire object is encapsulated in a 3 cm layer of lithium loaded polyethylene. The difference between the 3 figures is: (a) no lateral shield, (b) graphite shield along the beam and laterally, (c) graphite shield only laterally.

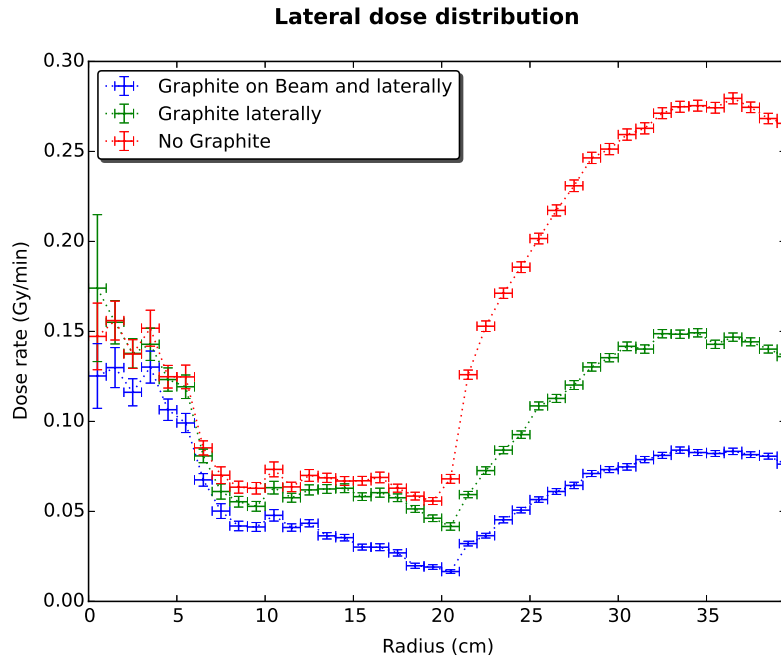


Figure 4.31: Neutron dose rate at the beam port as a function of the distance from the center of the beam. Comparison between the three configurations shown in Figure 4.30.

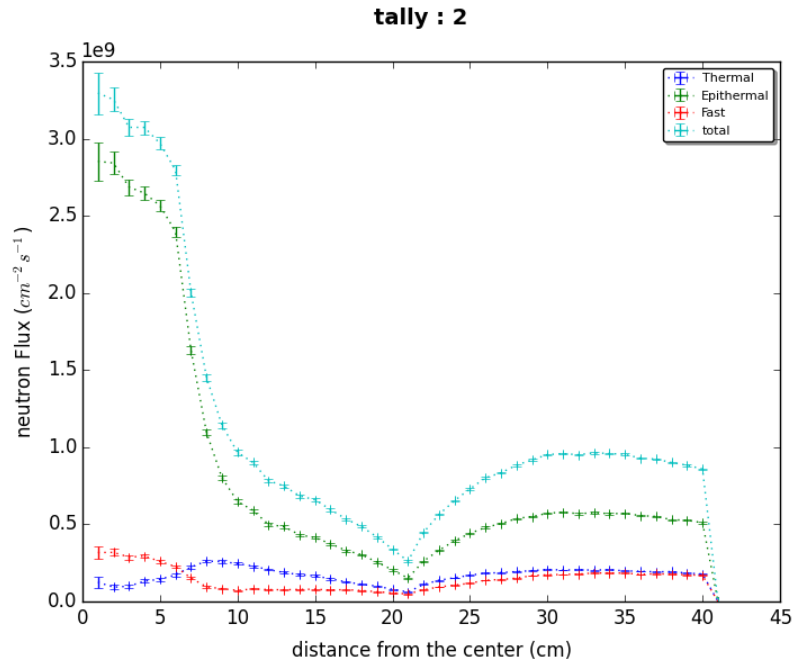


Figure 4.32: Neutron Flux at the beam port as a function of the distance from the center of the beam, for the geometrical configuration of Figure 4.30c

4.6. Final Epithermal Beam

Table 4.11: In-air parameters concerning the BSA configuration of Figure 4.30.

Neutron source	ϕ_{epi} ($10^9 \text{ cm}^{-2} \text{ s}^{-1}$)	$\frac{\dot{D}_f}{\phi_{epi}}$ (10^{-13} Gy cm^2)	$\frac{\dot{D}_\gamma}{\phi_{epi}}$ (10^{-13} Gy cm^2)
Figure 4.30a	2.7	6.8	6.2
Figure 4.30b	2.5	6.1	8.0
Figure 4.30c	2.6	6.5	6.3

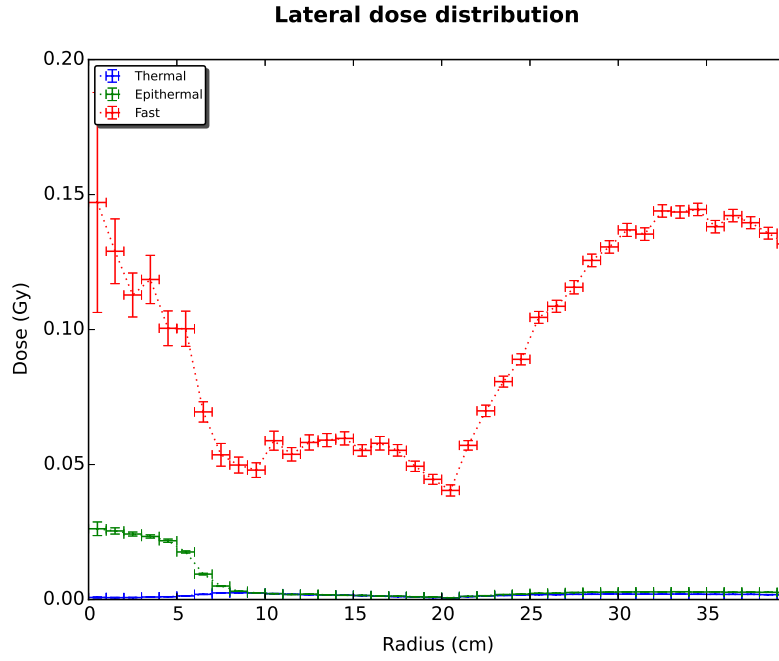


Figure 4.33: Neutron dose rate at the beam port as a function of the distance from the center of the beam, for the geometrical configuration of Figure 4.30c

4.6 Final Epithermal Beam

This section addresses the issue of lowering the photon component of the beam. This can be achieved by substituting all those materials having an high cross section for neutron interaction that emit photons, with elements having similar neutron moderation but negligible γ emission. For this reason a material that should be substituted is lithium loaded polyethylene which contains hydrogen emitting 2.2 MeV photons through the reaction $^1\text{H}(n,\gamma)^2\text{H}$. Consequently, materials like heavy water and lithium carbonate were tested in this section. Another way to decrease the gamma component is absorbing thermal neutrons, which are the main cause of photon production via radiative capture. This can

be achieved by placing lithium in strategic positions within the beam.

Figure 4.34 and Figure 4.35 show the two geometrical set-up considered in this section. Actually the first one represents three configurations, in all of them the central bulk is composed by: 0.5 cm LiF, 34.5 cm AlF₃, 0.5 cm LiF, 1cm AlF₃, 1 cm Ti, 0.5 cm Bi. Surrounding the central aluminium fluoride bulk there is lead, while the materials filling the external white and purple volumes are the ones that distinguish the three configurations. Here, combinations of: lithium loaded polyethylene, graphite, heavy water and lithium carbonate are used as shown in Table 4.12. The latter figure has a more complicated geometry and material composition; this BSA contains thin layers of lithium fluoride (LiF) within the 36 cm block of AlF₃. To further absorb thermal neutrons the entire BSA is encapsulated in 1cm thick layer of LiF. The external coat is composed by lithium carbonate (centrally) and lithium loaded polyethylene (laterally). For simplicity the BSA set-up are listed here:

- (1) – Central: 0.5 cm LiF, 34.5 cm AlF₃, 0.5 cm LiF, 1cm AlF₃, 1 cm Ti, 0.5 cm Bi
 – Shield: lead
 – Lateral moderator: graphite
 – Coat: lithium loaded polyethylene
- (2) – Central: 0.5 cm LiF, 34.5 cm AlF₃, 0.5 cm LiF, 1cm AlF₃, 1 cm Ti, 0.5 cm Bi
 – Shield: lead
 – Lateral moderator: graphite
 – Coat: lithium carbonate
- (3) – Central: 0.5 cm LiF, 34.5 cm AlF₃, 0.5 cm LiF, 1cm AlF₃, 1 cm Ti, 0.5 cm Bi
 – Shield: lead
 – Lateral moderator: heavy water
 – Coat: lithium carbonate
- (4) – Central: 0.5 cm LiF, 10 cm AlF₃, 0.25 cm LiF, 10 cm AlF₃, 0.25 cm LiF, 10 cm AlF₃, 0.25 cm LiF, 6 cm AlF₃, 0.25 cm LiF, 1 cm Ti, 0.5 cm Bi
 – Shield: lead & lithium fluoride
 – Lateral moderator: graphite & lithium fluoride
 – Coat: lithium loaded polyethylene & lithium carbonate & lithium loaded polyethylene

4.6. Final Epithermal Beam

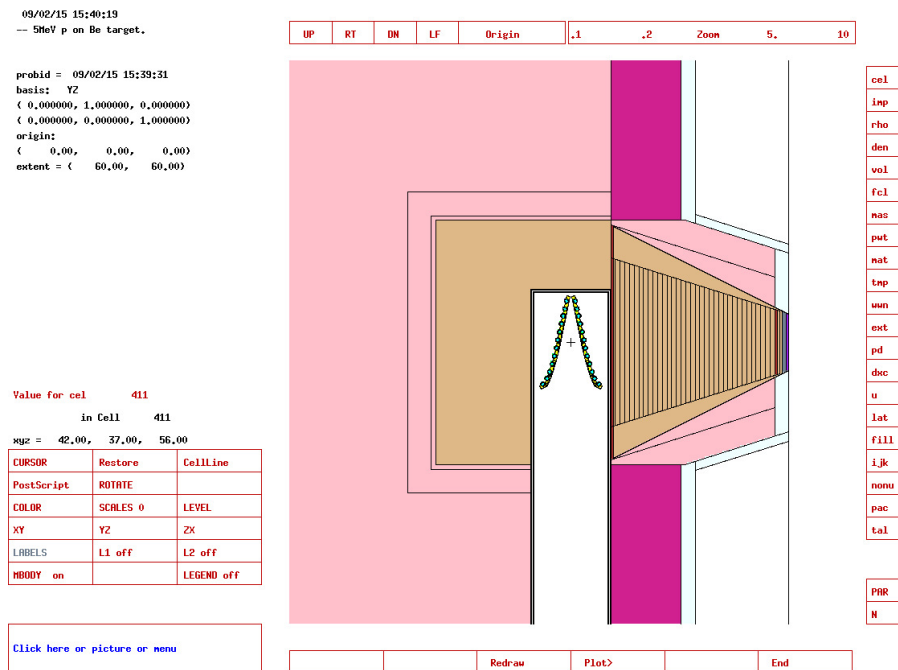


Figure 4.34: The central cone is composed by: 0.5 cm LiF, 34.5 cm AlF_3 , 0.5 cm LiF, 1cm AlF_3 , 1 cm Ti, 0.5 cm Bi. Laterally to the beam there is lead while in this section three configurations of the white and purple materials were tested as shown in Table 4.12

4. Design of an epithermal neutron beam for limb osteosarcoma

Table 4.12: Material configuration taking Figure 4.34 as a reference.

Beam	Purple	White
Figure 4.34 1	graphite	lithium loaded polyethylene
Figure 4.34 2	graphite	lithium carbonate
Figure 4.34 3	Heavy Water	lithium carbonate

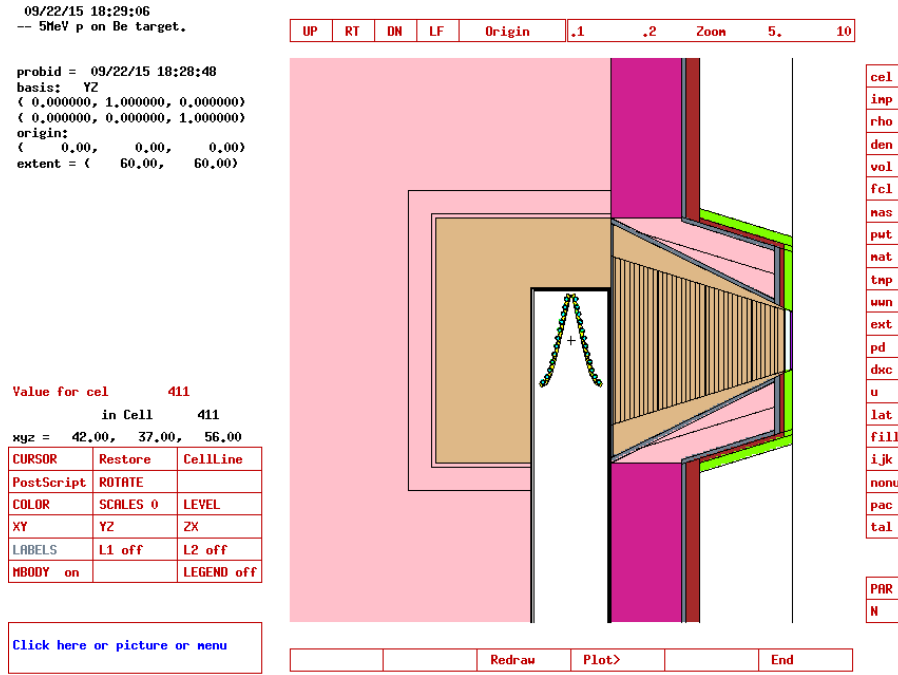


Figure 4.35: The central cone is composed by: 0.5 cm LiF, 10 cm AlF_3 , 0.25 cm LiF, 10 cm AlF_3 , 0.25 cm LiF, 10 cm AlF_3 , 0.25 cm LiF, 6 cm AlF_3 , 0.25 cm LiF, 1 cm Ti, 0.5 cm Bi. Filling the cone of the beam there is 1cm layer of LiF, lead, 1cm lithium polyethylene and 2 cm of lithium carbonate. Externally there are 15 cm of graphite, 1cm of LiF and a final 3 cm layer of lithium polyethylene.

The in air figure of merit of those BSA configurations are shown in Table 4.13. Configuration 1 gives the best neutronic response while 2, 3 and 4 are less performing. Anyhow the latter three configurations have less photon contamination, consequently the advantages and disadvantages may be balanced. Compared to the IAEA guidelines none of those beam are perfectly suited for a BNCT treatment. Another consideration may be deduced from Figure 4.36 which shows the normalized neutron energy spectra⁶. The most important difference is in the epithermal energy region: the configuration 2, 3 and 4 provide a spectrum with a higher flux in the energy range between 1

⁶The normalization was performed on the area, imposing a unitary value.

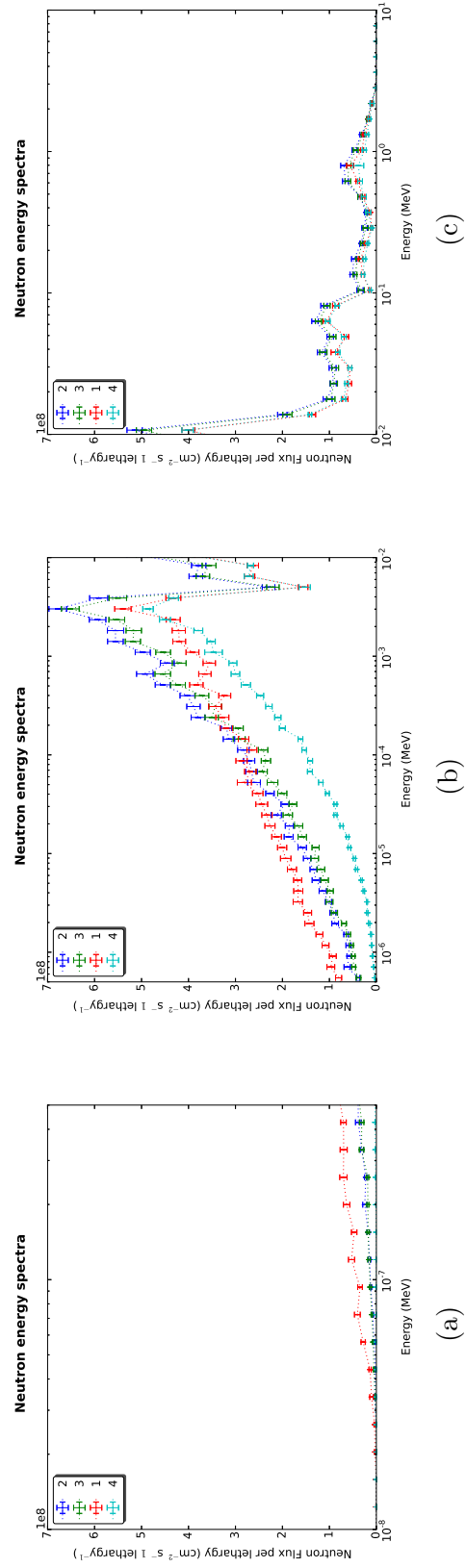


Figure 4.36: Neutron energy spectra comparison at the beam port separated in thermal, epithermal and fast neutron energy ranges respectively in Figure (a), (b) and (c).

Table 4.13: FOM results of the beams of Table 4.12.

Neutron source	ϕ_{epi} ($10^9 \text{ cm}^{-2} \text{ s}^{-1}$)	$\frac{\dot{D}_f}{\phi_{epi}}$ (10^{-13} Gy cm^2)	$\frac{\dot{D}_\gamma}{\phi_{epi}}$ (10^{-13} Gy cm^2)
1	2.6	7.1	6.3
2	2.8	8.9	3.7
3	2.6	9.0	3.9
4	1.6	7.6	2.8

and 10 keV, as desired.

As previously mentioned, figures of merit based on physical properties of the beams may not be sufficient to evaluate the performance in case of clinical applications. The goal of BNCT is in fact to deliver a therapeutic dose to the tumour while keeping the dose delivered to normal tissues as low as possible, and always below their tolerance limits. The achievement of this goal depends on the quality of the beam, but also on boron distribution, on tumour depth, geometry and location. Thus, in order to assess BNCT feasibility given a beam designed in order to keep as high as possible its quality, it is necessary to test the obtained dosimetry with treatment planning simulations. The treatment planning in clinical relevant examples allow the calculations of DVH for the organs of interest and for the tumour, and this can help in the comprehension of the optimal beam to be employed. A more macroscopical calculations of the dose in the peripheral organs using a geometrical model of the whole body, helps in evaluating the effects of the lateral contamination of the beam. These calculations will be described in the next section.

4.7 Beam efficiency clinical cases comparison

This dissertation develops in the framework of a BNCT project on osteosarcoma as stated in Chapter 1. Consequently the beam performance was tested on a real clinical case of patient affected by Osteosarcoma of the knee. The CT scan was provided by medical doctors, who also contoured the PTV⁷. The CT scan was translated into MCNP geometry using NCTPlan code, that produces a voxelized model made up of a lattice of 1 cm³ cells. Materials are assigned to each voxel according to the hounsfield numbers read in the CT scan, up to a maximum of 256 possible materials. NCTPlan also allow establishing the irradiation configurations, writing the neutron source in the chosen orientation to simulate beam directions. Finally, it provides some tools to superimpose the isodose curves to the CT images. DVHTool is another computational environment that allows to calculate DVH taking as inputs the MCNP output files

⁷Planned Treatment Volume

and the CT scans of the patient. Biological dose is calculated by multiplying the absorbed dose component by the CBE and RBE factors chosen by user (See Equation 3.4). Having calculated the dose rate delivered to the organ of interest, the dose prescription was decided by imposing a maximum of 22 Gy_{Eq} to the skin, considered the organ at risk. This prescription fixes the maximum irradiation time and allows the calculation of minimum, mean and maximum dose delivered to the tumour and to the other tissues. An adequate criterium to compare the performance of different beams is to compare the minimum dose to tumour at the same maximum dose to skin. Another important information is the uniformity of dose distribution in tumour, that was proven to be a major factor of therapeutic success in radiobiological experiments [136].

Having fixed the irradiation configuration and the treatment time, the MIRD phantom was used to calculate dose in: trunk, lung, stomach, kidney, spleen, liver, head, small intestines, large intestines, bladder, brain, thyroid, testes, pancreas, pharynx, bone marrow, adrenals, thymus and skin.

The evaluation of the BNCT treatment from the epithermal beams shown in Table 4.13 was performed by generating a neutron source at the beam port. Consequently neutrons were not generated and transported from the beryllium target, but directly extracted at the beam port plane. The extraction, validation and implementation of this neutron source is treated in Appendix A.2.

4.7.1 Osteosarcoma TPS

In this section the outcome of the treatment planning performed with NCTPlan will be exposed and discussed. The output of the software is the biological weighted dose in tumour, muscle and skin calculated with the parameters of Table 4.14. The boron concentration values for brain, skin, liver and lung are values commonly found in literature for BPA after four hours of infusion. On the other hand, boron concentration for muscle and tumour (Osteosarcoma) were measured in Pavia through the technique exposed in Chapter 2, as show Figure 2.11.

Table 4.14: RBE and CBE factors employed to calculate biological dose in different tissues [137, 138, 139]. The assumed normal tissue boron concentration obtained by BPA is shown in the last column, for a mean blood boron concentration of $15\mu\text{g/g}$.

Tissue	RBE_γ	RBE_n	CBE_B	^{10}B Concentration ($\mu\text{g/g}$)
Brain	1	3.2	1.3	15
Skin	1	3.2	2.5	22.5
Liver	1	3.2	4.25	30
Lung	1	3.2	2.3	15
muscle	1	3.2	1.8	15
Tumor	1	3.2	3.8	60

CBE and RBE determination for Osteosarcoma

The curves of the cell survival as a function of the absorbed dose in the three different experiments (irradiation with ^{60}Co X-rays, irradiation with neutrons, irradiation with neutrons in presence of boron) give the possibility to calculate the factors classically employed to express the total BNCT dose in common photon-equivalent units. This would allow comparing the BNCT protocols to conventional photon irradiation ones, especially concerning the tolerance dose of the different tissues and the prescription dose of the treatments. Different LET radiations have different effects on biological tissues and different effectiveness in destroying tumour cells. Each of the high LET components is thus weighted for biological factor experimentally determined and then summed in order to obtain the total biologically-weighted dose, expressed in Gy-Eq. The first factor, RBE is the ratio of the dose necessary to obtain a chosen endpoint with a reference X-ray radiation and the dose that gives the same effect due to irradiation with the high LET radiation under study. In our case, the RBE due to protons coming from capture in nitrogen and from scattering in hydrogen is calculated for the endpoint of 50% cell survival (ED_{50}), comparing the curve obtained with X-rays of ^{60}Co and the curve obtained with neutrons only. The formula to calculate RBE is:

$$\text{RBE} = \frac{\text{X}_{ray} \text{ED}_{50} - \gamma \text{Dose}}{\text{proton ED}_{50}} \quad (4.1)$$

Effectiveness of BNCT is related to boron biodistribution and especially to its microdistribution: depending on the ability of the carrier to obtain suitable boron concentrations and in the most advantageous localizations inside the cells, the neutron irradiation will ensure a selective therapeutic effect. The

4.7. Beam efficiency clinical cases comparison

factor to describe the effectiveness of the boron component of the high-LET radiation is the CBE and it is calculated comparing the reference X-ray survival curve with the one obtained by neutron irradiation in presence of boron. The CBE is calculated fixing the same endpoint of 50% survival, occurring at the dose ED_{50} , through the following relation:

$$CBE = \frac{[Xray\ ED_{50}] - [Beam\ Component\ of\ ED_{50}] \cdot Beam\ RBE}{Boron\ Component\ of\ ED_{50}} \quad (4.2)$$

where Beam Component of ED_{50} and Boron Component of ED_{50} are calculated on the basis of the relative percentages of the total dose due to neutron irradiation in presence of boron. Beam RBE is calculated following the previous equation without separating the gamma component of the dose.

In the frame of the feasibility study of BNCT for Osteosarcoma, cell survival curves as a function of the dose were produced [140]. Figure 4.37 shows the survival curves for the UMR106 murine osteosarcoma cell line irradiated with Co^{60} gamma rays, with thermal neutrons only and with thermal neutrons after BPA administration. From these curves, RBE and CBE factors for this tumour were calculated as described in [141], for the endpoint of 1% survival the results are:

CBE 4.8

RBE 1.8

For the proton dose due to scattering the convention is to use the same RBE measured for the protons produced by capture in nitrogen because the energies are similar.

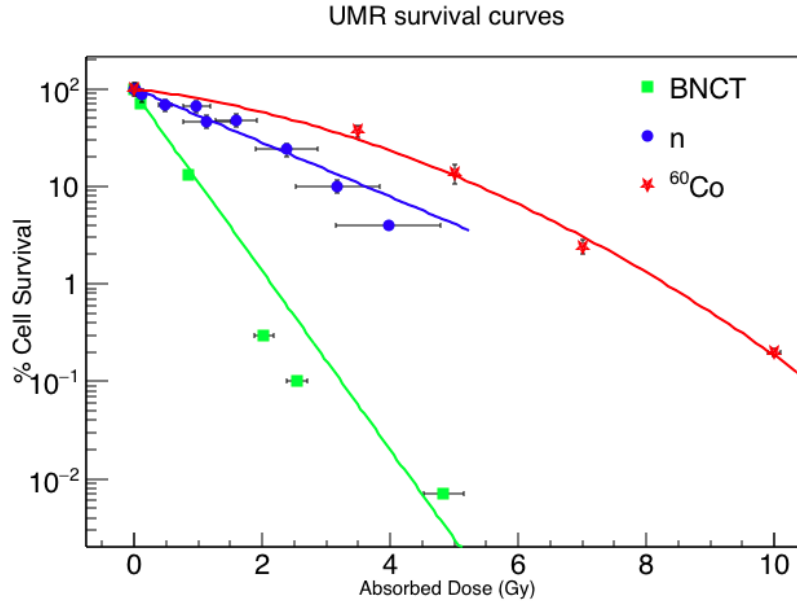


Figure 4.37: Survival curves for the UMR106 murine osteosarcoma cell line irradiated with Co^{60} gamma rays, with thermal neutrons only and with thermal neutrons after BPA administration.

4.7.2 Treatment Planning

The treatment planning was performed with two opposite beams. A series of preliminary calculations were performed in order to assess the best configurations and energy, using ideal beams of 1 or 10 keV, and with 1 or 2 beam ports. The results demonstrated that the most useful energy is around 1 keV with two beam ports. Figure 4.38 shows the position of the beams.

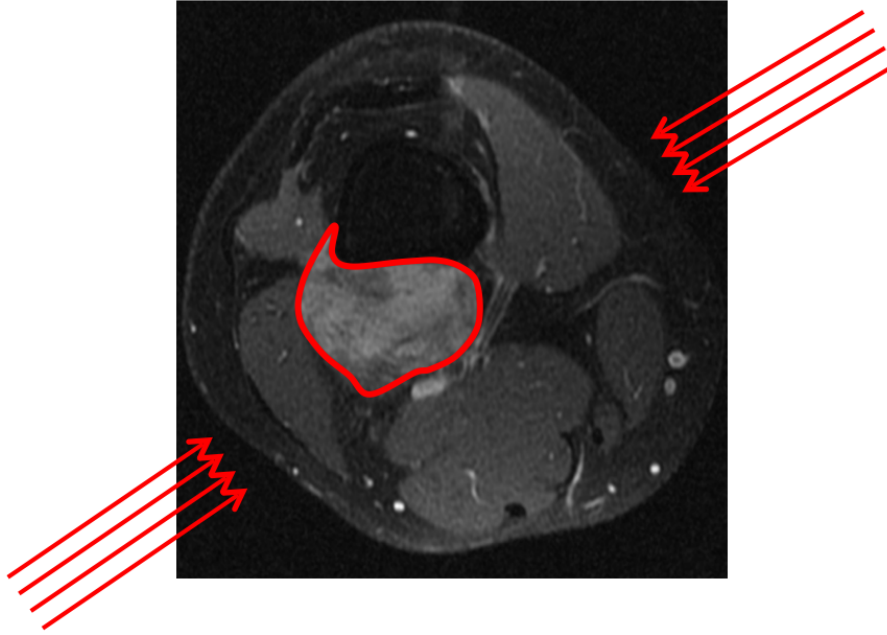


Figure 4.38: Treatment planning beam direction. The treatment is divided in 2 fractions as indicated by the red arrows.

Figure 4.39 shows four DVH response of the four BSA configurations described in Section 4.6. Configurations 2 and 3 are very interesting, since the equivalent dose to the tumor is around 80 Gy for both beams. Configurations 1 and 4 are not as effective as 2 and 3 in depositing dose inside the cancerous tissue. Taking another point of view, Figure 4.40 shows the performance of the beams on a radar plot. The parameters that are shown are the minimum and maximum dose to the tumour, the maximum dose in soft tissue and the maximum dose to the skin. All the graphs coincide on the maximum dose to the skin since the treatment plan has this constraint. Once again, beams 2 and 3 show a very similar behaviour.

Figure 4.41 shows the equivalent dose in MIRD organs normalized to the maximum treatment time calculated with the dose limit to be delivered to skin. Regarding peripheral dose, the most advantageous beams are 1 and 4, that have a better neutron suppression compared to beam 2 and 3, as shown in Figure 4.42. Anyhow, all of the tested beam deliver dose to the considered organs well below the tolerance dose. Table 4.15 shows the dose deposited in

4.7. Beam efficiency clinical cases comparison

all the organs of the MIRD phantom.

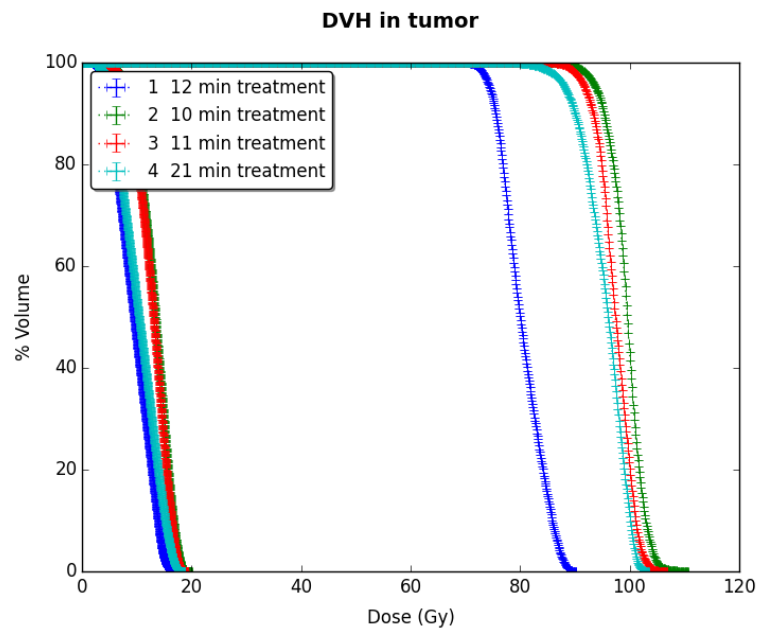


Figure 4.39: Dose to Volume Histograms of BNCT treatments with the beams shown in Table 4.13.

4. Design of an epithermal neutron beam for limb osteosarcoma

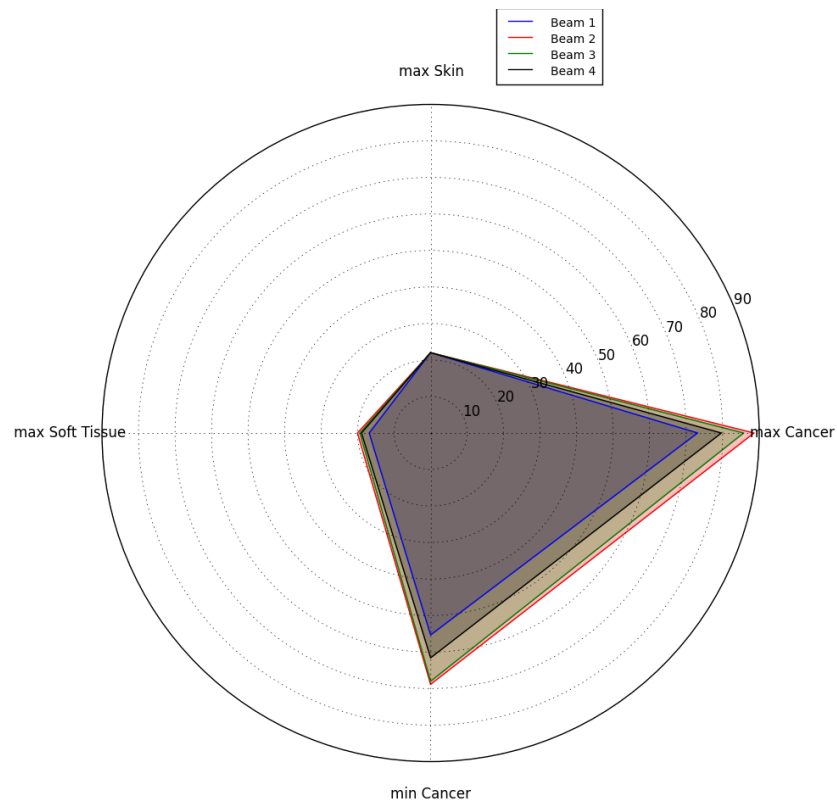


Figure 4.40: Radar plot of the equivalent dose in skin (maximum), soft tissue (maximum) and tumour (maximum and minimum) for the beams shown in Table 4.13.

4.7. Beam efficiency clinical cases comparison

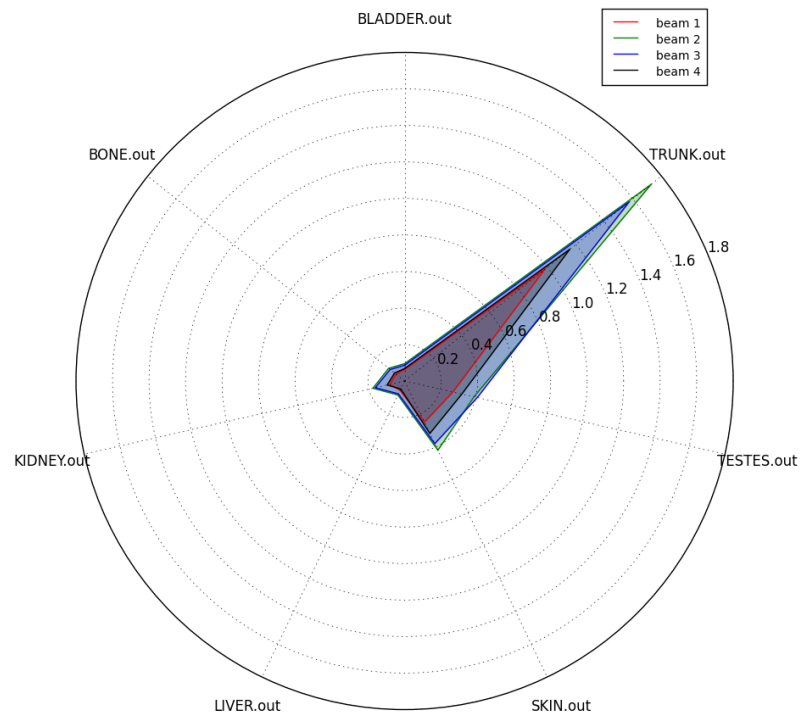


Figure 4.41: Radar plot of the equivalent dose to MIRD phantom organs (Bladder, Bone, Kidney, Liver, Skin, Testes, Trunk) for the beams shown in Table 4.13.

4. Design of an epithermal neutron beam for limb osteosarcoma

Table 4.15: MIRD phantom dose evaluation (Gy-eq) to organs after a BNCT treatment.

Organ	beam	beam	beam	beam
	1	2	3	4
	(Gy-eq)	(Gy-eq)	(Gy-eq)	(Gy-eq)
Adrenals	2.35E-02	5.33E-02	5.24E-02	3.34E-02
Bladder	6.30E-02	9.49E-02	8.61E-02	6.81E-02
Bone marrow	6.15E-02	1.12E-01	1.01E-01	7.02E-02
Brain	5.20E-03	5.91E-03	6.78E-03	3.57E-03
Head	2.15E-02	2.61E-02	2.26E-02	1.60E-02
Kidney	8.34E-02	1.78E-01	1.65E-01	9.82E-02
Large intestines	7.33E-02	1.15E-01	1.07E-01	7.78E-02
Liver	5.71E-02	8.52E-02	7.81E-02	4.88E-02
Lung	3.68E-03	9.42E-03	7.84E-03	5.40E-03
Pancreas	6.74E-02	1.13E-01	1.13E-01	7.35E-02
Pharynx	4.84E-02	1.13E-02	1.03E-02	1.83E-02
Skin	2.51E-01	4.21E-01	3.81E-01	3.19E-01
Small intestines	1.93E-01	3.17E-01	3.04E-01	2.07E-01
Spleen	6.92E-02	1.22E-01	9.74E-02	6.51E-02
Stomach	2.93E-02	4.97E-02	4.21E-02	2.53E-02
Testes	2.71E-01	3.90E-01	4.08E-01	3.22E-01
Thymus	1.27E-02	2.18E-02	1.61E-02	1.20E-02
Thyroid	9.41E-03	1.09E-02	3.01E-03	1.24E-02
Trunk	9.85E-01	1.73E+00	1.57E+00	1.16E+00

4.7. Beam efficiency clinical cases comparison

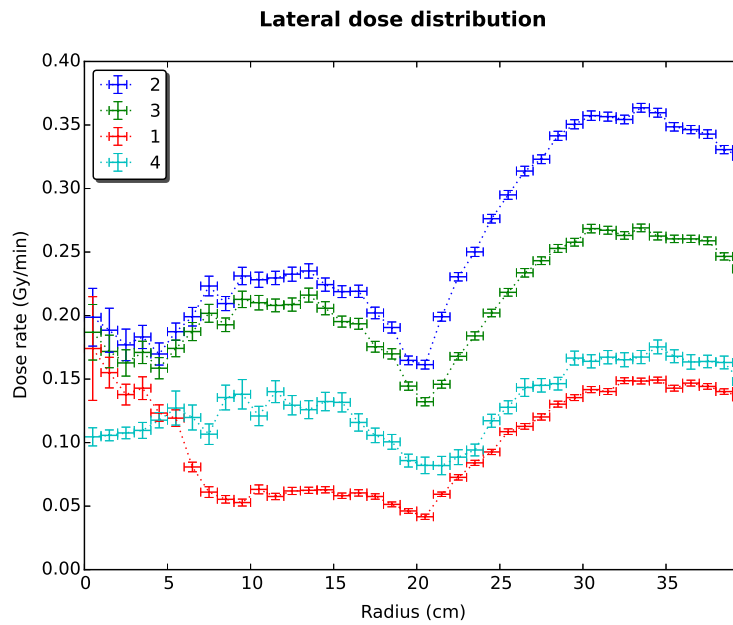


Figure 4.42: Radial dose profile at the beam port for the beams shown in Table 4.13.

Table 4.16: Computed FOM and clinical results of the beams listed in Section 4.6.

Neutron source	ϕ_{epi} ($10^9 \text{ cm}^{-2} \text{ s}^{-1}$)	$\frac{D_f}{\phi_{epi}}$ (10^{-13} Gy cm^2)	$\frac{D_\gamma}{\phi_{epi}}$ (10^{-13} Gy cm^2)	T (min)	minimum D_T Tumour (Gy)	maximum D_S skin (Gy)	$\frac{\text{Max } D_T}{\text{Min } D_T}$
1	2.6	7.1	6.3	13	55.3	22	1.33
2	2.8	8.9	3.7	10	68.8	22	1.29
3	2.6	9.0	3.9	11	68.0	22	1.26
4	1.6	10.0	2.7	19	61.6	22	1.29

The results of this section are summarized in Table 4.16, showing table shows the in air figures of merit compared to the: treatment time, minimum dose to the tumour, maximum dose to the most sensible organ and the rate of minimum and maximum dose to the tumour. The latter parameter gives a numerical interpretation to the steepness of the DVH slope. It is commonly accepted that a steeper slope, representing the uniformity of dose distribution in tumour, generally recognized as a success factor for the treatment outcome. The most performing beam for clinical BNCT treatment of osteosarcoma is the configuration beam 2. This beam has the highest minimum dose delivered to the tumour when setting the treatment time to cope with the maximum tolerable dose to the skin.

4.8 INFN RFQ epithermal beam V.S. ideal 1 keV beam

In this chapter it is shown that, from the 5 MeV proton interaction on a beryllium target, a performing epithermal beam was tailored. This was achieved by using a bulk layer of aluminium fluoride (35.5 cm) enclosed in 2 layers of lithium fluoride of 0.5 cm each finalized with Titanium and Bismuth layer. The reflecting material surrounding the neutron source was chosen to be aluminium fluoride, while the shielding is filled with lead. The entire beam is then coated with a 3 cm layer of lithium carbonate while externally to the beam there is a 15 cm layer of graphite, as shown in Figure 4.34. The performances of this beam, measured at the beam port, are shown in:

Figure 4.43 : Isodose curves;

Figure 4.44 : Neutron energy spectra;

Figure 4.45 : Photon energy spectra;

Figure 4.46 : Radial neutron flux profile;

Figure 4.47 : Radial photon flux profile.

It is interesting to compare the clinical DVH outcome of the chosen epithermal beam with the an ideal 1 keV neutron beam. This check was performed by simulating the an ideal neutron spectra with a mono-energetic peak at 1 keV all directed along the beam axis. Together with this ideal beam a the photon source of beam 2 was used to compute this analysis. The outcome of this comparison is shown in Figure 4.48, it is straight forward that the ideal beam is indeed more performing than the tailored one. Anyhow an other information can be deduced from the latter result, Despite the mono-energetic energy spectra of the ideal beam, the treatment time is limited to 12 min. This is the time to stay beneath the tolerable dose to the skin, which in this case is mainly due to photons. Consequently future improvements in the tailoring of

the INFN-RFQ epithermal neutron beam may come from the reduction of the photon component.

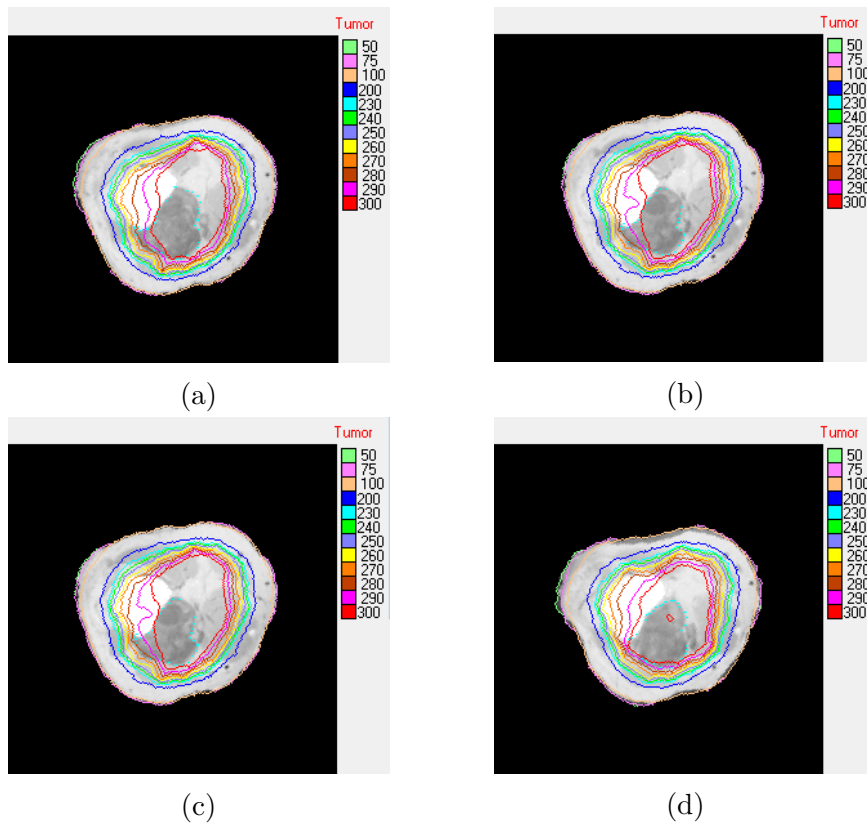


Figure 4.43: Tumor isodose curves. They represent the percentage of dose that the tumour receives with respect to the global maximum delivered to normal tissues. The four images show different sections of the treated volume and the isodose that contains the tumour is the 280% circle.

4.8. INFN RFQ epithermal beam V.S. ideal 1 keV beam

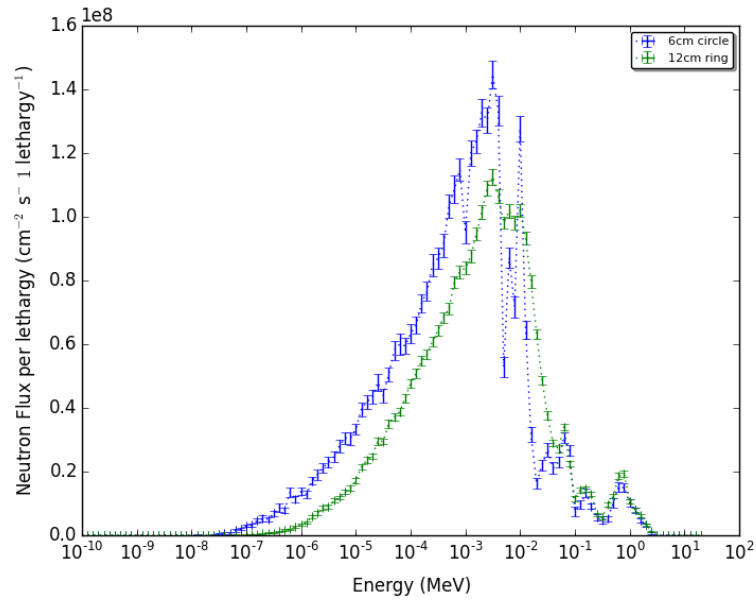


Figure 4.44: Neutron energy spectrum of the most performing epithermal beam. These graphs shows the spectrum of the central circle of the BSA (blue data) compared to the spectrum in the external ring (green data).

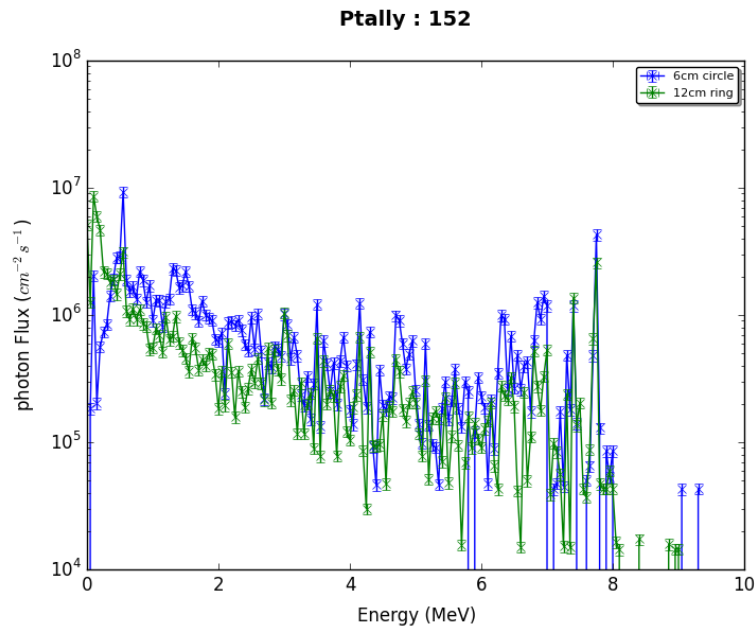


Figure 4.45: Photon energy spectrum of the most performing epithermal beam. This graphs shows the spectrum of the central circle of the BSA (blue data) compared to the spectrum in the external ring (green data).

4. Design of an epithermal neutron beam for limb osteosarcoma

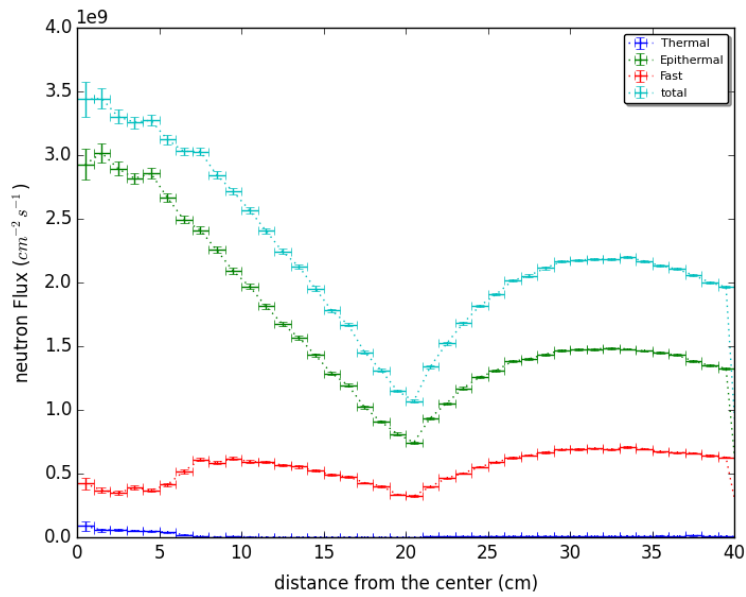


Figure 4.46: Radial neutron flux distribution computed at the beam port.

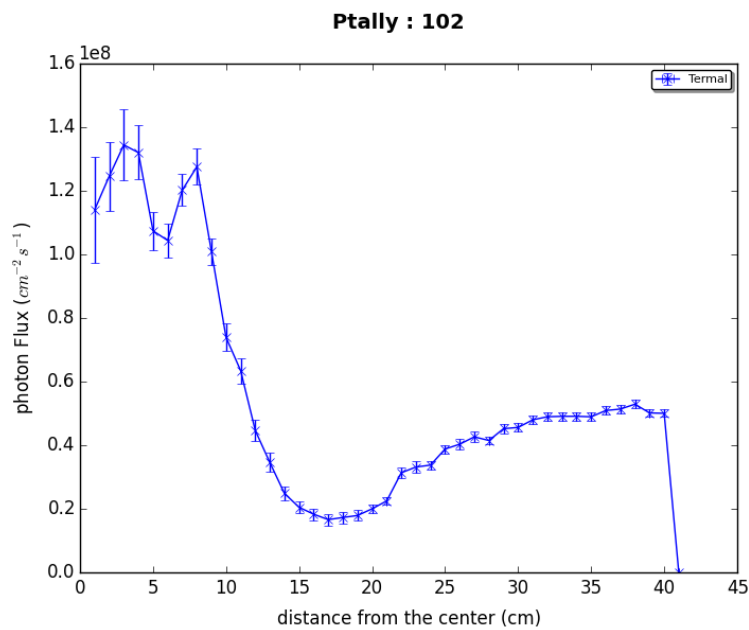


Figure 4.47: Radial photon flux distribution computed at the beam port.

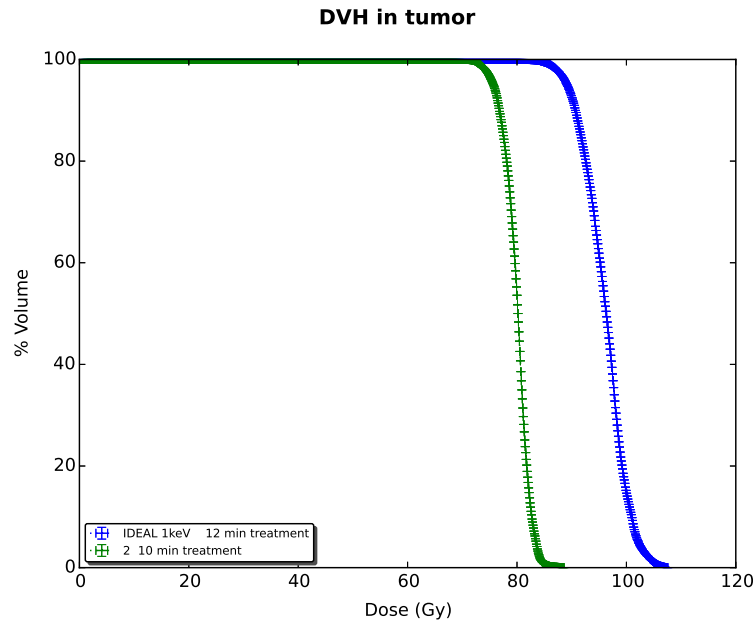


Figure 4.48: Radial neutron flux distribution computed at the beam port.

What emerges from this analysis is that the evaluation of the figure of merit related to the physical parameters are not exhaustive for the evaluation of an epithermal beam for clinical BNCT. the IAEA guidelines for the tailoring of a BNCT beam should be taken as a reference to reach a good quality, but the dosimetric assessment on realistic clinical scenarios are a more powerful tool to chose a configuration. In particular, depending on the type of tissues involved, on the type and location of tumour, beam that not comply perfectly with these requirements may provide advantageous dosimetry in clinical application. This highlights the necessity to develop other methods for epithermal beam evaluation, a possibility may be to probe the tailored beam on standardized clinical cases. Recent international collaborations have been established in order to compare the performances of different beams, based on reactors and/or accelerators, following this criteria.

Chapter 5

Conclusions and future perspectives

Multiple fields of BNCT were treated in this dissertation. The first part of this work was devoted to upgrade the autoradiography set-up for the measurements of boron concentration in tissue and liquid samples. The technique was optimized by changing the etching conditions, which in change decreased procedure time and at the same time reduced the proton track contamination. The calibration curve obtained using standard samples with known boron concentration is satisfactory since the relative error of the slope is lower than the error affecting the measurement of each sample. This calibration was then used in combination with a complete image scan of the sample. The position of each sub-image inside the tissue section is known and from this knowledge it was possible to reconstruct the boron concentration map within the sample. This information is particularly interesting in BNCT because it gives an insight in the micro-distribution of boron in tissues that, in turn, leads to a more precise dosimetry. In the past few years it has been highlighted that a homogeneous distribution of boron in tumour might play an important role for the positive outcome of BNCT. This evidence suggests that it is important not only to develop a new drug ensuring higher tumor to tissue boron concentration ratio, but also a low intra-tissue variability of ^{10}B content within the tumor mass and healthy tissue.

This method was applied to measure cell cultures samples, treated with boron. In particular, UMR-106 Osteosarcoma cells were cultured in presence of BPA and new boronated formulations. During this work the autoradiography results were compared to the one of alpha spectrometry ¹. This inter-comparison was then extended to boron measuring techniques used by the Argentinian BNCT group working at CNEA. This collaboration successfully ended in a publication showing that the techniques are in good agreement, supporting that they are all suitable for the determination of boron concentration

¹which is another technique for ^{10}B concentration measurement used in Pavia

in biological samples.

To date, no non-invasive online methodology to estimate boron concentration in patients during BNCT has been set-up, apart from PET mediated by fluorinated BPA. This technique has still the limitation that cannot provide precise concentration measurements, but it only gives information on gross boron concentration ratios between tumor and healthy tissues. Thus, the clinical trials are based on the assumption that the tissue boron values for a particular patient can be directly extrapolated from blood boron concentration. Waiting for the development of new *in-vivo* boron measurement techniques as MRI guided boron imaging or SPECT BNCT taking advantage of the gamma emitted from Li7 dis-excitation, neutron autoradiography allows obtaining more precise results and it may be useful also in clinical BNCT because bioptic samples could be analysed. On the other hand, also concentration in blood represents an important knowledge for external BNCT irradiation, because neutron capture in boron could damage the blood vessels. For this reason, the autoradiography technique was employed to measure samples of blood mixed with BPA at known concentrations, prepared by forming strips on the CR-39 surface, the result of this first attempt are still under analysis.

The experiments performed during this dissertation work, show that osteosarcoma cells uptake boron if exposed to some of the new boronated formulations tested, in particular, the most promising values were obtained with liposomes loaded by LCBO. Further experiment are needed in order to confirm the observed cell behaviour. On the other hand, experiments *in-vivo*, with a rat model bearing knee osteosarcoma and treated with BPA, shows that with an intraperitoneal injection, after 4 hours a tumour to normal tissue ratio of 4 is achieved, with high absolute concentration in tumour. Neutron autoradiography was proved to be a powerful tool to analyse both liquid and solid biological samples and will be routinely employed by BNCT research group working at University of Pavia.

Osteosarcoma cell line has been employed to assess survival curves as a function of the absorbed dose in case of irradiation with photons, with neutrons and with neutrons in presence of BPA. These information are then used to evaluate the Compound Biological Effectiveness (CBE) of the boronated formulation as well as the Relative Biological Effectiveness (RBE) factor for the used beam. The CBE factors are used in clinical BNCT to express the absorbed physical dose in photon equivalent dose. This is useful since it enables to compare clinical BNCT results with conventional radiotherapy. Anyhow, these CBE values are being questioned along with the entire dosimetric evaluation of BNCT. Indeed a new paradigm is needed to evaluate the energy deposited in biological matter of the complex mixed radiation field. A possible model for a more refined BNCT dosimetry has been proposed by Gonzalez and Santa Cruz [142]. In the work performed for this dissertation there was no attempt to develop a new dosimetry for BNCT. Anyhow in Chapter 3 some simulations were performed to evaluate the energy deposition and nucleus hit

probability at cellular level. This work was performed by trying to reproduce realistic cell and tissue geometries along with various boron distributions at cellular level. It resulted that the energy deposition in the cell nucleus is highly dependent on the position of boron. When boron concentrates outside the cell the mean energy deposited in the nucleus is less than 500 keV, while if boron uniformly distributes inside the cell the mean energy deposited in the nucleus is greater than 1 MeV. The results of these simulations is that the nucleus hit probability and energy deposit depends both on the cell morphology and boron distribution at cellular level. Anyhow this work can be further improved by using real three dimensional images to represent the cellular and tissue morphology. Moreover the nuclear energy deposition and hit probability can be used in a micro-dosimetric model to compare in-vitro survival curves to the simulated ones.

The last issue covered in this work is the tailoring of an epithermal neutron beam from the accelerator neutron source. It has been shown that the most performing way to moderate neutrons, yielded by 5 MeV protons on a beryllium target, towards the epithermal energy range is aluminium fluoride. This material is capable of reducing the fast neutron component of the ${}^9\text{Be}(p,n){}^9\text{B}$ reaction without accumulating neutrons in the thermal energy range. The objective of the BSA was to accumulate neutrons from 1 keV to 10 keV which results to be the optimal energy range for the treatment of deep seated tumours such as lung tumours and osteosarcoma. The neutron peak at 1 keV was increased by using mixture of: titanium which absorbs neutrons in the range 20 to 100 keV, and lithium fluoride which is a good thermal and fast neutron absorber. In the development of the BSA special attention was put in reduction of the photon contamination. Therefore hydrogenous material was avoided and lithium fluoride was dosed to capture the thermal neutron component before it could yield to photon contamination through neutron capture reactions.

The development of the epithermal neutron beam was performed in the framework of the INFN project that lead to the development and production of a 30 mA and 5 MeV proton accelerator, yielding neutrons from the nuclear interaction on beryllium. This project aims to develop a accelerator based BNCT facility. To this end, it was decided not only to comply as much as possible with the standard recommendations for a BNCT beam, but also to evaluate the dosimetric performance through treatment planning simulations. It is in fact growing the idea that the physical parameters of the beams are not sufficient to decide if it would be optimal for a particular class of tumours. A wide collaboration is being established between different research group starting in Argentina, with the aim of comparing the performances of different beams, obtained from accelerators and reactors, for the same clinical cases. The figures of merit were used during the starting part of the project, to have a guideline for the development of the beam. The final beam selection was performed by simulating a clinical BNCT treatment with NTCPlan of a limb

affected by Osteosarcoma (OS). The clinical outcome where then compared through the computed equivalent dose and DVH of skin, soft tissue and neoplastic volume. In the case of OS the sensible organ is skin, consequently the treatments were all compared by imposing a limit on the maximum tolerable dose to the skin. The outcome of the treatment performed with different BSA did not comply with all the IAEA FOM guidelines. The treatment planning simulations demonstrated that in some cases worst quality in terms of IAEA figures of merit leads to better dosimetric distributions. For example, a beam with a higher fast neutron component led to a better tumour irradiation if compared to a beam that matched better the requirements. In this work it was noticed that an epithermal energy spectra with distinct peak around 1 keV is more effective than a beam with a distributed peak ranging from 0.5 eV to 10 keV. Consequently, a parameter that indicates the mean energy of an epithermal beam might be more efficient guideline for the development of an epithermal neutron beam aiming to clinical BNCT treatment after a complete study on representative clinical cases of tumours located in different parts of the body.

Even though BNCT has not been widely employed yet to treat cancers, in the next future it could become a viable option for all those diseases that are radio resistant and metastatic, not excluding the application of BNCT as adjuvant therapy of the presently used techniques. This dissertation shows how an accelerator-based neutron source can be adapted for the BNCT treatment of Osteosarcoma. The results are very encouraging also from the treatment planning standpoint, as shown by the treatment computed DVH. Nevertheless, to pursue the goal of a BNCT clinical facility it is essential to engage a broad collaboration with medical centres.

Appendix A

A - MCNP: Monte Carlo Code

MCNP stands for Monte Carlo Neutron Particle transport code. The version used in this dissertation is MCNP6 which is the evolution of MCNP5 and MCNPX. This transport code is able to simulate nuclear interactions of neutrons with matter on a wide energy range and it is widely used in the framework of BNCT neutron source development. In this appendix some parts of the simulating code is shown. Therefore a brief introduction to MCNP and it's input file is needed. To simulate the transport of neutrons with MCNP and ASCII file is needed to describe the "world" where the code will generate, transport neutrons and collect information. This text file is divide in three regions each separated by a vertical space as shown below: Cell definitions, Surface definitions and Cards.

```
This is a Title
c First Region - Cell definition
1 1 -1 -10 imp:n=1$ Simulating world
2 0 10 imp:n=0 $external World

c Second Region - Surface definition
10 rpp -10 10 -10 10 -10 10 $ cube of 20cm side

c Third Region - Card definition
c Materials
m1 1001 2
    8016 1
c default source card
SDEF
c tally card
f2:n 1.6
e2 1e-10 99log 10
c simulation characteristics
mode n
nps 1e6
```

The cell definition region is where the geometrical world is defined and is commonly called universe. To perform this action the surfaces defined in the second region are used along with the materials implemented in the third region. In the example above there are two cells defined, one is the world where neutrons are transported while the other is the region where the transport stops. The implementation of a cell starts by defining the "name" of the cell by giving a number. The second argument should be a number greater than 0, to recall a material defined in the third region, followed by a third argument that defines its density. If no material has to be associated to a cell the

second argument should be 0 and there is no need to define the associated density. Once the material is defined the code needs to know which region of the universe has to be filled, this is done by recalling the number that defines a certain surface. In this example surface 10 is used, so in cell 1 -10 is specified as 4th. The minus sign tells the code to fill with material 1 the inner part of surface 10. On the other hand cell 2 fills with void the outer region of surface 10. Finally the last argument is imp:n which tells the code what is the importance of that cell for neutrons. The world where the simulations will be performed has a neutron importance greater than 1, while the rest of the universe will have importance 0.

The Surface definition is in the second region. Each kind of surface has its own card, in the example above rpp is a macrobody that describes a rectangular parallelepiped of 20 cm side centred in (0 0 0). More surface definition cards are shown in MCNP's user manual. Though, generally a surface is defined by giving a "name" which is a number greater than zero followed by the card of the wanted surface. This card will then be followed by arguments needed to define the position and or the dimensions of the surface in space.

The last region of MCNP's input file is where: the materials, the neutron source, the physics and tallys are defined. Following the order seen in the previous example, material are defined by the card m followed by a number. This number is then used to define materials in a cell. The atomic composition of materials is then characterized by specifying the A00Z number, where A is the atomic number while Z is the mass number of the wanted atom. Each element is then followed by a number, if that number is positive it represents the atomic composition. Else if the number is negative it describes the material mass composition. After the material card the SDEF card appears, this time without arguments. This means that the example uses the default source card. This card generates an isotropic neutron point source in (0,0,0) with 14 MeV energy. The next card is a tally, the region of the world where data is collected. In this case the tally is number 2 which collects the neutron flux at the surface. This tally card is followed by the energy card, which is interrelated to the tally card with its number. So the meaning of this tally is to collect the neutronic flux through surface 1.6 as a function of the energy going from 10e-10 MeV till 10 MeV with 99 logarithmic steps. Finally the simulations characteristics are defined, imposing to MCNP the simulation of neutron (mode n) and generating one million particles from the SDEF source (nps 1e6).

A.1 MCNP $^9\text{Be}(p,n)^9\text{B}$ neutron source

```

c      9Be(p,n)9B point like neutron source
c
c      yielding directions:      180,160,130,120,110,100,95,90
c                                85,80,70,60,50, 40, 30, 20,10, 0
c
c
si4    A  -1 -0.98481 -0.866
        -0.6428 -0.5 -0.342 -0.17365 -0.087156 0 0.087156
        0.17365 0.342 0.5 0.6428 0.766 0.866 0.9397
        0.98481 1

```

A.1. MCNP $^9\text{Be}(\text{p},\text{n})^9\text{B}$ neutron source

```

c
c   yileding direction probability (% total)
sp4  5.5130168453 5.5130168453 5.5130168453
      5.6151097499 5.5640632976 5.5130168453 5.4619703931
      5.3088310362 5.1556916794 5.1301684533 5.1046452272
      4.8494129658 4.5941807044 5.6661562021 6.7381316998
      7.6569678407 8.5758039816 9.213884635 9.8519652884

c
c   source spectra in 18 yileding directions
c
ds5 S 39 40 41 31 31 32 32 33 33 34 34 35 35 36 36 37 37 38
c
c   energy bin (MeV) and yielding
c
c   -----*-----*-----*-----*-----*-----*-----*-----*
si39  0.298 1.819
sp39  0 1
si40  0.298 1.942
sp40  0 1
si41  0.298 2.065
sp41  0 1
si31 A 0.298 0.328 0.358 0.391 0.426 0.464 0.503
      0.543 0.585 0.627 0.67 0.714 0.758 0.802
      0.847 0.891 0.936 0.982 1.027 1.074 1.12
      1.166 1.212 1.259 1.306 1.353 1.4 1.448
      1.495 1.542 1.59 1.638 1.685 1.733 1.781
      1.829 1.877 1.925 1.973 2.021 2.069 2.118
sp31  114600 90240 99160 117300 125500 132300 129900
      129300 127900 125300 121900 117900 114100 111200
      110000 110800 113000 115900 118200 121000 123800
      127300 131700 137700 144300 151300 158700 166500
      172700 177000 178900 177700 173100 165500 152700
      132300 106400 78360 51220 27620 9915 170.783
si32 A 0.298 0.328 0.358 0.391 0.426 0.464 0.503
      0.543 0.585 0.627 0.67 0.714 0.758 0.802
      0.847 0.891 0.936 0.982 1.027 1.074 1.12
      1.166 1.212 1.259 1.306 1.353 1.4 1.448
      1.495 1.542 1.59 1.638 1.685 1.733 1.781
      1.829 1.877 1.925 1.973 2.021 2.069 2.118
      2.166 2.214 2.263 2.311
sp32  38440 30970 71370 120000 148300 148800 147900
      144700 141400 137000 130800 124100 118300 114000
      111500 110800 111500 112800 113500 114500 115400
      116000 116800 118400 120200 121700 122600 123700
      124200 124400 124900 125900 126700 127900 128300
      127900 126100 122500 115800 103600 85980 65280
      43680 24090 8909 119.127
si33 A 0.263 0.297 0.331 0.37 0.411 0.454 0.499
      0.545 0.592 0.639 0.687 0.736 0.785 0.834
      0.883 0.933 0.983 1.034 1.084 1.135 1.185
      1.237 1.288 1.339 1.391 1.442 1.494 1.546
      1.598 1.65 1.702 1.754 1.806 1.858 1.91
      1.963 2.015 2.067 2.12 2.172 2.225 2.277
      2.33 2.383 2.435
sp33  51530 48330 74410 102900 115500 127600 133000
      133600 131700 128600 124700 120800 117400 114700
      113000 111900 110600 109400 108400 107700 107200
      107400 107900 108400 108800 108600 108200 108000
      107700 107500 106900 106000 104500 102800 100500
      97220 91520 84190 74040 61470 47220 32570
      18750 8621 1594
si34 A 0.298 0.328 0.358 0.391 0.426 0.464 0.503
      0.543 0.585 0.627 0.67 0.714 0.758 0.802
      0.847 0.891 0.936 0.982 1.027 1.074 1.12
      1.166 1.212 1.259 1.306 1.353 1.4 1.448
      1.495 1.542 1.59 1.638 1.685 1.733 1.781
      1.829 1.877 1.925 1.973 2.021 2.069 2.118
      2.166 2.214 2.263 2.311 2.359 2.408 2.456
      2.505 2.554
sp34  158000 126100 168400 177000 166400 151600 138900
      128000 119200 113000 109000 106200 104700 104200
      104300 104400 104300 103800 103200 103100 103000
      102700 102100 101000 99300 97370 95310 93220
      91060 89060 87150 85240 83360 81900 80420
      78790 76890 74750 72540 70120 66770 62240
      56430 49410 41120 32080 23130 14920 7958
      2861 57.499
si35 A 0.298 0.328 0.358 0.391 0.426 0.464 0.503
      0.543 0.585 0.627 0.67 0.714 0.758 0.802
      0.847 0.891 0.936 0.982 1.027 1.074 1.12
      1.166 1.212 1.259 1.306 1.353 1.4 1.448
      1.495 1.542 1.59 1.638 1.685 1.733 1.781
      1.829 1.877 1.925 1.973 2.021 2.069 2.118
      2.166 2.214 2.263 2.311 2.359 2.408 2.456
      2.505 2.554 2.602 2.651 2.699 2.748 2.797
sp35  129600 103700 137700 152700 167000 163600 161600
      156100 147800 137200 125500 117300 111900 106600
      102500 99910 98460 97630 96750 95970 95070
      93970 92570 90720 88310 85420 82210 78820
      75300 71730 68210 64820 61510 58400 55610
      53160 51130 49280 47590 46060 44680 43550

```

```

42440 41530 40680 39570 37860 34730 30330
25240 19760 14260 9224 4932 1779 35.616
si36 A 0.298 0.328 0.358 0.391 0.426 0.464 0.503
0.543 0.585 0.627 0.67 0.714 0.758 0.802
0.847 0.891 0.936 0.982 1.027 1.074 1.12
1.166 1.212 1.259 1.306 1.353 1.4 1.448
1.495 1.542 1.59 1.638 1.685 1.733 1.781
1.829 1.877 1.925 1.973 2.021 2.069 2.118
2.166 2.214 2.263 2.311 2.359 2.408 2.456
2.505 2.554 2.602 2.651 2.699 2.748 2.797
2.845 2.894 2.942 2.991
sp36 205800 165700 263000 318200 285700 257000 223400
211400 198900 181300 163100 149100 134400 122000
111900 104800 99920 96550 93870 91640 89650
87800 86070 84540 83100 81650 80080 78430
76640 74840 73120 71460 69840 68480 67350
66440 65790 65440 65320 65630 66600 68330
70330 72880 76400 80650 85440 90830 95620
100200 103100 103600 100100 90670 76600 59140
40280 22660 8370 52.247
si37 A 0.298 0.328 0.358 0.391 0.426 0.464 0.503
0.543 0.585 0.627 0.67 0.714 0.758 0.802
0.847 0.891 0.936 0.982 1.027 1.074 1.12
1.166 1.212 1.259 1.306 1.353 1.4 1.448
1.495 1.542 1.59 1.638 1.685 1.733 1.781
1.829 1.877 1.925 1.973 2.021 2.069 2.118
2.166 2.214 2.263 2.311 2.359 2.408 2.456
2.505 2.554 2.602 2.651 2.699 2.748 2.797
2.845 2.894 2.942 2.991 3.04 3.089 3.138
sp37 99170 79918.8 128122 214508 235282 226634 235564
236598 228044 212628 192042 169764 150306 134984
123892 116466 111108 106596 102366 98230 94376
90644.2 87344.8 84543.6 82212.4 80266.6 78781.4 77879
77409 77333.8 77672.2 78386.6 79411.2 80990.4 82992.6
85474.2 88557.4 92289.2 96350 100768 105374 110450
115902 121918 129062 136206 143538 151904 159800
168354 177002 183206 187342 185368 177472 161398
138368 111390 82438 54491.8 29816.8 10922.8 213.6432
si38 A 0.298 0.328 0.358 0.391 0.426 0.464 0.503
0.543 0.585 0.627 0.67 0.714 0.758 0.802
0.847 0.891 0.936 0.982 1.027 1.074 1.12
1.166 1.212 1.259 1.306 1.353 1.4 1.448
1.495 1.542 1.59 1.638 1.685 1.733 1.781
1.829 1.877 1.925 1.973 2.021 2.069 2.118
2.166 2.214 2.263 2.311 2.359 2.408 2.456
2.505 2.554 2.602 2.651 2.699 2.748 2.797
2.845 2.894 2.942 2.991 3.04 3.089 3.138
3.186
sp38 84790 69520 237900 266000 270600 266900 256700
254800 227700 189200 165800 141800 128800 120100
115100 113100 111400 109700 107700 105300 102500
98950 95270 91980 89420 87450 85840 84580
83640 83290 83850 85270 87270 90110 93570
97560 101900 106500 111200 116200 121900 129000
136500 145100 155100 165600 177400 190400 202600
215100 226400 234000 238700 237300 229000 210000
183100 152200 118900 86040 55620 29810 10640
21.166
c ccccccccccccccccccccccccccccccccccccccc
c sdef end
c ccccccccccccccccccccccccccccccccccccccc

```

A.2 MCNP neutron source at beam port

Transporting and moderating neutrons from the source till the beam port is a time consuming process to perform with a Monte Carlo transport code. Therefore it would be interesting to implement an MCNP neutron source at the beam port for the treatment planning simulation. To perform this with good accuracy it is important to reproduce the achieved neutron moderation as good as possible through the SDEF. With this "function" of the MCNP code it is possible to implement a particle source, some explanation of this card will be covered later in this section. Before starting the implementation of the neutron source it is trivial to study the neutron spectra at the beam port. To perform this a surface tally was placed at the beam port and this surface was then sectioned by 41 cylinder with increasing radius, 1 cm at a time. On this 40 circular rings the energy spectra was measured for 21 neutron exiting angles

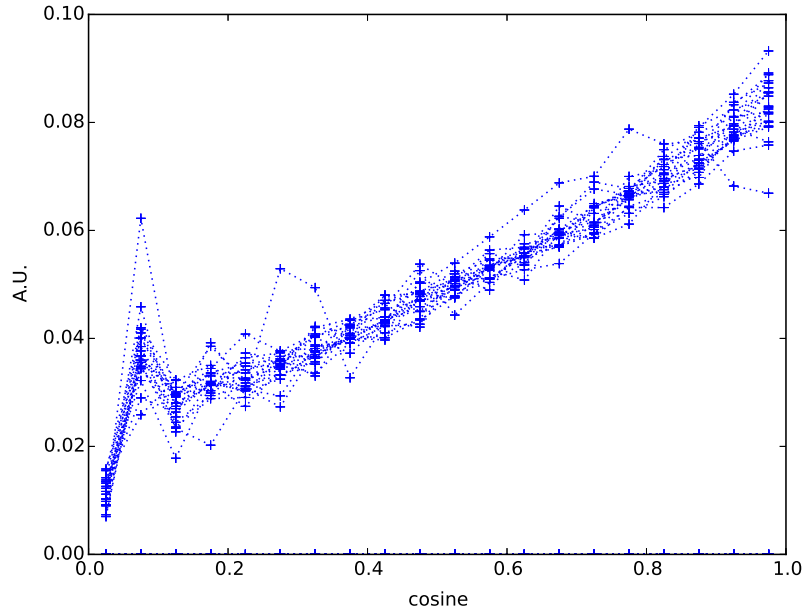


Figure A.1: Neutron emission direction from the beam axis. Each line represents the neutron energy spectra on a section of a circle between a radius $r1$ and a radius $r2$.

with respect to the beam axis: one is the backward direction from -1 to 0 as $\cos(\theta)$ and the other 20 bins divide the forward direction from 0 till 1 in equal $\cos(\theta)$ bins.

The neutron exiting direction along the beam port plane is shown in Figure A.1, which shows the difference in the angular probability distribution for each annular. From the plot it is clear that the emission angle doesn't have a strong dependence along the beam port plane. Consequently the neutron source distribution for the emission angle can be assumed to be one. On the other hand, Figure A.2 shows the neutron energy spectra for each emission angle on a single annular. It is clear that there is no dependency between emission angle and energy spectra, this simplifies the neutron source definition. The last check that was performed is the dependency between neutron energy spectra and annular position, Shown in Figure A.3. From which is clear that there are two distribution along the beam port plane. The separation of these two spectra is at the ring going from 7 till 8 cm from the beam axis as shown in Figure A.4.

As a consequence it is safe to generate 2 neutron sources, one for the annular going from 1 till 7 cm and a second one for the annular starting at 7 cm and ending at 40 cm from the beam axis. The implementation of the SDEF MCNP source card is shown here:

```
sur=d1 rad=fsur d2 erg=fsur d3 dir=d4
s11 L 1071 1072
sp1 6.005e+00 7.980e+00
ds2 S 11 12
```

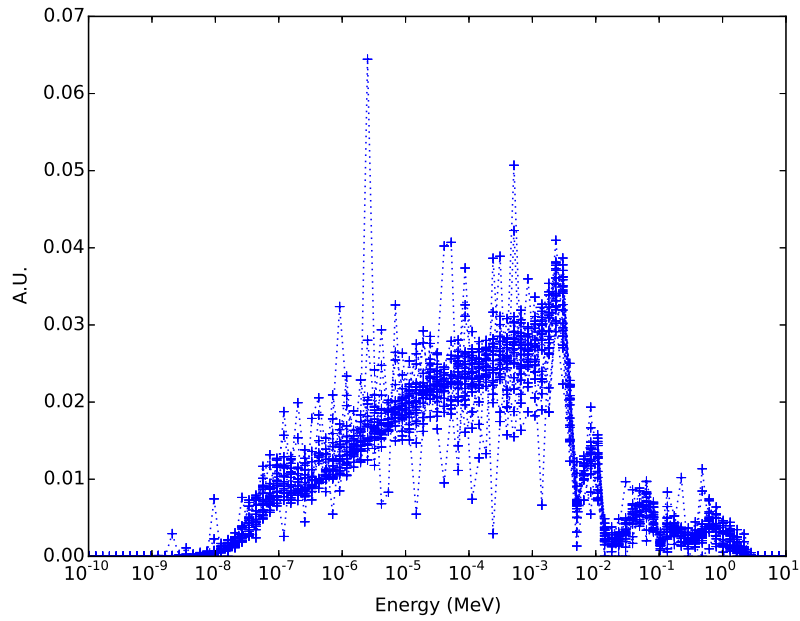


Figure A.2: Neutron energy Spectra at the beam port. Each line represents the neutron energy spectra for 20 emission angles between 0 and 90 with respect to the beam axis.

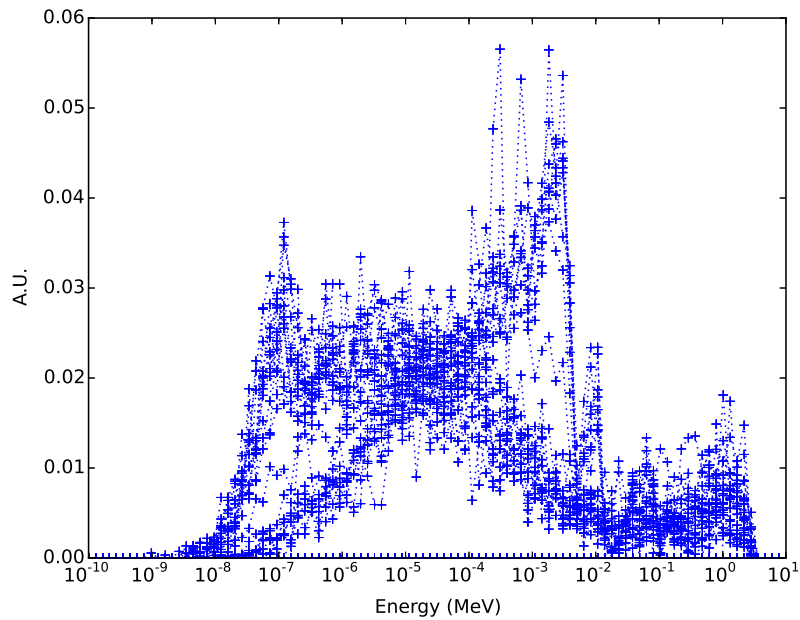


Figure A.3: Neutron energy Spectra at the beam port. Each line represents the neutron energy spectra on a section of a circle between a radius r_1 and a radius r_2 .

A.2. MCNP neutron source at beam port

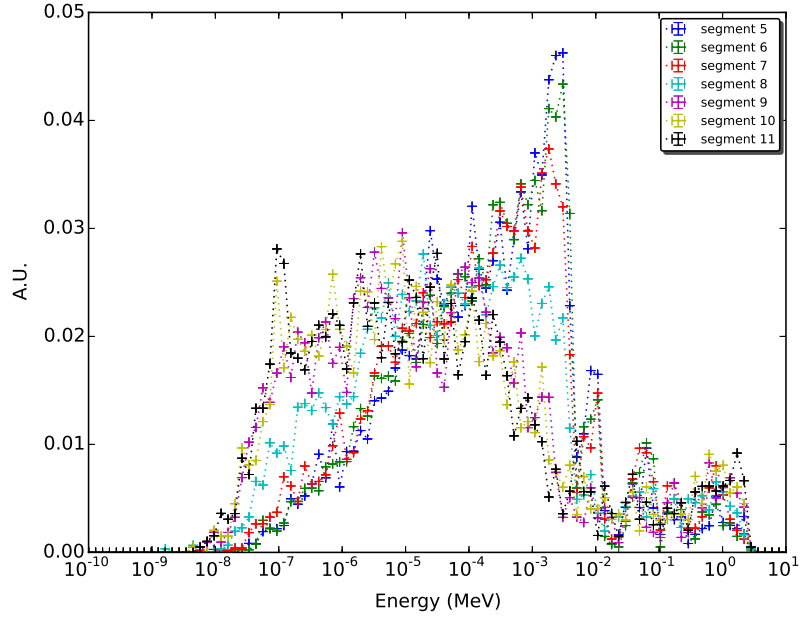


Figure A.4: Neutron energy Spectra at the beam port. The lines represented in this figures are for the annular going from 5 cm till 12 cm.

```

si11 A 0 0.5 1.5 2.5 3.5 4.5 5.5 6.5 7.5
sp11 0 7.087e-02 2.099e-01 3.305e-01 4.626e-01 5.746e-01 6.613e-01
5.600e-01 4.687e-01
si12 A 7.5 8.5 9.5 10.5 11.5 12.5 13.5 14.5
15.5 16.5 17.5 18.5 19.5 20.5 21.5 22.5
23.5 24.5 25.5 26.5 27.5 28.5 29.5 30.5
31.5 32.5 33.5 34.5 35.5 36.5 37.5 38.5 39.5
sp12 4.687e-01 4.176e-01 3.950e-01 4.068e-01 3.873e-01 4.025e-01 3.974e-01
4.111e-01 3.973e-01 3.795e-01 3.657e-01 3.326e-01 2.841e-01 2.308e-01
4.137e-01 5.461e-01 6.607e-01 7.695e-01 8.795e-01 9.508e-01 1.045e+00
1.125e+00 1.208e+00 1.257e+00 1.289e+00 1.347e+00 1.382e+00 1.414e+00
1.418e+00 1.449e+00 1.453e+00 1.463e+00 1.458e+00
ds3 s 21 22
# si21 si22
a a
0 0
5.000e-11 5.000e-11
1.130e-10 1.130e-10
1.422e-10 1.422e-10
1.790e-10 1.790e-10
2.254e-10 2.254e-10
2.837e-10 2.837e-10
3.572e-10 3.572e-10
4.496e-10 4.496e-10
5.661e-10 5.661e-10
7.127e-10 7.127e-10
8.972e-10 8.972e-10
1.130e-09 1.130e-09
1.422e-09 1.422e-09
1.790e-09 1.790e-09
2.254e-09 2.254e-09
2.837e-09 2.837e-09
3.571e-09 3.571e-09
4.496e-09 4.496e-09
5.661e-09 5.661e-09
7.127e-09 7.127e-09
8.972e-09 8.972e-09
1.129e-08 1.129e-08
1.422e-08 1.422e-08
1.790e-08 1.790e-08
2.253e-08 2.253e-08
2.837e-08 2.837e-08
3.571e-08 3.571e-08
4.496e-08 4.496e-08
5.661e-08 5.661e-08
7.126e-08 7.126e-08
8.972e-08 8.972e-08

```

1.130e-07	1.130e-07
1.422e-07	1.422e-07
1.790e-07	1.790e-07
2.254e-07	2.254e-07
2.837e-07	2.837e-07
3.571e-07	3.571e-07
4.497e-07	4.497e-07
5.661e-07	5.661e-07
7.126e-07	7.126e-07
8.971e-07	8.971e-07
1.129e-06	1.129e-06
1.422e-06	1.422e-06
1.790e-06	1.790e-06
2.253e-06	2.253e-06
2.837e-06	2.837e-06
3.571e-06	3.571e-06
4.497e-06	4.497e-06
5.661e-06	5.661e-06
7.127e-06	7.127e-06
8.972e-06	8.972e-06
1.129e-05	1.129e-05
1.422e-05	1.422e-05
1.790e-05	1.790e-05
2.254e-05	2.254e-05
2.837e-05	2.837e-05
3.571e-05	3.571e-05
4.497e-05	4.497e-05
5.661e-05	5.661e-05
7.127e-05	7.127e-05
8.972e-05	8.972e-05
1.130e-04	1.130e-04
1.422e-04	1.422e-04
1.790e-04	1.790e-04
2.253e-04	2.253e-04
2.837e-04	2.837e-04
3.571e-04	3.571e-04
4.497e-04	4.497e-04
5.661e-04	5.661e-04
7.127e-04	7.127e-04
8.971e-04	8.971e-04
1.129e-03	1.129e-03
1.422e-03	1.422e-03
1.790e-03	1.790e-03
2.253e-03	2.253e-03
2.837e-03	2.837e-03
3.572e-03	3.572e-03
4.497e-03	4.497e-03
5.661e-03	5.661e-03
7.127e-03	7.127e-03
8.972e-03	8.972e-03
1.129e-02	1.129e-02
1.422e-02	1.422e-02
1.790e-02	1.790e-02
2.253e-02	2.253e-02
2.837e-02	2.837e-02
3.571e-02	3.571e-02
4.496e-02	4.496e-02
5.661e-02	5.661e-02
7.126e-02	7.126e-02
8.972e-02	8.972e-02
1.130e-01	1.130e-01
1.422e-01	1.422e-01
1.790e-01	1.790e-01
2.253e-01	2.253e-01
2.837e-01	2.837e-01
3.571e-01	3.571e-01
4.496e-01	4.496e-01
5.661e-01	5.661e-01
7.127e-01	7.127e-01
8.972e-01	8.972e-01
1.129e+00	1.129e+00
1.422e+00	1.422e+00
1.790e+00	1.790e+00
2.253e+00	2.253e+00
2.837e+00	2.837e+00
3.571e+00	3.571e+00
4.496e+00	4.496e+00
5.661e+00	5.661e+00
7.127e+00	7.127e+00
8.971e+00	8.971e+00
1.129e+01	1.129e+01
1.422e+01	1.422e+01
1.790e+01	1.790e+01
# sp21	sp22
0	0
0.000e+00	0.000e+00
0.000e+00	0.000e+00
0.000e+00	0.000e+00
0.000e+00	0.000e+00
0.000e+00	0.000e+00
0.000e+00	0.000e+00
0.000e+00	0.000e+00

A.2. MCNP neutron source at beam port

0.000e+00	0.000e+00
0.000e+00	0.000e+00
0.000e+00	0.000e+00
0.000e+00	0.000e+00
0.000e+00	0.000e+00
0.000e+00	0.000e+00
0.000e+00	0.000e+00
0.000e+00	5.842e+04
5.814e+04	0.000e+00
4.107e+04	1.880e+05
0.000e+00	3.075e+05
2.555e+04	2.098e+05
4.413e+04	3.688e+05
0.000e+00	7.006e+05
4.043e+04	4.103e+05
1.014e+04	6.336e+05
1.109e+04	8.302e+05
5.544e+04	1.073e+06
5.546e+04	1.092e+06
6.173e+04	1.085e+06
1.453e+05	1.201e+06
1.737e+05	1.187e+06
1.977e+05	1.172e+06
1.669e+05	1.055e+06
1.273e+05	7.881e+05
1.686e+05	6.548e+05
1.121e+05	4.609e+05
1.174e+05	3.720e+05
9.441e+04	3.225e+05
8.718e+04	2.308e+05
6.055e+04	2.148e+05
6.218e+04	1.557e+05
4.520e+04	1.269e+05
4.304e+04	1.105e+05
4.032e+04	8.831e+04
3.051e+04	7.760e+04
3.018e+04	5.873e+04
2.679e+04	4.404e+04
2.117e+04	3.643e+04
1.900e+04	2.834e+04
1.557e+04	2.503e+04
1.234e+04	1.836e+04
1.036e+04	1.507e+04
8.308e+03	1.257e+04
7.120e+03	1.042e+04
5.986e+03	7.741e+03
5.136e+03	6.265e+03
4.093e+03	4.605e+03
3.522e+03	4.092e+03
2.815e+03	3.021e+03
2.353e+03	2.304e+03
2.015e+03	1.866e+03
1.593e+03	1.595e+03
1.278e+03	1.121e+03
9.927e+02	9.456e+02
8.125e+02	7.023e+02
7.088e+02	5.564e+02
5.712e+02	4.514e+02
4.789e+02	3.541e+02
3.961e+02	2.414e+02
2.992e+02	1.990e+02
2.857e+02	1.513e+02
2.053e+02	1.174e+02
1.832e+02	9.878e+01
1.227e+02	6.654e+01
1.196e+02	5.055e+01
9.926e+01	4.148e+01
7.995e+01	3.186e+01
6.329e+01	2.261e+01
5.890e+01	1.748e+01
4.018e+01	1.233e+01
1.138e+01	7.315e+00
1.594e+01	5.931e+00
1.005e+01	4.232e+00
1.616e+01	3.734e+00
5.823e+00	2.538e+00
2.197e+00	1.596e+00
7.920e-01	8.502e-01
8.760e-01	6.741e-01
9.111e-01	5.217e-01
6.831e-01	3.857e-01
4.746e-01	3.427e-01
6.445e-01	2.781e-01
4.255e-01	1.533e-01
6.067e-02	1.265e-01
6.938e-02	9.873e-02
8.127e-02	6.607e-02
4.836e-02	6.379e-02
2.223e-02	5.847e-02
1.075e-02	3.786e-02
1.591e-02	3.507e-02

```

2.321e-02 3.687e-02
2.412e-02 3.766e-02
2.631e-02 2.931e-02
1.028e-02 1.903e-02
8.605e-03 1.362e-02
4.229e-03 7.382e-03
2.314e-03 4.054e-03
4.262e-04 1.140e-03
2.233e-05 4.431e-05
0.000e+00 0.000e+00
0.000e+00 0.000e+00
0.000e+00 0.000e+00
0.000e+00 0.000e+00
0.000e+00 0.000e+00
0.000e+00 0.000e+00
0.000e+00 0.000e+00
0.000e+00 0.000e+00
si4 a -1 0 0.000e+00 2.000e-02 4.000e-02 6.000e-02 8.000e-02 1.000e-01
1.200e-01 1.400e-01 1.600e-01 1.800e-01 2.000e-01 2.200e-01
2.400e-01 2.600e-01 2.800e-01 3.000e-01 3.200e-01 3.400e-01
3.600e-01 3.800e-01 4.000e-01 4.200e-01 4.400e-01 4.600e-01
4.800e-01 5.000e-01 5.200e-01 5.400e-01 5.600e-01 5.800e-01
6.000e-01 6.200e-01 6.400e-01 6.600e-01 6.800e-01 7.000e-01
7.200e-01 7.400e-01 7.600e-01 7.800e-01 8.000e-01 8.200e-01
8.400e-01 8.600e-01 8.800e-01 9.000e-01 9.200e-01 9.400e-01
9.600e-01 9.800e-01 1.000e+00
sp4 0 0 0.000e+00 1.191e-04 3.096e-04 9.287e-04 1.500e-03 1.834e-03
1.977e-03 2.215e-03 3.001e-03 4.001e-03 4.120e-03 4.144e-03
5.120e-03 5.977e-03 7.025e-03 7.216e-03 7.716e-03 8.263e-03
1.007e-02 9.883e-03 1.131e-02 1.198e-02 1.265e-02 1.298e-02
1.419e-02 1.515e-02 1.686e-02 1.762e-02 1.831e-02 1.984e-02
2.043e-02 2.289e-02 2.315e-02 2.429e-02 2.555e-02 2.858e-02
2.934e-02 3.003e-02 2.958e-02 3.355e-02 3.605e-02 3.798e-02
3.829e-02 4.051e-02 4.206e-02 4.420e-02 4.679e-02 4.870e-02
5.144e-02 5.239e-02 5.789e-02

```

This neutron source definition was then implemented at the beam port surface and for validation it was compared to the transported neutron source from the beryllium target. This comparison is shown in Figure A.5 and it is clear that the implementation of the neutron source at the beam port was performed correctly. The same test was performed also for the photon component as shown in Figure A.6

```

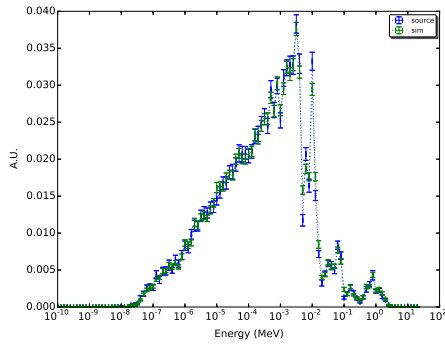
#!/usr/bin/python
# Filename: SDEF.py

import math
import numpy as np
import sys
import matplotlib.pyplot as plt

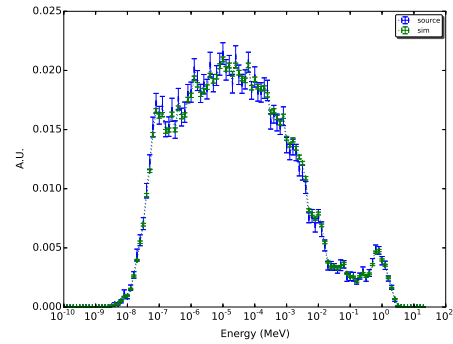
version = '0.1'
color=['b','g','r','c','m','y','k']
#
# Genero la sorgente da inserire in MCNP
#
def genSDEF(DIR,RAD,ENG1,ENG2):
    print "sur=d1_rad=fsur_d2_erg=fsur_d3_dir=d4"
    print "si1_L1071_1072"
    print "sp1_L1071_1072" % (sum(RAD[1][0:7]),sum(RAD[1][7:41]))
    print "ds2_S111_112"
    print "#L1071_1072"
    print "A"
    print "0"
    for i in range(1,8):
        print "L1071_1072" % (float(i)-float(0.5))
    print "#sp1"
    print "0"
    for i in range(1,8):
        dump = RAD[1][i-1]
        if(i>1):
            dump = RAD[1][i-1]
        print "L1071_1072" % dump
    print "#L1071_1072"
    print "A"
    for i in range(7,41):
        print "L1071_1072" % (float(i)-float(0.5))
    print "#sp1"
    for i in range(7,41):
        dump = RAD[1][i-1]
        if(i>1):
            dump = RAD[1][i-1]
        print "L1071_1072" % dump
    print "ds3_S21_22"
    print "#si21_L1071_1072"
    print "A"

```

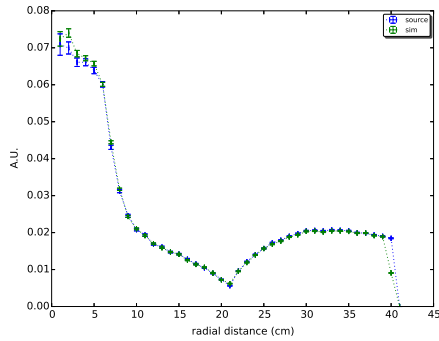
A.2. MCNP neutron source at beam port



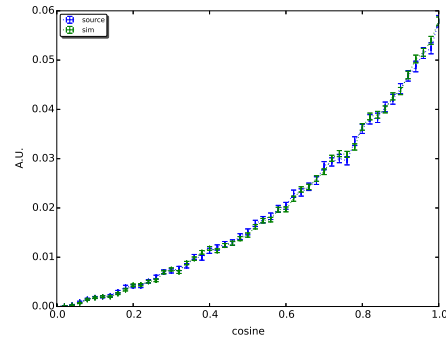
(a) Neutron energy Spectra for the annular range 0 till 7 cm.



(b) Neutron energy Spectra for the annular range 7 till 40 cm.

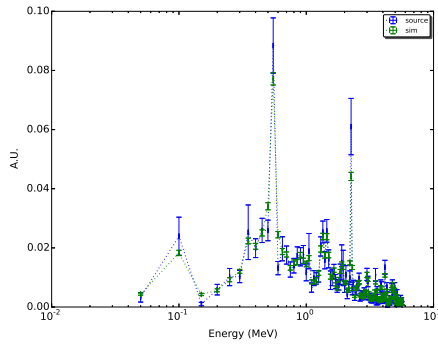


(c) Radial beam development.

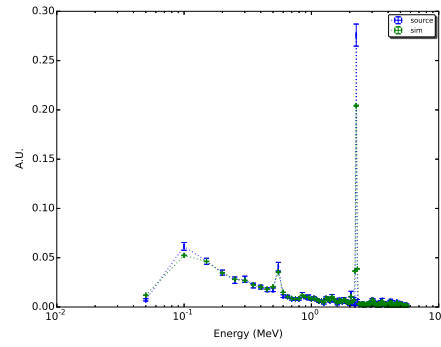


(d) Neutron emission angle.

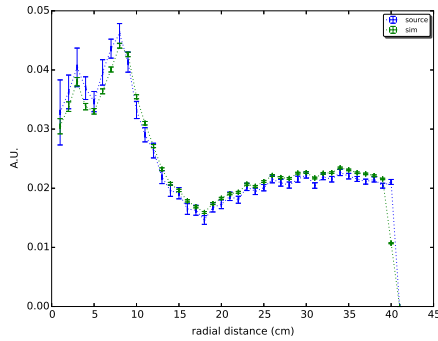
Figure A.5: SDEF neutron generation compared to neutrons transported from the beryllium target.



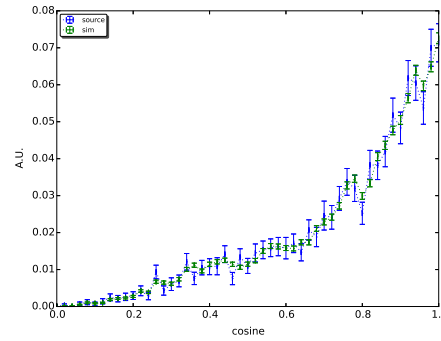
(a) Neutron energy Spectra for the annular range 0 till 7 cm.



(b) Neutron energy Spectra for the annular range 7 till 40 cm.



(c) Radial beam development.



(d) Neutron emission angle.

Figure A.6: SDEF neutron generation compared to neutrons transported from the beryllium target.

A.3. MIRD Analitical phantom

```
print "0"
for i in range(len(ENG1[0])):
    prec1=0
    prec2=0
    if(i>0):
        prec1=ENG1[0][i-1]
        prec2=ENG2[0][i-1]
    print "%1.3e%1.3e"%((ENG1[0][i]+prec1)/2,(ENG2[0][i]+prec2)/2)
print "#sp21sp22"
print "0"
for i in range(len(ENG1[0])):
    prec1=0
    prec2=0
    if(i>0):
        prec1=ENG1[0][i-1]
        prec2=ENG2[0][i-1]
    print "%1.3e%1.3e"%(ENG1[1][i]/(ENG1[0][i]-prec1),ENG2[1][i]/(ENG2[0][i]-prec2))
print "#s14"
print "a"
print "-1"
print "0"
for i in range(len(DIR[0])):
    print "%1.3e"%(DIR[0][i])
print "#sp4"
print "0"
print "0"
for i in range(len(DIR[1])):
    prec=0
    if(i>0):
        prec=DIR[0][i-1]
    print "%1.3e"%(DIR[1][i])#*(math.cos(DIR[0][i])-math.cos(prec))

def ComparePlot(D1,D2,Title,xaxis,yaxis,xscale,yscale,fname):
    fig, ax = plt.subplots()
    fig.suptitle(Title, fontsize=14, fontweight='bold')

    plt.errorbar(D1[0],D1[1], D1[1]*D1[2], 0,label=r'source',fmt=':',color=color[0])
    plt.errorbar(D2[0],D2[1], D2[1]*D2[2], 0,label=r'sim',fmt=':',color=color[1])

    plt.legend(loc='best',fontsize=8,numpoints=1,fancybox=True,shadow=True,ncol=1)
    ax.set_yscale(yscale)
    ax.set_xscale(xscale)
    ax.set_xlabel(xaxis,labelpad=8)
    ax.set_ylabel(yaxis,labelpad=8)
    plt.savefig(fname)

def ParticleDistr(P,direct):
    DIR=np.loadtxt(direct+P+"DIR.out")
    RAD=np.loadtxt(direct+P+"Nor.out")
    ENG1=np.loadtxt(direct+P+"ENG1.out")
    ENG2=np.loadtxt(direct+P+"ENG2.out")
    Area=np.loadtxt("tally.area")
    J=np.array([Area[i]*RAD[i][1] for i in range(40)])
    return [DIR[:,0],DIR[:,1],DIR[:,2]],[RAD[40:0],J,RAD[40:2]],[ENG1[:,0],ENG1[:,1],ENG1[:,2]],[ENG2[:,0],ENG2[:,1],ENG2[:,2]]

def PlotDistr(D1,Title,xaxis,yaxis,xscale,yscale,fname):
    fig, ax = plt.subplots()
    fig.suptitle(Title, fontsize=14, fontweight='bold')

    plt.errorbar(D1[0],D1[1], D1[2]*D1[1], 0,label=r'source',fmt=':',color=color[0])

    plt.legend(loc='best',fontsize=8,numpoints=1,fancybox=True,shadow=True,ncol=1)
    ax.set_yscale(yscale)
    ax.set_xscale(xscale)
    ax.set_xlabel(xaxis,labelpad=8)
    ax.set_ylabel(yaxis,labelpad=8)
    plt.savefig(fname)

def Norm(D1):
    return D1/sum(D1)

# END of SDEF.py
```

A.3 MIRD Analitical phantom

The analytical human phantom model MIRD-MIT (Medical Internal Radiation Dose) is available as example input in MCNP5. It was used in this dissertation to evaluate the dose deposited to organs that are not along the neutron beam axis of the beam port. The phantom shown in Figure A.7 reproduces a male. It consists in a Mathematical Cardio Torso (MCAT) model without arteries

with in addition organs such as : testes, thyroid, bladder and intestines. The organs composition are described through the implementation of 4 biological materials: soft tissue, skin, lung and bone. Moreover, each organ is defined by a single cell which decreases the computational memory load for the evaluation of the mean dose.

To evaluate the dose deposition in MCNP two tallies for each organ were implemented. Through The F4:N tally for neutrons the reaction rate ($\text{cm}^{-2} \cdot \text{g}^{-1}$) for the reactions: $^{10}\text{B}(\text{n},\alpha)^7\text{Li}$, $^1\text{H}(\text{n},\text{n}')^1\text{H}$, $^{14}\text{N}(\text{n},\text{p})^{14}\text{C}$ and $^1\text{H}(\text{n},\gamma)^2\text{H}$ is computed. These results are then used as input in a python script to compute the dose rate ($\text{Gy} \cdot \text{g}^{-1} \cdot \text{s}^{-1}$) deposited in each organ by normalizing with this factor:

$$x \cdot \frac{N_a}{M} \cdot \phi \cdot \text{barn} \cdot Q \quad (\text{A.1})$$

Where x is the mass percent of the atom in the taken material, N_a is the Avogadro number, M is the molar mass of the atom in Kg, ϕ is the neutron flux $\text{cm}^{-2} \text{ s}^{-1}$, barn is a normalization factor 10^{-24} cm^{-2} , Q is the energy deposited by the tallied reaction in J.

Photon energy deposit is computed through the F6:P, this tally deposits the energy in the point where the photon is created. Therefore, overestimating the photon dose in those volumes were the Charged Particle Equilibrium (CPE) is not reached.

```
message:      outp=body.o  runtpe=body.r  mctal=body.m

Example of Whole Body phantom
c      MCNP4B --- GMCNPSAM
c      Manray 1.0      Sam Yam
c      Manray 3.0      Jacquelyn Yanch
c
c      "Xman1" This file represents a male. He is comprised of the MCAT phantom
c      plus testes, thyroid, legs, bladder, and intestines. All arteries
c      have been removed.
c
c
c
c
c      Melissa Lambeth
c
c      CELLS
1      3 -0.0013 #61 (-2600 1403 -1420 1410):#61(-2600 1451 -1470 1420)
c      #61(-2600 1458 1470):#61(-2600 1401 1402 -1410):(-2600 -1402)
c      $outside torso
2      5 -1.46 (-700 701 702 -1170)      $outer spine
3      4 -1.06 (-701 702 -1170)      $inner spine
4      7 -0.03 #5 #46 #45 #23 #28 (-800 801 1513)      $left lung
49     7 -0.03 #32 #45 #27 #29 #30 #31 (-802 801 1515)      $right lung
5      4 -1.06 (-1000)      $stomach
6      5 -1.46 (-1100 1103 -1104 1101 -1102)      $manubrium
7      5 -1.46 (-1105 1106 -1103)      $mesosternum
8      5 -1.46 (-1120 -1106)      $xyphoid process
9      4 -1.06 (-1200 -1203):(-1202 1201)      $kidneys
10     4 -1.06 (-1300 1310 -1320 -1330)      $lower liver
c      upper abdomen
11     4 -1.06 #2 #3 #5 #8 #9 #10 #47 #57 #54
c      (((-901 906):(-906 -903 -913):(-906 -905 913)) 1016 -1320)
c      lower abdomen
24     4 -1.06 #41 #2 #3 #34 #35 #42 #66 #9 #43 #47 #44 (((-901 906):
c      (-906 -903 -913):(-906 -905 913)) -1016 1410)
c      lower thorax
12     4 -1.06 #2 #3 #4 #49 #5 #8 #32 #46 (((-901 906):(-906 -903 -913):
c      (-906 -905 913)) 1320 -1440)
c      mid thorax (outside heart)
13     4 -1.06 #2 #3 #4 #49 #5 #7 #8 #58
c      #32 #46 (((-901 906):(-906 -903 -913):
c      (-906 -905 913)) 1440 -1430) ((1513 1504 1501):(1514 -1504 1501)
c      :(1515 -1504 -1501):(1516 1504 -1501))
c      upper thorax
14     4 -1.06 #2 #3 #4 #49 #6 #7 #45 #52 #55 #58
c      (((-901 906):(-906 -903 -913):(-906 -905 913)) 1430 -1420)
c      upper shell
15     4 -1.06 #2 #3 #6 #7 #8 #17 #18 #19 #21 #22 #33 #36
c      ((901 906 -1400 1320 -1420):(903 -913 -906 -1400 1320 -1420):
c      (905 913 -906 -1400 1320 -1420))
c      lower shell
```

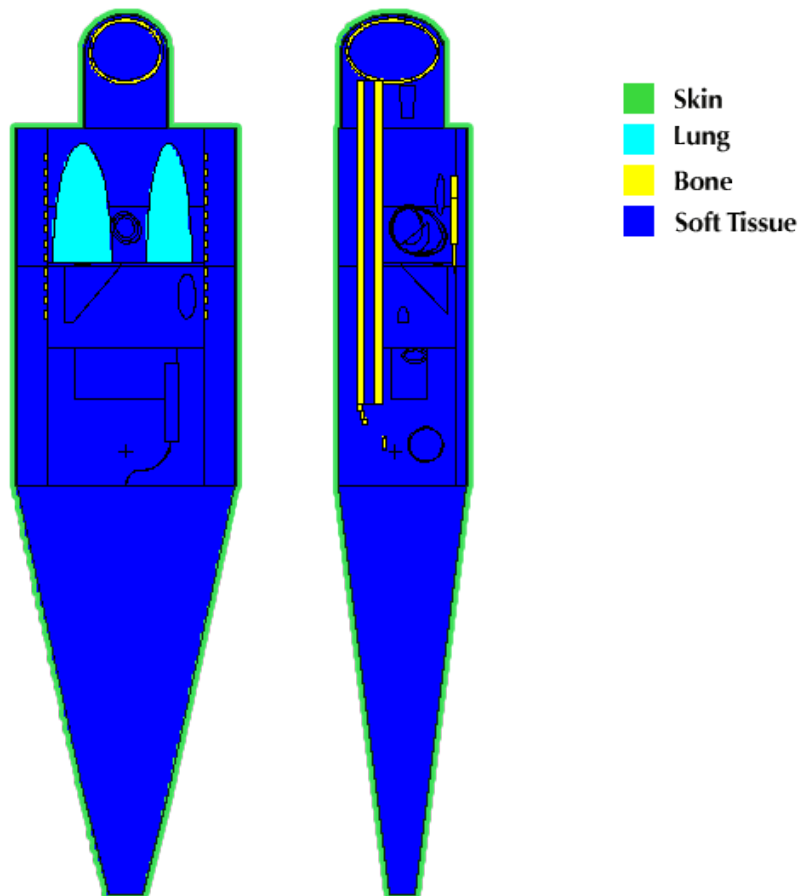



Figure A.7: Schematic view of the analytical phantom model MIRD-MIT. This human like geometry was used for the evaluation of the peripheral dose deposited in a patient during a treatment. In the image shown two cuts: on the left the frontal cut and on the right a lateral cut of the phantom.

```

16 4 -1.06 #2 #3 #8 #19 #20 #22 #34 #35 #36
   ((901 906 -1400 -1320 1410):(903 -913 -906 -1400 -1320 1410):
   (905 913 -906 -1400 -1320 1410))
c   transverse process above torso
17 5 -1.46 #2 ((-1122:-1121) 1126 -1170)((-1123 1124):(-1125 1126):
   (1169 -1170))
18 5 -1.46 #2 ((-1122:-1121) 1132 -1127)((-1127 1128) $in between
19 5 -1.46 #2 ((-1122:-1121) 1162 -1129)((-1129 1130):(-1131 1132)
   :(-1133 1134):(-1135 1136):(-1137 1138):(-1139 1140):(-1141 1142)
   :(-1143 1144):(-1145 1146):(-1147 1148):(-1149 1150)
   :(-1151 1152):(-1153 1154):(-1155 1156):(-1157 1158):(-1159 1160)
   :(-1161 1162))
c   front half of ribs
20 5 -1.46 #6 (-900 901 906 ((-909 910 (-911:912)):(-914 915 (-916:917)):
   (-920 921 (-923:924)):(-925 926 (-927:928))))
21 5 -1.46 #6 (-900 901 906 ((-937 938 (-939:940)):(-941 942 (-943:944)):
   (-945 946 (-947:948)):(-949 950 (-951:952)):(-953 954 (-955:956)):
   (-957 958 (-959:960)):(907 -908 (-918:919))))
22 5 -1.46 (700 -906 (((-902 903 -913):(-904 905 913)) ((-909 910)
   :(-914 915):(-920 921):(-925 926):(-929 930):(-933 934):(-937 938)
   :(-941 942):(-945 946):(-949 950):(-953 954):(-957 958))))
c   heart
23 4 -1.06 (1501 -1500 1502 1503) $left ventricle
25 4 -1.06 #23 (1501 -1504 -1505 1506) $right ventricle
26 4 -1.06 (-1501 1504 -1507 1508) $left atrium
27 4 -1.06 #23 (-1501 -1504 -1509 1510 -1512) $left atrium
28 4 -1.06 (-1502 1501)
c   space defined within the left ventricle and atrium
29 4 -1.06 (-1501 ((-1508 1504):(-1504 -1510)))
30 4 -1.06 #23 #27 #29 (-1501 -1504 -1511 1512) $right atrium
31 4 -1.06 (-1506 1500 1501 -1504):(-1501 -1504 -1512 1509)
c   space defined within the right ventricle and atrium
32 4 -1.06 (1320 -1380 -1330 -1340) $upper liver
33 5 -1.46 (1700 -1710 -1740 -1730 1750 -1760 -906):
   (1700 -1710 -1740 -1730 1750 -906) $shoulder blades
34 5 -1.46 #2 #3 #35 (1800 -1810 1840 -1845):(1820 -1830 1840 -1845):
   (1860 -1865 -1870 1880 -1840 1850 1855 1890 -1895) $pelvis
35 5 -1.46 (-710 -702 720):(-730 -720 740):(-750 -740 760) $tailbone
36 5 -1.46 #6 (-900 901 906 ((-929 930 (-931:932)):(-933 934 (-935:936))))
c   back half of ribs
40 4 -1.06 #43 (-1401 1402 -1410) $legs
41 4 -1.06 #42 #66 (-1012 1014 -1016 -1018 1020) $small intestine
42 4 -1.06 (-1022 1024 1026 -1028):(-1030 1032 1034 -1036) $up lg intestine
66 4 -1.06 (-1038 -1028 1042):(-1044 -1203 -1048 1050):
   (-1052 1054 1203 1410 -1053) $lower lg intestine
43 4 -1.06 (-2000:-2002) $testes
44 4 -1.06 (-2010 2012) $bladder
45 4 -1.06 ((1500 -1513 1504 1501):(1505 -1514 -1504 1501)
   :(1511 -1515 -1504 -1501):(1507 -1516 1504 -1501)) $heart membrane
46 4 -1.06 (1000 -1010 801) $stomach membrane
47 4 -1.06 (-1220) $spleen
48 4 -1.06 #2 #3 #17 #18 #50 #51 #52 #55 ((-1450 1420 -1470):(-1455 1470))
c   neck and head
50 5 -1.46 #2 #3 (-1456 1457) $skull
51 4 -1.06 -1457 $brain
52 4 -1.06 (-2120 ((-2110 -2140):(-2100 2130))) $thyroid
54 4 -1.06 (-2200 ((2240 1310):(-2210 -1310)) (1201:1310)) $pancreas
55 4 -1.06 (-2310 2332 -2320) $pharynx
57 4 -1.06 (-2500 2515):(-2510 2515) $adrenals
58 4 -1.06 (-2520) $thymus
60 0 2600
61 6 -11.3 (-2700 -2750 2760 (2710:-2720:2730:-2740)) $lead cylinder
62 4 -1.06 ((1400 -1403 1410 -1420):(-1451 1450 1420 -1470):
   (-1458 1455 1470)) $skin
c   64 3 -.0013 #61 (-2600 2610 2630 -2620 1451 1420 -1470)
c   $area outside head
c   65 3 -.0013 #61 (-2600 2610 2630 -2620 1458 1470 -2640)
c   $area outside crown
c   67 3 -.0013 #61 (-2600 2610 2630 -2620 1401 1402 -1410)
c   $area outside leg

C   SURFACES
700 1 SQ 0 6.25 4 0 0 0 -25 0 0 -6.6
701 1 SQ 0 1 .64 0 0 0 -6.4 0 0 -6.6
702 1 PX -34 $spine lengthened by 5.5 cm
c   tailbone
710 1 SQ 0 .25 20.25 0 0 0 -5.0625 -34 0 -8.5
720 1 PX -35.5
730 1 SQ 0 .25 9 0 0 0 -1 -36 0 -8
740 1 PX -37
750 1 SQ 0 .25 2.25 0 0 0 -.5625 -37 0 -7.5
760 1 PX -38
800 1 SQ 1169.64 32400 11977.1 0 0 0 -673712.6 -6.5 -8.5 0 $left lung
801 1 PX -6.5
802 1 SQ 2025 32400 20736 0 0 0 -1166400 -6.5 8.5 0 $right lung
900 1 SQ 0 118.81 256 0 0 0 -30415.4 0 0 0 $ribs
901 1 SQ 0 108.16 240.25 0 0 0 -25985.4 0 0 0
902 1 SQ 0 72.25 81 0 0 0 -5852.25 0 -7 0
903 1 SQ 0 64 72.25 0 0 0 -4624 0 -7 0
904 1 SQ 0 72.25 81 0 0 0 -5852.25 0 7 0
905 1 SQ 0 64 72.25 0 0 0 -4624 0 7 0

```

A.3. MIRD Analitical phantom

```

906 1 PZ 0
907 1 SQ 0 0 0 -174.4 0 -88.8 5866 0 0 0 $clavicles
908 1 SQ 0 0 0 -174.4 0 -88.8 5378.75 0 0 0 $clavicles
909 1 SQ 0 0 0 -174.4 0 -88.8 -6315.5 0 0 0
910 1 SQ 0 0 0 -174.4 0 -88.8 -5828.25 0 0 0
911 1 PY -6.244
912 1 PY 6.244
913 1 PY 0
914 1 SQ 0 0 0 -174.4 0 -88.8 -5341 0 0 0
915 1 SQ 0 0 0 -174.4 0 -88.8 -4853.75 0 0 0
916 1 PY -5.976
917 1 PY 5.976
918 1 PY -3.028
919 1 PY 3.028
920 1 SQ 0 0 0 -174.4 0 -88.8 -4366.5 0 0 0
921 1 SQ 0 0 0 -174.4 0 -88.8 -3879.25 0 0 0
923 1 PY -5.708
924 1 PY 5.708
925 1 SQ 0 0 0 -174.4 0 -88.8 -3392 0 0 0
926 1 SQ 0 0 0 -174.4 0 -88.8 -2904.75 0 0 0
927 1 PY -5.44
928 1 PY 5.44
929 1 SQ 0 0 0 -174.4 0 -88.8 -2417.5 0 0 0
930 1 SQ 0 0 0 -174.4 0 -88.8 -1930.25 0 0 0
931 1 PY -5.172
932 1 PY 5.172
933 1 SQ 0 0 0 -174.4 0 -88.8 -1443 0 0 0
934 1 SQ 0 0 0 -174.4 0 -88.8 -955.75 0 0 0
935 1 PY -4.904
936 1 PY 4.904
937 1 SQ 0 0 0 -174.4 0 -88.8 -468.5 0 0 0
938 1 SQ 0 0 0 -174.4 0 -88.8 18.75 0 0 0
939 1 PY -4.636
940 1 PY 4.636
941 1 SQ 0 0 0 -174.4 0 -88.8 506 0 0 0
942 1 SQ 0 0 0 -174.4 0 -88.8 993.25 0 0 0
943 1 PY -4.368
944 1 PY 4.368
945 1 SQ 0 0 0 -174.4 0 -88.8 1480.5 0 0 0
946 1 SQ 0 0 0 -174.4 0 -88.8 1967.75 0 0 0
947 1 PY -4.1
948 1 PY 4.1
949 1 SQ 0 0 0 -174.4 0 -88.8 2455 0 0 0
950 1 SQ 0 0 0 -174.4 0 -88.8 2942.25 0 0 0
951 1 PY -3.832
952 1 PY 3.832
953 1 SQ 0 0 0 -174.4 0 -88.8 3429.5 0 0 0
954 1 SQ 0 0 0 -174.4 0 -88.8 3916.75 0 0 0
955 1 PY -3.564
956 1 PY 3.564
957 1 SQ 0 0 0 -174.4 0 -88.8 4404.25 0 0 0
958 1 SQ 0 0 0 -174.4 0 -88.8 4891.5 0 0 0
959 1 PY -3.296
960 1 PY 3.296
c G-I Tract
1000 3 SQ 576 1024 144 0 0 0 -9216 0 0 0 $stomach
1010 3 SQ 1204.78 1901.83 365.19 0 0 0 -28926.87 0 0 0
1012 1 C/X 0 3.8 11.3 $small intestine
1014 1 PX -33
1016 1 PX -23
1018 1 PZ 4.86
1020 1 PZ -2.2
1022 1 C/X 8.5 2.36 2.5 $ascending colon
1024 1 C/X 8.5 2.36 1.79
1026 1 PX -35.55
1028 PX -26
1030 1 SQ 6.25 0 2.25 0 0 0 -14.0625 -24.5 0 2.36 $transverse colon
1032 1 SQ 3.89 0 .95 0 0 0 -3.68 -24.5 0 2.36
1034 1 PY -10.5
1036 1 PY 10.5
1038 SQ 0 4.54 3.53 0 0 0 -16.03 -26 -9 0 $descendingcolon
1042 PX -41.28
1044 TZ -41.3 -3 0 5.72 1.57 1.57 $sigmoid colon
1048 PX -41.3
1050 TZ -41.3 -3 0 5.72 .91 .91
1052 TZ -50 -3 0 3 1.57 1.57
1053 px -25.925 $surface added to try to correct geometry
1054 TZ -50 -3 0 3 .91 .91
1100 1 SQ 9.766 14.06 0 0 0 0 -137.33 9.37 0 0 $manubrium
1101 1 PZ 9.53
1102 1 PZ 10.69
1103 1 PX 6.12
1104 1 PX 10.62
1105 1 SQ 0 .3364 1.66 0 0 0 -.56 0 0 10.11 $mesosternum
1106 1 PX -2.85
1120 1 SQ .0645 3.23 21.83 0 0 0 -2.13 -2.85 0 10.11 $xyphoid process
1121 7 SQ 0 1 2.77778 0 0 0 -1 0 0 0 $transverse process
1122 8 SQ 0 1 2.77778 0 0 0 -1 0 0 0
1170 1 PX 29.26 $index=-5
1169 1 PX 27.86
1123 1 PX 26.46 $index=-3

```

```

1124 1 PX 25.06
1125 1 PX 23.66 $index=-1
1126 1 PX 22.26
1127 1 PX 20.86 $index=1
1128 1 PX 19.46
1129 1 PX 18.06 $index=3
1130 1 PX 16.66
1131 1 PX 15.26 $index=5
1132 1 PX 13.86
1133 1 PX 12.46 $index=7
1134 1 PX 11.06
1135 1 PX 9.66 $index=9
1136 1 PX 8.26
1137 1 PX 6.86 $index=11
1138 1 PX 5.46
1139 1 PX 4.06 $index=13
1140 1 PX 2.66
1141 1 PX 1.26 $index=15
1142 1 PX -.14
1143 1 PX -1.54 $index=17
1144 1 PX -2.94
1145 1 PX -4.34 $index=19
1146 1 PX -5.74
1147 1 PX -7.14 $index=21
1148 1 PX -8.54
1149 1 PX -9.94 $index=23
1150 1 PX -11.34
1151 1 PX -12.74 $index=25
1152 1 PX -14.14
1153 1 PX -15.54 $index=27
1154 1 PX -16.94
1155 1 PX -18.34 $index=29
1156 1 PX -19.74
1157 1 PX -21.14 $index=31
1158 1 PX -22.54
1159 1 PX -23.94 $index=33
1160 1 PX -25.34
1161 1 PX -26.74 $index=35
1162 1 PX -28.14
1200 4 SQ 49 96.04 294.12 0 0 0 -1176.49 -19.5 0 0
c left kidney
1201 1 PY 3
1202 5 SQ 49 96.04 294.12 0 0 0 -1176.49 -19.5 0 0
c right kidney
1203 PY -3
1220 6 SQ 49 144 441 0 0 0 -1764 -13 0 0 $spleen
1300 1 SQ 0 64 204.5 0 0 0 -13287.4 -7 -1.8 .7 $lower liver
1310 1 PX -18
1320 1 PX -7
1330 1 SQ 0 0 0 -1800 -2115 -1880 0 -7 -7.5 8
1340 1 SQ 0 0 0 0 -45 -40 0 -7 -7.5 8
1380 1 SQ 70585.86 1186.1 3657.83 0 0 0 -553393.16 -9.1 -1.8 .7 $upper liver
1400 1 SQ 0 156.25 466.56 0 0 0 -72900 0 0 0 $torso y=21.6 z=12.5
1401 1 SQ -.0001 .00214 .0064 0 0 0 0 -150 0 0 $legs based on MIRD with
1402 1 PX -130 $MCAT dimensions
1403 1 SQ 0 161.3 475.24 0 0 0 -76651.46 0 0 0 $skin layer .2 cm
1410 1 PX -50
1420 1 PX 20
1430 1 PX 4.6
1440 1 PX -6.3
c neck dimensions from Cristy et al
c neck is approx. 9.7 cm long
1450 1 SQ 0 100 64 0 0 0 -6400 26 0 -2 $head
1451 1 SQ 0 104.04 67.24 0 0 0 -6995.649 26 0 -2 $skin around head
1455 1 SQ 6400 5112.25 3271.84 0 0 0 -327184 35 0 -2 $crown
1458 1 SQ 6995.649 5620.5 3632.473 0 0 0 -377922.48 35 0 -2 $crown skin
1456 1 SQ 4970.25 3907.5 2487.5 0 0 0 -209993.06 35 0 -2 $outer skull
1457 1 SQ 3221.7 2445.3 1440.2 0 0 0 -106517.37 35 0 -2 $inner skull
c skull modeled from Cristy et al dimensions
c 1460 1 C/X 0 -3.7 6.3 $neck
c 1461 1 C/X 0 -3.7 6.5 $neck skin
1470 1 PX 35
c heart
1500 2 SQ 216.09 906.01 1304.65 0 0 0 -15982 0 0 0
1501 2 PX 0
1502 2 SQ 40.7 257.9 448.2 0 0 0 -2169.14 0 0 0
1503 2 SQ 1.74 1.69 2.94 22.65 0 0 70.67 0 0 0
1504 2 PZ 0
1505 2 SQ 745.29 3124.81 1304.65 0 0 0 -55121.6 0 0 0
1506 2 SQ 529.5 2227.84 973.44 0 0 0 -33885.4 0 0 0
1507 2 SQ 216.1 318.6 458.8 0 0 0 -5620.5 0 0 0
1508 2 SQ 155.75 235.9 350.4 0 0 0 -3588.5 0 0 0
1509 2 SQ 110.25 162.56 458.82 0 0 0 -2867.6 0 0 0
1510 2 SQ 73.6 111.5 350.4 0 0 0 -1696.1 0 0 0
1511 2 SQ 745.29 1098.92 458.82 0 0 0 -19384.99 0 0 0
1512 2 SQ 584.7 885.7 350.4 0 0 0 -13470.85 0 0 0
1513 2 SQ 292.41 1143.79 1604 0 0 0 -23161.79 0 0 0 $corresponds to 1500
1514 2 SQ 936.36 3662.67 1604 0 0 0 -74169.08 0 0 0 $corresponds to 1505
1515 2 SQ 936.36 1348.35 590.49 0 0 0 -27304.26 0 0 0 $corresponds to 1511
1516 2 SQ 292.41 421.07 590.49 0 0 0 -8526.67 0 0 0 $corresponds to 1507
c shoulder blades

```

A.3. MIRD Analitical phantom

```

1700 1 SQ 0 110.25 289 0 0 0 -31862.25 0 0 0
1710 1 SQ 0 127.69 316.84 0 0 0 -40457.3 0 0 0
1720 1 PY 7
1730 1 PY -7
1740 1 PX 18
1750 1 SQ 0 0 0 .75 1 0 4 0 0 0
1760 1 SQ 0 0 0 -.75 1 0 -4 0 0 0
c    pelvis
1800 1 S -33 9 -.5 7
1810 1 S -33 9 -.5 7.8
1820 1 S -33 -9 -.5 7
1830 1 S -33 -9 -.5 7.8
1840 1 PX -36
1845 1 PZ -5
1850 1 PX -43
1855 1 PZ -7
1860 1 C/Y -42 -11 7
1865 1 C/Y -42 -11 7.8
1870 1 PY 11.3
1880 1 PY -11.3
1890 1 S -35 0 -8 7
1895 1 S -36 0 -8 11.3
c    testes , bladder
2000 1 SQ 3.8 11.9 8.94 0 0 0 -20.12 -52.4 1.3 10.5 $right testes
2002 1 SQ 3.8 11.9 8.94 0 0 0 -20.12 -52.4 -1.3 10.5 $left testes
2010 1 SQ 293.94 142.99 293.94 0 0 0 -3510 -42 0 4.5 $bladder
2012 1 SQ 228.59 106.17 228.59 0 0 0 -2360 -42 0 4.5
2100 1 SQ 3.0625 25 76.5625 0 0 0 -76.5625 19.5 -1.75 -.5 $thyroid
2110 1 SQ 3.0625 25 76.5625 0 0 0 -76.5625 19.5 1.75 -.5
2120 1 PZ -.5
2130 1 PY -1.75
2140 1 PY 1.75
c    pancreas
2200 1 SQ 368.64 15.68 2787.8 0 0 0 -4014.5 -18 7 0
2210 1 PY 8
2240 1 SQ 0 0 0 -1800 -2115 -1880 0 -7 -8.5 8
c    pharynx
2310 1 SQ -.00564 .5 1.414 0 0 0 5.5 0 .9
2320 1 PX 28.2
2332 1 PX 22
c    adrenals
2500 1 SQ 1 .36 14.06 0 0 0 -2.25 -14.6 4.5 -6
2510 1 SQ 1 .36 14.06 0 0 0 -2.25 -14.6 -4.5 -6
2515 1 PX -14.59
c    thymus
2520 1 SQ 1.44 10.44 36 0 0 0 -23.04 7 0 7.3
c    outside cube
2600 1 so 225
c    2610 1 PZ -180
c    2620 1 PY 60
c    2630 1 PY -60
c    2640 1 PX 60
c    2650 1 PX -160
c    lead cylinders
2700 1 C/y 0 0 50
2710 1 PX 2
2720 1 PX -2
2730 1 Pz 1.5
2740 1 Pz -1.5
2750 1 Py -102.7
2760 1 Py -107.7
c    surface segments
2800 1 C/y 0 0 4
c    surface per tally
1071 1 pz -24.5
1072 1 pz -24.5

tr1 0 0 0 1 0 0 0 1 0 0 0 1 1
tr2 0 -1 1.7 -.573576 -.671010 .469846 -.819152 .469846 -.328990
    0 -.573576 -.819152 1
tr3 -11 -7.5 3 -.405580 -.579228 .707107 -.405580 -.579228 -.707107
    .819152 -.573576 0 1
tr4 0 -4.5 -5 1 0 0 0 .70710678 .70710678 0 -.70710678 .70710678 1
tr5 0 3.5 -4.8 1 0 0 0 .70710678 -.70710678 0 .70710678 .70710678 1
tr6 0 -11 -3.5 1 0 0 0 .70710678 -.70710678 0 .70710678 .70710678 1
tr7 0 2.4 -8.5 1 0 0 0 .70710678 -.70710678 0 .70710678 .70710678 1
tr8 0 -2.4 -8.5 1 0 0 0 .70710678 .70710678 0 -.70710678 .70710678 1
mode p n
sdef pos= -83 0 -24.5
    vec= 0 0 1
    axs= 0 0 1
    sur=d1 rad=fsur d2 erg=fsur d3 dir=d4
sil L 1071 1072
sp1 9.912e-02 9.009e-01
ds2 S 11 12
#    sil1
#    A
#    0
#    0.5
#    1.5
#    2.5

```

```

3.5
4.5
5.5
6.5
# sp11
0
2.472e-03
7.230e-03
1.178e-02
1.643e-02
1.983e-02
2.221e-02
1.917e-02
# si12
A
6.5
7.5
8.5
9.5
10.5
11.5
12.5
13.5
14.5
15.5
16.5
17.5
18.5
19.5
20.5
21.5
22.5
23.5
24.5
25.5
26.5
27.5
28.5
29.5
30.5
31.5
32.5
33.5
34.5
35.5
36.5
37.5
38.5
39.5
# sp12
1.917e-02
1.655e-02
1.460e-02
1.425e-02
1.366e-02
1.384e-02
1.416e-02
1.443e-02
1.428e-02
1.429e-02
1.331e-02
1.317e-02
1.179e-02
1.009e-02
8.502e-03
7.096e-03
1.655e-02
2.054e-02
2.319e-02
2.758e-02
3.092e-02
3.513e-02
3.727e-02
4.006e-02
4.254e-02
4.386e-02
4.653e-02
4.859e-02
4.845e-02
4.946e-02
4.965e-02
4.925e-02
4.882e-02
4.847e-02
ds3 s 21 22
# si21 si22
a a
0 0
5.000e-11 5.000e-11
1.130e-10 1.130e-10
1.422e-10 1.422e-10

```

A.3. MIRD Analitical phantom

1.790e-10	1.790e-10
2.254e-10	2.254e-10
2.837e-10	2.837e-10
3.572e-10	3.572e-10
4.496e-10	4.496e-10
5.661e-10	5.661e-10
7.127e-10	7.127e-10
8.972e-10	8.972e-10
1.130e-09	1.130e-09
1.422e-09	1.422e-09
1.790e-09	1.790e-09
2.254e-09	2.254e-09
2.837e-09	2.837e-09
3.571e-09	3.571e-09
4.496e-09	4.496e-09
5.661e-09	5.661e-09
7.127e-09	7.127e-09
8.972e-09	8.972e-09
1.129e-08	1.129e-08
1.422e-08	1.422e-08
1.790e-08	1.790e-08
2.253e-08	2.253e-08
2.837e-08	2.837e-08
3.571e-08	3.571e-08
4.496e-08	4.496e-08
5.661e-08	5.661e-08
7.126e-08	7.126e-08
8.972e-08	8.972e-08
1.130e-07	1.130e-07
1.422e-07	1.422e-07
1.790e-07	1.790e-07
2.254e-07	2.254e-07
2.837e-07	2.837e-07
3.571e-07	3.571e-07
4.497e-07	4.497e-07
5.661e-07	5.661e-07
7.126e-07	7.126e-07
8.971e-07	8.971e-07
1.129e-06	1.129e-06
1.422e-06	1.422e-06
1.790e-06	1.790e-06
2.253e-06	2.253e-06
2.837e-06	2.837e-06
3.571e-06	3.571e-06
4.497e-06	4.497e-06
5.661e-06	5.661e-06
7.127e-06	7.127e-06
8.972e-06	8.972e-06
1.129e-05	1.129e-05
1.422e-05	1.422e-05
1.790e-05	1.790e-05
2.254e-05	2.254e-05
2.837e-05	2.837e-05
3.571e-05	3.571e-05
4.497e-05	4.497e-05
5.661e-05	5.661e-05
7.127e-05	7.127e-05
8.972e-05	8.972e-05
1.130e-04	1.130e-04
1.422e-04	1.422e-04
1.790e-04	1.790e-04
2.253e-04	2.253e-04
2.837e-04	2.837e-04
3.571e-04	3.571e-04
4.497e-04	4.497e-04
5.661e-04	5.661e-04
7.127e-04	7.127e-04
8.971e-04	8.971e-04
1.129e-03	1.129e-03
1.422e-03	1.422e-03
1.790e-03	1.790e-03
2.253e-03	2.253e-03
2.837e-03	2.837e-03
3.572e-03	3.572e-03
4.497e-03	4.497e-03
5.661e-03	5.661e-03
7.127e-03	7.127e-03
8.972e-03	8.972e-03
1.129e-02	1.129e-02
1.422e-02	1.422e-02
1.790e-02	1.790e-02
2.253e-02	2.253e-02
2.837e-02	2.837e-02
3.571e-02	3.571e-02
4.496e-02	4.496e-02
5.661e-02	5.661e-02
7.126e-02	7.126e-02
8.972e-02	8.972e-02
1.130e-01	1.130e-01
1.422e-01	1.422e-01
1.790e-01	1.790e-01

#

#

```

8.600e-01
8.800e-01
9.000e-01
9.200e-01
9.400e-01
9.600e-01
9.800e-01
1.000e+00
# sp4
0
0
1.135e-04
3.556e-04
6.001e-04
9.928e-04
1.366e-03
1.661e-03
2.392e-03
2.348e-03
3.103e-03
3.325e-03
4.216e-03
4.409e-03
4.813e-03
5.977e-03
6.977e-03
7.376e-03
7.954e-03
8.110e-03
1.004e-02
1.065e-02
1.143e-02
1.175e-02
1.371e-02
1.436e-02
1.494e-02
1.593e-02
1.737e-02
1.880e-02
1.911e-02
2.018e-02
2.186e-02
2.288e-02
2.559e-02
2.517e-02
2.836e-02
2.832e-02
3.077e-02
3.101e-02
3.402e-02
3.566e-02
3.783e-02
4.002e-02
4.163e-02
4.429e-02
4.580e-02
4.758e-02
5.027e-02
5.192e-02
5.519e-02
5.749e-02
phys:p 100 0 0
prdm:p 1000000 1000000
c print 110
imp:p 1 53r 0 1 1
m3 7014 .8 8016 .2 gas=1 $air
m4 1001 -.105 6000 -.414 7014 -.034 8016 -.439 15031 -.001 16032 -.002
17000 -.002 19000 -.002 26000 -.001 $soft tissue
m5 1001 -.060 6000 -.314 7014 -.031 8016 -.369 11023 -.001 12000 -.001
15031 -.070 16032 -.002 20000 -.152 $bone
m6 82000 1.0 $lead
m7 1001 -.1021 6000 -.1001 7014 -.028 8016 -.7596 $lung
c tallies (flux averaged over cell)
fc16 LUNG TALLIES
f16:p (4 49) T
sd16 3981 3981
fc26 STOMACH TALLY
f26:p 5
sd26 596.55
fc36 KIDNEY TALLIES
f36:p 9
sd36 287.4
fc46 SPLEEN TALLY
f46:p 47
sd46 175.9
fc56 LIVER TALLY
f56:p (10 32) T
sd56 1253.3 1253.3
fc66 HEAD TALLY
f66:p 48

```

A.3. MIRD Analitical phantom

```
sd66      937.5
fc106     BRAIN TALLY
f106:p    51
sd106     1470
fc76      SMALL INTESTINE TALLY
f76:p     41
sd76      1060
fc86      LARGE INTESTINE TALLY
f86:p     42 66
sd86      416.3 123
fc96      BLADDER TALLY
f96:p     44
sd96      248.2
fc116     THYROID TALLY
f116:p    52
sd116     20
fc126     TESTES TALLY
f126:p    43
sd126     37.6
fc146     PANCREAS TALLY
f146:p    54
sd146     90.7
fc156     PHARYNX TALLY
f156:p    55
sd156     16
fc176     BONE MARROW TALLY
f176:p    (2 3 17 18 19 20 21 22 33 34 50) T
sd176     5455.24 5455.24
fc186     ADRENALS TALLY
f186:p    57
sd186     15.7
fc196     THYMUS TALLY
f196:p    58
sd196     21.106
fc166     SURFACE (SKIN DOSE) Dose TALLY
f166:p    62
fs166     2800
sd166     1300.99 40.2
fc206     SKIN TALLY
f206:p    62
sd206     1987
fc226     TRUNK TALLY
f226:p    (11 12 24 13 14 15 16)
sd226     13968
c *****
c neutron tallies
c FM updated tallies
c *****
m11 1001.50 c 1
m12 5010.60 c 1
m13 7014.60 c 1
fc304     LUNG TALLIES
f304:n    (4 49) T
sd304     3981 3981
fm304     (1 12 107) (1 11 2 -4) (1 13 103) (1 11 102)
fc324     STOMACH TALLY
f324:n    5
sd324     596.55
fm324     (1 12 107) (1 11 2 -4) (1 13 103) (1 11 102)
fc334     KIDNEY TALLIES
f334:n    9
sd334     287.4
fm334     (1 12 107) (1 11 2 -4) (1 13 103) (1 11 102)
fc344     SPLEEN TALLY
f344:n    47
sd344     175.9
fm344     (1 12 107) (1 11 2 -4) (1 13 103) (1 11 102)
fc354     LIVER TALLY
f354:n    (10 32) T
sd354     1253.3 1253.3
fm354     (1 12 107) (1 11 2 -4) (1 13 103) (1 11 102)
fc364     HEAD TALLY
f364:n    48
sd364     937.5
fm364     (1 12 107) (1 11 2 -4) (1 13 103) (1 11 102)
fc404     BRAIN TALLY
f404:n    51
sd404     1470
fm404     (1 12 107) (1 11 2 -4) (1 13 103) (1 11 102)
fc374     SMALL INTESTINE TALLY
f374:n    41
sd374     1060
fm374     (1 12 107) (1 11 2 -4) (1 13 103) (1 11 102)
fc384     LARGE INTESTINE TALLY
f384:n    42 66
sd384     416.3 123
fm384     (1 12 107) (1 11 2 -4) (1 13 103) (1 11 102)
fc394     BLADDER TALLY
f394:n    44
sd394     248.2
fm394     (1 12 107) (1 11 2 -4) (1 13 103) (1 11 102)
```

```

fc414  THYROID TALLY
f414:n  52
sd414  20
fm414  (1 12 107) (1 11 2 -4) (1 13 103) (1 11 102)
fc424  TESTES TALLY
f424:n  43
sd424  37.6
fm424  (1 12 107) (1 11 2 -4) (1 13 103) (1 11 102)
fc444  PANCREAS TALLY
f444:n  54
sd444  90.7
fm444  (1 12 107) (1 11 2 -4) (1 13 103) (1 11 102)
fc454  PHARYNX TALLY
f454:n  55
sd454  16
fm454  (1 12 107) (1 11 2 -4) (1 13 103) (1 11 102)
fc474  BONE MARROW TALLY
f474:n  (2 3 17 18 19 20 21 22 33 34 50) T
sd474  5455.24 5455.24
fm474  (1 12 107) (1 11 2 -4) (1 13 103) (1 11 102)
fc484  ADRENALS TALLY
f484:n  57
sd484  15.7
fm484  (1 12 107) (1 11 2 -4) (1 13 103) (1 11 102)
fc494  THYMUS TALLY
f494:n  58
sd494  21.106
fm494  (1 12 107) (1 11 2 -4) (1 13 103) (1 11 102)
fc464  SURFACE (SKIN DOSE)Dose TALLY
f464:n  62
fs464  2800
sd464  1300.99 40.2
fm464  (1 12 107) (1 11 2 -4) (1 13 103) (1 11 102)
fc504  SKIN TALLY
f504:n  62
sd504  1987
fm504  (1 12 107) (1 11 2 -4) (1 13 103) (1 11 102)
fc524  TRUNK TALLY
f524:n  (11 12 24 13 14 15 16)
sd524  13968
fm524  (1 12 107) (1 11 2 -4) (1 13 103) (1 11 102)
c *****
c end neutron tallies
c *****
nps     1e6

```

Appendix B

B - GEANT4 and geometrical cell implementation

GEometry ANd Tracking [78] (GEANT4) is tool-kit for particle transport through matter. It is an object oriented programming language based on c++. This simulation tool is employed for applications like: high energy physics, nuclear physics, medical physics, accelerators and astrophysics. The simulations are implemented in the *main.cc* file by defying objects such as:

Geometry - This object is used to define the *physical world* where the particles are transported. Through the methods of this class the user can implement materials and geometrical structure of the world.

Source - The user can define the primary particles and their spacial distribution in the defined geometry.

Tracking - This object is used to follow the particle during the simulation. This class contains methods that can be used to store energy deposition and position of the particle.

Physics - GEANT4 gives the user the possibility to select which physics cross section library to use through this object. Here the physics detail of the simulation is selected, this means that this class has methods giving the ability to control the particles to simulate.

Run manager - This object helps the user to define the start of the simulation and it collects the information generated by the tracking of the particles. This class contains methods to initialize, collect data and conclude the particle transport.

Visualizer - If the user wants to use a graphical interface, GEANT4 contains a visualization object. This class is particularly useful during the troubleshooting of the application.

The application adopted in Chapter 3 derives from the *microbeam* advanced examples supplied by GEANT4. The difference are two:

Geometry - The microbeam geometry was stripped from the proton beam accelerator and only the cube containing the cell was maintained.

Phantom - The cellular voxelized phantom was reconstructed to fit the geometrical structure defined in Chapter 3.

The implementation of the voxelized phantom is divided in two steps. The first one concerns the biological cell definition, which is performed through a c++ program. The second step consist in the construction of a voxelized tissue like structure. This is performed by defining a cubic lattice of 3 by 3 by 3 cells, where the cell phantom is used as primary stamp. The code to implement basal keratinocytes, oligodendrocytes and hepatocytes is shown in the next sessions.

B.1 Basal keratinocytes

The following c++ code defines a cylindrical phantom with a radius of 7 μm and an height of 15 μm .

```
#include <iostream>

//passo valori nell sistema di riferimento reale
bool GetCell(int xx, int yy, int zz){
    return (xx*xx+yy*yy)<7*7;
}

int main(){
    // nx , ny , nz
    int nx=30,ny=30,nz=30;
    // dx , dy , dz pixel dimension
    float dx=0.5,dy=0.5,dz=0.5;
    int ox=0,oy=0,oz=0;
    int phantomTotPixel=0,nucleusTotPixel=0,citoTotPixel=0;
    for (int x=0; x<nx; x++){
        int xCentr=x-nx/2;
        for (int y=0; y<ny; y++){
            int yCentr=y-ny/2;
            for (int z=0; z<nz; z++){
                int zCentr=z-nz/2;
                if (GetCell(xCentr, yCentr, zCentr)) {
                    phantomTotPixel++;
                    if (( (xCentr*xCentr+yCentr*yCentr+zCentr*zCentr/1.5)<=4*4 )) {
                        nucleusTotPixel++;
                    } else {
                        citoTotPixel++;
                    }
                }
            }
        }
    }

    //EfPhantomTotalPixels , EfNucleusTotalPixels , EfCytoplasmTotalPixels
    std::cout<<phantomTotPixel<<" " <<nucleusTotPixel<<" " <<citoTotPixel<<std::endl;
    std::cout<<dx<<" " <<dy<<" " <<dz<<std::endl;
    std::cout<<ox<<" " <<oy<<" " <<oz<<std::endl;
    std::cout<<"1_10_1";
    std::cout<<std::endl<<"1_1.1_1";
    for (int x=0; x<nx; x++){
        int xCentr=x-nx/2;
        for (int y=0; y<ny; y++){
            int yCentr=y-ny/2;
            for (int z=0; z<nz; z++){
                int zCentr=z-nz/2;
                if (GetCell(xCentr, yCentr, zCentr)) {
                    if (( (xCentr*xCentr+yCentr*yCentr+zCentr*zCentr/1.5)<=4*4 )) {
                        std::cout<<std::endl<<xCentr<<" " <<yCentr<<" " <<zCentr<<"_2_1_0";
                    } else {
                        std::cout<<std::endl<<xCentr<<" " <<yCentr<<" " <<zCentr<<"_1_1_0";
                    }
                }
            }
        }
    }
}
```

B.2. Oligodendrocytes

```
        }
    }
    return 0;
}
```

The following bash script uses the cell phantom defined by the c++ code and it constructs a 3 by 3 by 3 cubic cell lattice.

```
: '
for tissue implementation
Z=0
    (x-104,y+54,z) (x,y+54,z) (x+104,y+54,z)
    (x-104,y,z) (NOTHING) (x+104,y,z)
    (x-104,y-54,z) (x,y-54,z) (x+104,y-54,z)
Z=1 same as z=0 only with z+50
Z=-1 same as z=0 only with z-50'

# Z=0
cat BUphantom.dat | awk '{ if (NR==1) print $1*27"_"$2*27"_"$3*27; else if (NR>1&&NR<=5) print $0;}'>phantom.dat #
0 0 0
cat BUphantom.dat | awk '{ if (NR>5) print $1-104"_"$2"_"$3"_"$4"_"$5"_"$6}'>>phantom.dat # -1
0 0
cat BUphantom.dat | awk '{ if (NR>5) print $1+104"_"$2"_"$3"_"$4"_"$5"_"$6}'>>phantom.dat # +1
0 0
cat BUphantom.dat | awk '{ if (NR>5) print $1"_"$2+54"_"$3"_"$4"_"$5"_"$6}'>>phantom.dat #
0 +1 0
cat BUphantom.dat | awk '{ if (NR>5) print $1"_"$2-54"_"$3"_"$4"_"$5"_"$6}'>>phantom.dat #
0 -1 0
cat BUphantom.dat | awk '{ if (NR>5) print $1-104"_"$2-54"_"$3"_"$4"_"$5"_"$6}'>>phantom.dat # -1 -1
0
cat BUphantom.dat | awk '{ if (NR>5) print $1+104"_"$2-54"_"$3"_"$4"_"$5"_"$6}'>>phantom.dat #
# +1 -1 0
cat BUphantom.dat | awk '{ if (NR>5) print $1-104"_"$2+54"_"$3"_"$4"_"$5"_"$6}'>>phantom.dat # -1 +1
0
cat BUphantom.dat | awk '{ if (NR>5) print $1+104"_"$2+54"_"$3"_"$4"_"$5"_"$6}'>>phantom.dat # +1 +1
0

# Z=1
cat BUphantom.dat | awk '{ if (NR>5) print $1"_"$2"_"$3+50"_"$4"_"$5"_"$6}'>>phantom.dat #
0 0 1
cat BUphantom.dat | awk '{ if (NR>5) print $1-104"_"$2"_"$3+50"_"$4"_"$5"_"$6}'>>phantom.dat # -1
0 1
cat BUphantom.dat | awk '{ if (NR>5) print $1+104"_"$2"_"$3+50"_"$4"_"$5"_"$6}'>>phantom.dat # +1
0 1
cat BUphantom.dat | awk '{ if (NR>5) print $1"_"$2+54"_"$3+50"_"$4"_"$5"_"$6}'>>phantom.dat #
0 +1 1
cat BUphantom.dat | awk '{ if (NR>5) print $1"_"$2-54"_"$3+50"_"$4"_"$5"_"$6}'>>phantom.dat #
0 -1 1
cat BUphantom.dat | awk '{ if (NR>5) print $1-104"_"$2-54"_"$3+50"_"$4"_"$5"_"$6}'>>phantom.dat # -1 -1
1
cat BUphantom.dat | awk '{ if (NR>5) print $1+104"_"$2-54"_"$3+50"_"$4"_"$5"_"$6}'>>phantom.dat #
# +1 -1 1
cat BUphantom.dat | awk '{ if (NR>5) print $1-104"_"$2+54"_"$3+50"_"$4"_"$5"_"$6}'>>phantom.dat # -1 +1
1
cat BUphantom.dat | awk '{ if (NR>5) print $1+104"_"$2+54"_"$3+50"_"$4"_"$5"_"$6}'>>phantom.dat # +1 +1
1

# Z=-1
cat BUphantom.dat | awk '{ if (NR>5) print $1"_"$2"_"$3-50"_"$4"_"$5"_"$6}'>>phantom.dat #
0 0 1
cat BUphantom.dat | awk '{ if (NR>5) print $1-104"_"$2"_"$3-50"_"$4"_"$5"_"$6}'>>phantom.dat # -1
0 1
cat BUphantom.dat | awk '{ if (NR>5) print $1+104"_"$2"_"$3-50"_"$4"_"$5"_"$6}'>>phantom.dat # +1
0 1
cat BUphantom.dat | awk '{ if (NR>5) print $1"_"$2+54"_"$3-50"_"$4"_"$5"_"$6}'>>phantom.dat #
0 +1 1
cat BUphantom.dat | awk '{ if (NR>5) print $1"_"$2-54"_"$3-50"_"$4"_"$5"_"$6}'>>phantom.dat #
0 -1 1
cat BUphantom.dat | awk '{ if (NR>5) print $1-104"_"$2-54"_"$3-50"_"$4"_"$5"_"$6}'>>phantom.dat # -1 -1
1
cat BUphantom.dat | awk '{ if (NR>5) print $1+104"_"$2-54"_"$3-50"_"$4"_"$5"_"$6}'>>phantom.dat #
# +1 -1 1
cat BUphantom.dat | awk '{ if (NR>5) print $1-104"_"$2+54"_"$3-50"_"$4"_"$5"_"$6}'>>phantom.dat # -1 +1
1
cat BUphantom.dat | awk '{ if (NR>5) print $1+104"_"$2+54"_"$3-50"_"$4"_"$5"_"$6}'>>phantom.dat # +1 +1
1
```

B.2 Oligodendrocytes

The following c++ code defines a triangular prism. The triangular face has a base of 40 μm and an height of 25 μm , while the thickness of the prism is 7.5

```

μm.

#include <iostream>

//passo valori nell sistema di riferimento reale
bool GetCell(int xx, int yy, int zz){
    return ((-xx*1.25+yy)<=25)&&((xx*1.25+yy)<=25);
}

int main(){
    // nx , ny , nz
    int nx=80,ny=50,nz=14;
    // dx , dy , dz dimensione dei pixel
    float dx=0.5,dy=0.5,dz=0.5;
    // offset ox,oy,oz;
    int ox=0,oy=0,oz=0;
    int phantomTotPixel=0,nucleusTotPixel=0,citoTotPixel=0;
    for (int x=0; x<=nx; x++) {
        int xCentr=x-nx/2;
        for (int y=0; y<=ny; y++) {
            int yCentr=y-ny/2;
            for (int z=0; z<=nz; z++) {
                int zCentr=z-nz/2;
                if (GetCell(xCentr, yCentr, zCentr)) {
                    phantomTotPixel++;
                    if (( (xCentr/2.1)*(xCentr/2.1)+((yCentr+10)/1.3)*((yCentr+10)/1.3)+(zCentr+10)/1.3)<=25) {
                        nucleusTotPixel++;
                    } else {
                        citoTotPixel++;
                    }
                }
            }
        }
    }

    //EfPhantomTotalPixels , EfNucleusTotalPixels , EfCytoplasmTotalPixels
    std::cout<<phantomTotPixel<<"_1_<<nucleusTotPixel<<"_2_<<citoTotPixel<<std::endl;
    std::cout<<dx<<"_1_<<dy<<"_2_<<dz<<std::endl;
    std::cout<<ox<<"_1_<<oy<<"_2_<<oz<<std::endl;
    std::cout<<"_1_10_1";
    std::cout<<std::endl<<"_1_1_1_1";
    for (int x=0; x<=nx; x++) {
        int xCentr=x-nx/2;
        for (int y=0; y<=ny; y++) {
            int yCentr=y-ny/2;
            for (int z=0; z<=nz; z++) {
                int zCentr=z-nz/2;
                if (GetCell(xCentr, yCentr, zCentr)) {
                    if (( (xCentr/2.1)*(xCentr/2.1)+((yCentr+10)/1.3)*((yCentr+10)/1.3)+(zCentr+10)/1.3)<=25) {
                        std::cout<<std::endl<<xCentr<<"_1_<<yCentr<<"_2_<<zCentr<<"_1_1_1_1";
                    } else {
                        std::cout<<std::endl<<xCentr<<"_1_<<yCentr<<"_2_<<zCentr<<"_1_1_1_1";
                    }
                }
            }
        }
    }
    return 0;
}

```

The following bash script uses the cell phantom defined by the c++ code and it constructs a 3 by 3 by 3 cubic cell lattice.

```

: '
for tissue like geometry
Z=0
    (x-50,y+50,z)    (x,y+50,z)    (x+50,y+50,z)
    (x-50,y,z)       (NOTHING)     (x+50,y,z)
    (x-50,y-50,z)    (x,y-50,z)    (x+50,y-50,z)
Z=1 same as z=0 only with z+50
Z=1 same as z=0 only with z-50'

# Z=0
cat BUphantom.dat | awk '{ if (NR==1) print $1*38"_1_"$2*38"_2_"$3*38; else if(NR>1&&NR<=5) print $0;}'>phantom.dat
0 0 0
cat BUphantom.dat | awk '{ if (NR>5) print $1-80"_1_"$2"_3_"$4"_5_"$6}' >> phantom.dat # -1
0 1
cat BUphantom.dat | awk '{ if (NR>5) print $1+80"_1_"$2"_3_"$4"_5_"$6}' >> phantom.dat # +1
0 1
cat BUphantom.dat | awk '{ if (NR>5) print $1+40"_1_"$2*(-1)+1"_3_"$4"_5_"$6}' >> phantom.dat #
0 +1 1
cat BUphantom.dat | awk '{ if (NR>5) print $1-40"_1_"$2*(-1)+1"_3_"$4"_5_"$6}' >> phantom.dat # -1 +1
1
cat BUphantom.dat | awk '{ if (NR>5) print $1"_1_"$2*(-1)+52+1"_3_"$4"_5_"$6}' >> phantom.dat #
0 0 1

```


B.3. Hepatocytes

```
cat BUphantom.dat | awk '{ if (NR>5) print $1+40"_"$2+52"_"$3"_"$4"_"$5"_"$6}' >> phantom.dat #
0 +1 1
cat BUphantom.dat | awk '{ if (NR>5) print $1-40"_"$2+52"_"$3"_"$4"_"$5"_"$6}' >> phantom.dat # -1 +1
1

cat BUphantom.dat | awk '{ if (NR>5) print $1"_"$2*(-1)-50-1"_"$3"_"$4"_"$5"_"$6}' >> phantom.dat #
0 0 1
cat BUphantom.dat | awk '{ if (NR>5) print $1-80"_"$2*(-1)-50-1"_"$3"_"$4"_"$5"_"$6}' >> phantom.dat #
0 1
cat BUphantom.dat | awk '{ if (NR>5) print $1+80"_"$2*(-1)-50-1"_"$3"_"$4"_"$5"_"$6}' >> phantom.dat #
0 1
cat BUphantom.dat | awk '{ if (NR>5) print $1+40"_"$2-50-2"_"$3"_"$4"_"$5"_"$6}' >> phantom.dat #
0 +1 1
cat BUphantom.dat | awk '{ if (NR>5) print $1-40"_"$2-50-2"_"$3"_"$4"_"$5"_"$6}' >> phantom.dat # -1 +1
1

# Z=1
cat BUphantom.dat | awk '{ if (NR>5) print $1"_"$2"_"$3+14"_"$4"_"$5"_"$6}' >> phantom.dat #
0 0 1
cat BUphantom.dat | awk '{ if (NR>5) print $1-80"_"$2"_"$3+14"_"$4"_"$5"_"$6}' >> phantom.dat # -1
0 1
cat BUphantom.dat | awk '{ if (NR>5) print $1+80"_"$2"_"$3+14"_"$4"_"$5"_"$6}' >> phantom.dat # +1
0 1
cat BUphantom.dat | awk '{ if (NR>5) print $1+40"_"$2*(-1)+1"_"$3+14"_"$4"_"$5"_"$6}' >> phantom.dat #
0 +1 1
cat BUphantom.dat | awk '{ if (NR>5) print $1-40"_"$2*(-1)+1"_"$3+14"_"$4"_"$5"_"$6}' >> phantom.dat # -1 +1
1

cat BUphantom.dat | awk '{ if (NR>5) print $1"_"$2*(-1)+52+1"_"$3+14"_"$4"_"$5"_"$6}' >> phantom.dat #
0 0 1
cat BUphantom.dat | awk '{ if (NR>5) print $1+40"_"$2+52"_"$3+14"_"$4"_"$5"_"$6}' >> phantom.dat #
0 +1 1
cat BUphantom.dat | awk '{ if (NR>5) print $1-40"_"$2+52"_"$3+14"_"$4"_"$5"_"$6}' >> phantom.dat # -1 +1
1

cat BUphantom.dat | awk '{ if (NR>5) print $1"_"$2*(-1)-50-1"_"$3+14"_"$4"_"$5"_"$6}' >> phantom.dat #
0 0 1
cat BUphantom.dat | awk '{ if (NR>5) print $1-80"_"$2*(-1)-50-1"_"$3+14"_"$4"_"$5"_"$6}' >> phantom.dat #
0 1
cat BUphantom.dat | awk '{ if (NR>5) print $1+80"_"$2*(-1)-50-1"_"$3+14"_"$4"_"$5"_"$6}' >> phantom.dat #
0 1
cat BUphantom.dat | awk '{ if (NR>5) print $1+40"_"$2-50-2"_"$3+14"_"$4"_"$5"_"$6}' >> phantom.dat #
0 +1 1
cat BUphantom.dat | awk '{ if (NR>5) print $1-40"_"$2-50-2"_"$3+14"_"$4"_"$5"_"$6}' >> phantom.dat # -1 +1
1

# Z=-1
cat BUphantom.dat | awk '{ if (NR>5) print $1"_"$2"_"$3-14"_"$4"_"$5"_"$6}' >> phantom.dat #
0 0 1
cat BUphantom.dat | awk '{ if (NR>5) print $1-80"_"$2"_"$3-14"_"$4"_"$5"_"$6}' >> phantom.dat # -1
0 1
cat BUphantom.dat | awk '{ if (NR>5) print $1+80"_"$2"_"$3-14"_"$4"_"$5"_"$6}' >> phantom.dat # +1
0 1
cat BUphantom.dat | awk '{ if (NR>5) print $1+40"_"$2*(-1)+1"_"$3-14"_"$4"_"$5"_"$6}' >> phantom.dat #
0 +1 1
cat BUphantom.dat | awk '{ if (NR>5) print $1-40"_"$2*(-1)+1"_"$3-14"_"$4"_"$5"_"$6}' >> phantom.dat # -1 +1
1

cat BUphantom.dat | awk '{ if (NR>5) print $1"_"$2*(-1)+52+1"_"$3-14"_"$4"_"$5"_"$6}' >> phantom.dat #
0 0 1
cat BUphantom.dat | awk '{ if (NR>5) print $1+40"_"$2+52"_"$3-14"_"$4"_"$5"_"$6}' >> phantom.dat #
0 +1 1
cat BUphantom.dat | awk '{ if (NR>5) print $1-40"_"$2+52"_"$3-14"_"$4"_"$5"_"$6}' >> phantom.dat # -1 +1
1

cat BUphantom.dat | awk '{ if (NR>5) print $1"_"$2*(-1)-50-1"_"$3-14"_"$4"_"$5"_"$6}' >> phantom.dat #
0 0 1
cat BUphantom.dat | awk '{ if (NR>5) print $1-80"_"$2*(-1)-50-1"_"$3-14"_"$4"_"$5"_"$6}' >> phantom.dat #
0 1
cat BUphantom.dat | awk '{ if (NR>5) print $1+80"_"$2*(-1)-50-1"_"$3-14"_"$4"_"$5"_"$6}' >> phantom.dat #
0 1
cat BUphantom.dat | awk '{ if (NR>5) print $1+40"_"$2-50-2"_"$3-14"_"$4"_"$5"_"$6}' >> phantom.dat #
0 +1 1
cat BUphantom.dat | awk '{ if (NR>5) print $1-40"_"$2-50-2"_"$3-14"_"$4"_"$5"_"$6}' >> phantom.dat # -1 +1
1
```

B.3 Hepatocytes

The following c++ code defines a regular octagonal prism phantom with an height of 15 μm while the octagonal face has side of length 6.2 μm .

```
#include <iostream>

//passo valori nell sistema di riferimento reale
bool GetCell(int xx, int yy, int zz){
    return ((xx+yy)<22)&&((xx-yy)<22)&&((-xx-yy)<22)&&((-xx+yy)<22);
```

```

}

int main(){
    // nx , ny , nz
    int nx=30,ny=30,nz=30;
    // dx , dy , dz dimensione dei pixel
    float dx=0.5,dy=0.5,dz=0.5;
    // offset ox,oy,oz;
    int ox=0,oy=0,oz=0;
    //param Et,Ey,Ez,Emat,Eden,Ettmp
    int phantomTotPixel=0,nucleusTotPixel=0,citoTotPixel=0;
    for (int x=0; x<nx; x++) {
        int xCentr=x-nx/2;
        for (int y=0; y<ny; y++) {
            int yCentr=y-ny/2;
            for (int z=0; z<nz; z++) {
                int zCentr=z-nz/2;
                if (GetCell(xCentr, yCentr, zCentr)) {
                    phantomTotPixel++;
                    if (( (xCentr*xCentr+yCentr*yCentr+zCentr*zCentr)<=7*7 )) {
                        nucleusTotPixel++;
                    } else {
                        citoTotPixel++;
                    }
                }
            }
        }
    }

    //EfPhantomTotalPixels, EfNucleusTotalPixels, EfCytoplasmTotalPixels
    std::cout<<phantomTotPixel<<"_"<<nucleusTotPixel<<"_"<<citoTotPixel<<std::endl;
    std::cout<<dx<<"_"<<dy<<"_"<<dz<<std::endl;
    std::cout<<ox<<"_"<<oy<<"_"<<oz<<std::endl;
    std::cout<<"1_10_1";
    std::cout<<std::endl<<"1_1.1_1";
    for (int x=0; x<nx; x++) {
        int xCentr=x-nx/2;
        for (int y=0; y<ny; y++) {
            int yCentr=y-ny/2;
            for (int z=0; z<nz; z++) {
                int zCentr=z-nz/2;
                if (GetCell(xCentr, yCentr, zCentr)) {
                    if (( (xCentr*xCentr+yCentr*yCentr+zCentr*zCentr/1.5)<=7*7 )) {
                        std::cout<<std::endl<<xCentr<<"_"<<yCentr<<"_"<<zCentr<<"_2_1_0";
                    } else {
                        std::cout<<std::endl<<xCentr<<"_"<<yCentr<<"_"<<zCentr<<"_1_1_0";
                    }
                }
            }
        }
    }
    return 0;
}

```

The following bash script uses the cell phantom defined by the c++ code and it constructs a 3 by 3 by 3 cubic cell lattice.

```

: '
for tissue like geometry
Z=0
    (x-104,y+54,z)  (x,y+54,z)  (x+104,y+54,z)
    (x-104,y,z)     (NOTHING)   (x+104,y,z)
    (x-104,y-54,z) (x,y-54,z)  (x+104,y-54,z)
Z=1 same as z=0 only with z+50
Z=1 same as z=0 only with z-50'

# Z=0
cat BUphantom.dat | awk '{ if (NR==1) print $1*27"_"$2*27"_"$3*27; else if(NR>1&&NR<=5) print $0;}'>phantom.dat
0 0 0
cat BUphantom.dat | awk '{ if (NR>5) print $1-104"_"$2"_"$3"_"$4"_"$5"_"$6}' >> phantom.dat # -1
0 0
cat BUphantom.dat | awk '{ if (NR>5) print $1+104"_"$2"_"$3"_"$4"_"$5"_"$6}' >> phantom.dat # +1
0 0
cat BUphantom.dat | awk '{ if (NR>5) print $1"_"$2+54"_"$3"_"$4"_"$5"_"$6}' >> phantom.dat #
0 +1 0
cat BUphantom.dat | awk '{ if (NR>5) print $1"_"$2-54"_"$3"_"$4"_"$5"_"$6}' >> phantom.dat #
0 -1 0
cat BUphantom.dat | awk '{ if (NR>5) print $1-104"_"$2-54"_"$3"_"$4"_"$5"_"$6}' >> phantom.dat # -1 -1
0
cat BUphantom.dat | awk '{ if (NR>5) print $1+104"_"$2-54"_"$3"_"$4"_"$5"_"$6}' >> phantom.dat # +1 -1
0
cat BUphantom.dat | awk '{ if (NR>5) print $1-104"_"$2+54"_"$3"_"$4"_"$5"_"$6}' >> phantom.dat # -1 +1
0
cat BUphantom.dat | awk '{ if (NR>5) print $1+104"_"$2+54"_"$3"_"$4"_"$5"_"$6}' >> phantom.dat # +1 +1
0
# Z=1

```

B.3. Hepatocytes

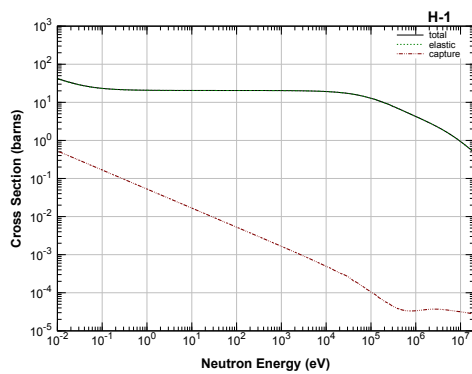
```
cat BUphantom.dat | awk '{ if (NR>5) print $1"_"$2"_"$3+50"_"$4"_"$5"_"$6}' >> phantom.dat #
0 0 1
cat BUphantom.dat | awk '{ if (NR>5) print $1-104"_"$2"_"$3+50"_"$4"_"$5"_"$6}' >> phantom.dat # -1
0 1
cat BUphantom.dat | awk '{ if (NR>5) print $1+104"_"$2"_"$3+50"_"$4"_"$5"_"$6}' >> phantom.dat # +1
0 1
cat BUphantom.dat | awk '{ if (NR>5) print $1"_"$2+54"_"$3+50"_"$4"_"$5"_"$6}' >> phantom.dat #
0 +1 1
cat BUphantom.dat | awk '{ if (NR>5) print $1"_"$2-54"_"$3+50"_"$4"_"$5"_"$6}' >> phantom.dat #
0 -1 1
cat BUphantom.dat | awk '{ if (NR>5) print $1-104"_"$2-54"_"$3+50"_"$4"_"$5"_"$6}' >> phantom.dat # -1 -1
1
cat BUphantom.dat | awk '{ if (NR>5) print $1+104"_"$2-54"_"$3+50"_"$4"_"$5"_"$6}' >> phantom.dat #
# +1 -1 1
cat BUphantom.dat | awk '{ if (NR>5) print $1-104"_"$2+54"_"$3+50"_"$4"_"$5"_"$6}' >> phantom.dat # -1 +1
1
cat BUphantom.dat | awk '{ if (NR>5) print $1+104"_"$2+54"_"$3+50"_"$4"_"$5"_"$6}' >> phantom.dat # +1 +1
1
# Z=-1
cat BUphantom.dat | awk '{ if (NR>5) print $1"_"$2"_"$3-50"_"$4"_"$5"_"$6}' >> phantom.dat #
0 0 1
cat BUphantom.dat | awk '{ if (NR>5) print $1-104"_"$2"_"$3-50"_"$4"_"$5"_"$6}' >> phantom.dat # -1
0 1
cat BUphantom.dat | awk '{ if (NR>5) print $1+104"_"$2"_"$3-50"_"$4"_"$5"_"$6}' >> phantom.dat # +1
0 1
cat BUphantom.dat | awk '{ if (NR>5) print $1"_"$2+54"_"$3-50"_"$4"_"$5"_"$6}' >> phantom.dat #
0 +1 1
cat BUphantom.dat | awk '{ if (NR>5) print $1"_"$2-54"_"$3-50"_"$4"_"$5"_"$6}' >> phantom.dat #
0 -1 1
cat BUphantom.dat | awk '{ if (NR>5) print $1-104"_"$2-54"_"$3-50"_"$4"_"$5"_"$6}' >> phantom.dat # -1 -1
1
cat BUphantom.dat | awk '{ if (NR>5) print $1+104"_"$2-54"_"$3-50"_"$4"_"$5"_"$6}' >> phantom.dat #
# +1 -1 1
cat BUphantom.dat | awk '{ if (NR>5) print $1-104"_"$2+54"_"$3-50"_"$4"_"$5"_"$6}' >> phantom.dat # -1 +1
1
cat BUphantom.dat | awk '{ if (NR>5) print $1+104"_"$2+54"_"$3-50"_"$4"_"$5"_"$6}' >> phantom.dat # +1 +1
1
```


Appendix C

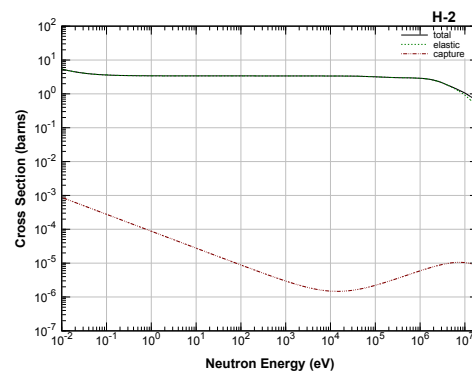
C - Cross Section Table and MCNP Material compositions

C.1 Cross Sections

C.1.1 Hydrogen



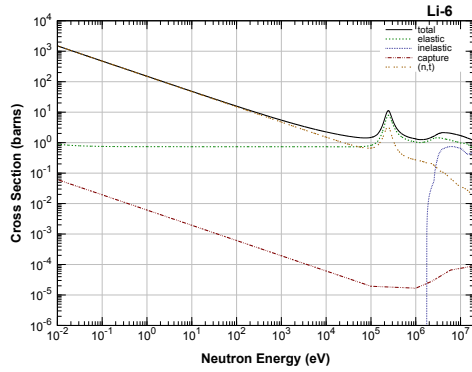
(a) ^1_1H neutron cross section.



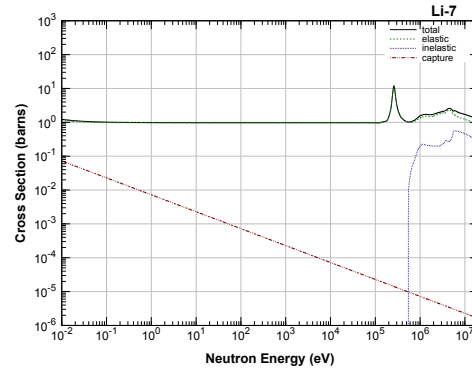
(b) ^2_1H neutron cross section.

Figure C.1: Figures C.1a and C.1b show the neutron cross section of natural isotopes of hydrogen[143], the abundance of those atoms are respectively: 99,985% and 0.015% .

C.1.2 Lithium



(a) ${}^6_3\text{Li}$ neutron cross section.



(b) ${}^7_3\text{Li}$ neutron cross section.

Figure C.2: Figures C.2a and C.2b show the neutron cross section of natural isotopes of lithium[143], the abundance of those atoms are respectively: 7,5% and 92,5% .

C.1.3 Beryllium

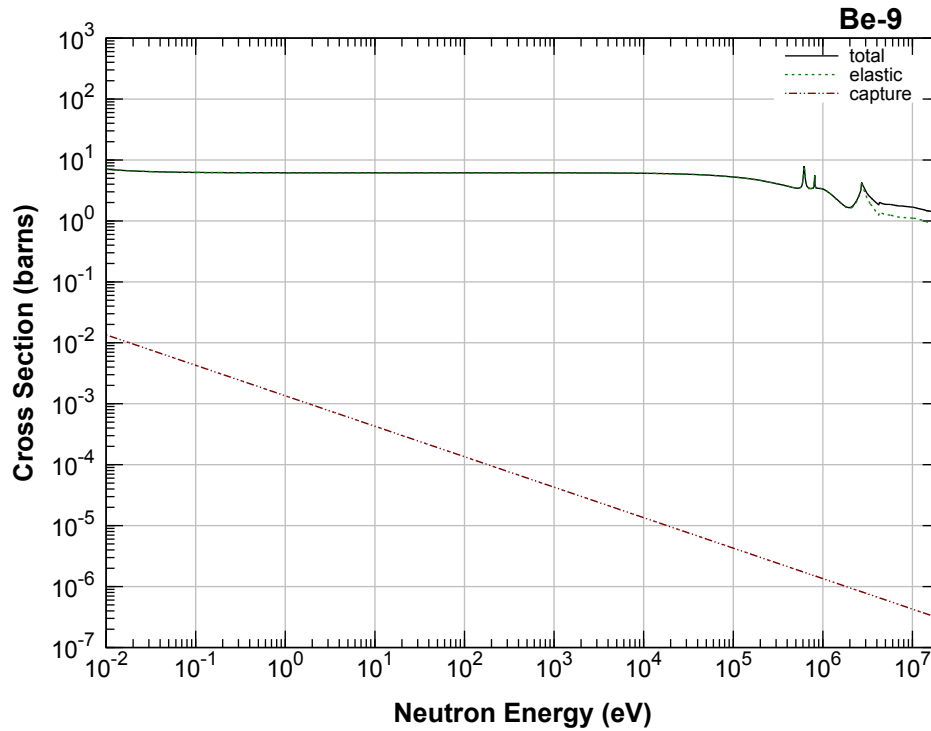


Figure C.3: ${}^9_4\text{Be}$ neutron cross section[143].

C.1.4 Carbon

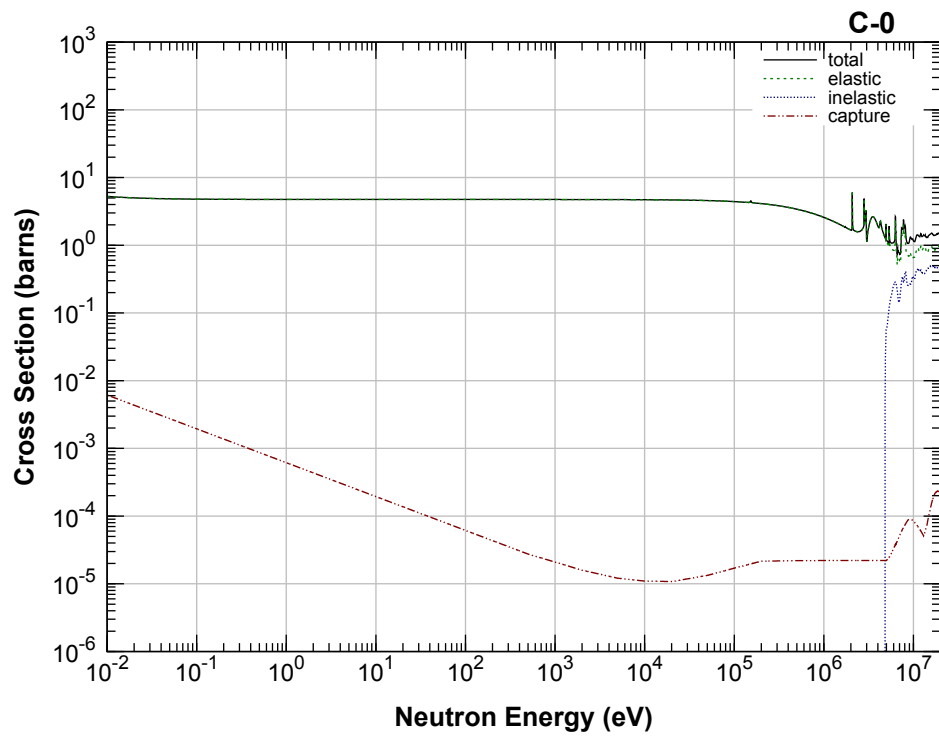


Figure C.4: ^{12}C neutron cross section[143].

C.1.5 Oxygen

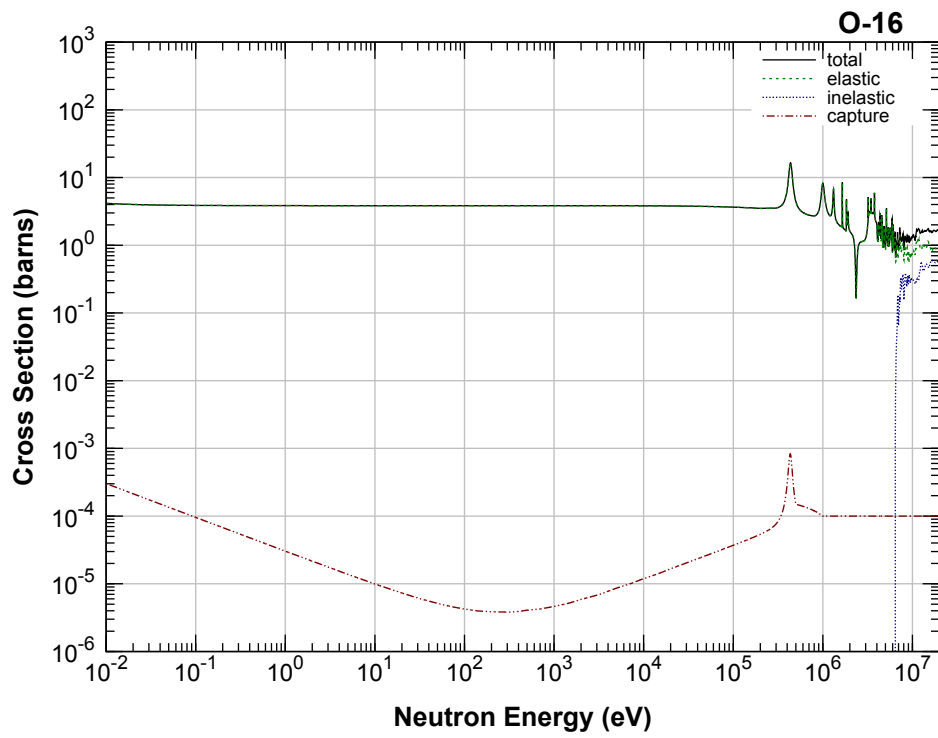


Figure C.5: ^{16}O neutron cross section[143].

C.1.6 Fluorine

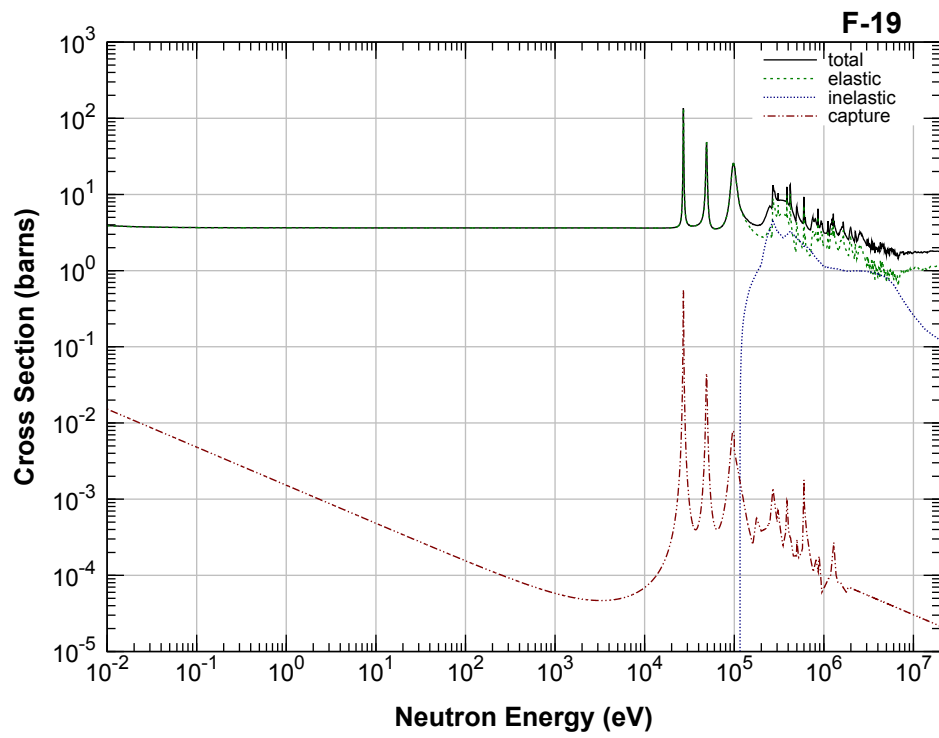
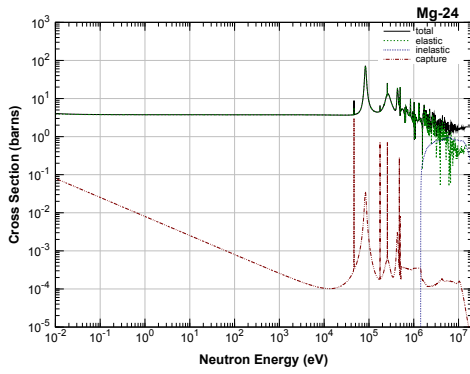
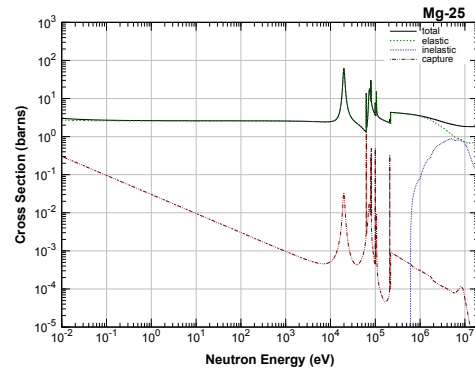


Figure C.6: ^{19}F neutron cross section[143].

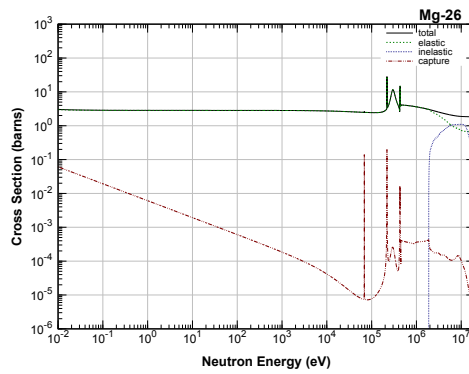
C.1.7 Magnesium



(a) ^{24}Mg neutron cross section.



(b) ^{25}Mg neutron cross section.



(c) ^{26}Mg neutron cross section.

Figure C.7: Figures C.7a, C.7b and C.7c show the neutron cross section of natural isotopes of magnesium [143], the abundance of those atoms are respectively: 78.99%, 10% and 11.01% .

C.1.8 Aluminium

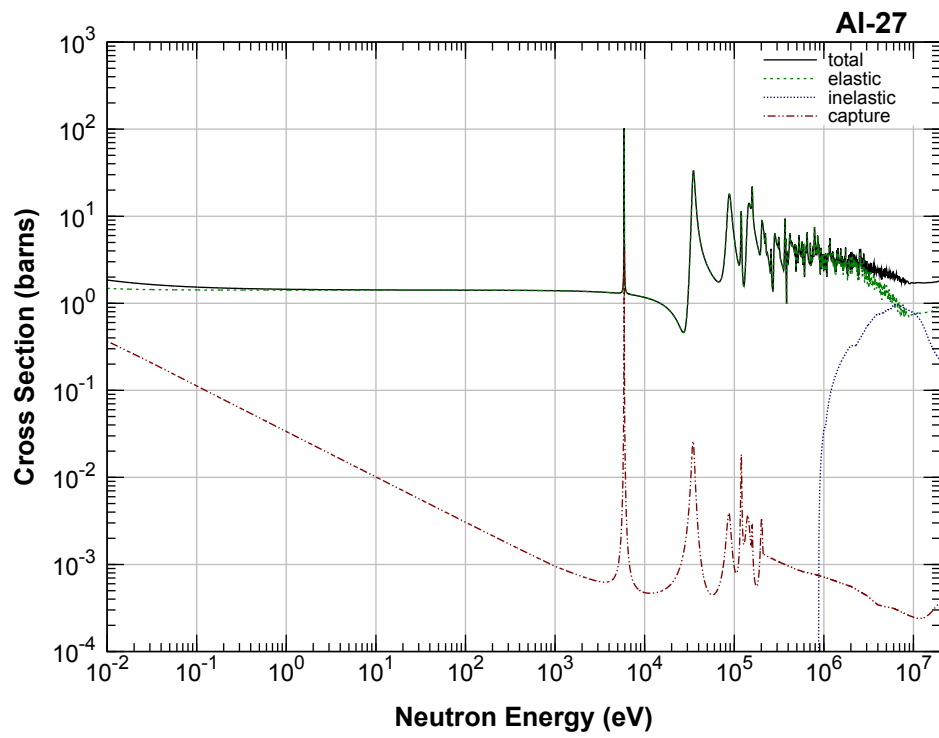
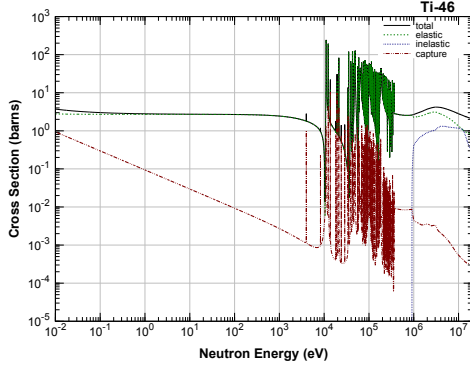
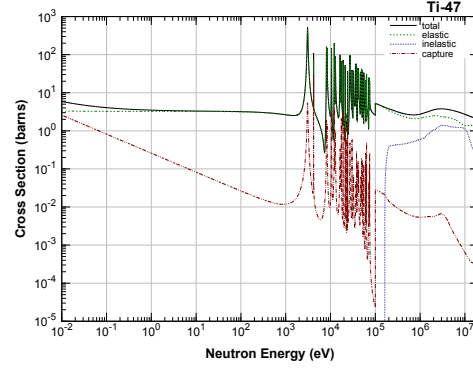


Figure C.8: $^{27}_{13}\text{Al}$ neutron cross section[143].

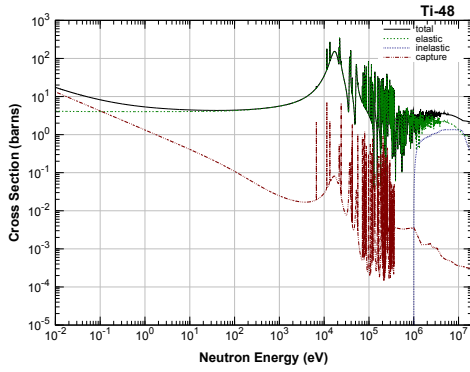
C.1.9 Titanium



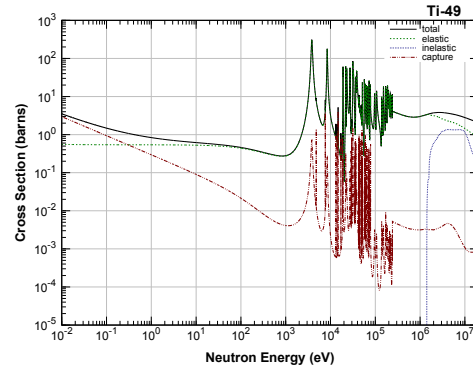
(a) $^{46}_{22}\text{Ti}$ neutron cross section.



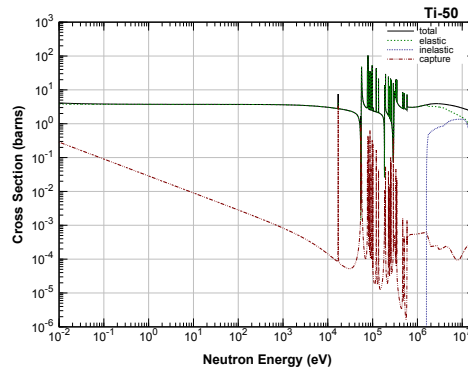
(b) $^{47}_{22}\text{Ti}$ neutron cross section.



(c) $^{48}_{22}\text{Ti}$ neutron cross section.



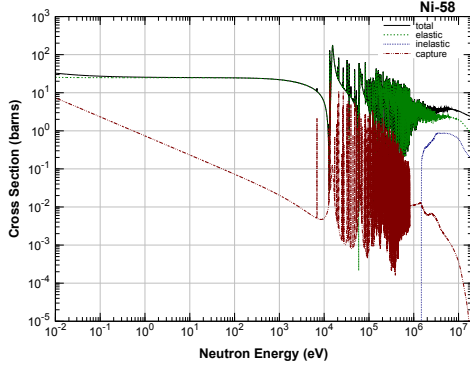
(d) $^{49}_{22}\text{Ti}$ neutron cross section.



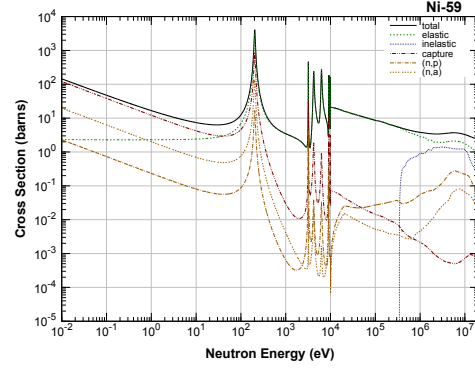
(e) $^{50}_{22}\text{Ti}$ neutron cross section.

Figure C.9: Figures C.9a, C.9b, C.9c, C.9d and C.9e show the neutron cross section of natural isotopes of Titanium[143], the abundance of those atoms are respectively: 8%, 7.3%, 73.8%, 5.5%, 5.4% .

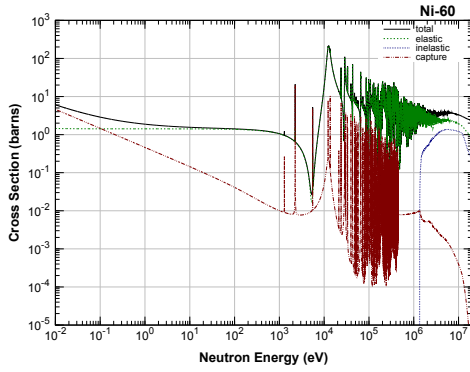
C.1.10 Nickel



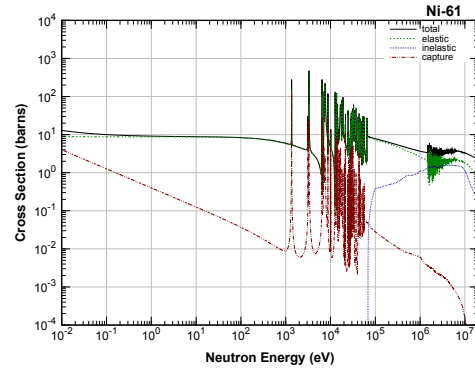
(a) ^{58}Ni neutron cross section.



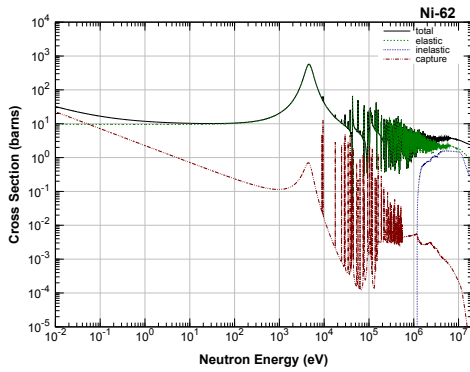
(b) ^{59}Ni neutron cross section.



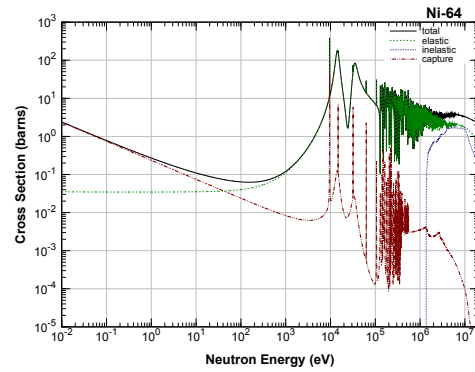
(c) ^{60}Ni neutron cross section.



(d) ^{61}Ni neutron cross section.



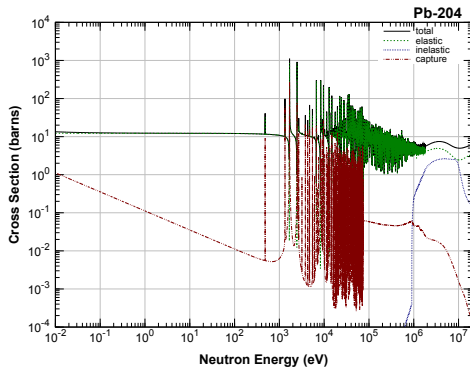
(e) ^{62}Ni neutron cross section.



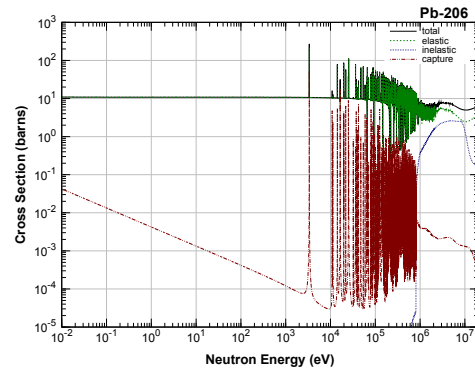
(f) ^{64}Ni neutron cross section.

Figure C.10: Figures C.10a, C.10b, C.10c, C.10d, C.10e and C.10f show the neutron cross section of natural isotopes of nickel [143], the abundance of those atoms are respectively: 68.077%, 0% , 26.233% , 1.14%, 3.634% and 0.926% .

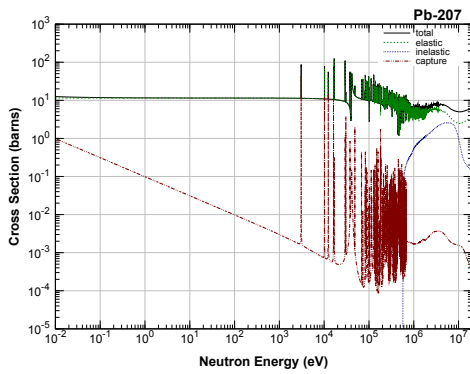
C.1.11 Lead



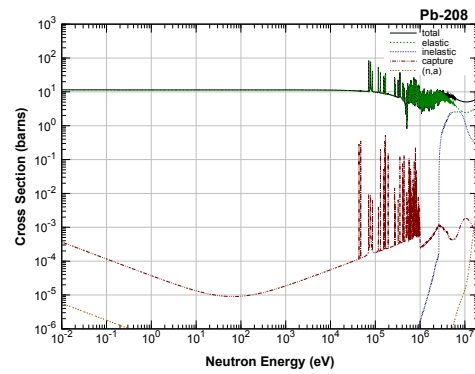
(a) $^{204}_{82}\text{Pb}$ neutron cross section.



(b) $^{206}_{82}\text{Ni}$ neutron cross section.



(c) $^{207}_{82}\text{Pb}$ neutron cross section.



(d) $^{208}_{82}\text{Pb}$ neutron cross section.

Figure C.11: Figures C.11a, C.11b, C.11c and C.11d show the neutron cross section of natural isotopes of lead [143], the abundance of those atoms are respectively: 1.4%, 24.1% , 22.1% and 52.4% .

C.1.12 Bismuth

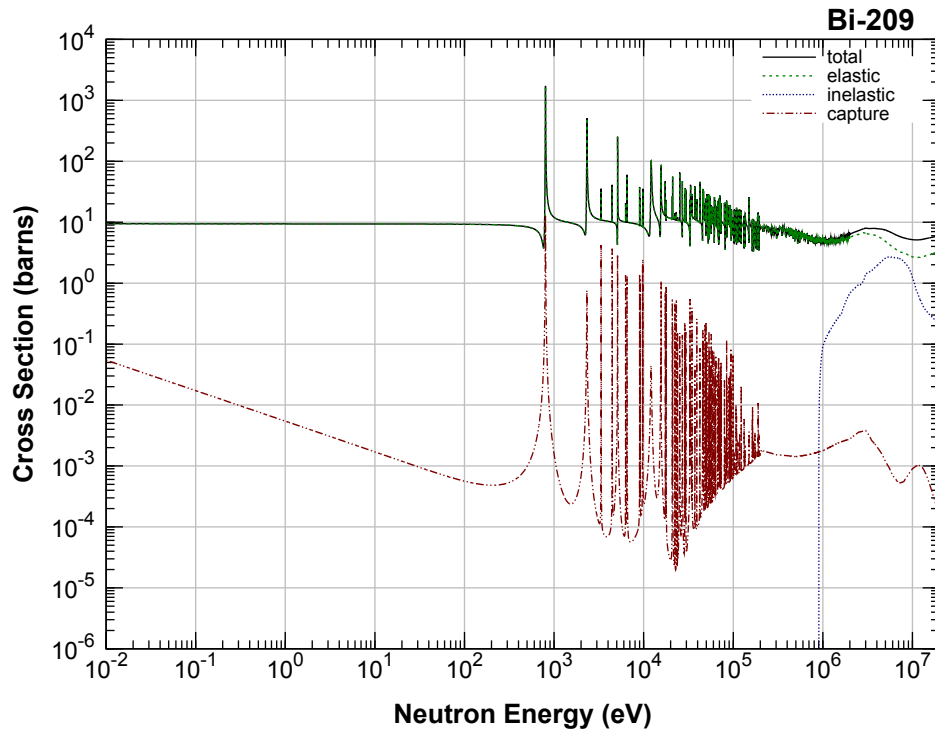


Figure C.12: $^{209}_{83}\text{Bi}$ neutron cross section[143].

C.2 MCNP Material composition

C.2.1 Aluminium Alloys

Table C.1: Aluminium fluoride (AlF_3) with a density of $3.1 \text{ g}\cdot\text{cm}^3$

Athom	Atomic density	MCNP material
$^{27}_{13}\text{Al}$	1	13027.70c
$^{19}_9\text{F}$	3	9019.70c

Table C.2: Magnox (MgAl) with a density of $1.74 \text{ g}\cdot\text{cm}^3$

Athom	Mass density	MCNP material
$^{27}_{13}\text{Al}$	0.01	13027.70c
$^{12}_{12}\text{Mg}$	0.99	12000.62c

C.2.2 Lithium fluoride

Table C.3: Lithium fluoride (LiF) with a density of $2.635 \text{ g}\cdot\text{cm}^3$

Athom	Atomic density	MCNP material
^6_3Li	0.03735	3006.60c
^7_3Li	0.46265	3007.60c
$^{19}_9\text{F}$	0.5	9019.60c

C.2.3 Lithium loaded polyethylene

Table C.4: Lithium loaded polyethylene with a density of $1.06 \text{ g}\cdot\text{cm}^3$

Athom	Atomic density	MCNP material
^1_1H	0.6155	1001.60c
^6_3Li	0.0058	3006.60c
^7_3Li	0.0710	3007.60c
$^{12}_6\text{C}$	0.3077	6000.60c

C.2.4 Lithium carbonate

Table C.5: Lithium carbonate with a density of $2.1 \text{ g}\cdot\text{cm}^3$

Athom	Atomic density	MCNP material
$^{16}_8\text{O}$	3	8016.60c
^6_3Li	0.15	3006.60c
^7_3Li	1.85	3007.60c
$^{12}_6\text{C}$	1	6000.60c

C.2.5 Titanium

m23 22000.60c -0.90 13027.70c -0.06 23051 -0.4

Table C.6: Ti6Al4V alloy with a density of $4.42 \text{ g}\cdot\text{cm}^3$

Athom	Mass density	MCNP material
$_{22}\text{Ti}$	0.90	22000.60c
$_{13}^{27}\text{Al}$	0.06	13027.70c
$_{23}^{51}\text{V}$	0.04	23051

Appendix D

List of publications

- 1 - MA Gadan, S Bortolussi, I Postuma, F Ballarini, P Bruschi, N Protti, D Santoro, S Stella, L Cansolino, A Clerici, et al. Set-up and calibration of a method to measure ^{10}B concentration in biological samples by neutron autoradiography. *Nuclear Instruments and Methods in Physics Research Section B: Beam Interactions with Materials and Atoms*, 274:51–56, 2012
- 2 - Silva Bortolussi, Laura Ciani, Ian Postuma, Nicoletta Protti, Luca Reversi, Piero Bruschi, Cinzia Ferrari, Laura Cansolino, Luigi Panza, Sandra Ristori, et al. Boron concentration measurements by alpha spectrometry and quantitative neutron autoradiography in cells and tissues treated with different boronated formulations and administration protocols. *Applied Radiation and Isotopes*, 88:78–80, 2014
- 3 - Laura Ciani, Silva Bortolussi, Ian Postuma, Laura Cansolino, Cinzia Ferrari, Luigi Panza, Saverio Altieri, and Sandra Ristori. Rational design of gold nanoparticles functionalized with carboranes for application in boron neutron capture therapy. *International journal of pharmaceutics*, 458(2):340–346, 2013
- 4 - Paolo Colautti, Davide Moro, S Chiriotti, Valeria Conte, Laura Evangelista, Saverio Altieri, Silvia Bortolussi, Nicoletta Protti, and Ian Postuma. Microdosimetric measurements in the thermal neutron irradiation facility of lena reactor. *Applied Radiation and Isotopes*, 88:147–152, 2014
- 5 - Nicoletta Protti, Sergio Manera, Michele Prata, Daniele Alloni, Francesca Ballarini, Andrea Borio di Tigliole, Silva Bortolussi, Piero Bruschi, Marcella Cagnazzo, Maria Garioni, et al. Gamma residual radioactivity measurements on rats and mice irradiated in the thermal column of a triga mark ii reactor for bnct. *Health physics*, 107(6):534–541, 2014
- 6 - S Altieri, F Ballarini, S Bortolussi, I Postuma, N Protti, R Nano, C Rovelli, L Cansolino, AM Clerici, C Ferrari, et al. Neutron capture therapy

- research at infn and university of pavia. In *ANTICANCER RESEARCH*, volume 34, pages 7479–7479. INT INST ANTICANCER RESEARCH EDITORIAL OFFICE 1ST KM KAPANDRITIOU-KALAMOU RD KAPANDRITI, PO BOX 22, ATHENS 19014, GREECE, 2014
- 7 - Daniela Pietrangeli, Angela Rosa, Antonietta Pepe, Saverio Altieri, Silva Bortolussi, Ian Postuma, Nicoletta Protti, Cinzia Ferrari, Laura Cansolino, Anna Maria Clerici, et al. Water-soluble carboranyl-phthalocyanines for bnct. synthesis, characterization, and in vitro tests of the zn (ii)-nido-carboranyl-hexylthiophthalocyanine. *Dalton Transactions*, 2015
- 8 - MP Carante, S Altieri, S Bortolussi, I Postuma, N Protti, and F Ballarini. Modeling radiation-induced cell death: role of different levels of dna damage clustering. *Radiation and environmental biophysics*, pages 1–12, 2015
- 9 - Agustina Portu, Ian Postuma, Mario Alberto Gadan, Gisela Saint Martin, María Silvina Olivera, Saverio Altieri, Nicoletta Protti, and Silva Bortolussi. Inter-comparison of boron concentration measurements at infn-university of pavia (italy) and cnea (argentina). *Applied Radiation and Isotopes*, 2015
- 10 - L Cansolino, AM Clerici, C Zonta, P Dionigi, G Mazzini, R Di Liberto, S Altieri, F Ballarini, S Bortolussi, MP Carante, et al. Comparative study of the radiobiological effects induced on adherent vs suspended cells by bnct, neutrons and gamma rays treatments. *Applied Radiation and Isotopes*, 2015
- 11 - N Protti, S Geninatti-Crich, D Alberti, S Lanzardo, A Deagostino, A Toppino, S Aime, F Ballarini, S Bortolussi, P Bruschi, et al. Evaluation of the dose enhancement of combined ^{10}B + ^{157}Gd neutron capture therapy (nct). *Radiation Protection Dosimetry*, page ncv300, 2015

Bibliography

- [1] M.B. Chadwick, M. Herman, P. Obložinský, M.E. Dunn, Y. Danon, A.C. Kahler, D.L. Smith, B. Pritychenko, G. Arbanas, R. Arcilla, R. Brewer, D.A. Brown, R. Capote, A.D. Carlson, Y.S. Cho, H. Derrien, K. Guber, G.M. Hale, S. Hoblit, S. Holloway, T.D. Johnson, T. Kawano, B.C. Kiedrowski, H. Kim, S. Kunieda, N.M. Larson, L. Leal, J.P. Leestone, R.C. Little, E.A. McCutchan, R.E. MacFarlane, M. MacInnes, C.M. Mattoon, R.D. McKnight, S.F. Mughabghab, G.P.A. Nobre, G. Palmiotti, A. Palumbo, M.T. Pigni, V.G. Pronyaev, R.O. Sayer, A.A. Sonzogni, N.C. Summers, P. Talou, I.J. Thompson, A. Trkov, R.L. Vogt, S.C. van der Marck, A. Wallner, M.C. White, D. Wiarda, and P.G. Young. Endf/b-vii.1 nuclear data for science and technology: Cross sections, covariances, fission product yields and decay data. *Nuclear Data Sheets*, 112(12):2887 – 2996, 2011. Special Issue on ENDF/B-VII.1 Library.
- [2] S. Altieri, M. Balzi, S. Bortolussi, P. Bruschi, L. Ciani, A. M. Clerici, P. Faraoni, C. Ferrari, M. A. Gadan, L. Panza, D. Pietrangeli, G. Ricciardi, and S. Ristori. Carborane derivatives loaded into liposomes as efficient delivery systems for boron neutron capture therapy. *J. Med. Chem.*, 52:7829–7832, 2009.
- [3] A Crivello, C Nervi, R Gobetto, S Geninatti Crich, I Szabo, A Barge, A Toppino, A Deagostino, P Venturello, and S Aime. Towards improved boron neutron capture therapy agents: evaluation of in vitro cellular uptake of a glutamine-functionalized carborane. *J Bio Inorg Chem*, 14:883–890, 2009.
- [4] S-I Masunaga, K Ono, M Kirihata, et al. Potential of alfa- amino alcohol p- boronphenylalaninol as a boron carrier in boron neutron capture therapy, regarding its enantiomers. *J Cancer Res Clin Oncol*, 129:21–28, 2003.
- [5] ZJ Lesnikowski and RF Schinazi. Boron containing oligonucleotides. *Nucleosides Nucleotides*, 17:635–647, 1998.
- [6] MF Hathorne, DA Feakes, and K Shelly. Recent results with liposomes as boron delivery vehicles from boron neutron capture therapy. *Mishima Y*,

- editor Cancer neutron capture therapy New York: Plenum Press*, 17:27–36, 1998.
- [7] RF Barth, DM Adams, AH Soloway, F Alam, and MV Darby. Boronated starburst dendrimer-monoclonal antibody immunoconjugates: evaluation as a potential delivery system for neutron capture therapy. *Bioconjug Chem*, 5:58–66, 1994.
- [8] G Wu, RF Barth, W Yang, et al. Site-specific conjugation of boron containing dendrimers to anti-egf receptor monoclonal antibody centuximab (imcc225) and its evaluation as a potential delivery agent for neutron capture therapy. *Bioconjug Chem*, 15:185–194, 2004.
- [9] Lothar Weissfloch, Michael Bremer, Peter Lemmen, Thomas Probst, Matthias Wagner, Michael Peller, Thomas Auberger, Reingard Senekowitsch-Schmidtke, Karlheinz Tempel, and Michael Molls. New drugs for bnct: An experimental approach. *Strahlentherapie und Onkologie*, 175:118–120, 1999.
- [10] L. Ciani, S. Bortolussi, I. Postuma, L. Cansolino, C. Ferrari, L. Panza, S. Altieri, and S. Ristori. Rational design of gold nanoparticles functionalized with carboranes for application in boron neutron capture therapy. *International Journal of Pharmaceutics*, 458:340 – 346, 2013.
- [11] DA Allen and TD Beynon. A design study for an accelerator-based epithermal neutron beam for bnct. *Physics in medicine and biology*, 40(5):807, 1995.
- [12] Christopher N Culbertson, Stuart Green, Anna J Mason, David Picton, Gareth Baugh, Richard P Hugtenburg, Zaizhe Yin, Malcolm C Scott, and John M Nelson. In-phantom characterisation studies at the birmingham accelerator-generated epithermal neutron source (bagins) bnct facility. *Applied radiation and isotopes*, 61(5):733–738, 2004.
- [13] DL Bleuel, RJ Donahue, BA Ludewigt, and J Vujic. Designing accelerator-based epithermal neutron beams for boron neutron capture therapy. *Medical physics*, 25(9):1725–1734, 1998.
- [14] B Montagnini, N Cerullo, J Esposito, V Giusti, F Mattioda, and R Varone. Spectrum shaping of accelerator-based neutron beams for bnct. *Nuclear Instruments and Methods in Physics Research Section A: Accelerators, Spectrometers, Detectors and Associated Equipment*, 476(1):90–98, 2002.
- [15] Sara J. González and Gustavo A. Santa Cruz. The photon-isoeffective dose in boron neutron capture therapy. *Radiation Research*, 178(6):609–621, 2012. PMID: 23148506.

-
- [16] Jürgen Rassow and Wolfgang A.G. Sauerwein. Prescribing, recording and reporting of bnct. In Wolfgang Sauerwein, Andrea Wittig, Raymond Moss, and Yoshinobu Nakagawa, editors, *Neutron Capture Therapy*, pages 277–285. Springer Berlin Heidelberg, 2012.
 - [17] D.M. Minsky, A.A. Valda, A.J. Kreiner, S. Green, C. Wojnecki, and Z. Ghani. First tomographic image of neutron capture rate in a {BNCT} facility. *Applied Radiation and Isotopes*, 69(12):1858 – 1861, 2011. Special Issue: 14th International Conference on Neutron Capture Therapy.
 - [18] I. Murata, T. Mukai, S. Nakamura, H. Miyamaru, and I. Kato. Development of a thick cdte detector for bnct-spect. *Applied Radiation and Isotopes*, 69(12):1706 – 1709, 2011. Special Issue: 14th International Conference on Neutron Capture Therapy.
 - [19] R.F. Barth, J.A. Coderre, M.G.H. Vincente, and T.E. Blue. Boron neutron capture therapy of cancer: current status and future prospects. *Clin Cancer Res*, 11:3987–4002, 2005.
 - [20] S Martini, S Ristori, A Pucci, C Bonechi, A Becciolini, G Martini, and C Rossi. Borophenylalanine insertion in cationic liposomes for boron neutron capture therapy. *Biophysical Chemistry*, 111:27–34, 2004.
 - [21] T Yamamoto, N Nakai, and A Matsumura. Boron neutron capture therapy for glioblastoma. *J Neurooncol*, 262:143–152, 2008.
 - [22] IB Sivaie and VI Bregadze. L-4-boronophenylalanine (all around the one molecule). *J Neurooncol*, pages 49–60, 2008.
 - [23] S Bortolussi, L Ciani, I Postuma, N Protti, L Reversi, P Bruschi, C Ferrari, L Cansolino, L Panza, S Ristori, and S Altieri. Boron concentration measurements by alpha spectrometry and quantitative neutron autoradiography in cells and tissues treated with different boronated formulations and administration protocols. *Applied Radiation and Isotopes, Pergamon.*, 2013.
 - [24] N.Protti. *The efficacy of Boron Neutron Capture Therapy on small animal models*. PhD thesis, University of Pavia, 2011.
 - [25] X MCNP. Monte carlo team, mcnp—a general purpose monte carlo n-particle transport code, version 5. Technical report, LA-UR-03-1987, Los Alamos National Laboratory, April 2003. The MCNP5 code can be obtained from the Radiation Safety Information Computational Center (RSICC), PO Box 2008, Oak Ridge, TN, 37831-6362, 5.
 - [26] SJ González. Nctplan, the new pc version of macnctplan: improvements and verification of a bnct treatment planning system. In *Proc. 10th Int. Congress on Neutron Capture Therapy for Cancer, Essen, Germany, 2002*, 2002.

- [27] A Stiller, C, S Bielack, S, G Jundt, and E Steliarova-Foucher. *Bone Tumours in European children and adolescents, 1978-1997. Report from Automated Childhood Cancer Information System project*, volume 42. 2006.
- [28] D. M. Parkin, C. A. Stiller, G. J. Draper, and C. A. Bieber. The international incidence of childhood cancer. *International Journal of Cancer*, 42(4):511–520, 1998.
- [29] LAG Ries, MA Smith, JG Gurney, M Linet, T Tamra, JL Young, and GR Bunin. *Cancer Incidence and Survival among Children and Adolescents: United States SEER Program 1975-1995*. National Cancer Institute, Bethesda, MD, 1999. SEER Program. NIH Pub. No. 99-4649.
- [30] M Klein and G Siegal. Osteosarcoma: Anatomic and histologic variants. *American Journal of Clinical Pathology*, 125:555–581, 2006.
- [31] C. Ferrari, C. Zonta, L. Cansolino, A.M. Clerici, A. Gaspari, S. Altieri, S. Bortolussi, S. Stella, P. Bruschi, P. Dionigi, and A. Zonta. Selective uptake of p-boronophenylalanine by osteosarcoma cells for boron neutron capture therapy. *Applied Radiation and Isotopes*, 67(7-8):341 – 344, 2009.
- [32] RC Marcove, V Miké, JV Hajek, AG Levin, and RV Hutter. Osteogenic sarcoma under the age of twenty-one a review of one hundred and forty-five operative cases. *J Bone Joint Surg Am.*, 1970.
- [33] Jaffe N, Bruland S, and Bielack S. *Pediatric and Adolescent Osteosarcoma*. Springer, 2009.
- [34] Piero Picci. Osteosarcoma (osteogenic sarcoma). *Orphanet Journal of Rare Diseases*, page 6, 2007.
- [35] G.M Gutierrez, E Kong, Y Sabbagh, N.E. Brown, J.S. Lee, M.B. Demay, D.M. Thomas, and P.W. Hinds. Impaired bone development and increased mesenchymal progenitor cells in calvaria of *rb1*^{-/-} mice. *Proceedings of the National Academy of Sciences of the United States of America*, pages 18402–18407, 2008.
- [36] B Cherrier, F Gouin, M-F Heymann, JP Thiery, F Redini, D Heymann, and F Duteille. A new experimental rat model of osteosarcoma established by intrafemoral tumor cell inoculation, useful for biology and therapy investigations. *Tumor Biol*, pages 121–130, 2005.
- [37] Hundsdoerfer P., Albrecht M, Ruhl U., Fengler R., Kulozik A.E., and Henze G. Long-term outcome after polychemotherapy and intensive local radiation therapy of high-grade osteosarcoma. *European journal of cancer*, 45, 2009.

-
- [38] Tsuboyama T., Tobuchida J., Kotoura Y., Kasahara K., Hiraoka M., and Nakamura T. Intra-operative radiation therapy for osteosarcoma in the extremities. *Int. Orthop.*, 24(4):202–207, 2000.
 - [39] S Ferrari, Palmerini E, Staals E. L., Mercuri M, Franco B, Picci P, and Bacci G. The treatment of nonmetastatic high grade osteosarcoma of the extremity: Review of the italian rizzoli experience. impact on the future. *Cancer Treatment and Research*, 152:275–287, 2010.
 - [40] Rubén O Farías, Silva Bortolussi, Pablo R Menéndez, and Sara J González. Exploring boron neutron capture therapy for non-small cell lung cancer. *Physica Medica*, 30(8):888–897, 2014.
 - [41] RF Barth. A critical assessment of boron neutron capture therapy: an overview. *J Neurooncol*, 62:111–121, 2003.
 - [42] S. Nievaart, K. Appelman, F. Stecher-Rasmussen, W. Sauerwein, A. Wittig, and R. Moss. Extension of the calibration curve for the pgra facility in petten. *Applied Radiation and Isotopes*, 67(7, Supplement):S362 – S364, 2009.
 - [43] Kent J Riley and Otto K Harling. An improved prompt gamma neutron activation analysis facility using a focused diffracted neutron beam. *Nuclear Instruments and Methods in Physics Research Section B: Beam Interactions with Materials and Atoms*, 143(3):414 – 421, 1998.
 - [44] T.U. Probst. Method for born analysis in boron neutron capture therapy (bnct) a review. *Fresenius J Anal Chem*, 364:391–403, 1999.
 - [45] S Bortolussi. *Boron Neutron Capture Therapy of Dissiminated Tumors*. PhD thesis, Università degli studi di pavia Dottorato di ricerca in fisica, 2008.
 - [46] S. Bortolussi and S. Altieri. Boron concentration measurement in biological tissues by charged particles spectrometry. *Radiat Environ Biophys*, 52:493–503, 2013.
 - [47] M.A Gadan, S Bortolussi, I Postuma, F Ballarini, P Bruschi, N Protti, D Santoro, S Stella, L Cansolino, A Clerici, C Ferrari, A Zonta, C Zonta, and S Altieri. Set-up and calibration of a method to measure ^{10}B concentration in biological samples by neutron autoradiography. *Nuclear Instruments and Methods*, pages 51–56, 2012.
 - [48] Agustina Mariana Portu, Andrés Eugenio Rossini, Mario Alberto Gadan, Omar Alberto Bernaola, Silvia Inés Thorp, Paula Curotto, Emiliano César Cayetano Pozzi, Rómulo Luis Cabrini, and Gisela Saint Martin. Experimental set up for the irradiation of biological samples and nuclear track detectors with uv c. *Reports of Practical Oncology & Radiotherapy*, 11 2014.

- [49] B.G. Cartwright, E.K. Shirk, and P.B. Price. A nuclear-track-recording polymer of unique sensitivity and resolution. *Nuclear Instruments and Methods*, 153:457–460, 1978.
- [50] D.A. Young. Etching of radiation damage in lithium fluoride. *Nature*, 182:375–7, 1958.
- [51] S. Altieri, S. Bortolussi, P. Bruschi, P. Chiari, F. Fossati, S. Stella, U. Prati, L. Roveda, A. Zonta, C. Zonta, C. Ferrari, A. Clerici, R. Nano, and T. Pinelli. Neutron autoradiography imaging of selective boron uptake in human metastatic tumours. *Applied Radiation and Isotopes*, 66(12):1850 – 1855, 2008.
- [52] Andrea Braj. Autoradiografia con neutroni applicata alla terapia per cattura neutronica (tcn) di tumori epatici. Master’s thesis, Università degli studi di Pavia, 1996.
- [53] R.L. Fleisher, P.B. Prince, and R.M. Walker. Nuclear tracks in solids: principles and applications. *University of California Press*, 1975.
- [54] R. Barillon, M. Fromm, A. Chambaudet, R. Katz, J.P. Stoquert, and A. Pape. Bond scission cross sections for alpha particles in cellulose nitrate. *Radiat. Meas.*, 31:71–75, 1999.
- [55] D Nikezic and K.N. Yu. Formation and growth of tracks in nuclear track materials. *Material Science and Engineering*, 46:51–123, 2004.
- [56] N. Bohr. On the constitution of atoms and molecules. i. *Phil. Mag.*, 26:1, 1913.
- [57] H. Bethe. Zur theorie des durchgangs schneller korpuskularstrahlen durch materie. *Annalen der Physik*, 3:325–400, 1930.
- [58] F. Bloch. Bremsvermogen von atomen mit mehreren elektronen. *Zeitschrift fur Physik a Hadrons and nuclei*, 81:363–376, 1933.
- [59] J.F. Ziegler, J.P. Biersack, and U. Littmark. The stopping and range of ions in solids, 1985. Pergamon Press, Oxford, the code is available on <http://www.srim.org>.
- [60] Matthias D. Ziegler James F. Ziegler, Jochen P. Biersack. *SRIM - The Stopping and Range of Ions in Matter*. Pergamon Pr, 2008.
- [61] Altieri S., Bortolussi S., Bruschi P., Chiari P., Fossati F., Stella S., Prati U., Roveda L., Zonta A., Zonta C., Ferrari C., Clerici A., Nano R., and Pinelli T. Neutron autoradiography imaging of selective boron uptake in human metastatic tumours. *Appl. Rad. Isotopes*, 66, 2008.

-
- [62] Wittig A, Michel J, Moss R., Stecher-Rasmussen F., Arlinghaus H., Bendel P., Mauri P., Altieri S., Hilger R., Salvadori P., Menichetti L., Zamenhof R., and Sauerwein W. Boron analysis and boron imaging in biological materials for boron neutron capture therapy (bnct). *Crit Rev Oncol Hematol*, 68, 2008.
 - [63] R. Brun and F. Rademakers. Root – an object oriented data analysis framework,. *Proceedings AIHENP'96 Workshop, Lausanne, Sep. 1996, Nucl. Inst. Meth. Phys. Res., See also <<http://.root.cern.ch/>>*, 1997.
 - [64] Image-pro plus software. Media Cybernetics, Silver Springs, MD.
 - [65] Ana J. Molinari, Silvia I. Thorp, Agustina M. Portu, Gisela Saint Martin, Emiliano C. C. Pozzi, Elisa M. Heber, Silva Bortolussi, Maria E. Itoiz, Romina F. Aromando, Andrea Monti Hughes, Marcela A. Garabalino, Saverio Altieri, Verónica A. Trivillin, and Amanda E. Schwint. Assessing advantages of sequential boron neutron capture therapy (bnct) in an oral cancer model with normalized blood vessels. *Acta Oncologica*, 0(0):1–8, 2014. PMID: 24960584.
 - [66] JW Hopewell, GM Morris, A Schwint, and JA Coderre. The radiobiological principles of boron neutron capture therapy: a critical review. *Applied Radiation and Isotopes*, 69(12):1756–1759, 2011.
 - [67] D Gabel, S. Foster, and R. G. Fairchild. Mc simulations of the biological effect of the $^{10}\text{b}(n,\alpha)^7\text{li}$ reaction in cells and tissues and it's implications for bnct. *Radiat. Res.*, 111:14–25, 1987.
 - [68] BJ Allen. Dose modification factors in boron neutron capture therapy. *Strahlentherapie und Onkologie: Organ der Deutschen Rontgengesellschaft...[et al]*, 169(1):29–33, 1993.
 - [69] BJ Allen, M Bilek, and DE Charlton. Monte carlo calculation of microdosimetry in nitrogen and boron neutron capture reactions. In AlbertH. Soloway, RolfF. Barth, and DavidE. Carpenter, editors, *Advances in Neutron Capture Therapy*, pages 221–224. Springer US, 1993.
 - [70] DE Charlton. Energy deposition in small ellipsoidal volumes by high-let particles: application to thermal neutron dosimetry. *International journal of radiation biology*, 59(3):827–842, 1991.
 - [71] RobertG. Zamenhof. Microdosimetry for boron neutron capture therapy: A review. *Journal of Neuro-Oncology*, 33(1-2):81–91, 1997.
 - [72] T. L. Nichols, G. W. Kabalka, L. F. Miller, M. T. McCormack, and A. Johnson. Implications for clinical treatment from the micrometer site dosimetric calculations in boron neutron capture therapy. *Appl Radiat Isot*, 67(7-8 Suppl):S161–163, Jul 2009.

- [73] T. L. Nichols, L. F. Miller, G. W. Kabalka, and T. M. Dudney. Microdosimetric study for interpretation of outcomes from boron neutron capture therapy clinical trials. *Radiat Prot Dosimetry*, 126(1-4):645–647, 2007.
- [74] T. L. Nichols, L. F. Miller, and G. W. Kabalka. The microdosimetry of boron neutron capture therapy in a randomised ellipsoidal cell geometry. *Radiat Prot Dosimetry*, 116(1-4 Pt 2):466–469, 2005.
- [75] T Goorley, M James, T Booth, F Brown, J Bull, LJ Cox, J Durkee, J Elson, M Fensin, RA Forster, et al. Initial mcnp6 release overview. *Nuclear Technology*, 180(3):298–315, 2012.
- [76] Alfredo Ferrari, Paola R Sala, Alberto Fasso, and Johannes Ranft. Fluka: A multi-particle transport code (program version 2005). Technical report, 2005.
- [77] Koji Niita, Tatsuhiko Sato, Hiroshi Iwase, Hiroyuki Nose, Hiroshi Nakashima, and Lembit Sihver. Phits—a particle and heavy ion transport code system. *Radiation measurements*, 41(9):1080–1090, 2006.
- [78] Sea Agostinelli, John Allison, K al Amako, J Apostolakis, H Araujo, P Arce, M Asai, D Axen, S Banerjee, G Barrand, et al. Geant4—a simulation toolkit. *Nuclear instruments and methods in physics research section A: Accelerators, Spectrometers, Detectors and Associated Equipment*, 506(3):250–303, 2003.
- [79] Gerard M Morris, Jeffrey A Coderre, John W Hopewell, Peggy L Micca, Marta M Nawrocky, Hungyuan B Liu, and Anthony Bywaters. Response of the central nervous system to boron neutron capture irradiation: Evaluation using rat spinal cord model. *Radiotherapy and Oncology*, 32(3):249–255, 1994.
- [80] H Fukuda, J Hiratsuka, C Honda, T Kobayashi, K Yoshino, H Karashima, J Takahashi, Y Abe, K Kanda, M Ichihashi, et al. Boron neutron capture therapy of malignant melanoma using with special reference to evaluation of radiation dose and damage to the normal skin. *Radiation research*, 138(3):435–442, 1994.
- [81] Jeffrey A Coderre, Michael S Makar, Peggy L Micca, Marta M Nawrocky, Hungyuan B Liu, Darrel D Joel, Daniel N Slatkin, and Howard I Amols. Derivations of relative biological effectiveness for the high-let radiations produced during boron neutron capture irradiations of the 9l rat gliosarcoma in vitro and in vivo. *International Journal of Radiation Oncology* Biology* Physics*, 27(5):1121–1129, 1993.

-
- [82] Yoshinobu Nakagawa, Kyonghon Pooh, Toru Kobayashi, Teruyoshi Kageji, Shinichi Uyama, Akira Matsumura, and Hiroaki Kumada. Clinical review of the japanese experience with boron neutron capture therapy and a proposed strategy using epithermal neutron beams. *Journal of neuro-oncology*, 62(1-2):87–99, 2003.
 - [83] S Incerti, H Seznec, M Simon, Ph Barberet, C Habchi, and Ph Moretto. Monte carlo dosimetry for targeted irradiation of individual cells using a microbeam facility. *Radiation protection dosimetry*, 2009.
 - [84] S Incerti, A Ivanchenko, M Karamitros, A Mantero, P Moretto, HN Tran, B Mascialino, C Champion, VN Ivanchenko, MA Bernal, et al. Comparison of geant4 very low energy cross section models with experimental data in water. *Medical physics*, 37(9):4692–4708, 2010.
 - [85] LE Farr, WH Sweet, HB Locksley, and JS Robertson. Neutron capture therapy of gliomas using boron. *Transactions of the American Neurological Association*, 13(79th Meeting):110–113, 1953.
 - [86] John T Godwin, Lee E Farr, William H Sweet, and James S Robertson. Pathological study of eight patients with glioblastoma multiforme treated by neutroncapture therapy using boron 10. *Cancer*, 8(3):601–615, 1955.
 - [87] A Zonta, U Prati, L Roveda, C Ferrari, P Valsecchi, F Trotta, A DeRobertto, C Rossella, G Bernardi, and R Nano. La terapia per cattura neutronica (bnct) dei tumori epatici. *Boll Soc Med Chir*, 114(2):123–144, 2000.
 - [88] A Zonta, T Pinelli, U Prati, L Roveda, C Ferrari, AM Clerici, C Zonta, G Mazzini, P Dionigi, S Altieri, et al. Extra-corporeal liver bnct for the treatment of diffuse metastases: What was learned and what is still to be learned. *Applied Radiation and Isotopes*, 67(7):S67–S75, 2009.
 - [89] Berta M Roth, Marcelo R Bonomi, and Sara J Gonzalez. Bnct clinical trials of skin melanoma patients in argentina. 2006.
 - [90] SJ González, MR Bonomi, GA Santa Cruz, HR Blaumann, OA Calzetta Larrieu, P Menéndez, R Jiménez Rebagliati, J Longhino, DB Feld, MA Dagrosa, et al. First bnct treatment of a skin melanoma in argentina: dosimetric analysis and clinical outcome. *Applied radiation and isotopes*, 61(5):1101–1105, 2004.
 - [91] Kristjan R Jessen and Rhona Mirsky. Glial cells in the enteric nervous system contain glial fibrillary acidic protein. 1980.
 - [92] Jenkins GW and Tortora GJ. *Anatomy and Physiology from science to life*. Wiley-VCH, 2013.

- [93] Michael Neumann, Ulrike Kunz, Heiner Lehmann, and Detlef Gabel. Determination of the subcellular distribution of mercaptoundecahydro-closo-dodecaborate (bsh) in human glioblastoma multiforme by electron microscopy. *Journal of Neuro-Oncology*, 57(2):97–104, 2002.
- [94] Subhash Chandra and Daniel R Lorey. Sims ion microscopy imaging of boronophenylalanine (bpa) and ^{13}C ^{15}N -labeled phenylalanine in human glioblastoma cells: relevance of subcellular scale observations to bpa-mediated boron neutron capture therapy of cancer. *International Journal of Mass Spectrometry*, 260(2):90–101, 2007.
- [95] MS Herrera, SJ González, DM Minsky, and AJ Kreiner. Evaluation of performance of an accelerator-based bnct facility for the treatment of different tumor targets. *Physica Medica*, 29(5):436–446, 2013.
- [96] E Bisceglie, P Colangelo, N Colonna, P Santorelli, and V Variale. On the optimal energy of epithermal neutron beams for bnct. *Physics in medicine and biology*, 45(1):49, 2000.
- [97] VA Nievaart, RL Moss, JL Kloosterman, THJJ van der Hagen, and H van Dam. A parameter study to determine the optimal source neutron energy in boron neutron capture therapy of brain tumours. *Physics in medicine and biology*, 49(18):4277, 2004.
- [98] S Sakamoto, WS Kiger III, and OK Harling. Sensitivity studies of beam directionality, beam size, and neutron spectrum for a fission converter-based epithermal neutron beam for boron neutron capture therapy. *Medical physics*, 26(9):1979–1988, 1999.
- [99] LE Farr, WH Sweet, JS Robertson, GS Forster, HB Locksley, DL Sutherland, ML Mendelsohn, and Stickey EE. Neutron capture therapy with boron in the treatment of glioblastoma multiforme. *Am J Roentgenol*, 71:279–291, 1954.
- [100] WH Sweet, AH Soloway, and GL Brownell. Boron-slow neutron capture therapy of gliomas. *Acta Radiologica: Therapy, Physics, Biology*, 1(2):114–121, 1963.
- [101] H Hatanaka, K Sano, and H Yasukochi. Clinical results of boron neutron capture therapy. In *Progress in neutron capture therapy for cancer*, pages 561–568. Springer, 1992.
- [102] Yutaka Mishima, Masamitsu Ichihashi, Susumu Hatta, Chihiro Honda, Akihiro Sasase, Keizo Yamamura, Keiji Kanda, Tooru Kobayashi, and Hiroshi Fukuda. Selective thermal neutron capture therapy and diagnosis of malignant melanoma: from basic studies to first clinical treatment. In *Clinical Aspects of Neutron Capture Therapy*, pages 251–260. Springer, 1989.

-
- [103] KJ Riley, PJ Binns, and OK Harling. Performance characteristics of the mit fission converter based epithermal neutron beam. *Physics in medicine and biology*, 48(7):943, 2003.
 - [104] CJ Tung, YL Wang, FY Hsu, SL Chang, and YW H Liu. Characteristics of the new thor epithermal neutron beam for bnct. *Applied radiation and isotopes*, 61(5):861–864, 2004.
 - [105] Iiro Auterinen, Pekka Hiismäki, Petri Kotiluoto, Rolf J Rosenberg, Seppo Salmenhaara, Tiina Seppälä, Tom Serén, Vesa Tanner, Carita Aschan, Mika Kortensniemi, et al. Metamorphosis of a 35 year-old triga reactor into a modern bnct facility. In *Frontiers in neutron capture therapy*, pages 267–275. Springer, 2001.
 - [106] Yoshinori Sakurai and Tooru Kobayashi. The medical-irradiation characteristics for neutron capture therapy at the heavy water neutron irradiation facility of kyoto university research reactor. *Medical physics*, 29(10):2328–2337, 2002.
 - [107] PJ Binns, KJ Riley, and OK Harling. Dosimetric comparison of six epithermal neutron beams using an ellipsoidal water phantom. *Research and Development in Neutron Capture Therapy*, pages 405–410, 2002.
 - [108] Hanna Koivunoro et al. Dosimetry and dose planning in boron neutron capture therapy: Monte carlo studies. 2012.
 - [109] Tooru Kobayashi, Gerard Bengua, Kenichi Tanaka, and Yoshinobu Nakagawa. Variations in lithium target thickness and proton energy stability for the near-threshold 7Li (p, n) 7Be accelerator-based bnct. *Physics in medicine and biology*, 52(3):645, 2007.
 - [110] S Halfon, M Paul, A Arenshtam, D Berkovits, M Bisyakoev, I Eliyahu, G Feinberg, N Hazenshrung, D Kijel, A Nagler, et al. High-power liquid-lithium target prototype for accelerator-based boron neutron capture therapy. *Applied Radiation and Isotopes*, 69(12):1654–1656, 2011.
 - [111] CL Lee and X-L Zhou. Thick target neutron yields for the 7Li (p, n) 7Be reaction near threshold. *Nuclear Instruments and Methods in Physics Research Section B: Beam Interactions with Materials and Atoms*, 152(1):1–11, 1999.
 - [112] AA Burlon, AJ Kreiner, AA Valda, DM Minsky, HR Somacal, ME Debray, and P Stoliar. Optimization of a neutron production target and a beam shaping assembly based on the 7Li (p, n) 7Be reaction for bnct. *Nuclear Instruments and Methods in Physics Research Section B: Beam Interactions with Materials and Atoms*, 229(1):144–156, 2005.

- [113] Brandon W Blackburn, Jacquelyn C Yanch, and Robert E Klinkowstein. Development of a high-power water cooled beryllium target for use in accelerator-based boron neutron capture therapy. *Medical physics*, 25(10):1967–1974, 1998.
- [114] J Esposito, P Colautti, S Fabritsiev, A Gervash, R Giniyatulin, VN Lomasov, A Makhankov, I Mazul, A Pisent, A Pokrovsky, et al. Be target development for the accelerator-based spes-bnct facility at infn legnaro. *Applied Radiation and Isotopes*, 67(7):S270–S273, 2009.
- [115] C-K Chris Wang and Brian R Moore. Thick beryllium target as an epithermal neutron source for neutron capture therapy. *Medical physics*, 21(10):1633–1638, 1994.
- [116] WB Howard, SM Grimes, TN Massey, SI Al-Quraishi, DK Jacobs, CE Brient, and JC Yanch. Measurement of the thick-target $^9\text{Be}(p, n)$ neutron energy spectra. *Nuclear science and engineering*, 138(2):145–160, 2001.
- [117] C Ceballos, J Esposito, S Agosteo, P Colautti, V Conte, D Moro, and A Pola. Towards the final bsa modeling for the accelerator-driven bnct facility at infn lnl. *Applied Radiation and Isotopes*, 69(12):1660–1663, 2011.
- [118] G Feinberg, M Paul, A Arenshtam, D Berkovits, D Kijel, A Nagler, and I Silverman. Lilit-a liquid-lithium target as an intense neutron source for nuclear astrophysics at the soreq applied research accelerator facility. *Nuclear Physics A*, 827(1):590c–592c, 2009.
- [119] Tooru Kobayashi, Kuniaki Miura, Noriyosu Hayashizaki, and Masanori Aritomi. Development of liquid-lithium film jet-flow for the target of $^7\text{Li}(p, n)^7\text{Be}$ reactions for bnct. *Applied Radiation and Isotopes*, 88:198–202, 2014.
- [120] JC Yanch, X-L Zhou, RE Shefer, and RE Klinkowstein. Accelerator-based epithermal neutron beam design for neutron capture therapy. *Medical physics*, 19(3):709–721, 1992.
- [121] Stuart Green. Developments in accelerator based boron neutron capture therapy. *Radiation Physics and Chemistry*, 51(4):561–569, 1998.
- [122] BF Bayanov, VP Belov, ED Bender, MV Bokhovko, GI Dimov, VN Kononov, OE Kononov, NK Kuksanov, VE Palchikov, VA Pivovarov, et al. Accelerator-based neutron source for the neutron-capture and fast neutron therapy at hospital. *Nuclear Instruments and Methods in Physics Research Section A: Accelerators, Spectrometers, Detectors and Associated Equipment*, 413(2):397–426, 1998.

-
- [123] AJ Kreiner, JW Kwan, AA Burlon, H Di Paolo, E Henestroza, DM Minsky, AA Valda, ME Debray, and H Somacal. A tandem-electrostatic-quadrupole for accelerator-based bnct. *Nuclear Instruments and Methods in Physics Research Section B: Beam Interactions with Materials and Atoms*, 261(1):751–754, 2007.
 - [124] S Halfon, M Paul, D Steinberg, A Nagler, A Arenshtam, D Kijel, I Polacheck, and M Srebnik. High power accelerator-based boron neutron capture with a liquid lithium target and new applications to treatment of infectious diseases. *Applied Radiation and Isotopes*, 67(7):S278–S281, 2009.
 - [125] A Pisent, P Colautti, J Esposito, L De Nardo, V Conte, D Agosteo, G Jori, PA Posocco, LB Tecchio, R Tinti, et al. Progress on the accelerator based spes-bnct project at infn legnaro. In *Journal of Physics: Conference Series*, volume 41, page 391. IOP Publishing, 2006.
 - [126] H Tanaka, Y Sakurai, M Suzuki, S Masunaga, T Mitsumoto, K Fujita, G Kashino, Y Kinashi, Y Liu, M Takada, et al. Experimental verification of beam characteristics for cyclotron-based epithermal neutron source (c-bens). *Applied Radiation and Isotopes*, 69(12):1642–1645, 2011.
 - [127] Horst Liskien and Arno Paulsen. Neutron production cross sections and energies for the reactions $7\text{ li (p, n) }7\text{ be}$ and $7\text{ li (p, n) }7\text{ be}^*$. *Atomic data and nuclear data tables*, 15(1):57–84, 1975.
 - [128] S Mathot. The trasco-spes rfq. 2004.
 - [129] M Comunian, G Lamanna, and A Pisent. Trasco rfq design. *LNL TRASCO-note*, 1(00), 2000.
 - [130] S Agosteo, P Colautti, J Esposito, A Fazzi, MV Introini, and A Pola. Characterization of the energy distribution of neutrons generated by 5mev protons on a thick beryllium target at different emission angles. *Applied Radiation and Isotopes*, 69(12):1664–1667, 2011.
 - [131] H Kumada, T Nakamura, M Komeda, and A Matsumura. Development of a new multi-modal monte-carlo radiotherapy planning system. *Applied Radiation and Isotopes*, 67(7):S118–S121, 2009.
 - [132] AY Chen, Y-WH Liu, and RJ Sheu. Radiation shielding evaluation of the bnct treatment room at thor: A tort-coupled mcnp monte carlo simulation study. *Applied Radiation and Isotopes*, 66(1):28–38, 2008.
 - [133] H Kumada, K Yamamoto, T Yamamoto, K Nakai, Y Nakagawa, T Kageji, and A Matsumura. Improvement of dose calculation accuracy for bnct dosimetry by the multi-voxel method in jcds. *Applied radiation and isotopes*, 61(5):1045–1050, 2004.

- [134] Jacopo Valsecchi. Thermal and epithermal neutron beam tailoring for bnct research at cn proton accelerator of infn legnaro national laboratories. Master's thesis, University of Pavia.
- [135] D Rorer, G Wambersie, et al. Current status of neutron capture therapy. *IAEA, 2001 (8)*, pages 75–77, 2001.
- [136] Ana J Molinari, Emiliano CC Pozzi, Andrea Monti Hughes, Elisa M Heber, Marcela A Garabalino, Silvia I Thorp, Marcelo Miller, Maria E Itoiz, Romina F Aromando, David W Nigg, et al. Tumor blood vessel “normalization” improves the therapeutic efficacy of boron neutron capture therapy (bnct) in experimental oral cancer. *Radiation research*, 177(1):59–68, 2011.
- [137] Minoru Suzuki, Shin-Ichiro Masunaga, Yuko Kinashi, Masao Takagaki, Yoshinori Sakurai, Toru Kobayashi, and Koji Ono. The effects of boron neutron capture therapy on liver tumors and normal hepatocytes in mice. *Cancer Science*, 91(10):1058–1064, 2000.
- [138] Jeffrey A Coderre, Julie C Turcotte, Kent J Riley, Peter J Binns, Otto K Harling, and WS Kiger. Boron neutron capture therapy: cellular targeting of high linear energy transfer radiation. *Technology in cancer research & treatment*, 2(5):355–375, 2003.
- [139] Jingli Liu Kiger, W Steadman Kiger III, Kent J Riley, Peter J Binns, Hemant Patel, John W Hopewell, Otto K Harling, Paul M Busse, and Jeffrey A Coderre. Functional and histological changes in rat lung after boron neutron capture therapy. 2009.
- [140] L Cansolino, AM Clerici, C Zonta, P Dionigi, G Mazzini, R Di Liberto, S Altieri, F Ballarini, S Bortolussi, MP Carante, et al. Comparative study of the radiobiological effects induced on adherent vs suspended cells by bnct, neutrons and gamma rays treatments. *Applied Radiation and Isotopes*, 2015.
- [141] Jeffrey A Coderre and Gerard M Morris. The radiation biology of boron neutron capture therapy. *Radiation research*, 151(1):1–18, 1999.
- [142] Sara J González and Gustavo A Santa Cruz. The photon-isoeffective dose in boron neutron capture therapy. *Radiation research*, 178(6):609–621, 2012.
- [143] Keiichi Shibata, Osamu Iwamoto, Tsuneo Nakagawa, Nobuyuki Iwamoto, Akira Ichihara, Satoshi Kunieda, Satoshi Chiba, Kazuyoshi Furutaka, Naohiko Otuka, Takaaki Ohasawa, et al. Jendl-4.0: a new library for nuclear science and engineering. *Journal of Nuclear Science and Technology*, 48(1):1–30, 2011.

-
- [144] MA Gadan, S Bortolussi, I Postuma, F Ballarini, P Bruschi, N Protti, D Santoro, S Stella, L Cansolino, A Clerici, et al. Set-up and calibration of a method to measure ^{10}B concentration in biological samples by neutron autoradiography. *Nuclear Instruments and Methods in Physics Research Section B: Beam Interactions with Materials and Atoms*, 274:51–56, 2012.
 - [145] Silva Bortolussi, Laura Ciani, Ian Postuma, Nicoletta Protti, Luca Reversi, Piero Bruschi, Cinzia Ferrari, Laura Cansolino, Luigi Panza, Sandra Ristori, et al. Boron concentration measurements by alpha spectrometry and quantitative neutron autoradiography in cells and tissues treated with different boronated formulations and administration protocols. *Applied Radiation and Isotopes*, 88:78–80, 2014.
 - [146] Laura Ciani, Silva Bortolussi, Ian Postuma, Laura Cansolino, Cinzia Ferrari, Luigi Panza, Saverio Altieri, and Sandra Ristori. Rational design of gold nanoparticles functionalized with carboranes for application in boron neutron capture therapy. *International journal of pharmaceutics*, 458(2):340–346, 2013.
 - [147] Paolo Colautti, Davide Moro, S Chiriotti, Valeria Conte, Laura Evangelista, Saverio Altieri, Silvia Bortolussi, Nicoletta Protti, and Ian Postuma. Microdosimetric measurements in the thermal neutron irradiation facility of lena reactor. *Applied Radiation and Isotopes*, 88:147–152, 2014.
 - [148] Nicoletta Protti, Sergio Manera, Michele Prata, Daniele Alloni, Francesca Ballarini, Andrea Borio di Tigliole, Silva Bortolussi, Piero Bruschi, Marcella Cagnazzo, Maria Garioni, et al. Gamma residual radioactivity measurements on rats and mice irradiated in the thermal column of a triga mark ii reactor for bnct. *Health physics*, 107(6):534–541, 2014.
 - [149] S Altieri, F Ballarini, S Bortolussi, I Postuma, N Protti, R Nano, C Rovelli, L Cansolino, AM Clerici, C Ferrari, et al. Neutron capture therapy research at infn and university of pavia. In *ANTICANCER RESEARCH*, volume 34, pages 7479–7479. INT INST ANTICANCER RESEARCH EDITORIAL OFFICE 1ST KM KAPANDRITIOU-KALAMOU RD KAPANDRITI, PO BOX 22, ATHENS 19014, GREECE, 2014.
 - [150] Daniela Pietrangeli, Angela Rosa, Antonietta Pepe, Saverio Altieri, Silva Bortolussi, Ian Postuma, Nicoletta Protti, Cinzia Ferrari, Laura Cansolino, Anna Maria Clerici, et al. Water-soluble carboranyl-phthalocyanines for bnct. synthesis, characterization, and in vitro tests of the zn (ii)-nido-carboranyl-hexylthiophthalocyanine. *Dalton Transactions*, 2015.

- [151] MP Carante, S Altieri, S Bortolussi, I Postuma, N Protti, and F Ballarini. Modeling radiation-induced cell death: role of different levels of dna damage clustering. *Radiation and environmental biophysics*, pages 1–12, 2015.
- [152] Agustina Portu, Ian Postuma, Mario Alberto Gadan, Gisela Saint Martin, María Silvina Olivera, Saverio Altieri, Nicoletta Protti, and Silva Bortolussi. Inter-comparison of boron concentration measurements at infn-university of pavia (italy) and cnea (argentina). *Applied Radiation and Isotopes*, 2015.
- [153] N Protti, S Geninatti-Crich, D Alberti, S Lanzardo, A Deagostino, A Toppino, S Aime, F Ballarini, S Bortolussi, P Bruschi, et al. Evaluation of the dose enhancement of combined $^{10}\text{B} + ^{157}\text{Gd}$ neutron capture therapy (nct). *Radiation Protection Dosimetry*, page ncv300, 2015.